

④

GL-TR-89-0093

AD-A210 431

A STUDY OF THE IMPACT OF SIMULATED 183 GHZ WATER VAPOR RETRIEVALS ON NUMERICAL WEATHER PREDICTION

C. Grassotti, R. Isaacs, R. N. Hoffman, J.-F. Louis, T. Nehr Korn, and M. Mickelson

Atmospheric and Environmental Research, Inc.
840 Memorial Drive
Cambridge, MA 02139-3794

31 March 1989

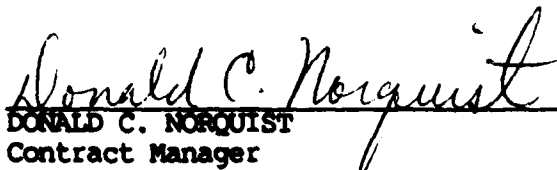
Scientific Report No. 6

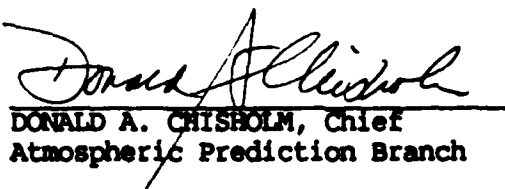
Approved for public release; distribution unlimited

GEOPHYSICS LABORATORY
AIR FORCE SYSTEMS COMMAND
UNITED STATES AIR FORCE
HANS COM AFB, MASSACHUSETTS 01731-5000

DTIC
S
2

This technical report has been reviewed and is approved for publication.


DONALD C. NORQUIST
Contract Manager


DONALD A. CHISHOLM, Chief
Atmospheric Prediction Branch

FOR THE COMMANDER


ROBERT A. MCCLATCHEY, Director
Atmospheric Sciences Division

This report has been reviewed by the ESD Public Affairs Office (PA) and is releasable to the National Technical Information Service (NTIS).

Qualified requestors may obtain additional copies from the Defense Technical Information Center. All others should apply to the National Technical Information Service.

If your address has changed, or if you wish to be removed from the mailing list, or if the addressee is no longer employed by your organization, please notify AFGL/DAA, Hanscom AFB, MA 01731. This will assist us in maintaining a current mailing list.

Do not return copies of this report unless contractual obligations or notices on a specific document require that it be returned.

REPORT DOCUMENTATION PAGE

1a. REPORT SECURITY CLASSIFICATION Unclassified			1b. RESTRICTIVE MARKINGS		
2a. SECURITY CLASSIFICATION AUTHORITY			3. DISTRIBUTION/AVAILABILITY OF REPORT Approved for public release; distribution unlimited.		
2b. DECLASSIFICATION/DOWNGRADING SCHEDULE			4. PERFORMING ORGANIZATION REPORT NUMBER(S)		
6a. NAME OF PERFORMING ORGANIZATION Atmospheric and Environmental Research, Inc.			6b. OFFICE SYMBOL (If applicable)		5. MONITORING ORGANIZATION REPORT NUMBER(S) GL-TR-89-0093
6c. ADDRESS (City, State, and ZIP Code) 840 Memorial Drive Cambridge, MA 02139-3794			7a. NAME OF MONITORING ORGANIZATION Geophysics Laboratory		
8a. NAME OF FUNDING/SPONSORING ORGANIZATION			8b. OFFICE SYMBOL (If applicable)		7b. ADDRESS (City, State, and ZIP Code) Hanscom AFB, MA 01731-5000
8c. ADDRESS (City, State, and ZIP Code)			9. PROCUREMENT INSTRUMENT IDENTIFICATION NUMBER F19628-86-C-0141		
			10. SOURCE OF FUNDING NUMBERS		
			PROGRAM ELEMENT NO. 35160F	PROJECT NO. 6670	TASK NO. 10
			WORK UNIT ACCESSION NO. CB		
11. TITLE (Include Security Classification) A Study of the Impact of Simulated 183 GHZ Water Vapor Retrievals on Numerical Weather Prediction					
12. PERSONAL AUTHOR(S) C. Grassotti, R. Isaacs, R.N. Hoffman, J.-F. Louis, T. Nehrkorn, and M. Mickelson					
13a. TYPE OF REPORT Scientific Report #6		13b. TIME COVERED FROM TO		14. DATE OF REPORT (Year, Month, Day) 31 March 1989	
				15. PAGE COUNT 184	
16. SUPPLEMENTARY NOTATION					
17. COSATI CODES			18. SUBJECT TERMS (Continue on reverse if necessary and identify by block number)		
FIELD	GROUP	SUB-GROUP	Data assimilation; Observing system simulation experiment; SSM/T; Numerical weather prediction; Satellite observations		
19. ABSTRACT (Continue on reverse if necessary and identify by block number)					
<p>Observing system simulation experiments (OSSEs) are conducted to assess the impact of the Special Sensor Microwave 183 GHz (SSM/T-2) water vapor sounder and the associated SSM/T-1 temperature sounder. Analyzed and forecast meteorological fields are improved by the addition of the SSM/T-1,2 temperature and humidity profiles. The greatest impacts occur in the Southern Hemisphere in the scenario when the civilian infrared sounder data are not available, i.e. when TOVS data are not assimilated. In order to calibrate the OSSE results, comparisons are made with real data observing system experiments (OSEs). These comparisons indicate that the expected impact of adding actual SSM/T-1,2 data with the stated geographic coverage and error characteristics, in the absence of TOVS data, would improve 500 mb height forecasts by approximately 12 hours in the Southern Hemisphere. However adding SSM/T-1,2 would have smaller impacts (8 h or less) in the Southern Hemisphere if added to the available TOVS data. Improvements for 200 mb wind forecasts in the tropics are: 36 hours for SSM/T-1,2 alone and 12 hours for SSM/T-1,2 and TOVS together. Little impact was seen in</p>					
20. DISTRIBUTION/AVAILABILITY OF ABSTRACT <input type="checkbox"/> UNCLASSIFIED/UNLIMITED <input checked="" type="checkbox"/> SAME AS RPT. <input type="checkbox"/> DTIC USERS			21. ABSTRACT SECURITY CLASSIFICATION Unclassified		
22a. NAME OF RESPONSIBLE INDIVIDUAL D. Norquist			22b. TELEPHONE (Include Area Code) 617-377-2962		22c. OFFICE SYMBOL AFGL/LYP

19. Abstract (continued)

moisture forecasts from the addition of SSM data, but moisture and cloud analyses were clearly improved when the SSM data was assimilated; a decrease in global root mean square error of about 5% was indicated.


Accession Number	
NTIS	<input checked="" type="checkbox"/>
DTIC	<input type="checkbox"/>
Unannounced	<input type="checkbox"/>
JPRS	
By	
Distribution /	
Availability Codes	
Special and/or	
Dist	Special
A-1	

TABLE OF CONTENTS

	<u>Page</u>
1. Introduction	1
2. Background	3
2.1 General OSSE strategy	3
2.2 Local biases from sensor simulation studies	7
3. Data Sources	8
3.1 Nature run	8
3.2 Simulated observations	9
4. Sensor Simulation Study of SSM/T D-matrix Retrievals	17
4.1 Generating dependent and independent data sets	17
4.2 Preprocessing set 1 and set 2 profiles	18
4.3 Computing brightness temperatures from geophysical profiles.....	18
4.4 D-matrix and statistical retrievals	21
4.5 Simulation of D-matrix retrievals	22
5. Statistical Analysis of Simulated Sensor Errors	32
5.1 Relative humidity retrieval error statistics	32
5.2 Temperature retrieval error statistics	34
6. OSSE Design	71
6.1 AFGL forecast and analysis system	71
6.1.1 Analysis	71
6.1.2 Forecast and initialization	74
6.2 Verification procedures	75
6.3 Spinup experiment	76
6.4 Schedule of impact experiments	76
7. OSSE Results	80
7.1 Subjective synoptic evaluation	80
7.2 Objective statistical evaluation	86
7.3 Evaluation of zonal cross sections	87
7.4 Calibration with OSE results	91
7.4.1 Rms difference between OSSE forecasts and radiosondes	92
7.4.2 Calibration procedure	94
7.4.3 Calibration results	96
7.4.4 Forecast biases	97
8. Summary and Conclusions	151
References	154
Appendix A. Microwave sounder fields-of-view for the 183 GHz OSSE	A-1

LIST OF TABLES

<u>Table</u>	<u>Page</u>
3.1 OESDs used to simulate FGGE IIB data for November	12
3.2 Biases used to simulate TIROS temperature retrievals for November	13
4.1 Geophysical categories used to generate retrieval error statistics. Also shown are the number of samples in each category.	26
4.2 Microwave mission sensor characteristics	27
4.3 Cloud type characteristics	28
4.4 Surface emissivity used for various surface types during radiative transfer simulations	29
4.5 183 GHz water vapor profile retrieval techniques	30
6.1 OESDs used in data assimilation experiments	77
7.1 Predictability impacts (days) for height (a), wind (b) and relative humidity (c) for the N.H. extratropics. Impacts for cases with R^2 less than 0.25 (i.e. for correlations less than 0.5) are not shown.	99
7.2 Predictability impacts (days) for height (a), wind (b) and relative humidity (c) for the tropics. Impacts for cases with R^2 less than 0.25 (i.e. for correlations less than 0.25) are not shown.	100
7.3 Predictability impacts (days) for height (a), wind (b) and relative humidity (c) for the S.H. extratropics. Impacts for cases with R^2 less than 0.25 (i.e. for correlations less than 0.5) are not shown.	101
7.4 Growth rate of forecast bias for height (m/day), temperature (K/day) and relative humidity (%/day for the N.H. extratropics. Impacts for cases with R^2 less than 0.64 (i.e. for correlations less than 0.8) are not shown.	102
A-1 DMSP satellite platform characteristics	A-4
A-2 Sensor characteristics for the SSM/T-1 and SSM/T-2 sensors	A-5

LIST OF FIGURES

<u>Figure</u>		<u>Page(s)</u>
3.1	Data coverage by standard FGGE IIb observations. Raob heights at $\sigma=0.5$ (a), cloud track winds at $\sigma=0.86$ and 0.72 (b), and $\sigma=0.27$ and 0.22 (c), aircraft winds at $\sigma=0.27$ and 0.22 (d), and TOVS heights at $\sigma=0.5$ (e)	14
4.1	Data coverage by SSM data. Height observations at $\sigma=0.5$	31
5.1	Relative humidity retrieval bias, Class 1	36
5.2	Relative humidity retrieval bias, Class 2	37
5.3	Relative humidity retrieval bias, Class 3	38
5.4	Relative humidity retrieval bias, Class 4	39
5.5	Relative humidity retrieval bias, Class 5	40
5.6	Relative humidity retrieval bias, Class 6	41
5.7	Relative humidity retrieval bias, Class 7	42
5.8	Relative humidity retrieval bias, Class 8	43
5.9	Relative humidity retrieval bias, Class 9	44
5.10	Relative humidity retrieval bias, Class 10	45
5.11	Relative humidity retrieval error, standard deviation, Class 1	46
5.12	Relative humidity retrieval error, standard deviation, Class 2	47
5.13	Relative humidity retrieval error, standard deviation, Class 3	48
5.14	Relative humidity retrieval error, standard deviation, Class 4	49
5.15	Relative humidity retrieval error, standard deviation, Class 5	50
5.16	Relative humidity retrieval error, standard deviation, Class 6	51
5.17	Relative humidity retrieval error, standard deviation, Class 7	52

LIST OF FIGURES

<u>Figure</u>		<u>Page(s)</u>
5.18	Relative humidity retrieval error, standard deviation, Class 8	53
5.19	Relative humidity retrieval error, standard deviation, Class 9	54
5.20	Relative humidity retrieval error, standard deviation, Class 10	55
5.21	Relative humidity retrieval vertical correlations with 1000 mb error, Class 1	56
5.22	Relative humidity retrieval vertical correlations with 500 mb error, Class 1	57
5.23	Temperature retrieval bias, Class 1	58
5.24	Temperature retrieval bias, Class 2	59
5.25	Temperature retrieval bias, Class 3	60
5.26	Temperature retrieval bias, Class 4	61
5.27	Temperature retrieval bias, Class 5	62
5.28	Temperature retrieval error, standard deviation, Class 1	63
5.29	Temperature retrieval error, standard deviation, Class 2	64
5.30	Temperature retrieval error, standard deviation, Class 3	65
5.31	Temperature retrieval error, standard deviation, Class 4	66
5.32	Temperature retrieval error, standard deviation, Class 5	67
5.33	Temperature retrieval vertical correlations with 1000 mb error, Class 1	68
5.34	Temperature retrieval vertical correlations with 500 mb error, Class 1	69
5.35	Temperature retrieval vertical correlations with 50 mb error, Class 1	70

LIST OF FIGURES

<u>Figure</u>		<u>Page(s)</u>
5.1	Vertical height error correlations of simulated SSM retrievals based on collocation with radiosondes. Solid curve is least squares fit to data used in OI.	78
6.2	Horizontal height error correlations of simulated SSM retrievals based on collocation with radiosondes. Shown are observed errors at 300 mb, 500 mb and function used in OI.	79
7.1	Northern hemisphere height analyses and analysis errors at 00 GMT 23 November. The contour interval in the 500 mb analyses is 80 m, at 1000 mb it is 40 m. The contour interval of the error maps is 40 m at both 1000 and 500 mb. Shown are 500 mb nature data (a), 1000 mb nature data (b).	103
7.2	Format as in Fig. 7.1. STATSAT analysis (a) and analysis error (b) at 500 mb, and at 1000 mb (c,d).	104
7.3	Format as in Fig. 7.1. SSMSAT analysis (a) and analysis error (b) at 500 mb, and at 1000 mb (c,d). Raob height residuals at $\sigma=0.5$ used in the analyses are marked by crosses in panel b.	106
7.4	Format as in Fig. 7.1. SSM+TOVS analysis (a) and analysis error (b) at 500 mb, and at 1000 mb (c,d). Raob height residuals at $\sigma=0.5$ used in the analyses are marked by crosses in panel b.	108
7.5	Northern hemisphere height analyses and analysis errors at 00 GMT 25 November. The contour interval in the 500 mb analyses is 80 m, at 1000 mb it is 40 m. The contour interval of the error maps is 40 m at both 1000 and 500 mb. Shown are 500 mb nature data (a), 1000 mb nature data (b).	110
7.6	Format as in Fig. 7.5. STATSAT analysis (a) and analysis error (b) at 500 mb, and at 1000 mb (c,d).	111
7.7	Format as in Fig. 7.5. SSMSAT analysis (a) and analysis error (b) at 500 mb, and at 1000 mb (c,d).	113
7.8	Format as in Fig. 7.5. SSM+TOVS analysis (a) and analysis error (b) at 500 mb, and at 1000 mb (c,d).	114
7.9	Northern hemisphere SSMSAT (a) and SSM+TOVS (b) analysis errors at 500 mb for 00 GMT 22 November.	117

LIST OF FIGURES

<u>Figure</u>		<u>Page(s)</u>
7.10	Northern hemisphere SSM+TOVS first guess errors at 500 mb (a) and 1000 mb (b) for 00 GMT 23 November. Raob height residuals at $\sigma=0.5$ used in the analysis are marked by crosses in panel a.	118
7.11	Southern hemisphere height analyses and analysis errors at 00 GMT 25 November. The contour interval in the 500 mb analyses is 80 m, at 1000 mb it is 40 m. The contour interval of the error maps is 40 m at both 1000 and 500 mb. Shown are 500 mb nature data (a), 1000 mb nature data (b).	119
7.12	Format as in Fig. 7.11. STATSAT analysis (a) and analysis error (b) at 500 mb, and at 1000 mb (c,d).	120
7.13	Format as in Fig. 7.11. SSMSAT analysis (a) and analysis error (b) at 500 mb, and at 1000 mb (c,d).	122
7.14	Format as in Fig. 7.11. SSM+TOVS analysis (a) and analysis error (b) at 500 mb, and at 1000 mb (c,d).	124
7.15	Analysis error for 850 mb relative humidity valid 00 GMT 23 November. (a) STATSAT, (b) SSMSAT, (c) SSM+TOVS. Contour interval is 25% with zero line omitted. Negative values are dashed.	126
7.16	Analysis error for 850 mb relative humidity valid 00 GMT 25 November. Format is as in Fig. 7.15.	127
7.17	Inferred low cloud cover from relative humidity valid 00 GMT 25 November. (a) Nature, (b) STATSAT analysis, (c) STATSAT - Nature. Contour interval is 25% with zero line omitted. In difference field, negative values are dashed.	128
7.18	Inferred low cloud cover from relative humidity valid 00 GMT 25 November. (a) SSMSAT analysis, (b) SSMSAT - Nature. Contour interval is 25% with zero line omitted. In difference field, negative values are dashed.	129
7.19	Rms height errors at 500 mb. (a) NOSAT, (b) STATSAT, (c) SSMSAT, (d) SSM+TOVS. Analysis errors are shown in solid curves, forecast errors in dashed curves. Julian day 322 corresponds to 00 GMT 18 November.	130

LIST OF FIGURES

<u>Figure</u>		<u>Page(s)</u>
7.20	Global rms analysis/forecast errors for 850 mb relative humidity. (a) STATSAT, (b) SSMSAT, (c) SSM+TOVS. Solid curves denote analysis, broken curves are forecasts.	132
7.21	Zonal time averaged u component of wind. (a) Nature, (b) STATSAT, (c) STATSAT - Nature, (d) WINDSAT, (e) WINDSAT - Nature, (f) SSMSAT, (g) SSMSAT - Nature. Contour interval is 2.5 ms^{-1} , negative values are dashed.	133
7.22	Zonal time averaged v component of wind. (a) Nature, (b) STATSAT, (c) STATSAT - Nature, (d) WINDSAT, (e) WINDSAT - Nature, (f) SSMSAT, (g) SSMSAT - Nature. Contour interval is 0.5 ms^{-1} , negative values are dashed.	135
7.23	Zonal time averaged temperature. (a) Nature, (b) STATSAT, (c) STATSAT - Nature, (d) WINDSAT, (e) WINDSAT - Nature, (f) SSMSAT, (g) SSMSAT - Nature. In analyses, values (in K) have been multiplied by 0.1, contour interval 0.5 (K/10). In differences values are unscaled, contour interval is 1K.	137
7.24	Zonal time averaged relative humidity. (a) Nature, (b) STATSAT, (c) STATSAT - Nature, (d) WINDSAT, (e) WINDSAT - Nature, (f) SSMSAT, (g) SSMSAT - Nature. Contour interval is 5 percent, negative values are dashed.	139
7.25	Forecast rms error growth, 500 mb height. (a) Northern hemisphere extratropics, (b) Tropics, (c) Southern hemisphere extratropics.	141
7.26	Forecast rms error growth, 200 mb wind vector. (a) Northern hemisphere extratropics, (c) Southern hemisphere extratropics.	142
7.27	Forecast rms error growth, 850 mb relative humidity. (a) Northern hemisphere extratropics, (b) Tropics, (c) Southern hemisphere extratropics.	143
7.28	Forecast rms error growth. (a) 850 mb relative humidity, global statistics, (b) 850 mb cloud cover, global statistics.	144
7.29	Forecast rms error growth, 50 mb height, northern hemisphere extratropics.	145

LIST OF FIGURES

<u>Figure</u>		<u>Page(s)</u>
7.30	Calibrated 500 mb height rms errors for southern hemisphere extratropics. (a) Winter OSEs, (b) Summer OSE's.	146
7.31	Calibrated 200 mb wind vector rms errors for tropics. (a) Winter OSEs, (b) Summer OSEs.	147
7.32	Calibrated 850 mb relative humidity summer OSSE rms errors for northern hemisphere extratropics. (a) Relative humidity, (b) Cloud cover.	148
7.33	Forecast 500 mb temperature bias for northern hemisphere extratropics.	149
7.34	Forecast 850 mb relative humidity bias for northern hemisphere extratropics.	150
A-1	SSM/T-1 and SSM/T-2 FOV scan line pattern	A-6
A-2	Geometry for location calculation	A-10
A-3	Scan angle geometry	A-11
A-4	Subsatellite trace for polar orbiting platform 24 hours of orbits)	A-12
A-5	Subsatellite points indicating coverage density for two weeks of orbits	A-13
A-6	Location of SSM/T-1 temperature soundings (1) and SSM/T-2 water vapor soundings (2) assuming FOV's of 180 and 50 km, respectively	A-14

1. Introduction

Improved capabilities to specify the moisture field (including water vapor, cloud, and precipitation) are potentially afforded by an optimally designed combination of satellite-based sensors. The implications for numerical weather prediction (NWP) are promising, since, radiatively, water in its many forms is the most active constituent of the troposphere (Isaacs et al., 1986). While infrared cloud contamination may often be circumvented by exploiting the high horizontal resolution of infrared sensors, microwave temperature retrievals suffer little degradation from the presence of cloud. This advantage also applies to some extent to the retrieval of the atmospheric moisture profile from millimeter wave data.

A strong feature with sufficient line strength for this application, is the ($3_{13}-2_{20}$) rotational line of water vapor, located at 183.31 GHz. Two instruments have been proposed to utilize the 183 GHz absorption line to obtain water vapor profiles in the 1990's time frame. These are: (a) the civilian Advanced Microwave Sounding Unit (AMSU)-B package, a five channel radiometer to be flown as part of the first NOAA-NEXT satellite, and (b) the Defense Meteorological Satellite Program (DMSP) SSM/T-2 millimeter wave moisture sounder, an enhancement of the current operational SSM/T-1 microwave temperature sounder.

This study presents the results of state of the art observing system simulation experiments (OSSEs) designed to assess the impact of the Special Sensor Microwave 183 GHz (SSM/T-2) water vapor sounder and the associated SSM/T-1 temperature sounder on NWP. A novel feature of the present study is the comprehensive approach we have taken to simulating the SSM/T microwave (T-1) and millimeter wave (T-2) data. Our study is based on the nature run prepared by the ECMWF and simulated FGGE data base prepared by NMC as described by Dey et al. (1985) for the period 10-30 November 1979. The forecast analysis system for the OSSE is the AFGL Global Spectral Model (GSM) (Brenner et al., 1984) and the AFGL Statistical Analysis Program (ASAP) (Norquist, 1986). Four observing system configurations are investigated: (1) in experiment NOSAT only the conventional upper air soundings and aircraft reports are used; (2) in experiment STATSAT, the currently operational civilian temperature soundings (TOVS) are added; while (3) in experiment SSMSAT the SSM/T temperature and moisture soundings are added to the NOSAT configuration; finally (4) in experiment SSM+TOVS, both the SSM and TOVS data are added.

As an aid to interpretation, our OSSE results are calibrated against results from (real data) observing system experiments (OSEs) described in more detail by Louis et al. (1988). In addition to conventional assessment indices (such as geopotential height fields, etc.), our analysis of the results also focuses on moisture related variables. We identified two measures of impact of particular interest: relative humidity and cloud amount. Due to the importance of moisture fields to the prediction of electro-optical systems effectiveness, it is useful to study a variable directly related to water vapor. Relative humidity is the parameter most commonly used as an input to propagation models (Moore and Peterson, 1984). This assessment will be important for situations with moderate to high relative humidities.

For situations near saturation, cloud prediction indices are most important. Therefore we have examined the rms and bias error of cloud fraction. Since cloud amounts were not saved during the nature run, truth is based on the diagnosis of large scale (i.e. non convective) cloudiness from the nature run relative humidity fields. We find that the statistical measures of impact based on cloud amount are closely related to those based on relative humidity. We note that special attention is given to the simulated retrieval errors in the presence of cloud. Cloud and retrievals over land are two situations where problems with the 183 GHz retrievals are expected based on previous retrieval simulation studies (Isaacs and Deblonde, 1985).

The plan of this report is the following: Section 2 discusses OSSE methodology in general and develops the methodology for realistic simulation of the SSM sensors. Background material describing the scientific basis for the 183 GHz sensor have already been reviewed by Isaacs (1987). This material is not repeated here. Section 3 describes the reference atmosphere and simulated conventional data. Section 4 describes the sensor simulation study of the SSM/T statistical (i.e. D-matrix) retrievals, and our plan for simulating SSM/T data for the OSSE. The simulated SSM/T data observational errors are based on the results of our sensor simulation retrieval study. These results are examined in Section 5. Section 6 contains the specific OSSE design we employed. Results are reported in Section 7. Finally, Section 8 contains a summary and our main conclusions.

The experiments described here were conducted in tandem with an OSSE to determine the impact of Doppler wind lidar instrument or WINDSAT. The WINDSAT

study makes use of the same baseline OSSEs and OSEs as the current study. The WINDSAT study is described in a companion report (Scientific Report No. 7) of the current effort. Each report may be read independently: To achieve this we have repeated some common material in both reports.

2. Background

OSSE studies run the gamut from simple insertion of grid point values into unsophisticated models to the use of complex radiative transfer models to simulate data for operational forecast analysis systems. The current study is relatively sophisticated and state of the art. As a reference point we discuss in Section 2.1, considerations which might lead to an ideal OSSE. We then describe our methodology for simulating remotely sensed data (Section 2.2). This methodology is later applied in Section 3 to the SSM/T-1,2.

2.1 General OSSE strategy

There are four components common to any OSSE:

- 1) A four dimensional reference atmosphere, often called the nature run. This is considered to be the "TRUTH".
- 2) A sampling procedure to obtain observations.
- 3) A data assimilation system, composed of a forecast model and analysis procedure.
- 4) A quantitative verification procedure.

Usually, the nature run is simply a long forecast made by an advanced NWP model or Global Circulation Model. The more sophisticated the nature model, the better. Remotely sensed data are influenced by many geophysical parameters, including sea surface temperature, atmospheric aerosol, clouds, etc. In some cases these parameters affect the accuracy of retrievals of other parameters or make such retrievals impossible. These parameters may be responsible for spatially correlated observing errors by inducing local geophysical biases in the retrieved fields (Hoffman, 1988). These parameters should be included in the nature run. For example, SSM/T should provide less accurate retrieval of atmospheric boundary layer humidity over the ocean when

wind speeds are high and the surface emission dominates the atmospheric emission.

From the point of view of NWP, the most important characteristics of any proposed remote sensing system are its geographical coverage, horizontal and vertical resolution and its error characteristics. In a simulation study these characteristics must be properly accounted for. These considerations lead immediately to a number of issues which bear on the interpretation of the results of OSSEs.

For NWP, it is not just accuracy of the measurement which is important, the measurement must be representative as well. NWP is really concerned with the spatially and temporally smoothed behavior of the atmosphere. Variations on the scale of meters and seconds, in fact on the scale of kilometers and minutes, are generally sub-grid scale and are parameterized within the model. Consequently, that part of the measured signal attributable to these scales is considered to be noise from the NWP point of view. This source of error can in some cases be predominant. A prime example is radiosonde observations (RAOBs). When two radiosondes are carried by the same balloon, agreement of the measured quantities is very good, but measurements made by two radiosondes, some distance apart, do not agree as well. One implication of this is that as models improve in resolution, this source of error decreases. No existing global model has fine enough resolution to represent all scales of motion which exist in nature. In fact the smallest scales represented by models are usually severely damped for computational reasons. A method to unfilter the nature run was suggested by Hoffman (1988).

The procedures for simulating data from the nature run should be as realistic as possible. The process of simulating the observations should be sophisticated enough to generate realistic observing error statistics.

When generating errors for an OSSE, we would like to divide the process into the following parts:

(1) Representational errors. The nature model state should be unfiltered to restore realistic small scales to the model state.

(2) Sampling. The realistic model state is interpolated to the observing locations. (Space and time interpolation are used as needed.)

(3) Geophysical local bias. Local biases, depending on the sensor type and on the geophysical parameters of the realistic model state, will be added. Global biases should be corrected by the data producer and may be ignored in an OSSE.

(4) Random error. The last error component is random. It might contain vertical and horizontal correlations. Note, however, that representational errors and geophysical local biases already induce vertical and especially horizontal correlations. We feel that horizontal correlations are mostly caused by representational errors and geophysical local biases. On the other hand, vertical errors may be correlated if the sensor retrieval algorithm interrelates several independent observations to a profile of retrieved temperature or other variable.

(5) Sensor filtering. When a sensor uses a statistical retrieval method, all its observations should be filtered by projecting onto the vertical basis functions which are used in the retrieval. This is also true for so-called physical retrieval methods.

Note that (3)-(5) above can be replaced by simulating the sensor and its retrieval scheme (e.g. Atlas et al., 1985). However, this is costly, and we would prefer instead to perform selected sensor simulation/retrieval studies in order to define reasonable local biases. For example, we might study retrieval bias as a function of cloud amount for each retrievable parameter. Such studies are of interest in themselves.

Spatially correlated errors are difficult for an analysis scheme to remove, because the data tend to corroborate each other. Real data tend to have correlated errors. Even for radiosondes, significant vertical error correlations are present. The data used in the present experiments had data errors which are almost totally uncorrelated. As a result the errors are too easy for the analysis to filter. Atlas (1988, pers. comm.) reports that he undertook some Perfect data experiments in which the random errors were absent. The results of these experiments are nearly identical to the results of the experiments which had random errors.

The data assimilation system forecast model and analysis procedures should be as realistic and up to date as possible. Impacts of observing systems depend to a certain extent on the forecast and analysis methods

used. In some cases, there may be a severe mismatch between the analysis system and the new data. For example, the AFGL analysis system does not presently include a surface pressure analysis nor does it use surface pressure observations in the upper air analysis; clearly adding a new source of surface pressure data would have no impact. In general it must be noted that operational analysis systems have been tuned for the data they normally receive. The best use of a novel data type may require considerable effort.

Verification of OSSE results is easy because we have total knowledge of the "TRUTH". In these experiments we may legitimately use the word error instead of difference when we compare an experiment to the nature run. Interpretation of these results is not so easy. As noted above, OSSE results are typically too good. The control case is often so good that there is little room for positive impact. There are two reasons for this: first, the forecast model is more similar to the model used to generate nature than it is to the real atmosphere. Second, the observational errors are too random and easy for the analysis to filter out. For these reasons it is desirable to calibrate the OSSE results to OSE results. In the present case we conduct two OSSEs, NOSAT and STATSAT, for which we have previously conducted analogous OSEs. We use only a very simple calibration procedure in Section 7.. Basically we assume OSSE impacts in statistical measures relative to STATSAT are proportional to corresponding OSE impacts in deriving our estimates of actual SSM/T-1,2 impacts.

It is possible to use a series of real analyses for the reference atmosphere, but the results of such experiments would be difficult to interpret for the following reasons. In this situation the "TRUTH" is the actual atmosphere, not the reference atmosphere. Therefore, in data rich areas, the reference atmosphere would agree well with the "TRUTH" while in data voids it would not. Consequently, simulated observations from the new observing instrument in data rich areas would add correct information, but have little impact because of the concentration of other observations already available, while simulated observations in data poor areas would add erroneous information, which would be carried by the model during the data assimilation cycle to other areas. If the results are then verified in data rich areas we might obtain a negative impact by adding a new observing system. Greater accuracy in the simulated observing system would not avoid adding erroneous data in data poor areas.

2.2 Sensor simulation methodology

Our general approach to sensor simulation, which is specialized to the SSM/T1,2 in Section 4 is described here. Consider a vector of geophysical parameters. Let t be true values and r be retrieved values from a sensor simulation study. We will study the error

$$e = r - t. \quad (2.1)$$

Our object is to model e in terms of a white noise process so that we may simulate realistic observations using a pseudo-random number generator. Since the retrieval has only a limited number of degrees of freedom, we project (2.1) onto the empirical orthogonal functions (EOFs) of the retrieval scheme, obtaining

$$\bar{e} = \bar{r} - \bar{t}. \quad (2.2)$$

Here, for example, \bar{t} is given by

$$\bar{t} = B^T(t - \mu) \quad (2.3)$$

where B is the matrix of EOFs and μ is the ensemble average. Our simulated values will be obtained by adding values of the modeled \bar{e} to values of \bar{t} sampled from nature and then transforming back to physical space.

We model \bar{e} in terms of geophysical parameters, g . To account for a constant term, we assume that the first element of g is one. Our analysis will yield

$$\bar{e} = Ag + \bar{n} \quad (2.4)$$

where \bar{n} is a noise process with zero mean and covariance matrix $\langle \bar{n} \bar{n}^T \rangle$. These \bar{n} may be modeled by

$$\hat{\bar{n}} = C\epsilon \quad (2.5)$$

where C is the matrix of eigenvectors of $\langle \bar{n} \bar{n}^T \rangle$ and the ϵ are white noise. Combining (2.2), (2.4) and (2.5) yields our model of r ,

$$\hat{r} = B(\bar{t} + Ag + C\epsilon) + \mu \quad (2.6)$$

In (2.6), \bar{t} is obtained by projecting the values from the nature run according to (2.3), g is a vector of geophysical parameters diagnosed from the nature run and ϵ are obtained from a random number generator. The B , A , C and μ are constants from the retrieval algorithm and our analysis of the sensor simulation data.

3. Data Sources

The data used in this study, the nature run and simulated observations exclusive of the SSM data were prepared by ECMWF and NMC respectively as described in a report by Dey et al. (1985), which we summarize below in Section 3.1 and 3.2 respectively. These data were prepared as part of a joint NMC-ECMWF-NASA/GLA effort to conduct WINDSAT experiments which began as a result of a workshop held at NMC in February, 1983. The 10 - 30 November period was chosen for this work because both ECMWF and GLA had already conducted real data OSEs for that period. Two TIROS satellites were in service during this period. Further details of our OSSE design are given in Section 6.

3.1 Nature run

ECMWF generated the nature run. The nature run is simply a 20 day forecast from the FGGE IIb analysis produced at ECMWF for 00 GMT 10 November 1979 (Bengtsson et al., 1982). The model used in the nature run forecast was a version of the 15 layer, 1.875° grid point model (Hollingsworth et al., 1980; Tiedtke et al., 1979). This model included fairly complete physics with a diurnal cycle.

To conserve storage space, as we unpacked the gridded nature run tapes we interpolated the 1.875° grid to a 2.5° grid which we have used for all our data sets and comparisons. A 2.5° grid is substantially finer than the spectral transform grid used by our R30 forecast model and is therefore more than adequate to present our results. In fact the nature run is rather

smooth, smoother than many of our analyses and forecasts, and the 2.5° grid is more than fine enough.

3.2 Simulated observations

NMC simulated the FGGE Level IIb data for the period, in the NMC format (Office Note 29) from the ECMWF nature run. Almost all Level IIb data were simulated. However NMC did not simulate constant level balloon data (COBAL), experimental satellite stratospheric sounding data (LIMS) and significant level data. Later GLA converted the NMC data to the standard FGGE format (WMO, 1986). We received copies of the nature run and FGGE format Level IIb data from GLA, courtesy of R. Atlas.

The simulated standard FGGE Level IIb data were created by replacing all the observed atmospheric variables in the real FGGE Level IIb data with values interpolated from the nature run corrupted by adding a simulated observing error. Therefore if a particular radiosonde report is missing in the real data, it is missing in the simulated data, if it is present in the real data, it is present in the simulated data and has the same quality control marks and missing data flags as the real observation. This yields very realistic data coverage and quality control in the simulated data. However certain discrepancies are possible: For example, CDWs may be present where the moisture field in the nature run is inconsistent with cloudiness. Typical data coverage by standard FGGE IIb data is shown in Fig. 3.1. The data points shown are those actually used by the analysis program, after a gross error and buddy checking quality control; all data with observation times in a 6-hour period centered on the analysis time are shown. The radiosonde locations are those with height observations used for an analysis at 00Z on 25 November, at the $\sigma = 0.5$ level. All other plots in Fig. 3.1 show data locations for 00Z on 21 November. Cloud track winds are most numerous at low levels ($\sigma = .86$ and $.72$) and upper levels ($\sigma = .27$ and $.22$), whereas aircraft wind reports are concentrated at upper levels ($\sigma = .27$ and $.22$). Coverage by the TOVS data, shown here for height observations at the $\sigma = 0.5$ level, illustrates the satellite tracks and the fact that retrievals over land were not used.

The value of the nature run at an observing location is determined by spatially interpolating the nature run at the closest synoptic time (00, 06, 12 or 18 GMT). The vertical interpolation is linear in $\ln(p)$ and the

horizontal interpolation is quadratic in latitude and longitude for height (Z), wind components (u,v), and temperature (T). For relative humidity (RH), the horizontal interpolations are linear.

The simulated observational error which is added to the value of the nature run at the observing location is composed of a bias and a random Gaussian error which is not correlated with anything else. The size of the random error, or observing error standard deviation (OESD) is appropriate for the particular observation. The OESDs depend on report type, variable and pressure level and are displayed in Table 3.1 reproduced from Dey et al. (1985). Biases are zero except for TIROS.

The TIROS biases depend on retrieval path and are displayed in Table 3.2 reproduced from Dey et al. (1985) which is based on Fig. 2 of Schlatter (1981). In actual practice, the retrieval paths, labeled A, B and C are set depending on whether the retrieval was deemed clear, partly cloudy or cloudy. Note that the OESDs in Table 3.1 for TIROS also depend on the retrieval path (and are based on Fig. 3 of Schlatter; 1981). In simulation the retrieval path was determined from the nature run total fractional cloud coverage, f , according to

$$\text{Path} = \begin{cases} A & \text{if } f \leq 60 \\ B & \text{if } 60 < f \leq 90 \\ C & \text{if } 90 < f \end{cases}$$

This relationship was tuned to give approximately the same proportion of the different retrieval types as were actually observed on 12 November 1979. The nature run cloud coverage in turn is deduced from the nature run RH as described below. Since the nature run RH field is spatially correlated, the TIROS observational errors will be also. All other errors are uncorrelated.

The nature run cloud fraction at 500, 700 and 850 kPa is determined using a version of Fye's (1978) cloud fraction to RH conversion algorithm. This algorithm is tuned to the ECMWF forecast so that the nature run cloud statistics are reasonable. Any effect of high cirrus cloud on the observation errors is ignored. Layer and total cloud amounts are then calculated assuming random overlap between individual cloud levels within the layer. (That is, cloud free fractions multiply as one progresses down through the atmosphere.)

The simulated data described here are quite complete and realistic, yet have two major failings. First the observational errors are uncorrelated. For example, consider the CDWs: The typical CDW OESD used is of the proper size (order 8 m/s), but real CDW errors have large horizontal correlations due to height assignment errors which are responsible for the largest part of the OESD. In reality, then, the CDW errors are not much reduced by the filtering of the analysis procedure. In the simulation experiments described here, on the other hand, the analysis is able to average out the CDW errors very effectively because they are uncorrelated and the observations are dense. Second the nature run has little energy in the smallest scales. Small scale energy present in the real atmosphere, must be considered part of the observational error and thereby induces spatially correlated errors for all observations. The absence of this source of error also contributes to the (unrealistic) ease with which the analysis averages out the observational errors in the simulation experiments.

Table 3.1 OESDs Used to Simulate FGGE IIb Data for November

SFCLT 1.0	SFCST 1.0	SFCBT 1.5	Surface Reports						SFCBP 2.0	SFCLW 0.0	SFCSW 2.5	SFC			
			SFCLP 1.0	SFCSP 1.0											
			Upper Air Reports												
Pressure	1000	890	700	500	400	300	250	200	150	100	70	50	30	20	1
RADT	1.1	1.1	1.1	1.3	1.5	1.7	1.9	2.0	2.1	2.2	2.5	3.0	3.5	4.1	4.
DRPT	1.1	1.1	1.1	1.3	1.5	1.7	1.9	2.0	2.1	2.2	2.5	3.0	3.5	4.1	4.
RADW	2.0	2.0	3.0	4.0	5.0	6.0	6.0	6.0	6.0	6.0	6.0	6.0	6.0	6.0	6.
DRPW	2.0	2.0	3.0	4.0	5.0	6.0	6.0	6.0	6.0	6.0	6.0	6.0	6.0	6.0	6.
PIBW	1.8	2.6	3.5	5.0	6.0	8.2	10.0	10.0	10.0	9.2	8.0	6.0	6.0	6.0	6.
AIRT	3.0	3.0	3.0	3.0	3.0	3.0	3.0	3.0	3.0	3.0	3.0	3.0	3.0	3.0	3
ASDT	3.0	3.0	3.0	3.0	3.0	3.0	3.0	3.0	3.0	3.0	3.0	3.0	3.0	3.0	3
AIRW	7.0	7.0	8.0	8.0	8.0	8.0	8.0	8.0	8.0	8.0	8.0	8.0	8.0	8.0	8
ASDW	2.0	2.0	3.0	4.0	5.0	6.0	6.0	6.0	6.0	6.0	6.0	6.0	6.0	6.0	6
COBW	5.0	5.0	5.0	5.0	5.0	5.0	5.0	5.0	5.0	5.0	5.0	5.0	5.0	5.0	5
SATN	4.0	4.0	5.0	7.0	7.0	8.0	8.0	8.0	8.0	8.0	8.0	8.0	8.0	8.0	8
SATJ	6.0	6.0	6.0	10.0	10.0	13.0	13.0	13.0	13.0	13.0	13.0	13.0	13.0	13.0	13
SATE	7.0	7.0	8.0	8.0	8.0	8.0	8.0	8.0	8.0	8.0	8.0	8.0	8.0	8.0	8
SATI	4.0	4.0	5.0	7.0	7.0	8.0	8.0	8.0	8.0	8.0	8.0	8.0	8.0	8.0	8
SATT	4.0	4.0	5.0	7.0	7.0	8.0	8.0	8.0	8.0	8.0	8.0	8.0	8.0	8.0	8
SATF	7.0	7.0	8.0	8.0	8.0	8.0	8.0	8.0	8.0	8.0	8.0	8.0	8.0	8.0	8
SATG	7.0	7.0	8.0	8.0	8.0	8.0	8.0	8.0	8.0	8.0	8.0	8.0	8.0	8.0	8
TIROS Soundings and WINDSAT															
TIRAB	2.0	1.8	1.7	1.8	1.8	1.9	1.9	2.0	2.0	2.2	2.4	2.5	2.6	2.8	2
TIRC	3.9	2.5	2.2	2.2	2.0	1.9	1.8	1.7	1.6	1.4	2.5	2.6	2.7	2.8	2
WSAT	1.0	1.3	1.6	2.0	2.3	2.5	2.6	2.7	2.8	2.9	2.9	3.0	3.0	3.0	3
Legend:	SFCL - Surface land	AIR - Aircraft	T - temperature (in °K)												
SFCS - Surface ship	ASD - ASDAR	W - wind (in ms ⁻¹)													
SFCB - Surface buoy	COB - COBOL	P - pressure (in mb)													
RAD - Radiosonde	SAT - Satellite cloud tracked winds	TIRAB - TIROS A&B retrievals													
DRP - Dropsonde	WSAT - WINDSAT	TIRC - TIROS C retrievals													
PIB - PIBAL															

Legend:

SFCL - Surface land
 SFCS - Surface ship
 SFCB - Surface buoy
 RAD - Radiosonde
 DRP - Dropsonde
 PIB - PIBAL

AIR - Aircraft
 ASD - ASDAR
 COB - COBOL
 SAT - Satellite cloud tracked winds
 WSAT - WINDSAT

T - temperature (in °K)
 W - wind (in ms⁻¹)
 P - pressure (in mb)
 TIRAB - TIROS A&B retrievals
 TIRC - TIROS C retrievals

Table 3.2 Biases Used to Simulate TIROS Temperature Retrievals for November

Retrieval Method			
Pressure Layer	A	B	C
50-70	0.0	0.0	0.0
70-100	-0.7	-0.7	-0.5
100-150	-0.5	+0.15	-0.1
150-200	-0.1	+0.3	+0.4
200-250	+0.5	+0.6	+1.2
250-300	+0.6	+0.5	+0.9
300-400	+0.1	-0.05	-0.15
400-500	-0.4	-0.3	-1.1
500-700	-0.5	-0.35	-1.2
700-850	-0.5	+0.35	-0.6
850-1000	-0.35	+0.3	+1.65

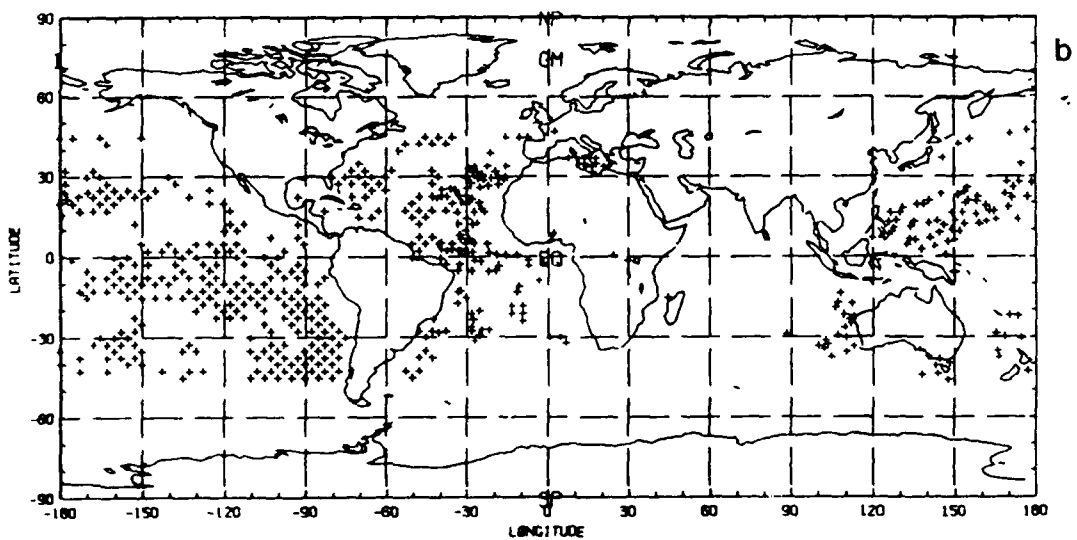
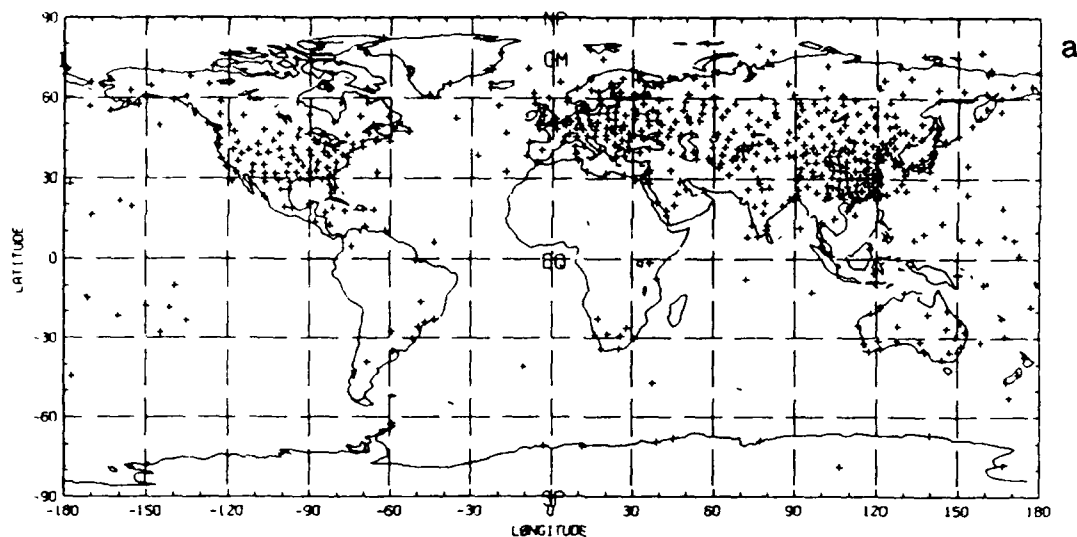


Figure 3.1 Data coverage by standard FGGE IIb observations. Raob heights at $\sigma=0.5$ (a), cloud track winds at $\sigma=0.86$ and 0.72 (b), and $\sigma=0.27$ and 0.22 (c), aircraft winds at $\sigma=0.27$ and 0.22 (d), and TOVS heights at $\sigma=0.5$ (e).

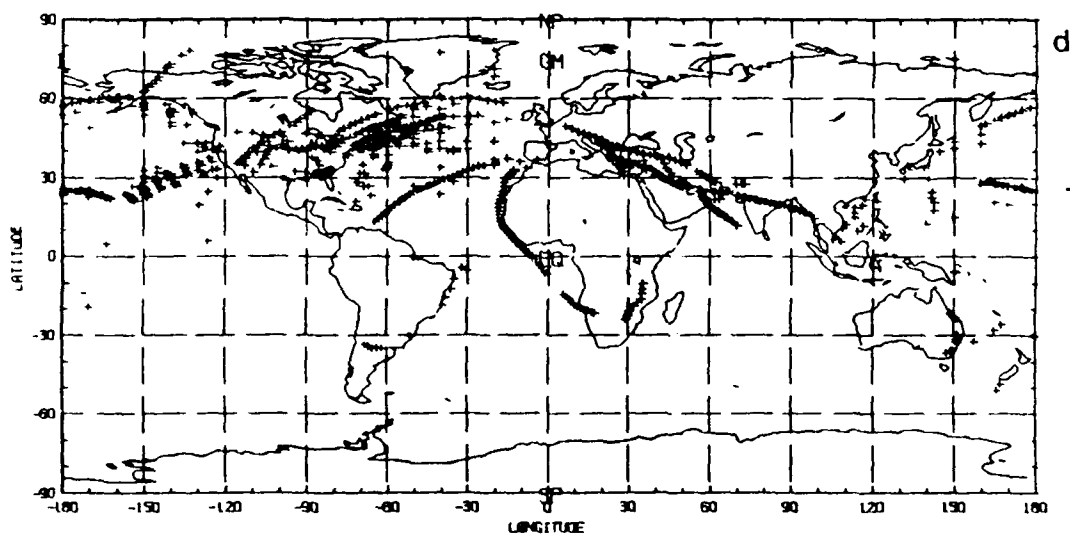
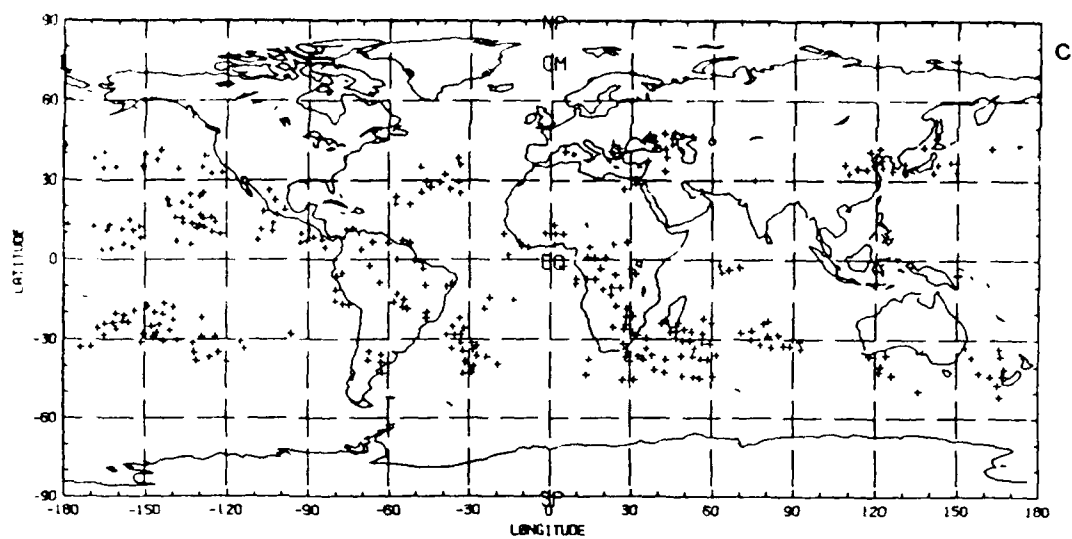


Figure 3.1 (continued).

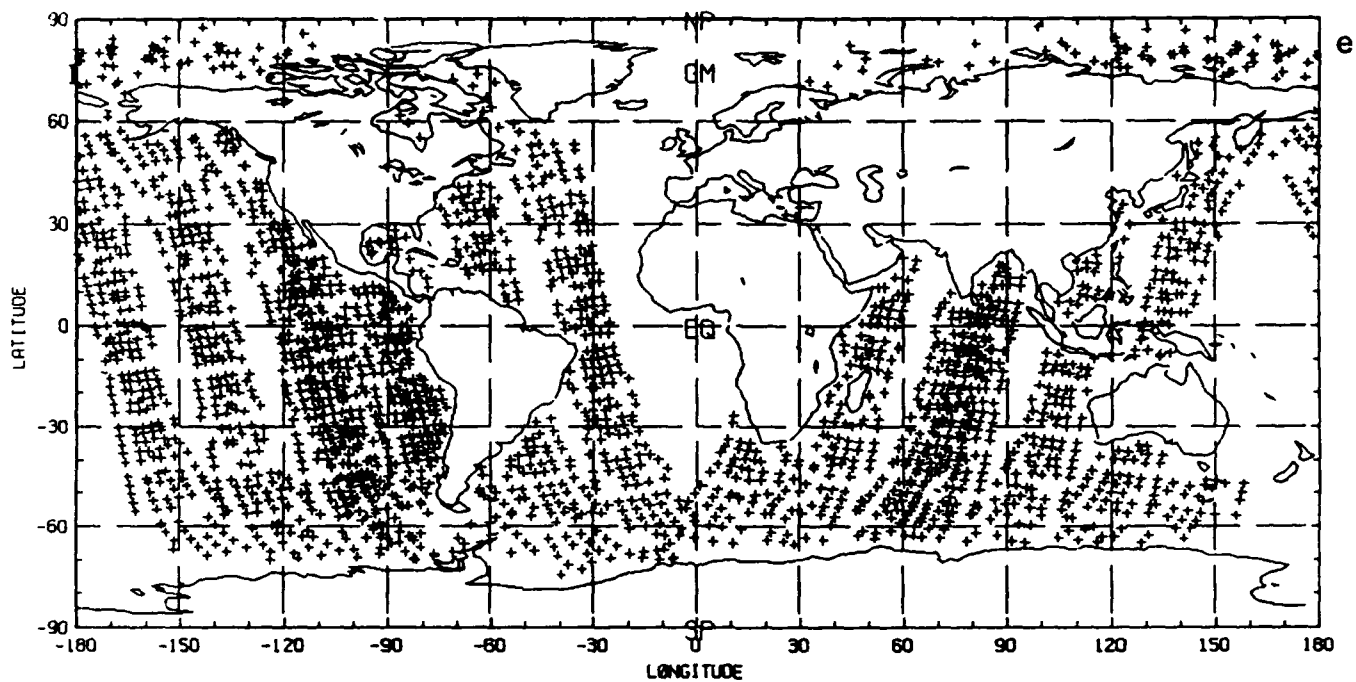


Figure 3.1 (continued).

4. Sensor Simulation Study of SSM/T D-Matrix Retrievals

Application of the methodology described in Section 2.2 above to simulate the T-1 and T-2 retrievals required several processing steps. These steps which include manipulation and extraction of the nature run data, radiative transfer simulations based on the extracted nature run data, and statistical analysis of the simulation data are described in greater detail below.

4.1 Generating dependent and independent data sets

The first step involved generation of two data sets containing selected temperature and relative humidity profiles culled from subsets of the nature run. The temperature and humidity data sets, labeled (Dependent) Set 1 and (Independent) Set 2, were the basis for conducting statistical retrievals and generating retrieval error statistics which were used to simulate retrievals for the OSSEs.

A particular objective of our work is to realistically reproduce the error characteristics of the millimeter/microwave observing system, including its spatial attributes. Some type of retrieval classification is necessary because geophysical parameters such as cloudiness or surface type directly affect the quality of the retrieval. The categories used to construct the matrix for the statistical retrievals (the so called D-Matrix) from Set 1 and retrieval error statistics from Set 2 are indicated in Table 4.1. Note that the number of categories for water vapor is twice that for temperature since cloudiness has little effect on temperature retrievals. We anticipated that having more retrieval verification categories would induce horizontal correlations in the OSSE retrievals.

Sampling of the nature run was conducted so that each category contained approximately 200 to 700 profiles. Set 1 profiles were extracted from nature run output valid at 00 GMT on 17 November and at 12 GMT on 26 November. Statistical retrievals were performed within the actual time period chosen for the assimilation experiments at 12 GMT on 21 November and 0 GMT on 22 November. Throughout the experiment only oceanic profiles were used since the impact of the data would be greatest in these regions.

In order to account for the effects of cloud and ocean surface roughness, 40% of all profiles were randomly flagged as cloudy and 30% of all profiles

were flagged as having high surface wind. These percentages are consistent with global wind (SEASAT) and cloud statistics, (personal communication, R. Atlas, 1988; Newell et al., 1974) and no attempt was made to assign cloud and wind flags based on actual geophysical features. During retrieval simulations, however, surface wind and relative humidity, acting as a surrogate for cloud cover, were used for classification. To insure realistic representativeness of the statistics all conditions are sampled rather than a random distribution.

4.2 Preprocessing geophysical profiles

The nature run temperature data are on 12 mandatory pressure levels ranging from 50 mb down to 1000 mb, while the relative humidity data is specified on the lowest 6 mandatory levels (1000 - 300 mb). Since the numerical model we have used to simulate radiative transfer in the millimeter/microwave spectral region, RADTRAN (Falcone et al., 1982), requires temperature and water vapor information on 64 pressure levels from 1 mb to 1000 mb, preprocessing of the extracted profiles was performed. Temperature profiles were interpolated vertically (linear in $\ln p$) between 1000 mb and 50 mb. Above 50 mb climatology from the U.S. Standard Atmosphere Supplements (1966) was used. Relative humidity profiles were converted to water vapor density and then interpolated vertically between 1000 mb and 300 mb, with climatology from the Phillips radiosonde set (Phillips et al., 1988) used above 300 mb.

4.3 Computing brightness temperatures from geophysical profiles

Radiative transfer simulations were run for each of the 12 instrument channels indicated in Table 4.2 (Falcone and Isaacs, 1987). The brightness temperature at frequency ν , $T_b(\nu)$, was evaluated from (Isaacs et al., 1988):

$$T_b(\nu) = \left\{ \epsilon_s T_s + (1 - \epsilon_s) [T_c r'_\nu(0) + \int_0^{p_s} T(p) dr'_\nu] \right\} r_\nu(p_s) + \int_{p_s}^0 T(p) dr_\nu \quad (4.1)$$

where

$$r_\nu(p) = \exp \left[- \int_0^p k(\nu, p') dp' / \mu \right] \quad (4.2)$$

and

$$\tau'_{\nu}(p) = \exp \left[- \int_p^{p_s} k(\nu, p') dp' / \mu \right] \quad (4.3)$$

Here μ is the cosine of the path zenith angle τ_{ν} and τ'_{ν} are the upward and downward transmission functions, and T_c is the cosmic background temperature. Since all simulations were performed for nadir fields-of-view, the zenith angle cosine, μ , in (4.2) and (4.3) above was set equal to unity.

The nonscattering radiative transfer equation (4.1) is used for all simulations since scattering by cloud size droplets is negligible. The cloud model drop size distributions (Table 4.3) have mode radii of less than 10 μm with appreciable numbers of drops falling off rapidly beyond 100 μm . The single scattering albedo for such drops at 183 GHz is about 10^{-4} . Generally, a single scattering albedo of 0.05 or greater is required before a significant scattering source function is attained. At 183 GHz, this implies significant numbers of drop sizes of a few millimeters or more, i.e. precipitation sized drops. Due to the nature of the cloud drop size distributions treated, there are few such large droplets (Deirmendjian, 1975).

Profiles of atmospheric absorption coefficients, $k(\nu, p)$, for each frequency of interest were calculated using the RADTRAN simulation algorithm, and these provided the transmission profiles (4.2), (4.3) necessary to evaluate channel brightness using (4.1). The channel set and design noise equivalent brightness temperatures (NEAT's) for the SSM/T-1 and T-2 sensors are given in Table 4.2. For Set 1 profiles no noise was added to computed brightness temperatures since these were only used to construct D-Matrices. During simulations using Set 2 profiles Gaussian noise with a mean of zero and standard deviation equal to the channel NEAT was added to each brightness temperature.

The procedure described above was applied to clear sky simulations. To simulate the effect of cloud within the field-of-view of the radiometer, a suitable set of cloud models was incorporated within the evaluation of the atmospheric attenuation profiles. The cloud models chosen were taken from the AFGL FASCODE model (Falcone et al., 1979). Mode radii, cloud liquid water

content (LWC), and the vertical extent of the five cloud models are given in Table 4.3.

Cloud attenuation, $\alpha(\nu, T, z)$, was calculated using the Rayleigh approximation (van de Hulst, 1957):

$$\alpha(\nu, T, z) = 6\pi\nu \operatorname{Im} \left(-\frac{m^2 - 1}{m^2 + 2} \right) \text{LWC} \quad (4.4)$$

where ν is the frequency in wavenumbers, m is the complex index of refraction of water evaluated using Ray's (1972) empirical expression, and LWC is the cloud liquid water content. Falcone et al., (1979) have shown that the use of the Rayleigh approximation instead of the full Mie theory for these cloud models is justified for frequencies less than about 300 GHz.

Clouds were incorporated into the brightness temperature simulation process by randomly selecting from among one of the cloud types with associated LWC given in Table 4.3 or choosing the option that the simulated scene was clear. Cloud attenuation calculated from (4.4) was then added to the clear sky absorption for each atmospheric layer within the vertical domain specified for the selected cloud type model. The effect of partially filled fields-of-view was then treated by multiplying the local cloud attenuation by a random number between 0 and 1. It was assumed that all cloud types were equally probable, and that only a single cloud layer was present. The second assumption tends to underestimate cloud impact, but we note that these assumptions could be relaxed given appropriate cloud coverage statistics and frequency of occurrence data. Given that beam filling is particularly unlikely for cumuliiform clouds with horizontal extents of a few kilometers this treatment of the field-of-view should be more accurate. Since the profiles of temperature and water vapor were given at constant pressure levels rather than at constant heights as are the cloud models, cloud vertical extent had to be interpolated to the appropriate pressure level within individual profiles. Within cloudy layers relative humidity was not adjusted to saturation.

Finally, for millimeter and microwave radiation surface emissivity is typically less than 1.0 and retrieval results are highly sensitive to characteristics of the underlying surface (Isaacs and Deblonde, 1987). During simulations we allowed the emissivity to vary with sensor and surface type

according to Table 4.4. These are consistent with the RADTRAN surface emissivity models given by Isaacs et al. (1989).

4.4 D-Matrix and statistical retrievals

A variety of possible retrieval approaches could be applied to the 183 GHz water vapor retrieval problem. These include both physically based methods and those relying on statistical principles. These are summarized in Table 4.5 (see Isaacs, 1987 for further details). For this study we have adopted a simple statistical approach.

The specific statistical inversion or D-Matrix approach to atmospheric parameter retrievals has been described by various investigators (Rodgers, 1976; Smith and Woolf, 1976; Gaut et al., 1975; Isaacs et al., 1985). It is essentially a least squares approach which finds the most likely combination of atmospheric parameters which yields the set of observed radiometric data. The method used here utilizes an eigenanalysis of the observed data and retrievable parameter covariance matrices. Briefly, an individual retrieval of temperature or relative humidity on k vertical levels from n channels of brightness temperature measurements is represented by the matrix equation:

$$p = Db$$

with

$$D = (PB^T) (\Phi \Lambda^{-1} \Phi^T)$$

where

- p is a vector containing the retrieved profile
- b is a vector containing n brightness temperatures
- P_{ks} is the retrievable atmospheric profile at k levels for s samples
- B_{ns} are brightness temperatures for n channels and s samples
- Φ are eigenvectors of BB^T
- Λ is a diagonal matrix whose elements are the corresponding eigenvalues

By setting some of the diagonal elements of Λ to zero, the method allows one to retain only those EOFs whose corresponding eigenvalues are relatively large. This yields a more stable matrix inversion and reduces the effect of

noise in the brightness temperature data. In this study, then, the temperature and relative humidity profiles and associated brightness temperatures from Set 1 were combined to construct D-Matrices for each of the categories shown in Table 4.1. An eigenvector was retained only if the ratio of its corresponding eigenvalue to the largest eigenvalue was greater than 1.0×10^{-6} .

Once the necessary D-Matrices were created, error statistics were calculated by simply retrieving relative humidity and temperature from Set 2 radiances using the Set 1 D-Matrices and comparing the retrieved profiles with the true profiles. Retrievals of both variables were done separately in that humidity was first retrieved using both SSM/T-1 and SSM/T-2 data, followed by temperature retrievals using the same radiometric data.

For each error statistic category in Set 2 the retrieval or observing error standard deviation (OESD) at each level, the mean retrieval error (bias), and the interlevel correlations of the retrieval error were computed. Subsequently, EOFs of the vertical correlations were also computed; these were needed to reconstruct the appropriate vertical errors during the retrieval simulations. A more detailed discussion of the actual retrieval errors which were used during simulation is contained in Section 5.

4.5 Simulation of D-Matrix retrievals

To conduct the OSSE the following sequence of steps was repeated for the location of each simulated retrieval:

- Compute the next satellite field-of-view (FOV) location and time.
- Interpolate the nature run data to the FOV location.
- Based on predefined criteria, determine the geophysical category of profile.
- Perturb the interpolated profile based on OESD, bias and vertical error correlations for that category.

Simulations were created for the entire assimilation period (6 Z 18 November 1979 - 0 Z 25 November 1979). Retrievals were organized in 6 hour

intervals, centered on the synoptic times to accommodate the AFGL statistical analysis system (Norquist, 1986).

Computation of the satellite surface FOV requires specification of (1) the orbital characteristics of the sensor-bearing platform, and (2) the scanning attributes of the sensor itself. The orbital parameters of the DMSP polar orbiting satellite are well documented and we have used these in our simulations. Although the operational T-1 and proposed T-2 instruments have different scan patterns we have assumed for consistency that both scan patterns are identical so that measurements from one sensor are coincident with another. This eliminates an additional preprocessing ambiguity in which smaller T-2 footprints would have to be combined and interpolated to the larger FOV of the T-1 sensor. Orbital and scan parameters as well as details of the FOV computation used in our simulations are described in Appendix A. Note that although scanning characteristics associated with the T-2 sensor are included in Appendix A they were not used during the OSSE.

Once the location of the current sounding location is computed, it is verified against a data base of surface type and any FOV falling over land is rejected. For an accepted FOV, nature run data is interpolated bilinearly in space and linearly in time from the nearest two nature run time levels to create the unperturbed or "true" profile.

The resulting data pattern for a typical 6-hour period (in this case 00Z on 25 November) is shown in Fig. 4.1.

Assignment of the profile into one of several geophysical classes is based on a number of criteria:

Surface type (ice/ocean): From an NMC data base which reflects November climatology, each gridpoint on the $2.5^\circ \times 2.5^\circ$ grid is flagged as either land, ice covered, or ocean.

Geographic location: Points poleward of approximately 30° which are not ice covered are flagged as midlatitude profiles. All other profiles are considered tropical. To allow for a smooth transition from tropical to midlatitude statistics, the crossover point for each satellite orbit was taken to be 30° plus a random Gaussian perturbation.

Sea surface roughness: Assuming that the 1000 mb wind in the unperturbed profile is equal to the surface wind, profiles with a horizontal wind speed less than or equal to 7 ms^{-1} are assigned a low wind/calm ocean flag. Those with a higher surface wind are assigned the high wind/rough ocean flag.

Cloud cover: Methods to infer cloud cover from relative humidity data (and vice-versa) vary in complexity. The approach we have adopted utilizes the Tibaldi scheme (Norquist, 1988) which is actually a means of converting cloud cover data to relative humidity in four atmospheric layers. We have adapted the method to solve the inverse problem, and since the scheme then yields a percent cloud cover in each vertical layer we convert this to a binary cloud/no cloud assignment. If the number of relative humidity levels in which the computed cloud cover exceeds 50% is greater than 3, then the profile is cloudy. In all other cases the profile is clear.

Finally, the profile derived from nature run output was perturbed by an amount which depends upon the error statistics associated with the geophysical category. Given an unperturbed profile of atmospheric parameters, P , the perturbation is of the form:

$$\hat{P} = P + E$$

where

P is the unperturbed profile obtained from the nature run

E is the retrieval error

\hat{P} is the retrieved profile.

The total retrieval error at any vertical level k may be written as

$$E_k = \bar{E}_k + E'_k$$

where

\bar{E}_k is the systematic component

E'_k is a random component.

For each profile to be retrieved the systematic component is the same for each category and level. The random component is computed from:

$$E'_k = \sum_{i=1}^N e B_{ik}$$

with

$$B_{ik} = \phi_{ik} \sigma_k$$

where

ϕ_{ik} is the value of the i^{th} EOF at level k determined from eigenanalysis of the vertical error correlations

σ_k is the retrieval error standard deviation

e is a random number from a Gaussian distribution with a mean of 0 and a standard deviation of 1

N is the number of EOFs.

Since the error correlation EOFs, the error standard deviation, and the systematic error are different for each geophysical category horizontal and vertical retrieval error statistics should be reproduced with greater fidelity.

Table 4.1 Geophysical categories used to generate retrieval error statistics. Also shown are the number of samples in each category.

Parameter	Set 1 Training Sub-Sample	Number of Profiles	Geophysical Category	Set 2 Independent Sub-Sample(s)	Number of Profiles
T	Ice	438	1	Ice	438
	Ocean	536	2	Calm ocean, Tropics	459
			3	Calm ocean, Mid-Latitudes	493
			4	Rough ocean, Tropics	583
			5	Rough ocean, Mid-Latitudes	629
RH	Ice, Clear	430	1	Ice, Clear	437
	Ice, Cloudy	452	2	Ice, Cloudy	440
	Ocean, Clear	430	3	Calm ocean, Tropics, Clear	425
			4	Calm ocean, Mid-Latitudes, Clear	523
			5	Rough ocean, Tropics, Clear	435
			6	Rough ocean, Mid-Latitudes, Clear	293
	Ocean, Cloudy	427	7	Calm ocean, Tropics, Cloudy	351
			8	Calm ocean, Mid-Latitudes, Cloudy	238
			9	Rough ocean, Tropics, Cloudy	392
			10	Rough ocean, Mid-Latitudes, Cloudy	259

Table 4.2 Microwave mission sensor characteristics

Instrument	Frequency (GHz)	Polarization (H or V)	FOV (km)	Response	NEAT (K)
SSM/T-1	50.5	H	200	surface	0.6
	53.2	H	200	T at 2 km	0.4
	54.35	H	200	T at 6 km	0.4
	54.9	H	200	T at 10 km	0.4
	58.825	V	200	T at 16 km	0.4
	59.4	V	200	T at 22 km	0.4
	58.4	V	200	T at 30 km	0.5
SSM/T-2	91.655±1.25	V	100	surface, water vapor	0.6
	150.00±1.25	V	60	surface, water vapor	0.6
	183.31±1	V	50	water vapor	0.8
	183.31±3	V	50	water vapor	0.6
	183.13±7	V	50	water vapor	0.6

Table 4.3 Cloud type characteristics

Model	Type	Mode Radius (μm)	Liquid Water Content (gm^{-3})	Vertical Extent (km)
1	Stratus	2.7	0.15	0.5 - 2.0
2	Cumulus	6.0	1.00	1.0 - 3.5
3	Altostratus	4.5	0.40	2.5 - 3.0
4	Stratocumulus	6.25	0.55	0.5 - 1.0
5	Nimbostratus	3.0	0.61	0.5 - 2.5

Table 4.4 Surface emissivity used for various surface types during radiative transfer simulations

Instrument	Ice	Calm Ocean	Rough Ocean
SSM/T-1	.85	.45	.58
SSM/T-2	.95	.70	.83

Table 4.5 183 GHz water vapor profile retrieval techniques

Investigators/ Date	Organization	Approach	Reference
Gaut et al., 1975	ERT	Use of 183 GHz and other channels for water vapor and cloud properties	AFGL-TR-75-0007.
Schaerer and Wilheit, 1979	NASA	Profile retrieval simulation using 5 channels and iterative method	<u>Radio Science</u> , <u>14</u> , 3, 371-375.
Rosenkranz et al., 1982	MIT	Statistical retrieval based on 60 GHz and 183 GHz simulations	<u>J. Appl. Meteor.</u> , <u>21</u> , 1364-1370.
Wang et al., 1983	NASA	Aircraft radiometer data and retrieval	<u>J. Clim. and Appl. Meteor.</u> , <u>22</u> , 779-788.
Kakar, 1983	JPL	Chahine-type retrieval	<u>J. Clim. and Appl. Meteor.</u> , <u>22</u> , 1282-1289.
Kakar and Lambrigsten, 1984	JPL	Statistical correlation technique	<u>J. Clim. and Appl. Meteor.</u> , <u>23</u> , 1110-1114.
Isaacs and Deblonde 1985, 1987	AER	Statistical retrieval	AFGL-TR-85-0040; AFGL-TR-85-0095. <u>Radio Science</u> , <u>22</u> 3, 367-377.
Isaacs et al., 1988	AER	Unified retrieval	AFGL-TR-88-0058.

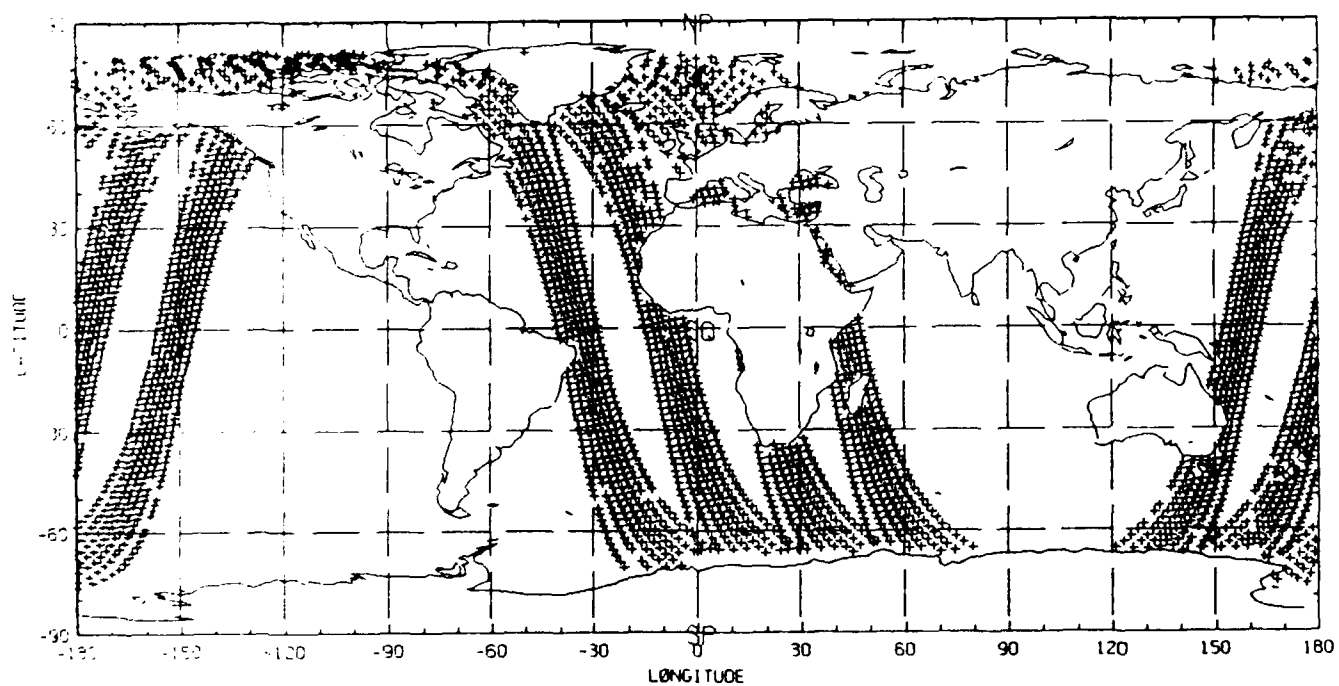


Figure 4.1 Data coverage by SSM data. Height observations at $\sigma=0.5$.

5. Statistical Analysis of Simulated Sensor Errors

After creating data sets 1 and 2 which contained selected relative humidity and temperature profiles spanning a range of geophysical conditions D-Matrix statistics were computed and retrievals were conducted as described in Section 4. These calculations resulted in a set of class dependent retrieval error statistics which were used in the subsequent observing system simulations.

5.1 Relative humidity retrieval error statistics

Retrieval bias

The systematic error or bias of the relative humidity (RH) retrievals which were obtained by retrieving set 2 profiles with set 1 D-Matrices are shown in Figs. 5.1 through 5.10. Each vertical profile is representative of a particular geophysical category; the categories themselves have been described in section 4.

Midlatitude profiles (Figs. 5.5, 5.6, 5.9, 5.10) have the same general shape consisting of mostly positive bias throughout with larger values (approximately 5 to 10 percent RH) in the mid troposphere decreasing to near zero at the surface and 300 mb. At the same time tropical bias profiles (Figs. 5.3, 5.4, 5.7, 5.8) tend to have a structure with negative values in the lower troposphere changing to positive values at higher levels. Profiles for polar ice surface retrievals show little, if any, bias at the six retrieval levels. And in all cases retrieval bias is generally small, in the range of 5 to 10 percent, but occasionally increasing to near 20 percent (see Class 3, 4, and 7 profiles).

Finally, there appears to be only a slight difference between corresponding clear and cloudy profiles, the only noticeable difference being a slight negative shift (about 5 percent) of the cloudy profiles to more negative (or less positive) values. This may be a function of the cloud models used and field-of-view beam filling effects, however the fact that separate D-Matrices for clear and cloudy conditions were used ought to minimize the cloud signature in the bias profiles.

Interpreting the nature of these systematic errors is not entirely straightforward. The relationship of variations in observed brightness temperatures to variations in water vapor amounts under conditions of non-unit surface emissivity is highly dependent upon the value of the emissivity and the structure of the low level temperature profile, as well as the water vapor amount itself. Moreover, the water vapor retrieval problem is inherently non-linear because variations in water vapor concentrations directly affect the atmospheric transmission and therefore, the vertical weighting functions. This implies that, for example, an increase in water vapor in the 1000 to 850 mb layer may produce either a positive or a negative change in the T-2 channel radiances and there is no clear way to state a priori what the sign of this change will be.

Retrieval error standard deviation

The OESD profiles for relative humidity retrievals are shown in Figs. 5.11 through 5.20. These profiles generally contain larger errors at 700 or 500 mb and lower errors at the surface. This is at variance with typical statistical retrieval errors which tend to have largest errors in near surface layers.

The range of errors in the OESD curves is considerably greater than the corresponding bias profiles with values between 8 and 25 percent. This means that, on average, random errors will tend to dominate the systematic error component and any error correlations in the horizontal between simulated retrievals will tend to be small. This was indeed the case when resulting retrieval error correlations of the OSSE were computed as a function of distance.

Geographical dependence of the OESD profiles is also evident. The essential feature here is that extratropical profiles (Figs. 5.15, 5.16, 5.19, 5.20) have larger values than corresponding tropical profiles (Figs. 5.13, 5.14, 5.17, 5.18). This is most likely a reflection of the greater atmospheric variance present in the midlatitudes than in the tropics. Since the retrieval scheme operates in a least squares sense, it tends, in the mean, to retrieve profiles reflective of the average atmospheric conditions which were used to construct the particular D-Matrix. Thus statistical retrievals of profiles from a population with higher variance will result in higher rms

error values. This tropical/extratropical distinction has probably been blurred somewhat by binning profiles from the northern hemisphere extratropics together with southern hemisphere extratropical profiles because conditions in the November southern hemisphere (emerging summer) are likely to be more similar to tropical conditions than those in the northern hemisphere atmosphere (emerging winter).

Finally, the effect of cloudiness is quite evident in these profiles. A comparison of clear/cloudy category pairs shows that cloudy profiles have errors 2 to 4 percent greater than their clear counterparts. Moreover, the effect is greatest at levels below 500 mb where most of the clouds in the forward model are found.

Vertical error correlations

Vertical correlations of the retrieval errors were computed for all categories and two examples are shown here. Fig 5.21 shows the correlation of errors at 1000 mb with all other levels for Class 1 retrievals. In this example the errors at levels 300 mb through 850 mb are only weakly correlated with that at the surface. Fig. 5.22 shows the interlevel correlations with respect to the 500 mb level. This is an example of a more typical bimodal structure with relatively high positive correlations at adjacent levels and smaller anticorrelations at more distant levels.

5.2 Temperature retrieval error statistics

Retrieval bias

Profiles of temperature retrieval systematic errors for five categories are shown in Figs. 5.23 through 5.27. The most significant differences among the profiles depend on latitude. For example, both midlatitude profiles (Figs. 5.25 and 5.27) are characterized by negative biases of order -0.5 to -1.0 K below 300 mb and smaller positive biases above this level. On the other hand, profiles obtained from tropical retrievals (Figs. 5.24 and 5.26) have generally positive biases of order 0.5 to 1.0 K in the lower to middle troposphere with negative errors at higher levels. These bias values in the lower atmosphere are somewhat puzzling. The statistics used to construct the retrieval matrix were an amalgam of both tropical (relatively warm) and

midlatitude (relatively cold) profiles. Since the single D-Matrix was used one might expect that there would be a tendency for the retrieved lower troposphere temperatures to be too high in midlatitude cases and too cold in tropical cases. The results indicated here may again be a reflection of the fact that northern hemisphere winter and southern hemisphere summer profiles were mixed in computing the midlatitude statistics. As is the case with RH retrievals, the effect of varying sea surface roughness (surface emissivity) upon the error profiles is quite weak.

Retrieval error standard deviation

All the temperature OESD profiles contain large values near the surface and also near the tropopause. This agrees with results found in previous efforts to retrieve temperature using microwave channels (Isaacs et al., 1988). And the latitude dependence of the vertical error structure is again consistent with notions of atmospheric variability which applied to the RH retrievals. That is, errors are higher by approximately 1.0 K in the midlatitude categories (Figs. 5.30 and 5.32) than in the tropical categories (Figs. 5.29 and 5.31). For all profiles the range of values is from 1.0 to 3.0 K at all levels.

Vertical error correlations

Lastly, the interlevel correlations of the temperature retrieval error were computed and several examples of correlations for Class 1 are shown in Figs. 5.33 through 5.35. Each curve has a clearly defined structure; retrieval errors are positively correlated at nearby levels and negatively correlated for levels which are more distant.

In sum, these statistics were compiled by performing actual D-Matrix retrievals using simulated brightness temperatures corresponding to a small subset of nature run data. These statistics, in turn, were an integral part of the OSSE which was conducted using the much larger data set of the week 18 - 25 November 1979.

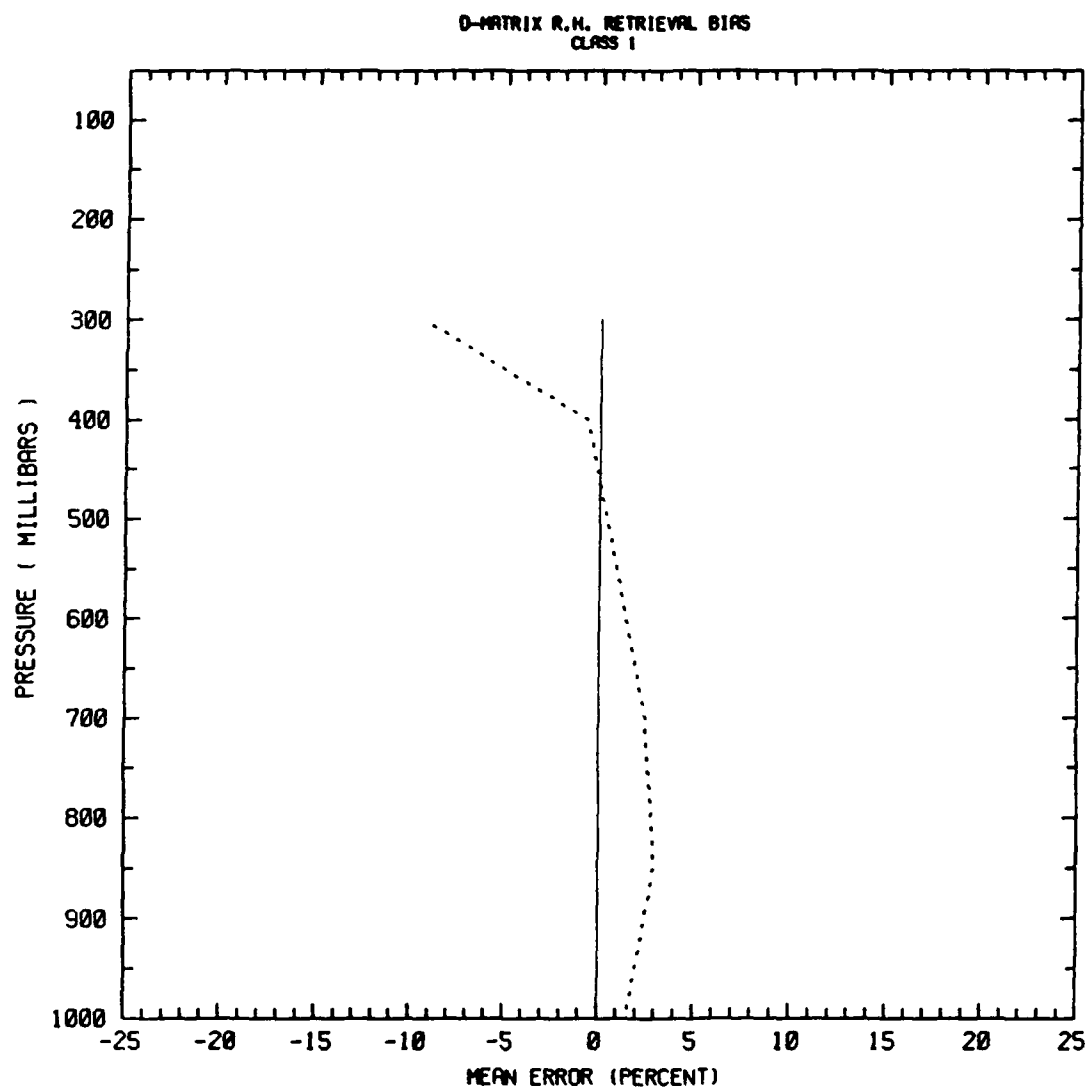


Figure 5.1 Relative humidity retrieval bias, Class 1.

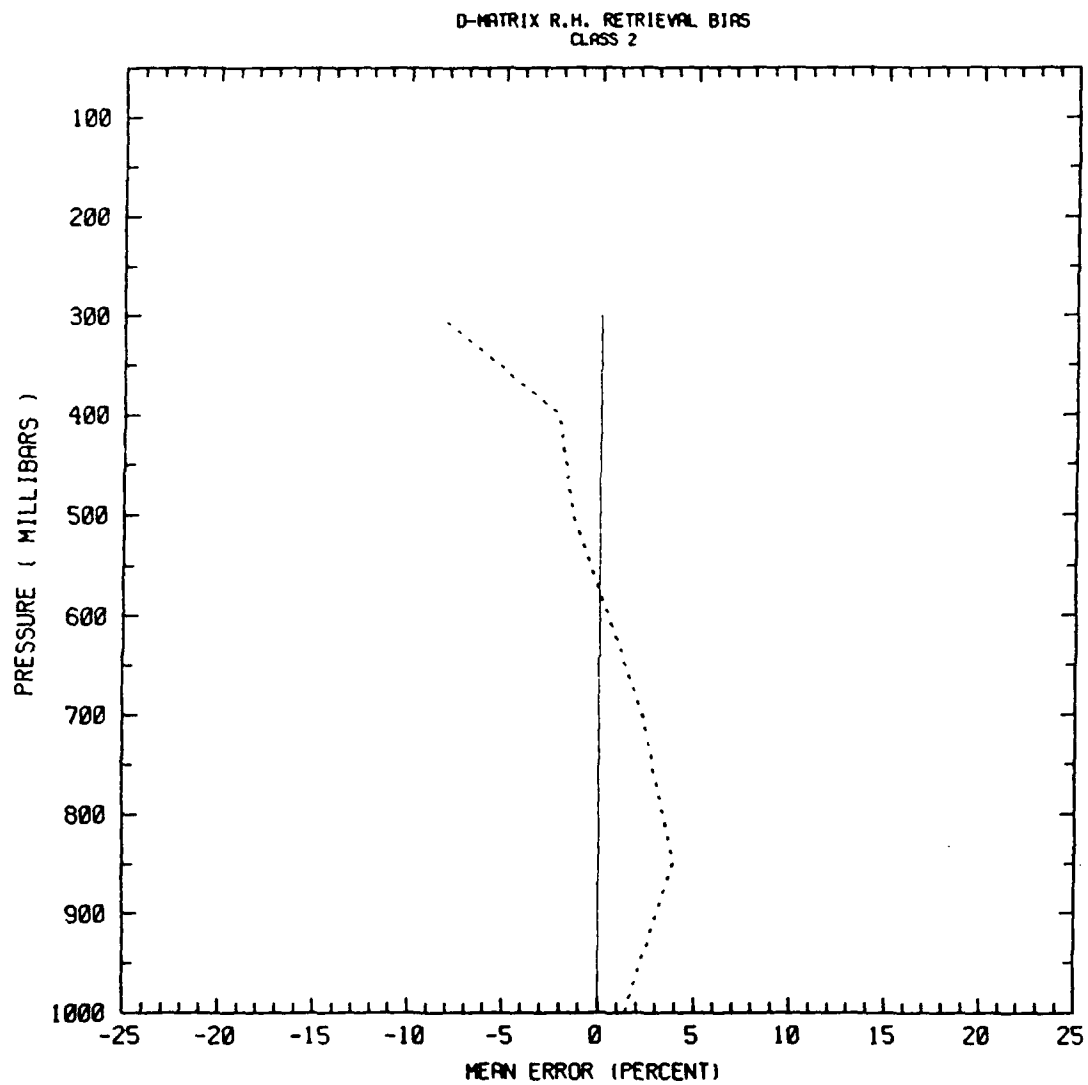


Figure 5.2 Relative humidity retrieval bias, Class 2.

D-MATRIX R.H. RETRIEVAL BIAS
CLASS 3

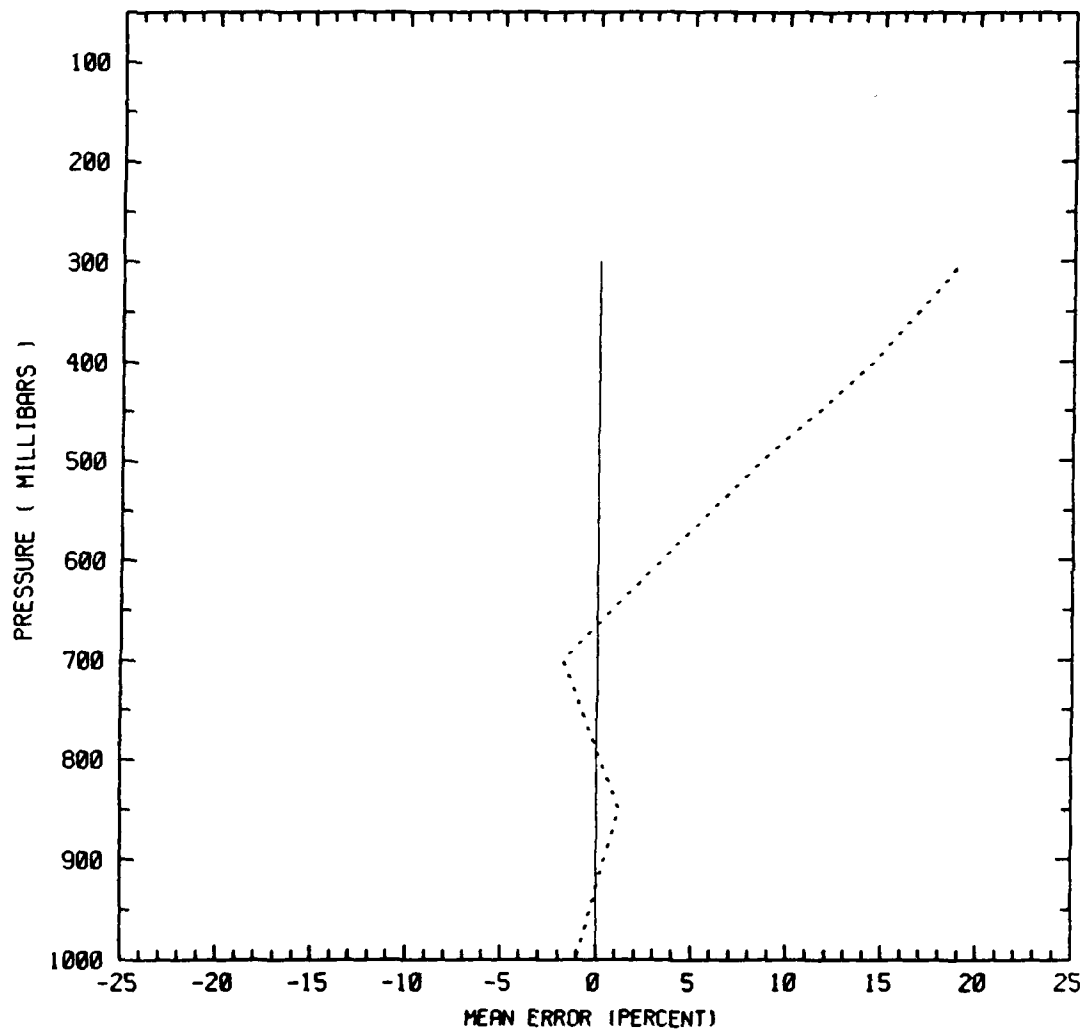


Figure 5.3 Relative humidity retrieval bias, Class 3.

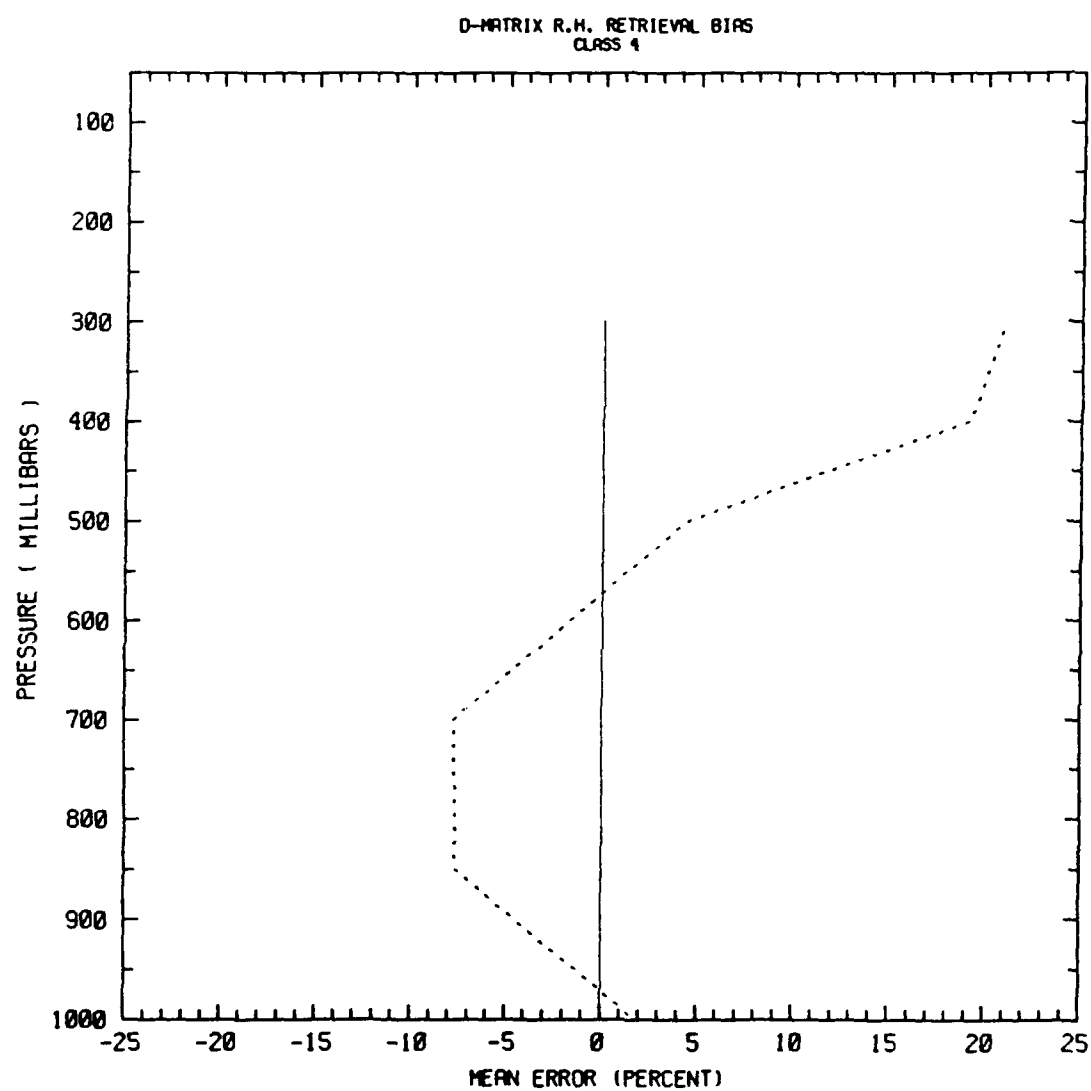


Figure 5.4 Relative humidity retrieval bias, Class 4.

O-MATRIX R.H. RETRIEVAL BIAS
CLASS 5

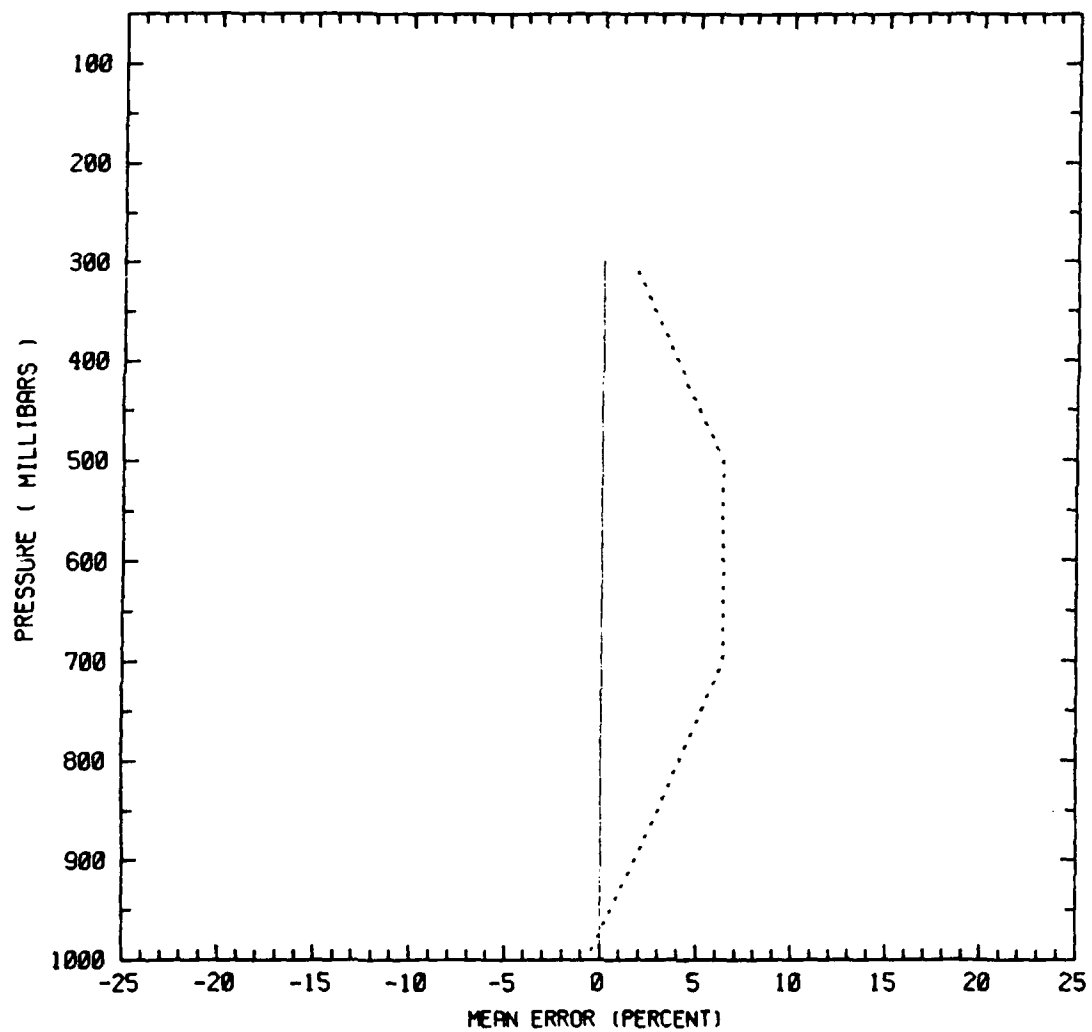


Figure 5.5 Relative humidity retrieval bias, Class 5.

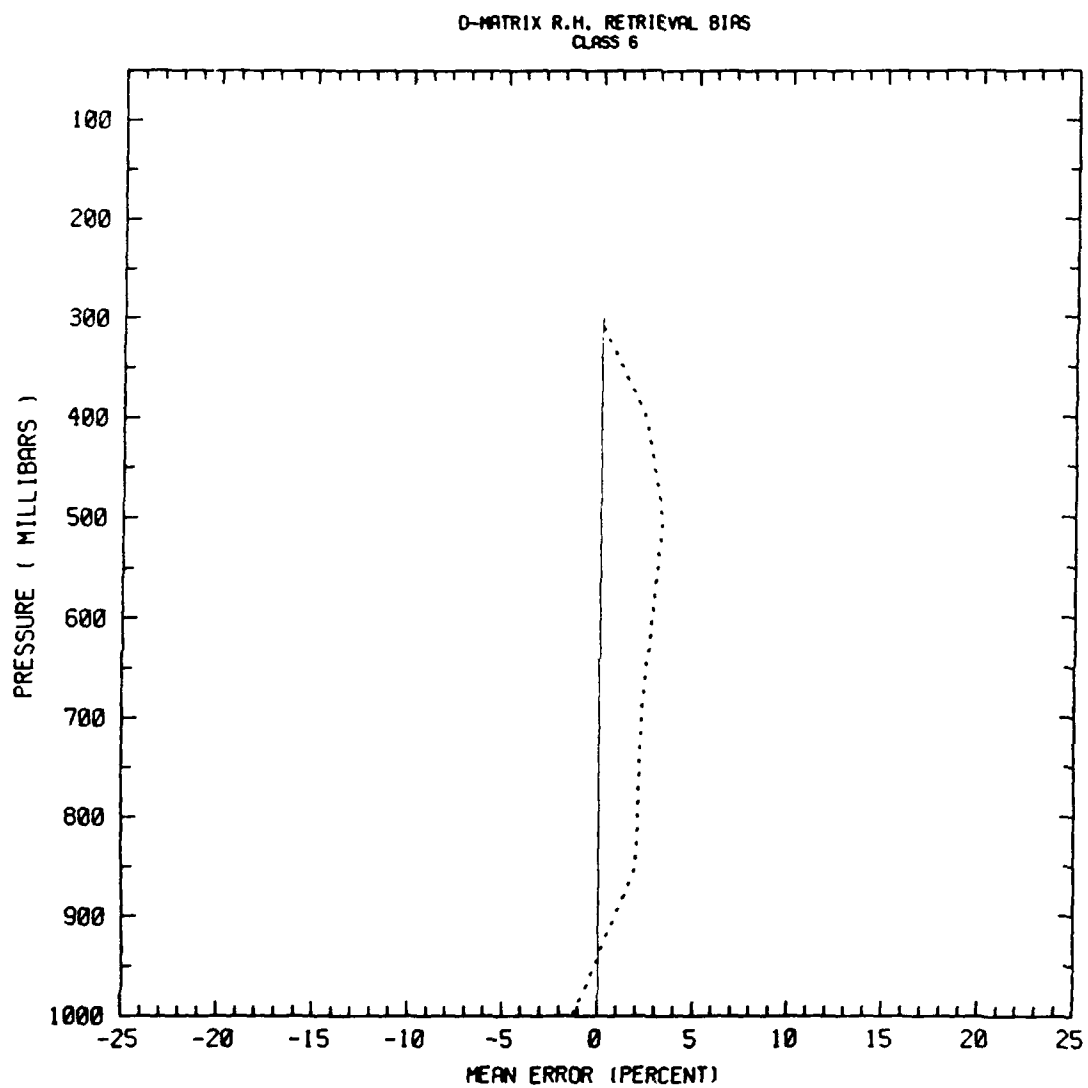


Figure 5.6 Relative humidity retrieval bias, Class 6.

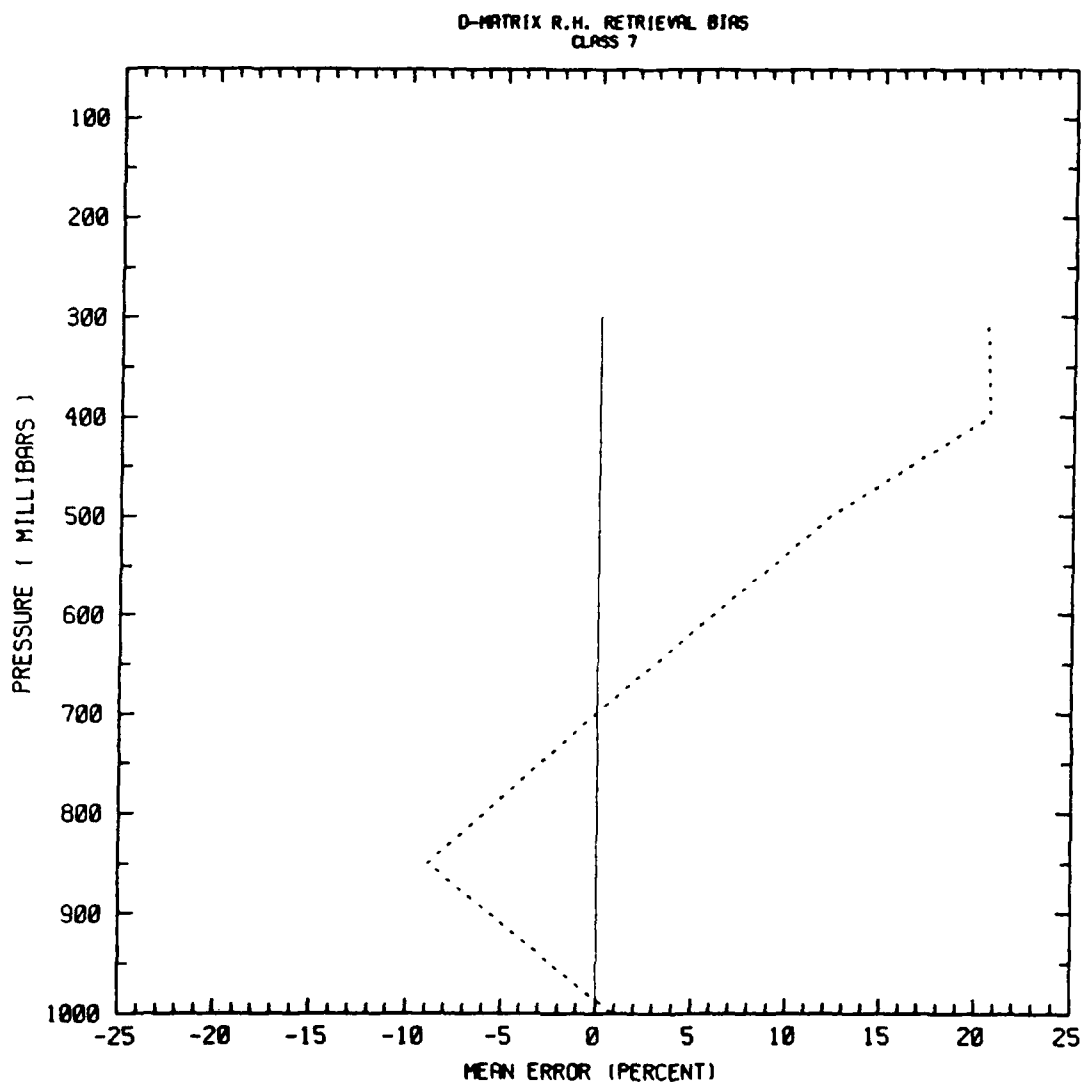


Figure 5.7 Relative humidity retrieval bias, Class 7.

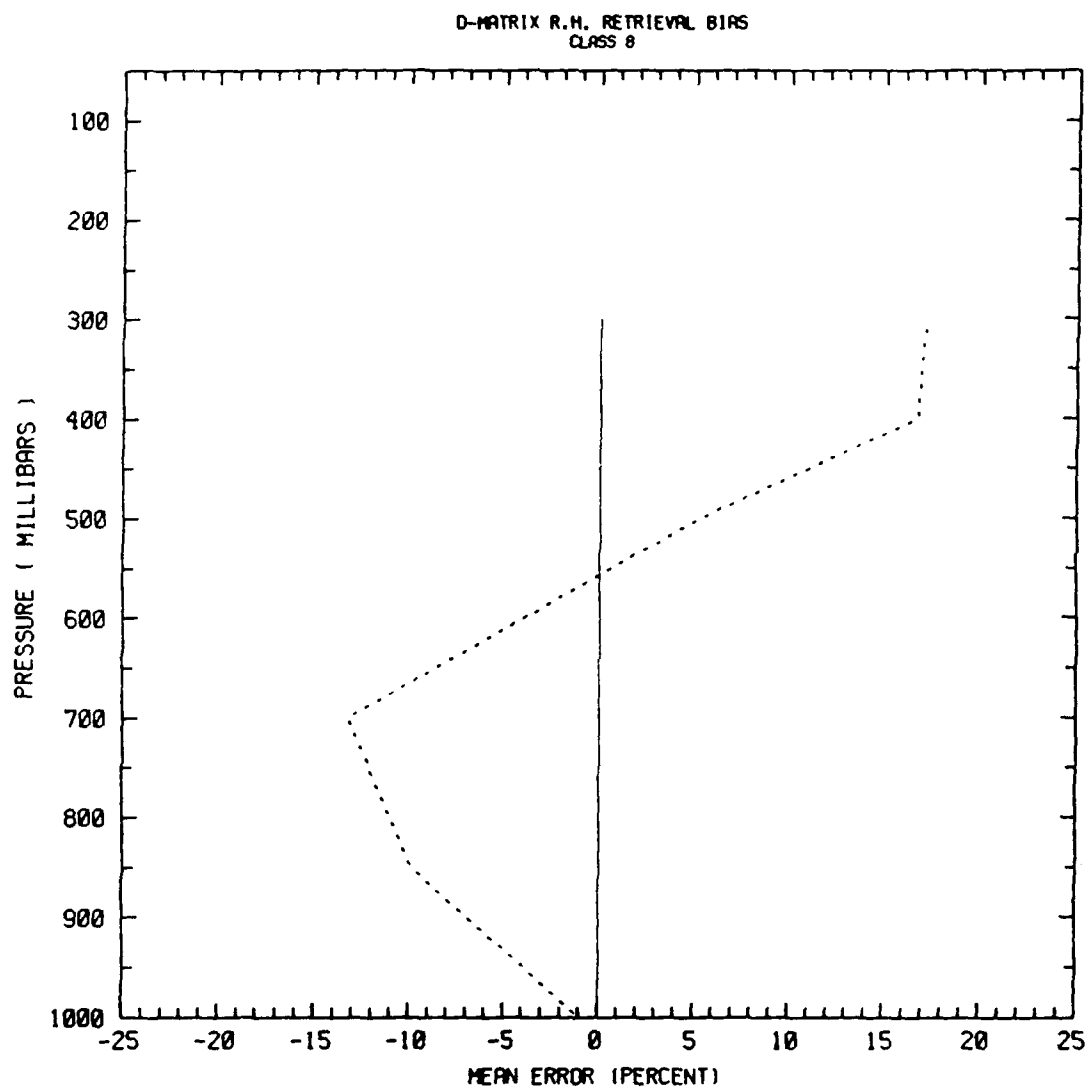


Figure 5.8 Relative humidity retrieval bias, Class 8.

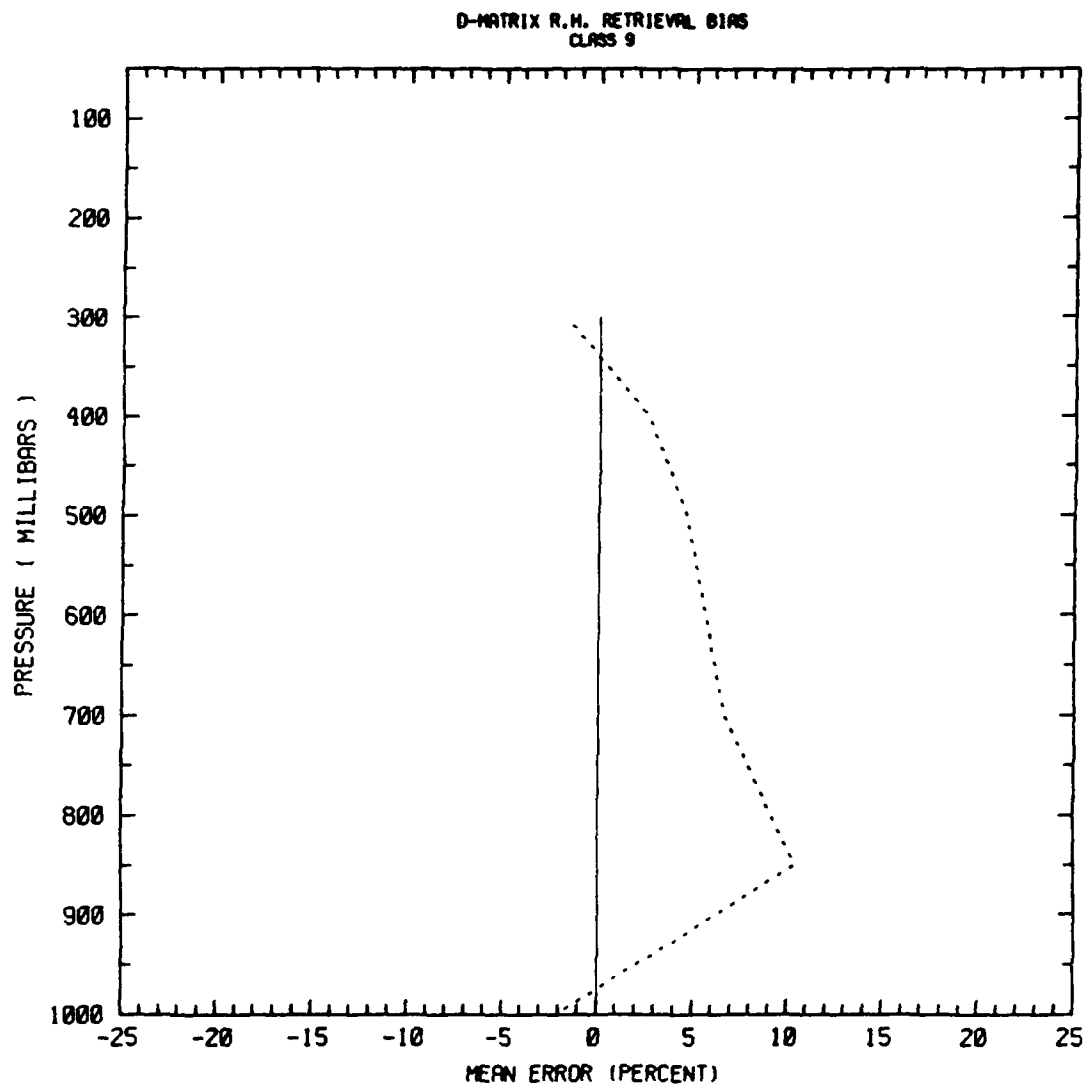


Figure 5.9 Relative humidity retrieval bias, Class 9.

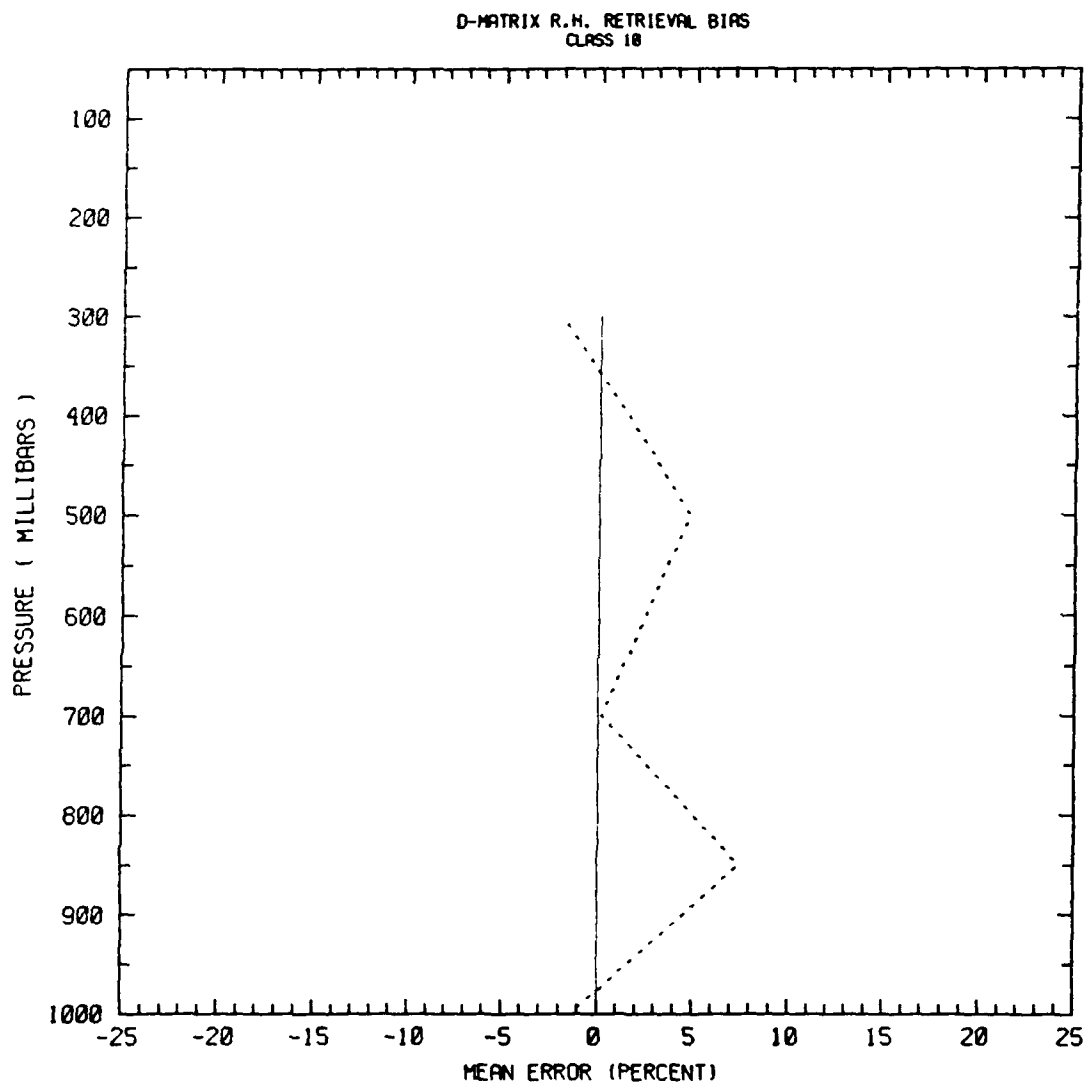


Figure 5.10 Relative humidity retrieval bias, Class 10.

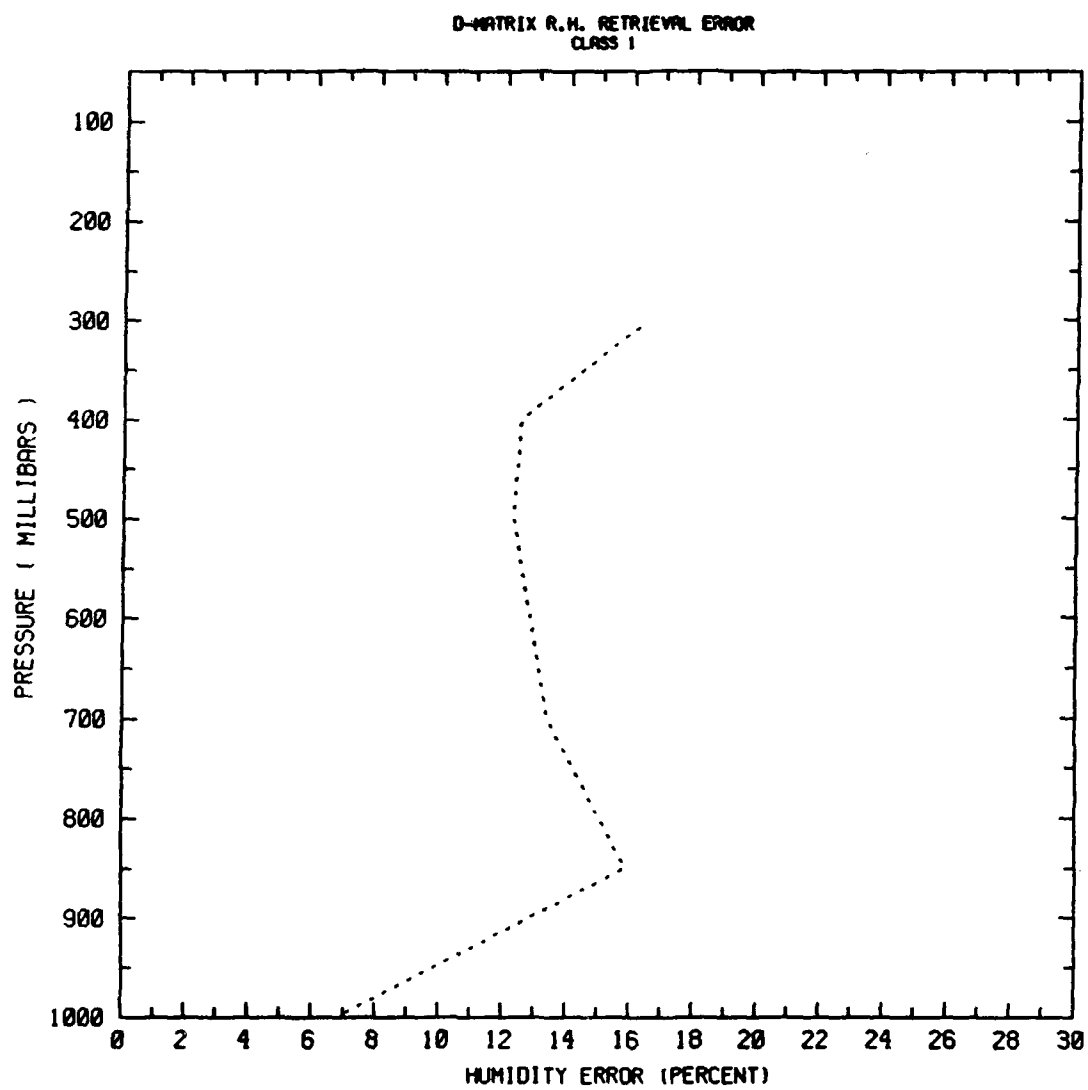


Figure 5.11 Relative humidity retrieval error, standard deviation, Class 1.

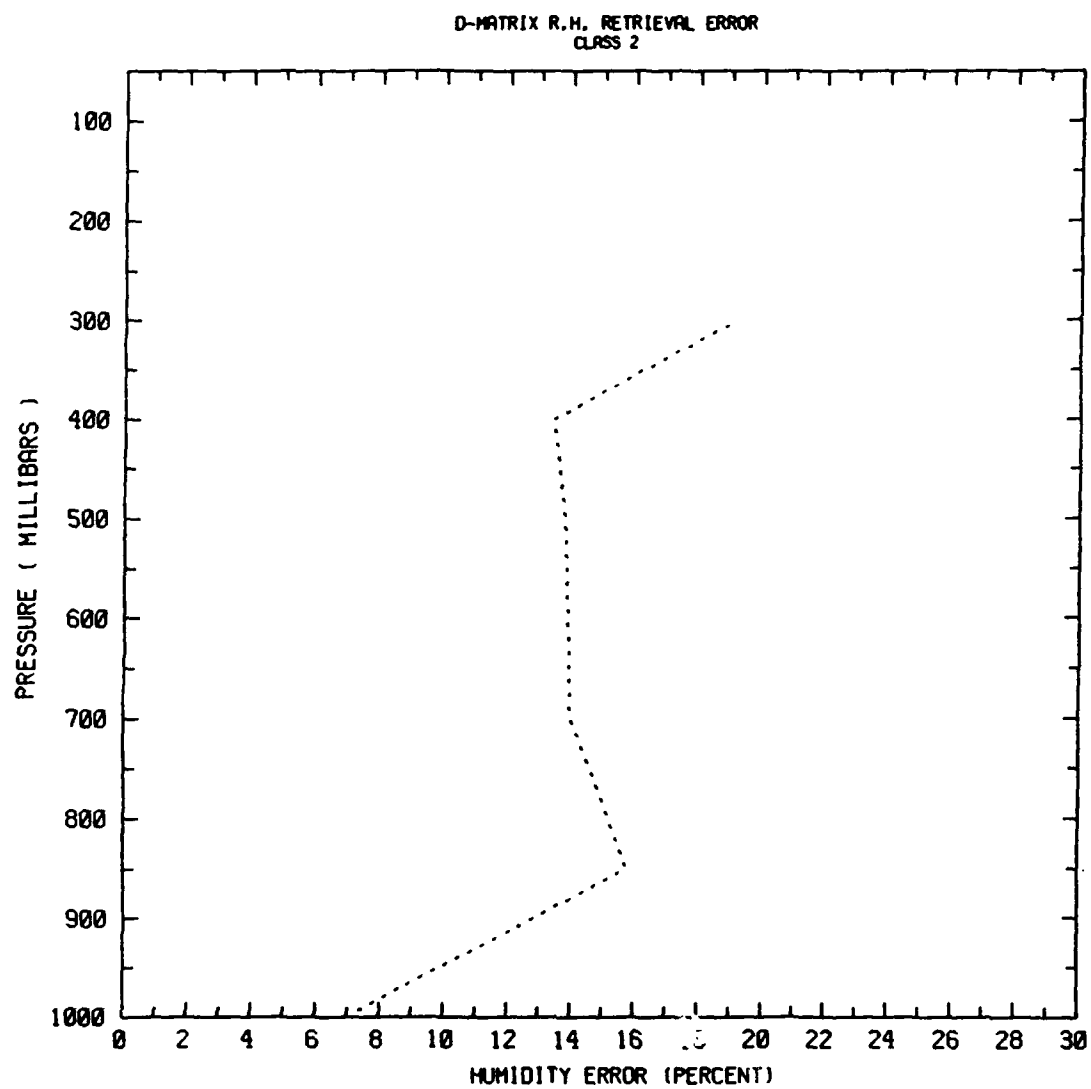


Figure 5.12 Relative humidity retrieval error, standard deviation, Class 2.

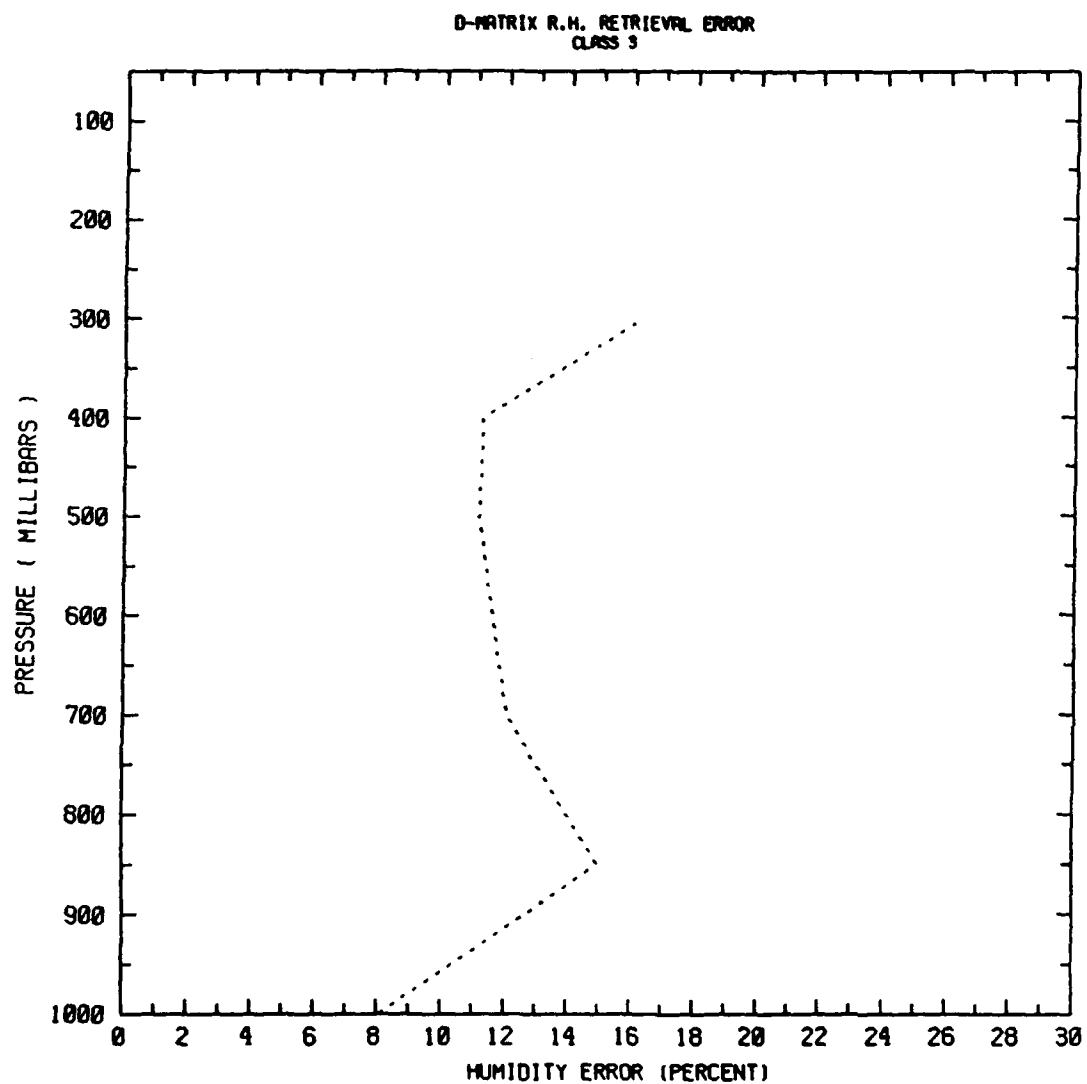


Figure 5.13 Relative humidity retrieval error, standard deviation, Class 3.

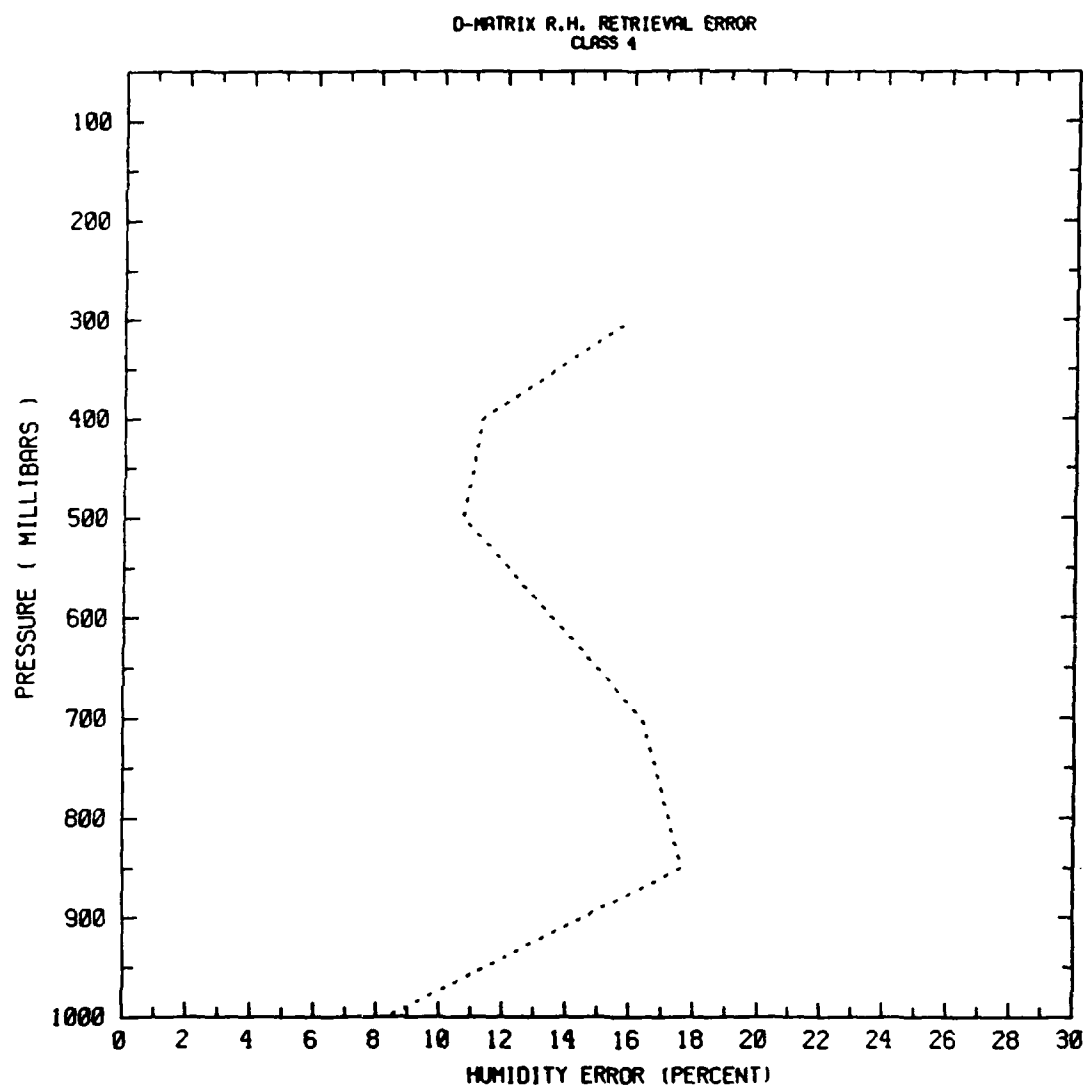


Figure 5.14 Relative humidity retrieval error, standard deviation, Class 4.

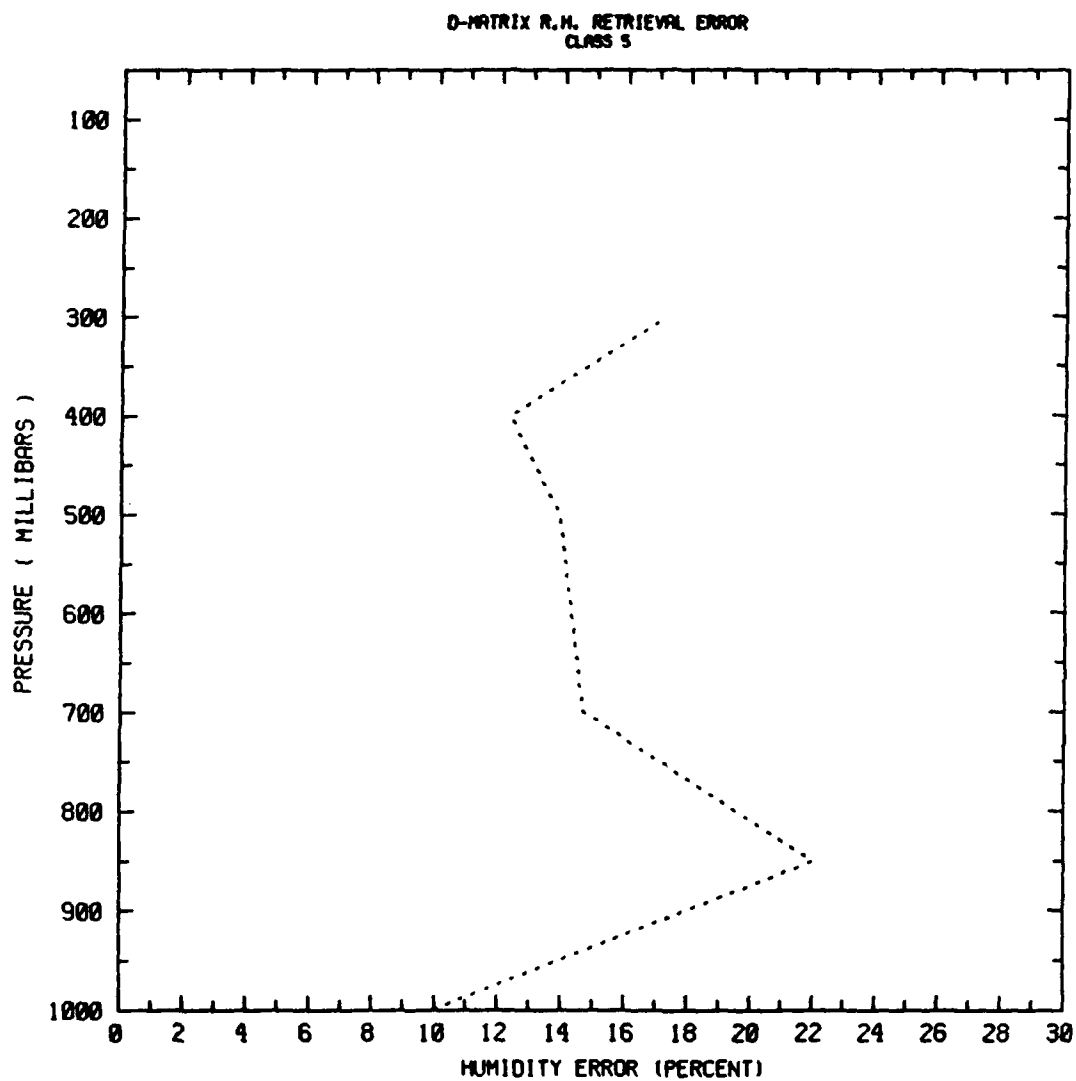


Figure 5.15 Relative humidity retrieval error, standard deviation, Class 5.

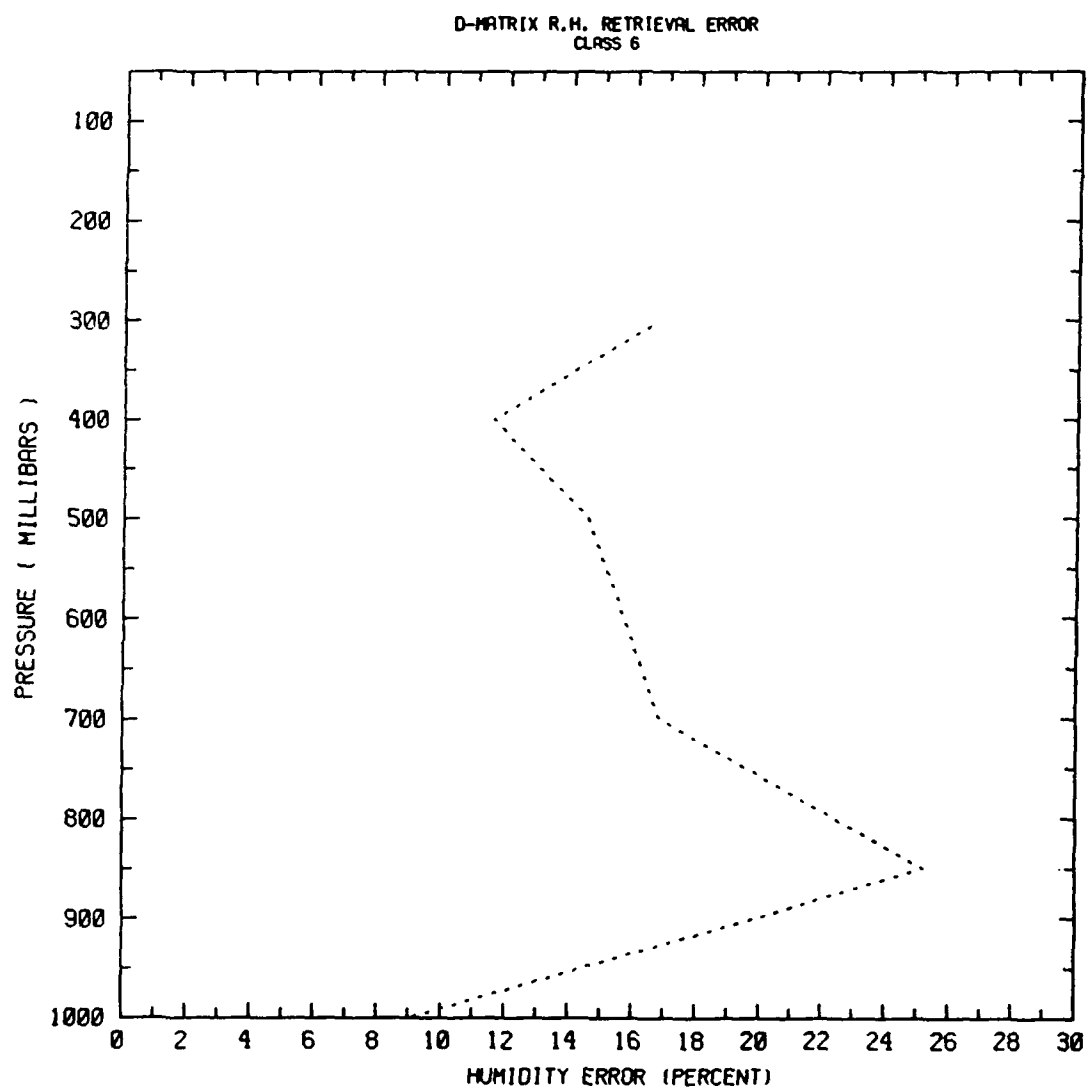


Figure 5.16 Relative humidity retrieval error, standard deviation, Class 6.

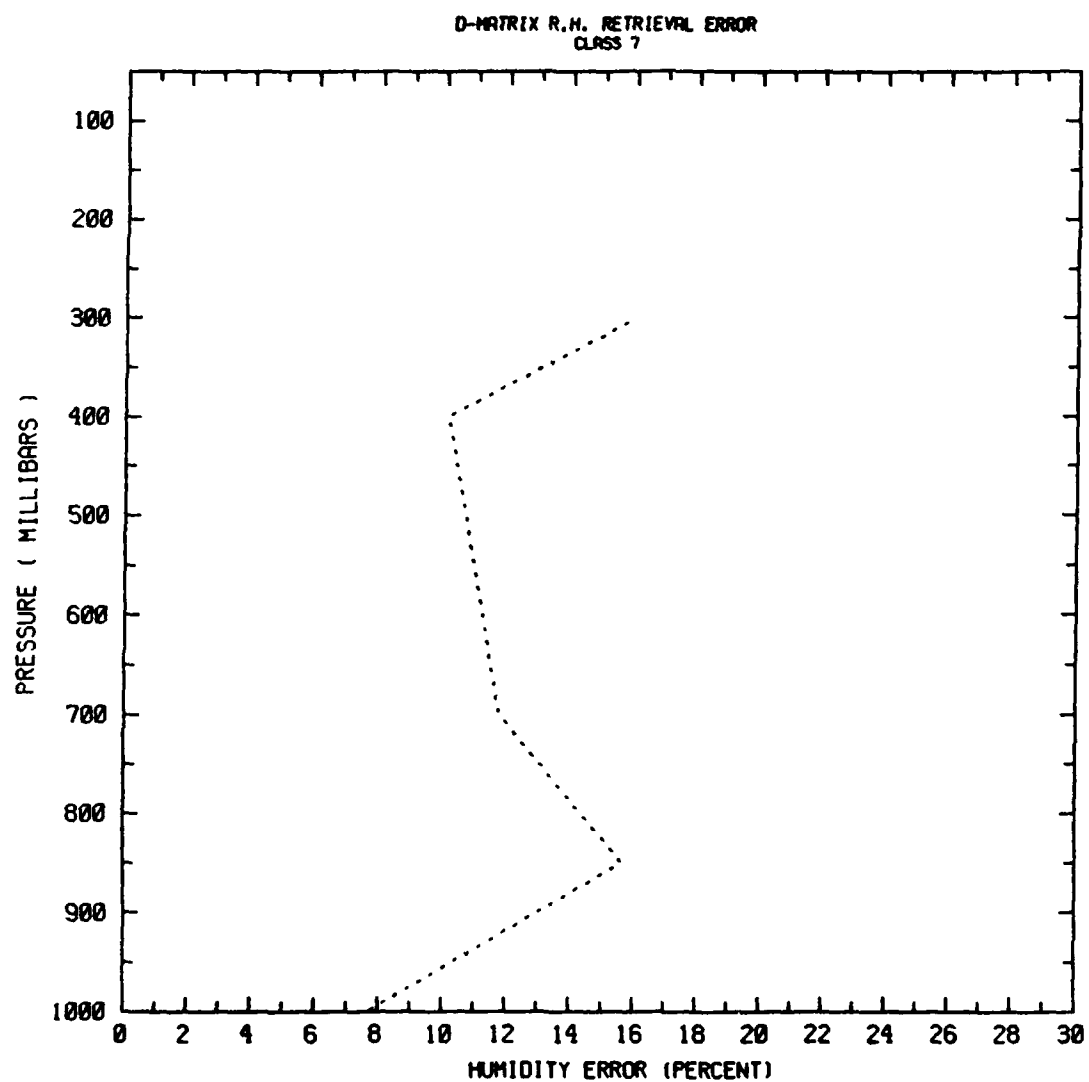


Figure 5.17 Relative humidity retrieval error, standard deviation, Class 7.

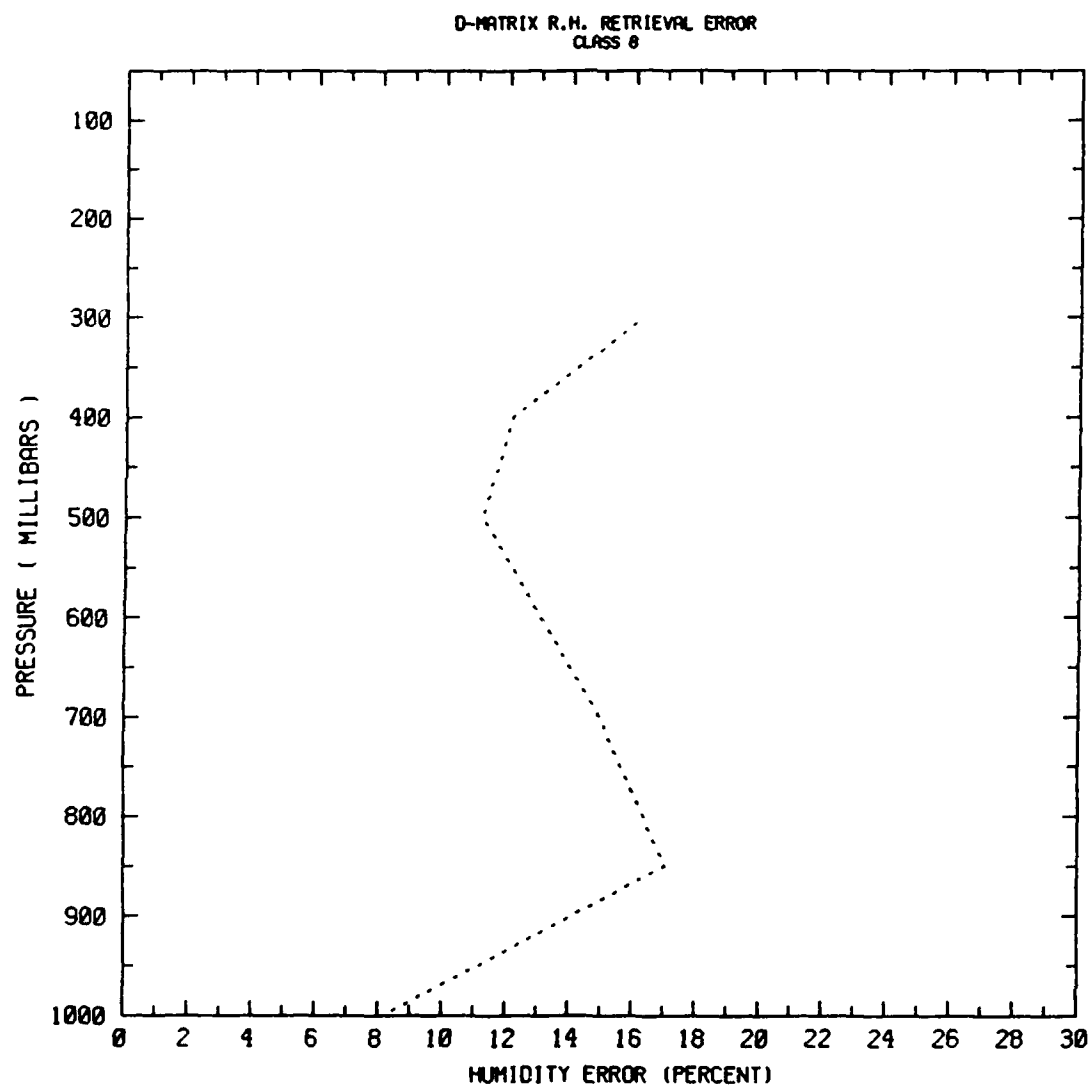


Figure 5.18 Relative humidity retrieval error, standard deviation, Class 8.

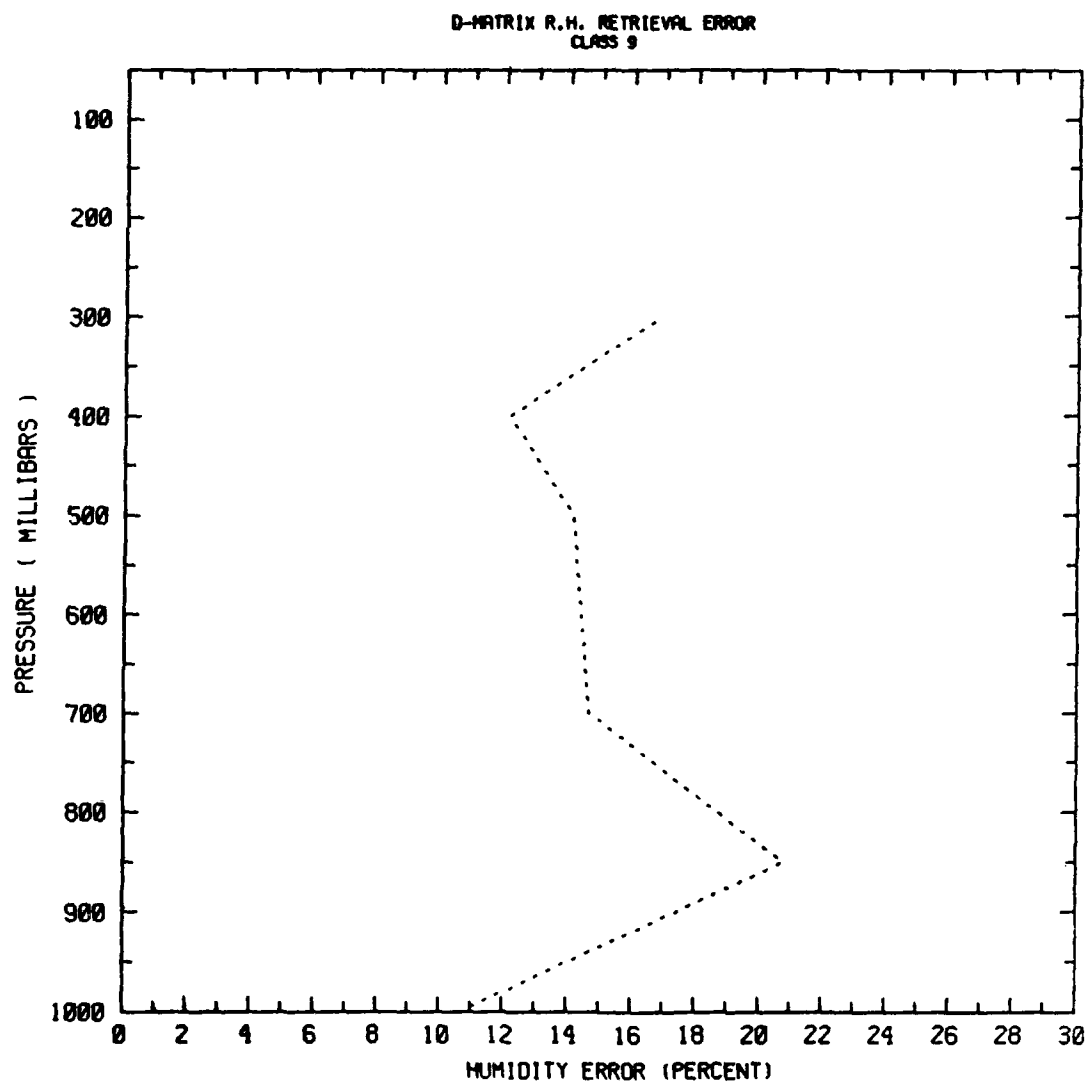


Figure 5.19 Relative humidity retrieval error, standard deviation, Class 9.

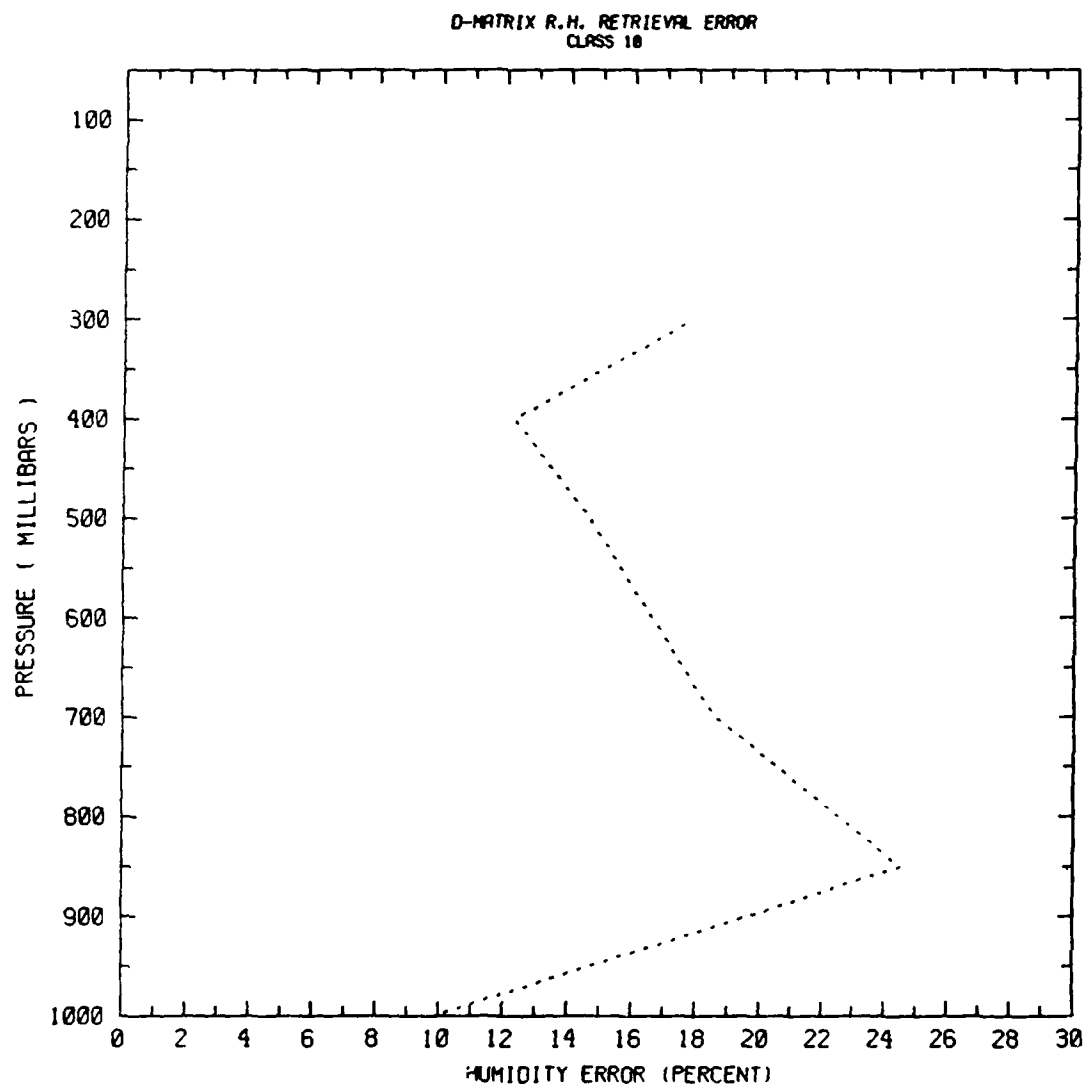


Figure 5.20 Relative humidity retrieval error, standard deviation, Class 10.

D-MATRIX R.H. RETRIEVAL VERTICAL ERROR CORRELATION
CLASS 1. CORRELATIONS WITH 1000 MB LEVEL

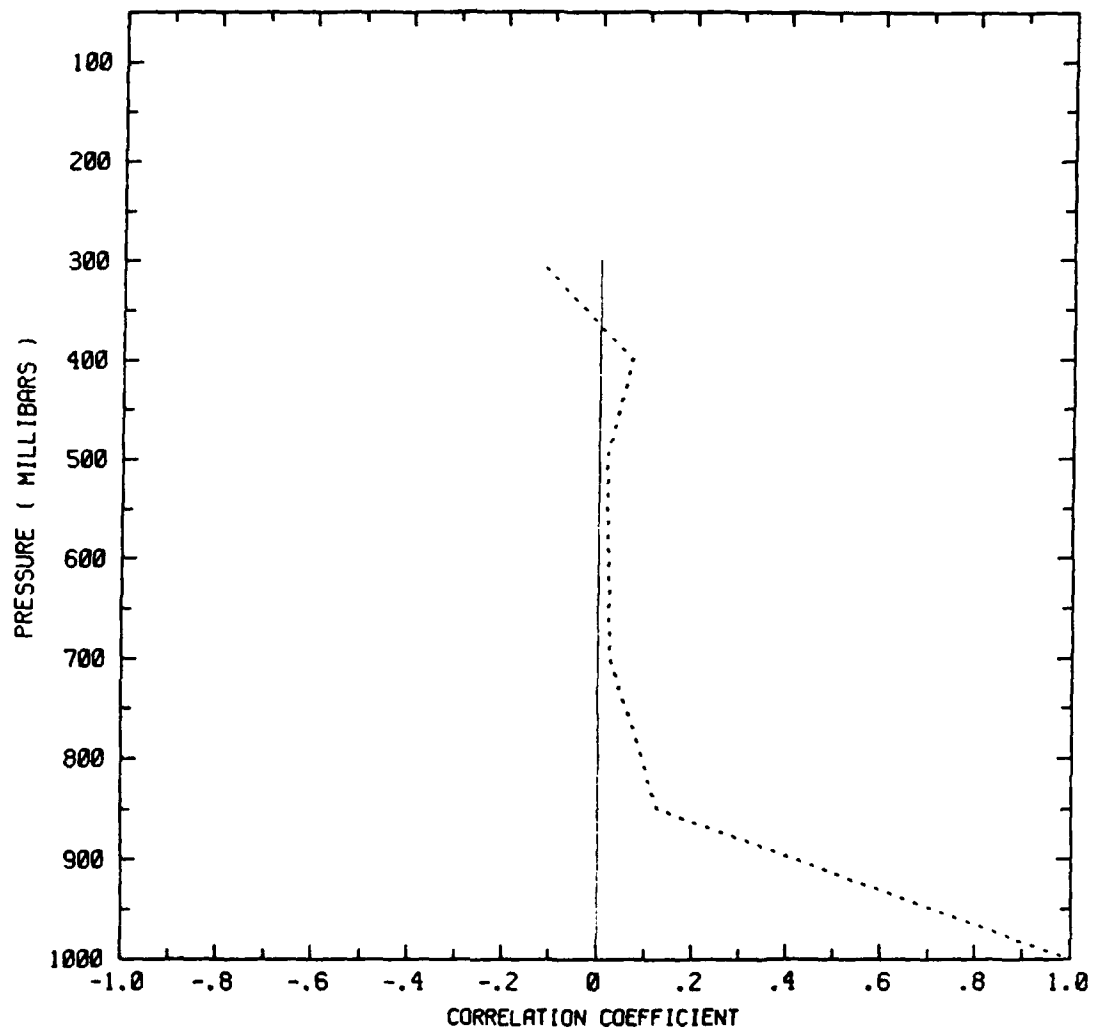


Figure 5.21 Relative humidity retrieval vertical correlations with 1000 mb error, Class 1.

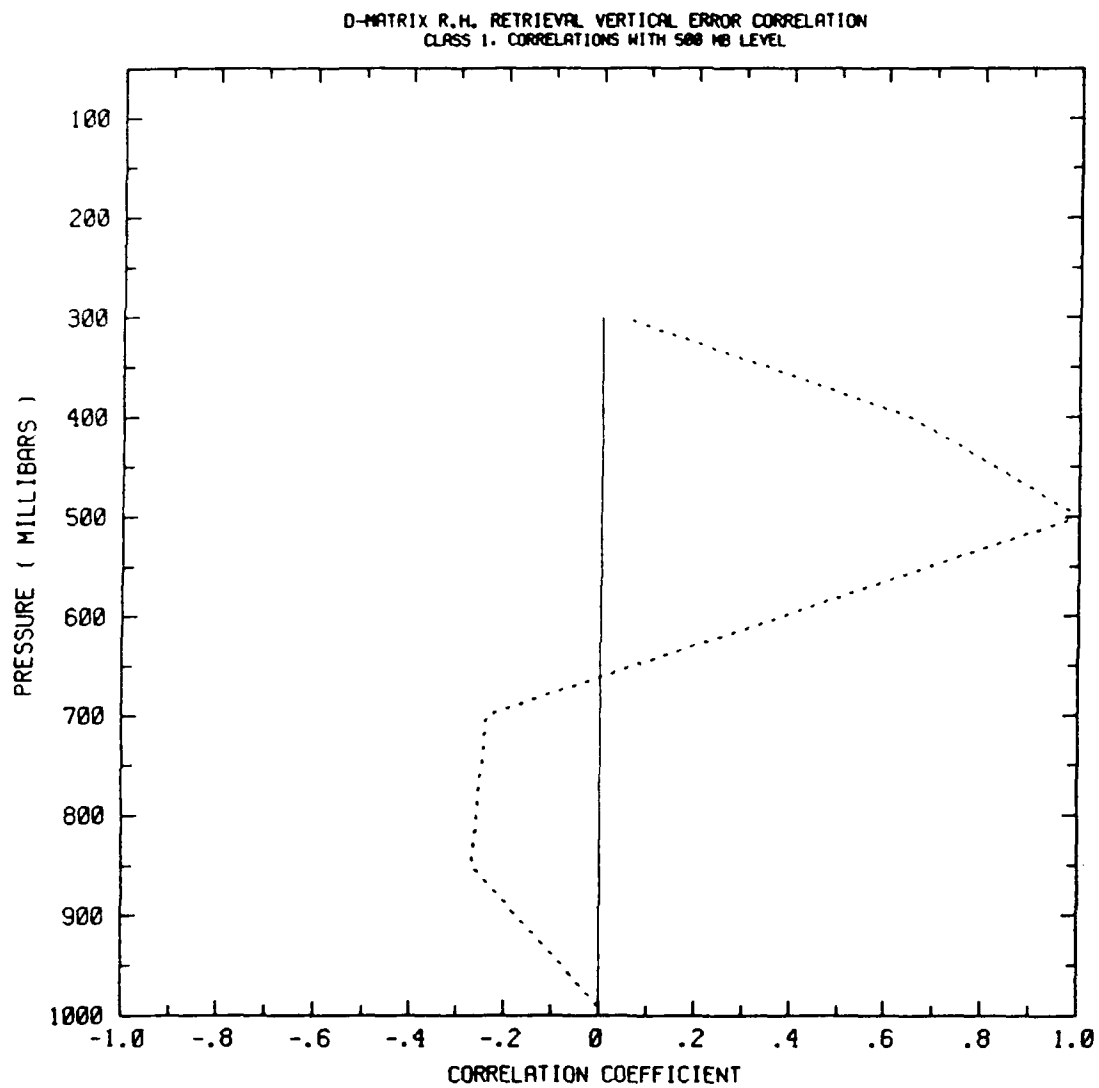


Figure 5.22 Relative humidity retrieval vertical correlations with 500 mb error, Class 1.

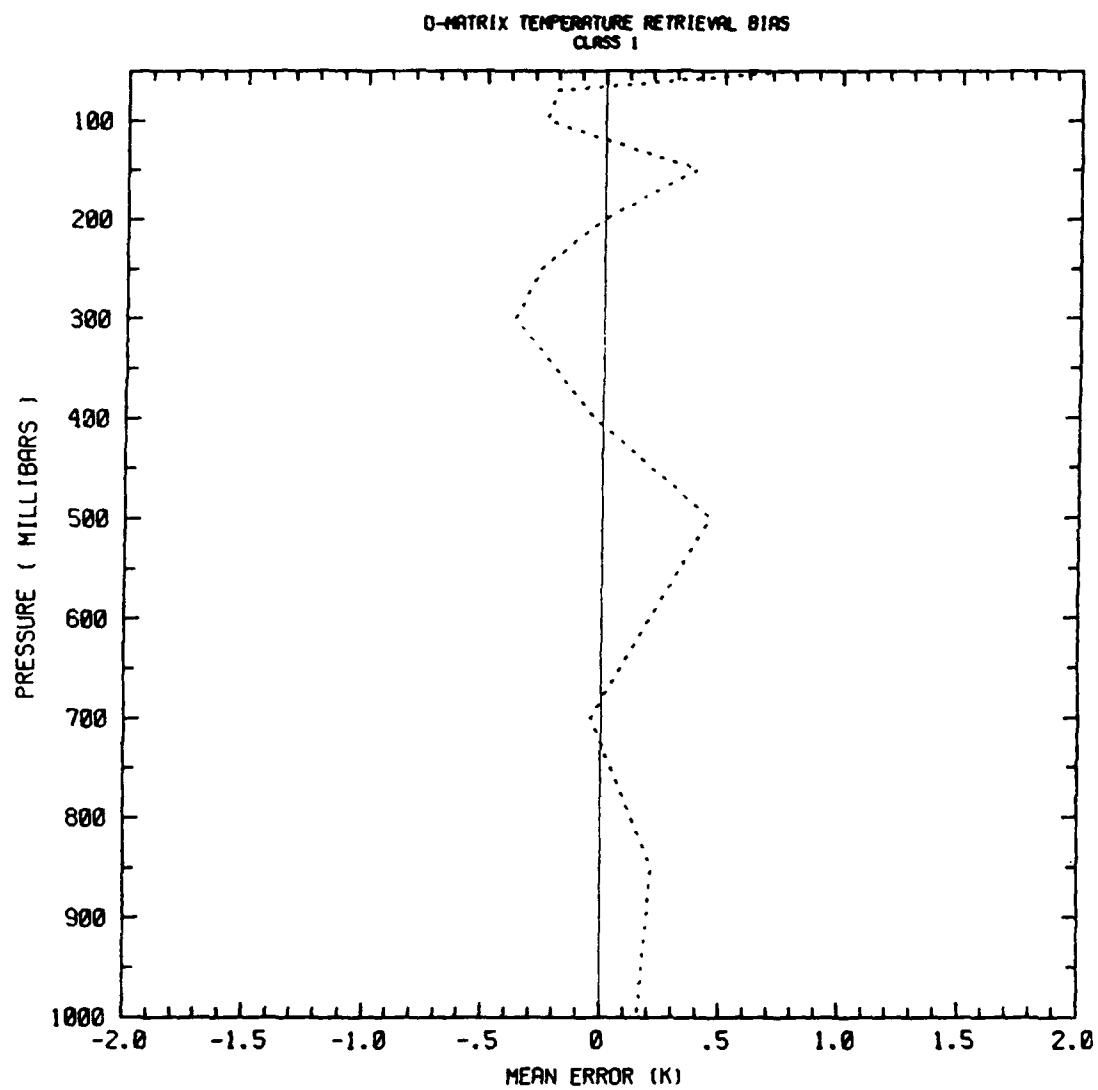


Figure 5.23 Temperature retrieval bias, Class 1.

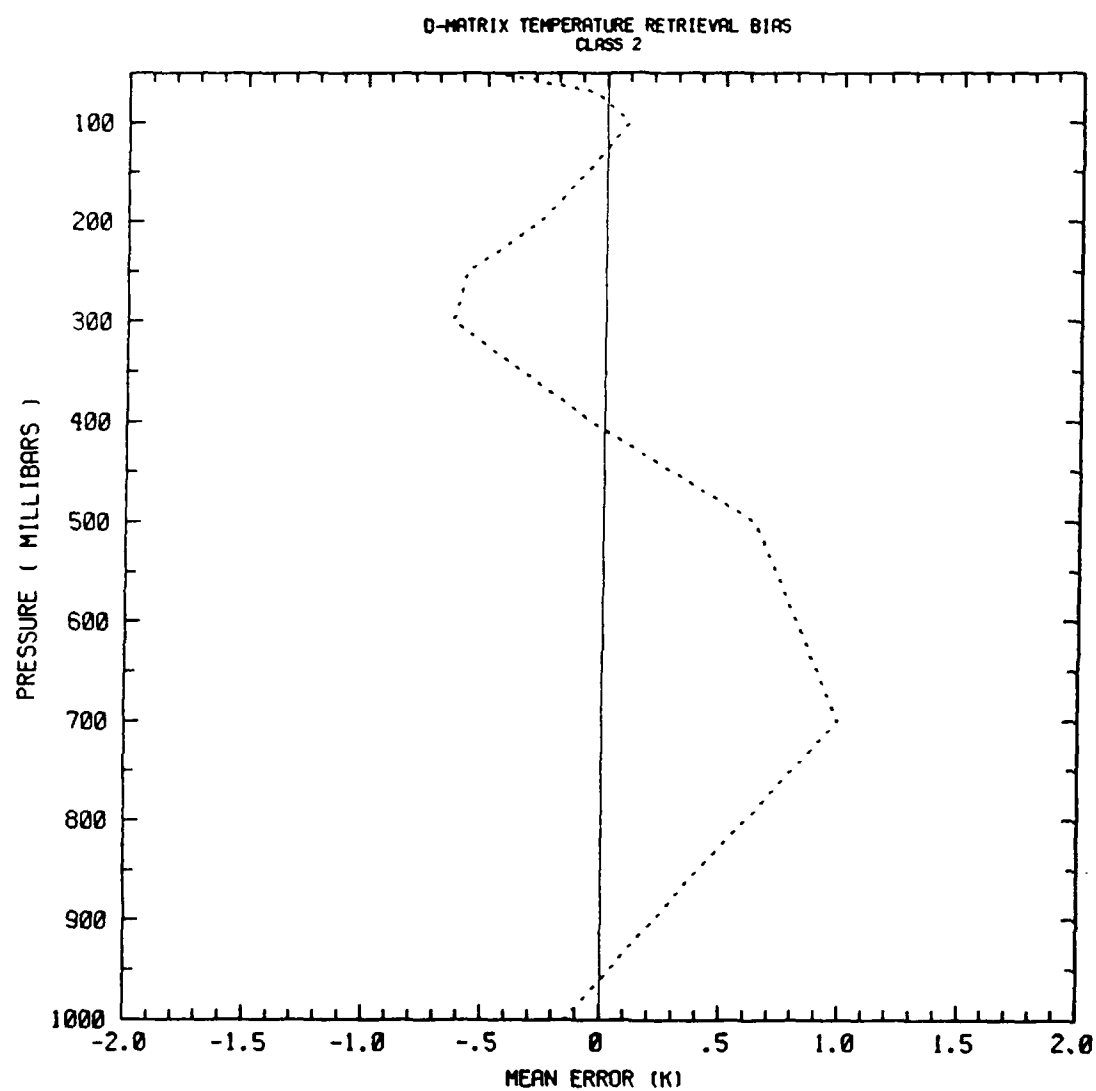


Figure 5.24 Temperature retrieval bias, Class 2.

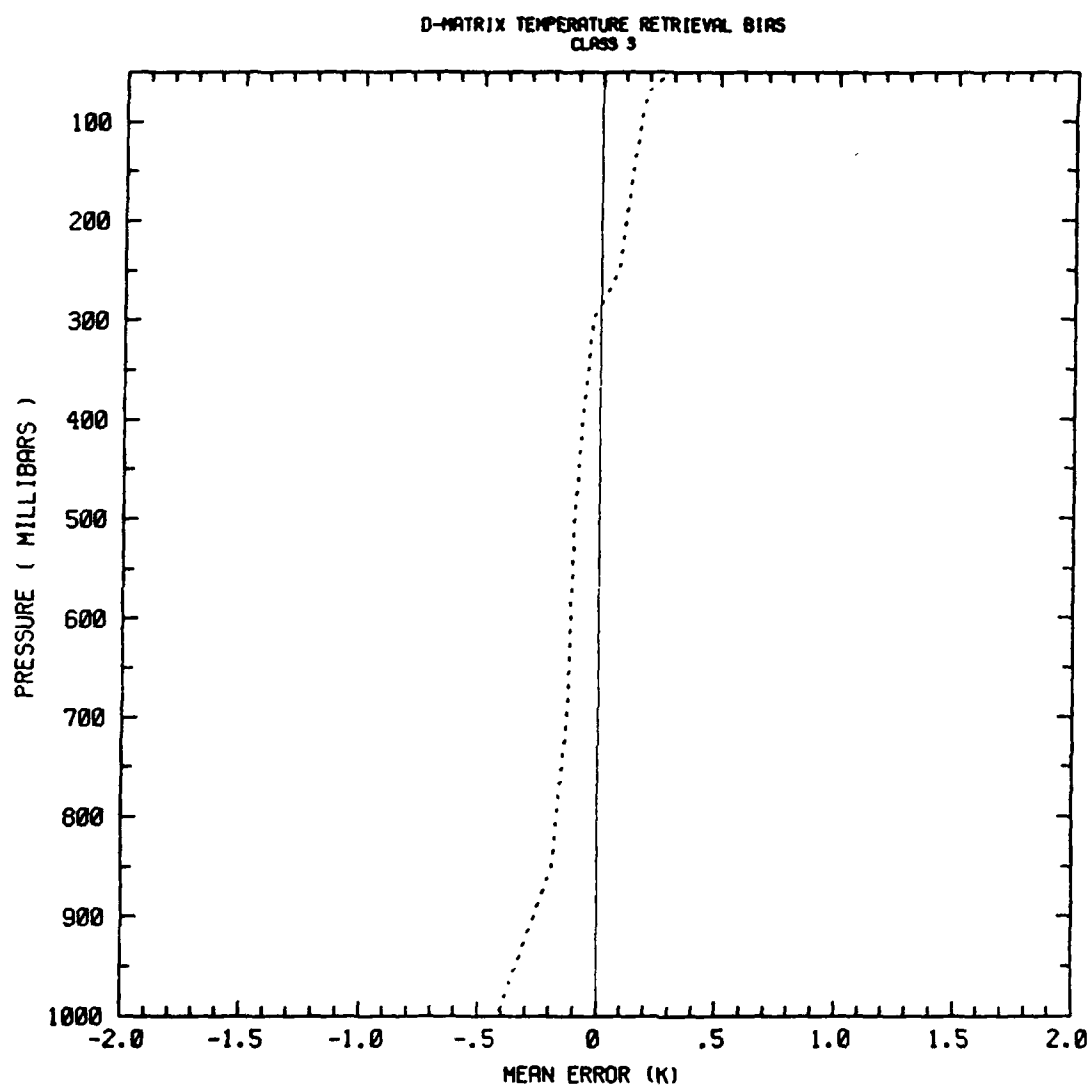


Figure 5.25 Temperature retrieval bias, Class 3.

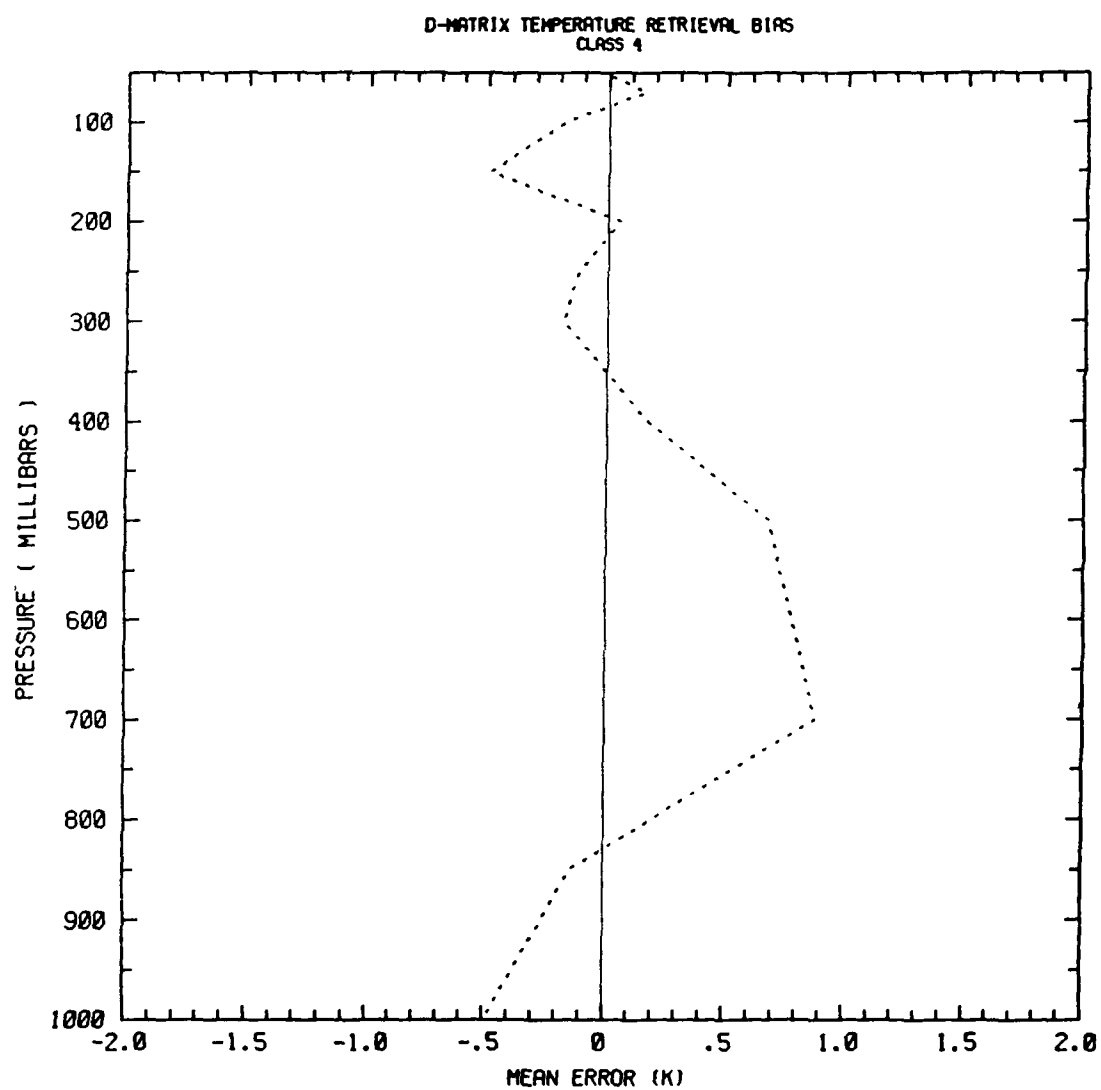


Figure 5.26 Temperature retrieval bias, Class 4.

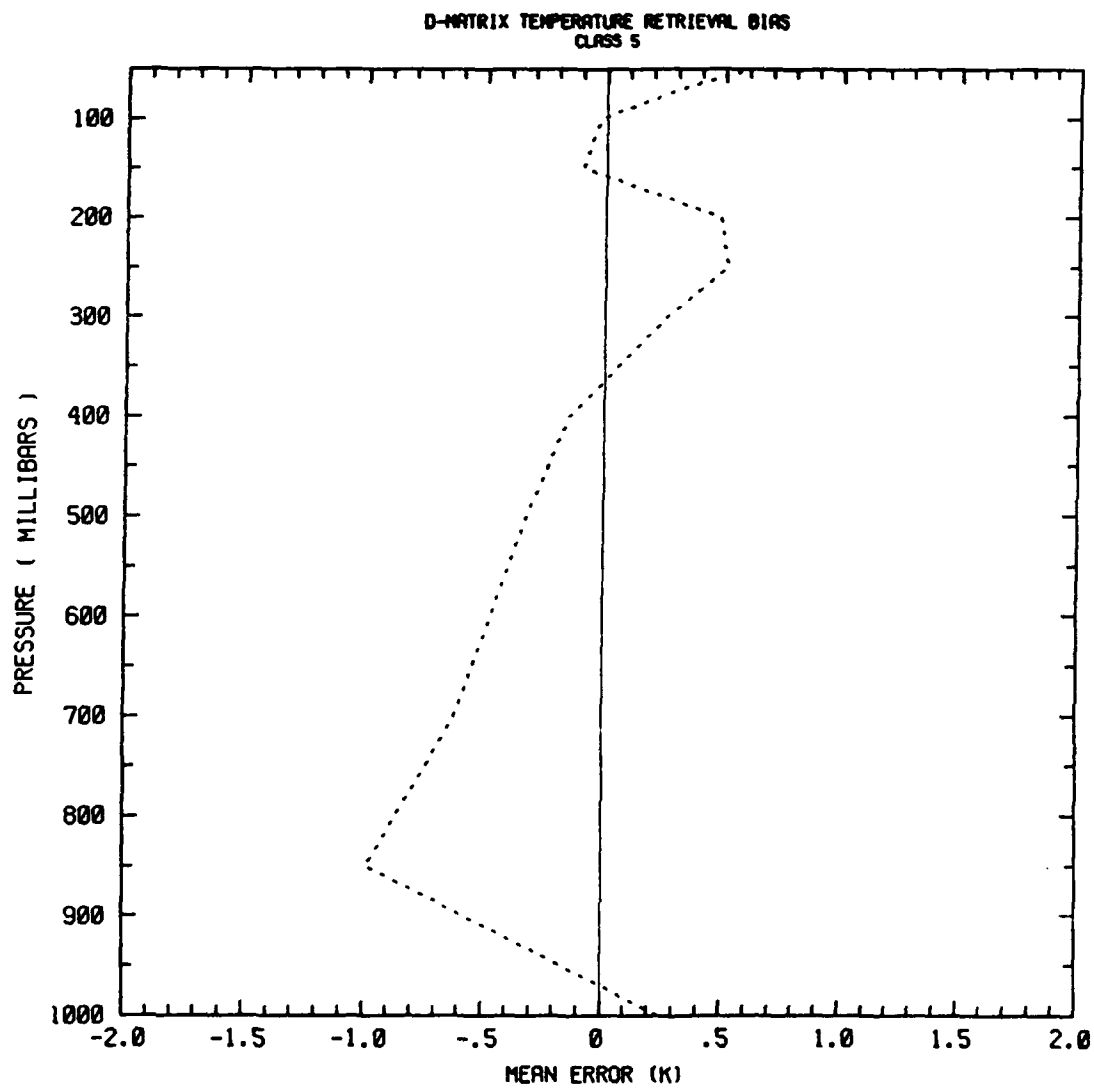


Figure 5.27 Temperature retrieval bias, Class 5.

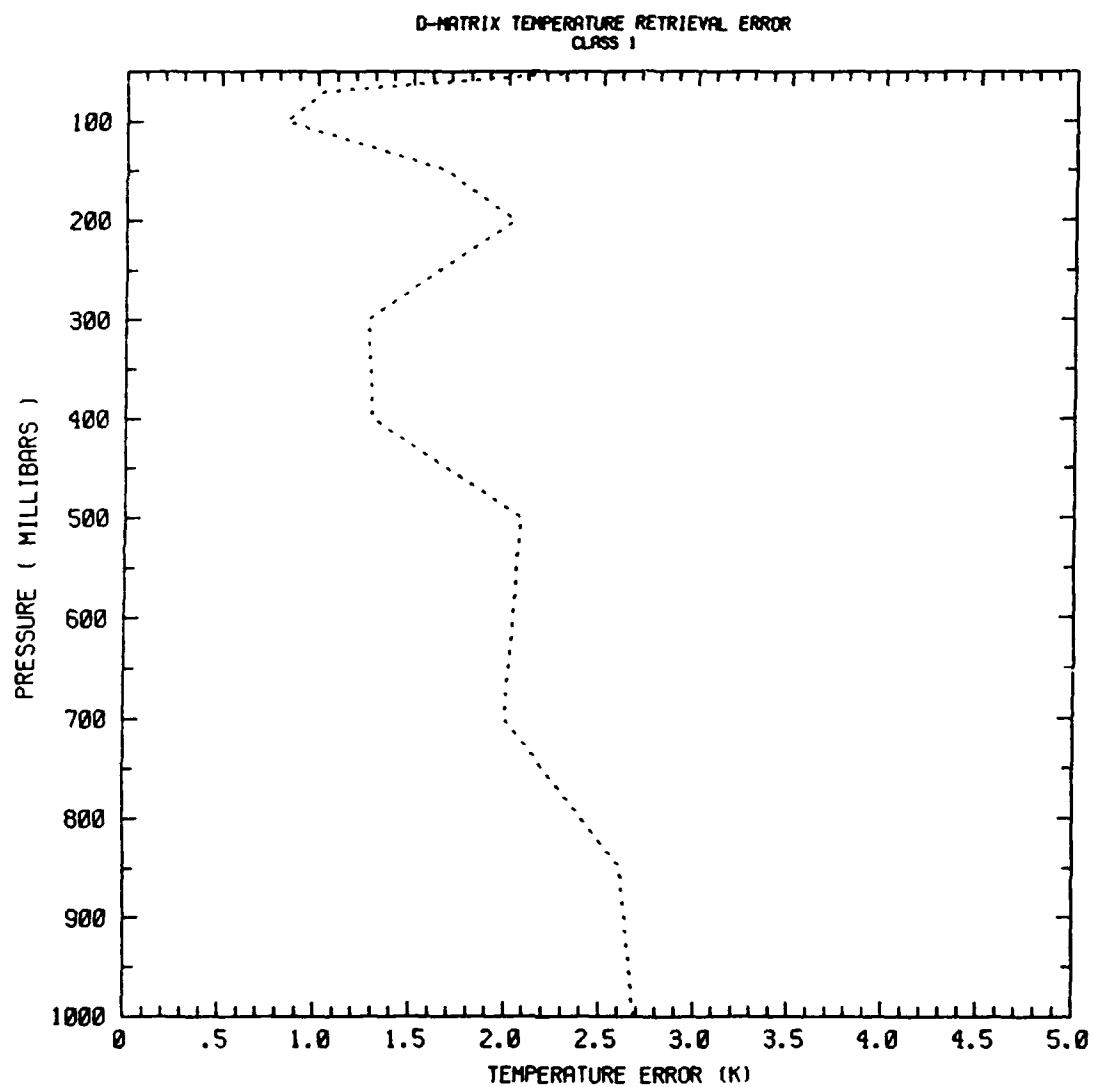


Figure 5.28 Temperature retrieval error, standard deviation, Class 1.

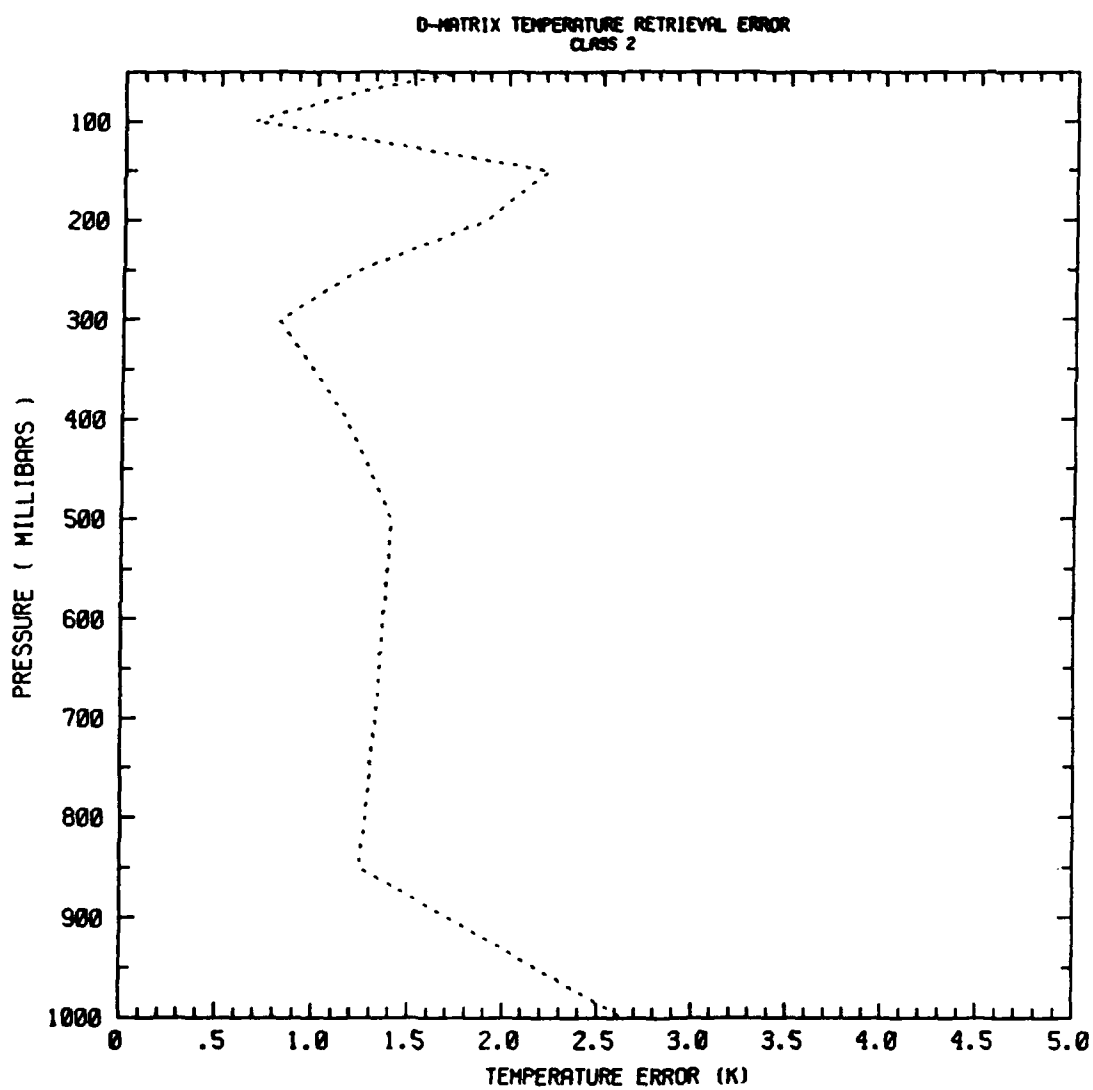


Figure 5.29 Temperature retrieval error, standard deviation, Class 2.

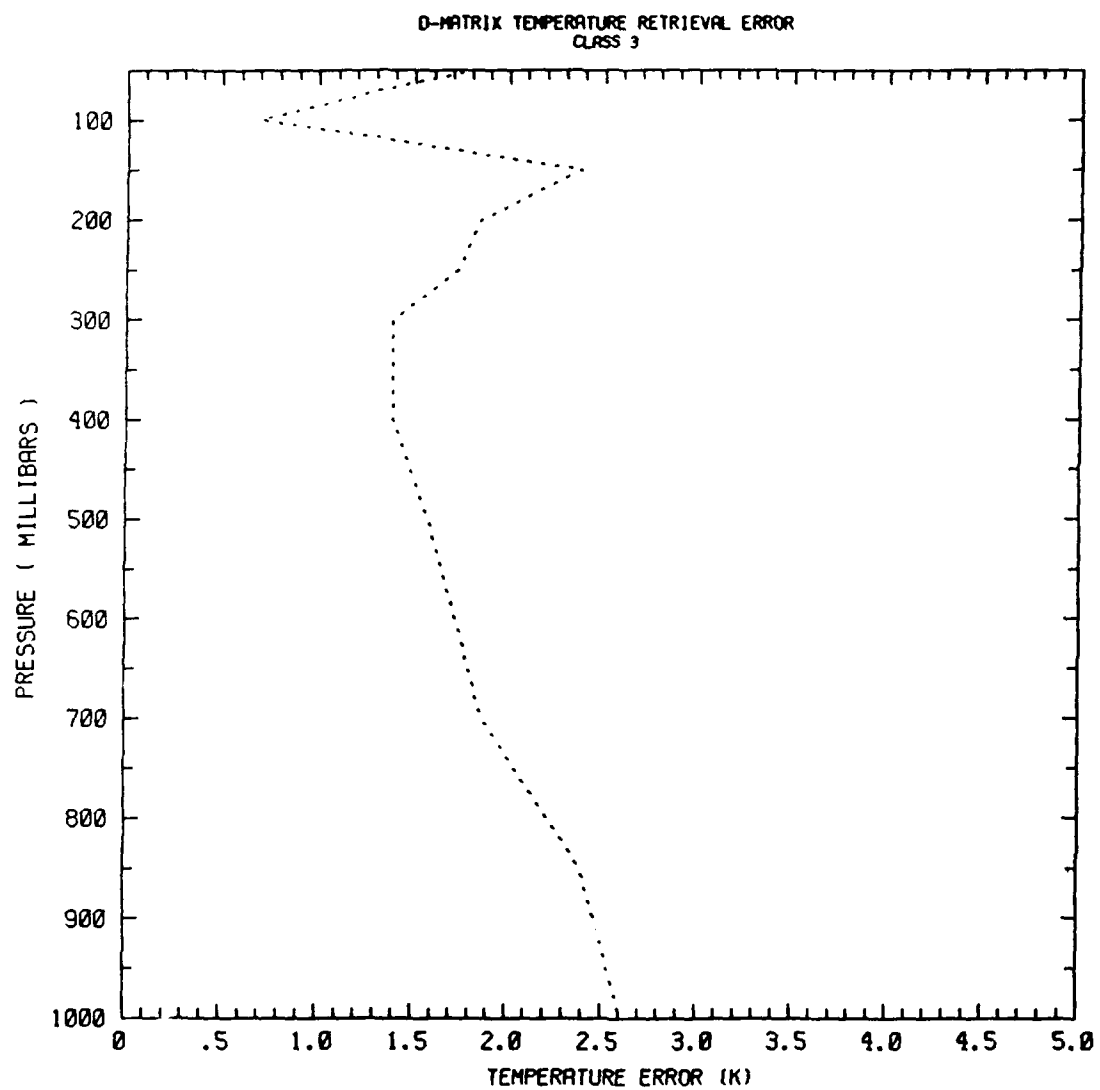


Figure 5.30 Temperature retrieval error, standard deviation, Class 3.

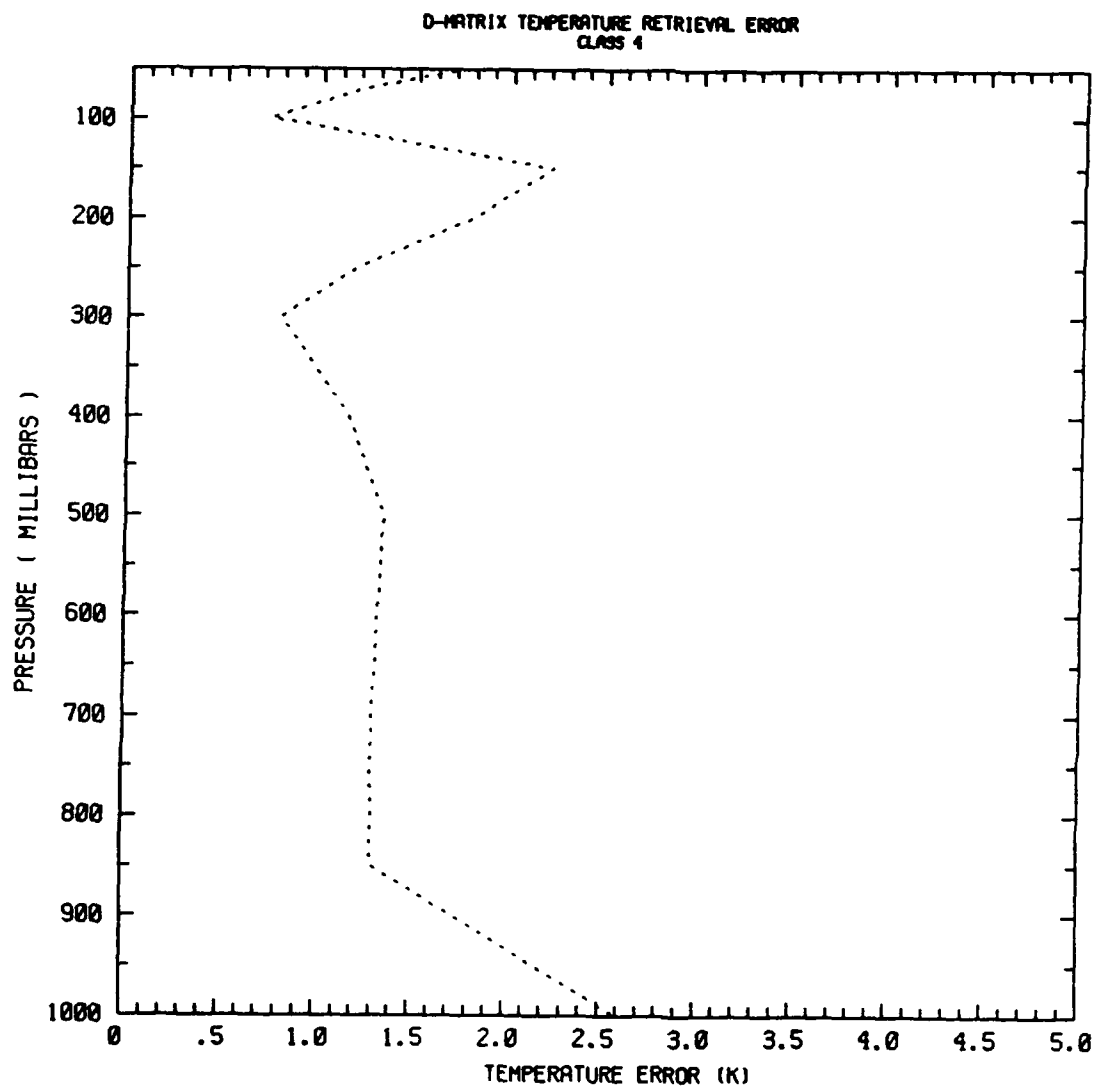


Figure 5.31 Temperature retrieval error, standard deviation, Class 4.

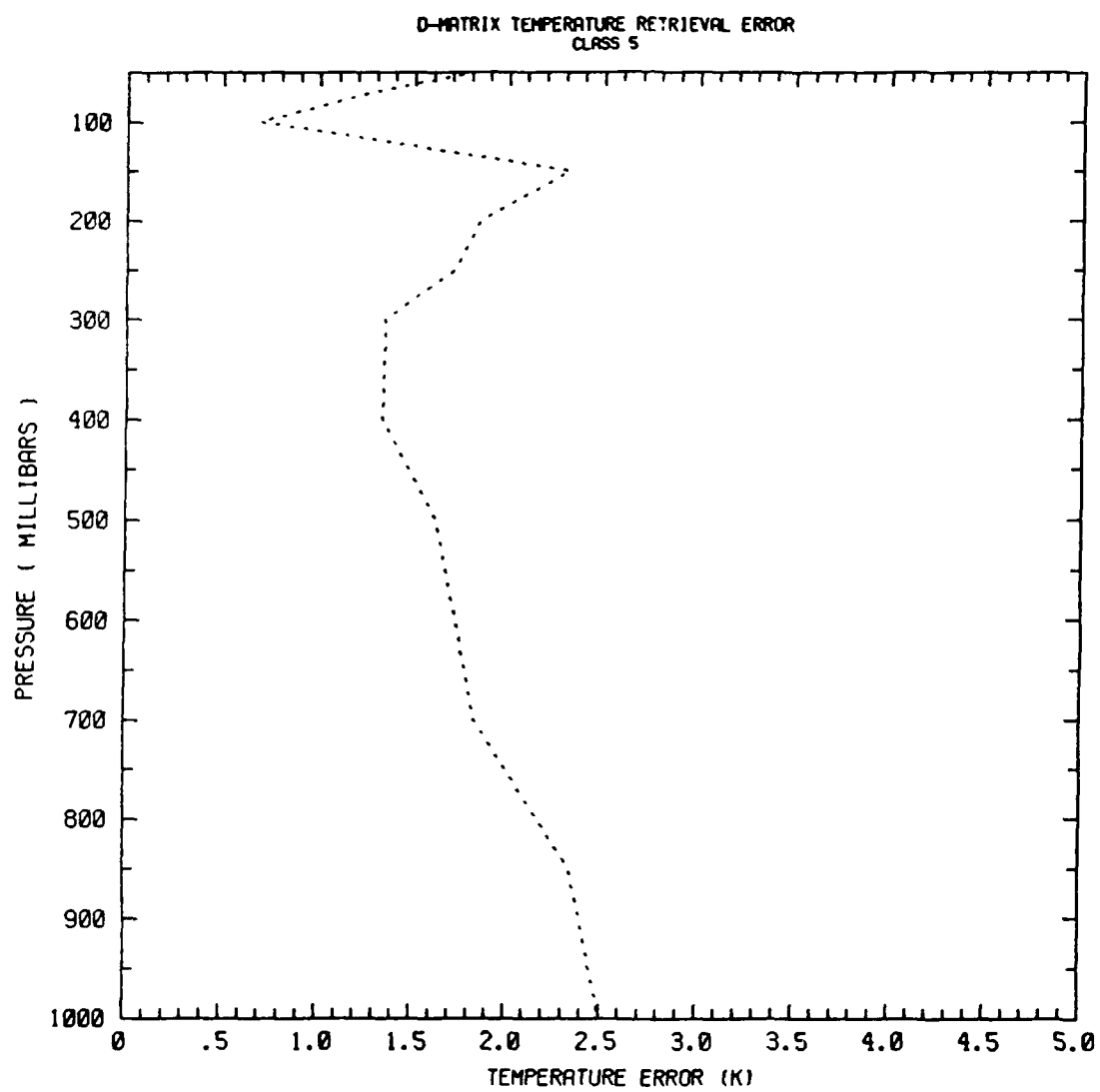


Figure 5.32 Temperature retrieval error, standard deviation, Class 5.

O-MATRIX TEMPERATURE RETRIEVAL VERTICAL ERROR CORRELATION
CLASS 1. CORRELATIONS WITH 1000 MB LEVEL

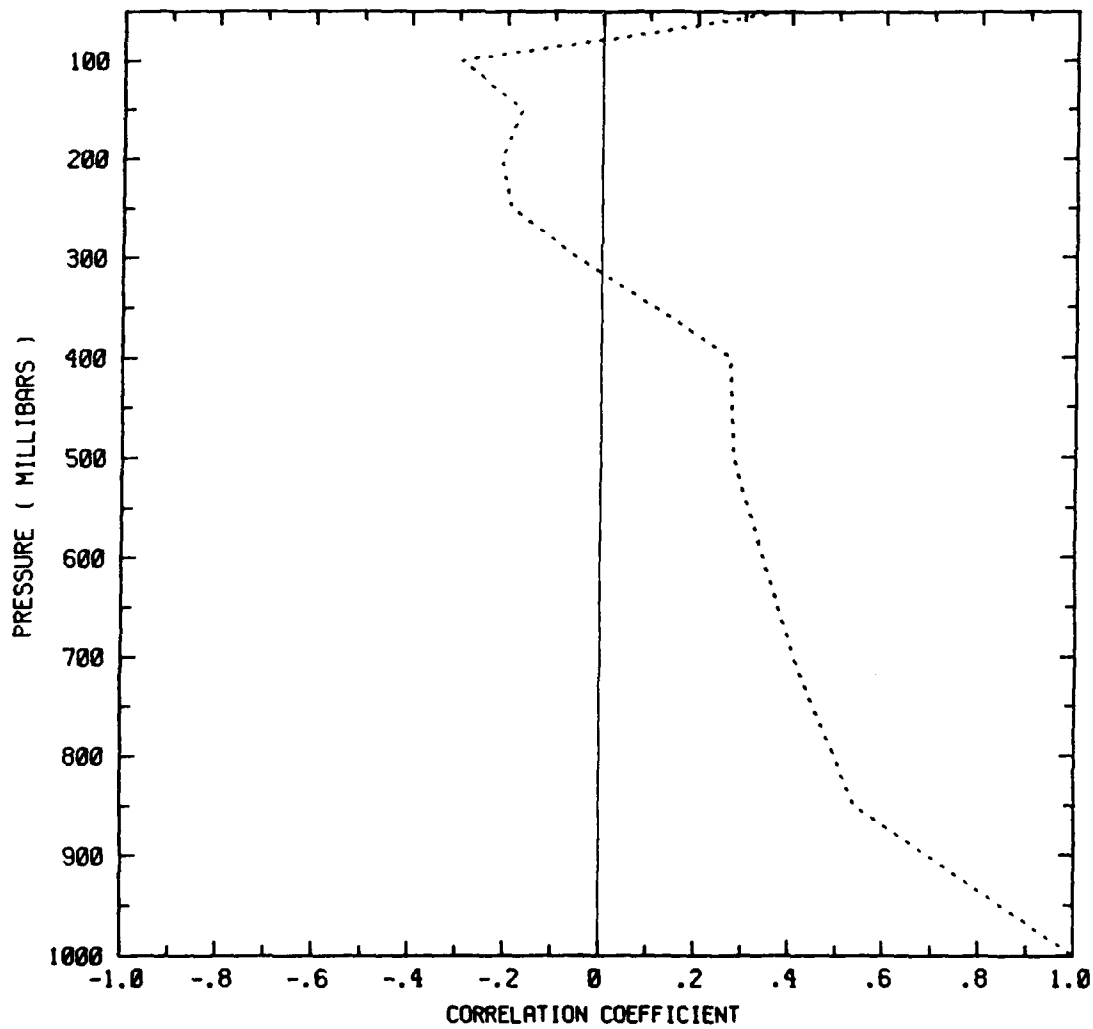


Figure 5.33 Temperature retrieval vertical correlations with 1000 mb error, Class 1.

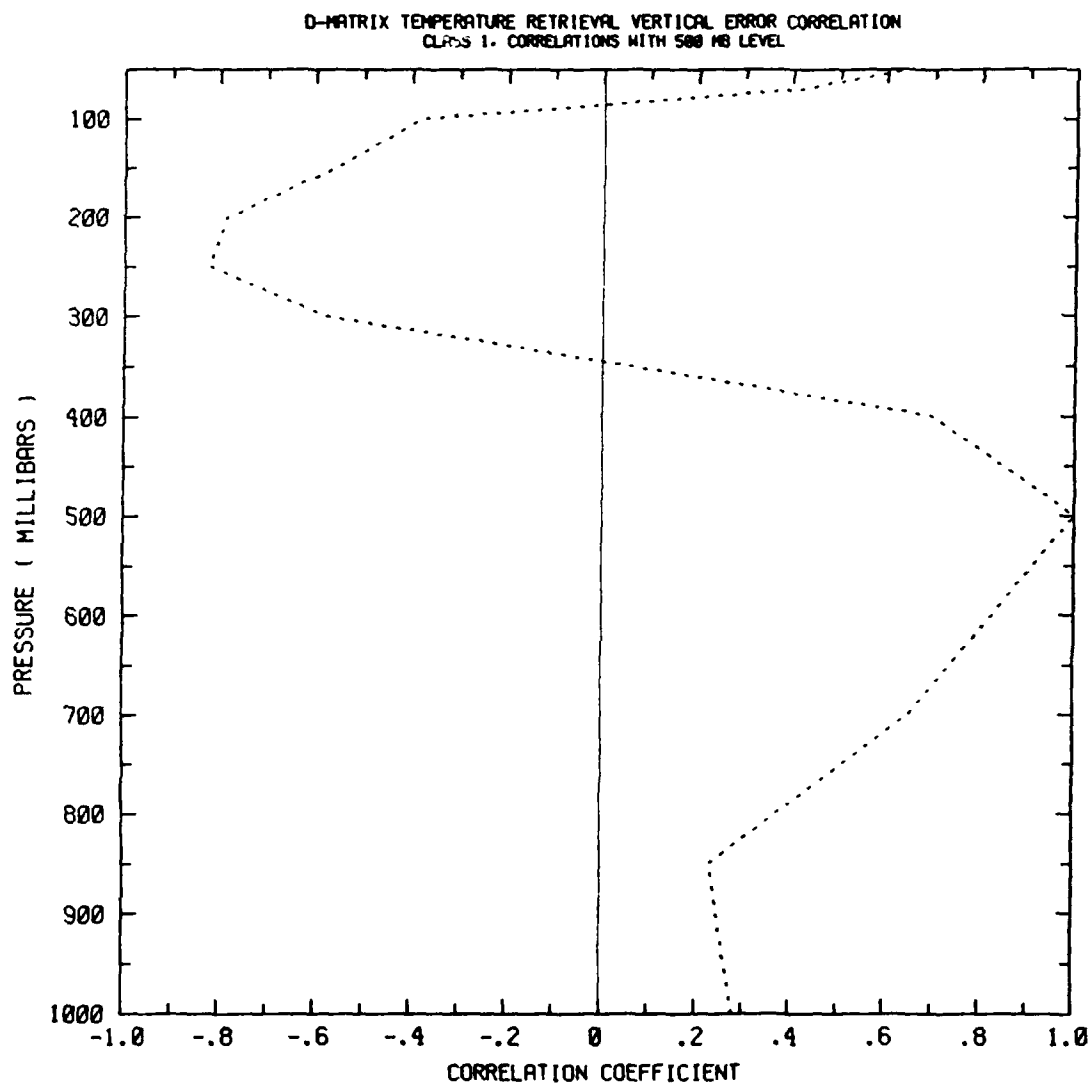


Figure 5.34 Temperature retrieval vertical correlations with 500 mb error, Class 1.

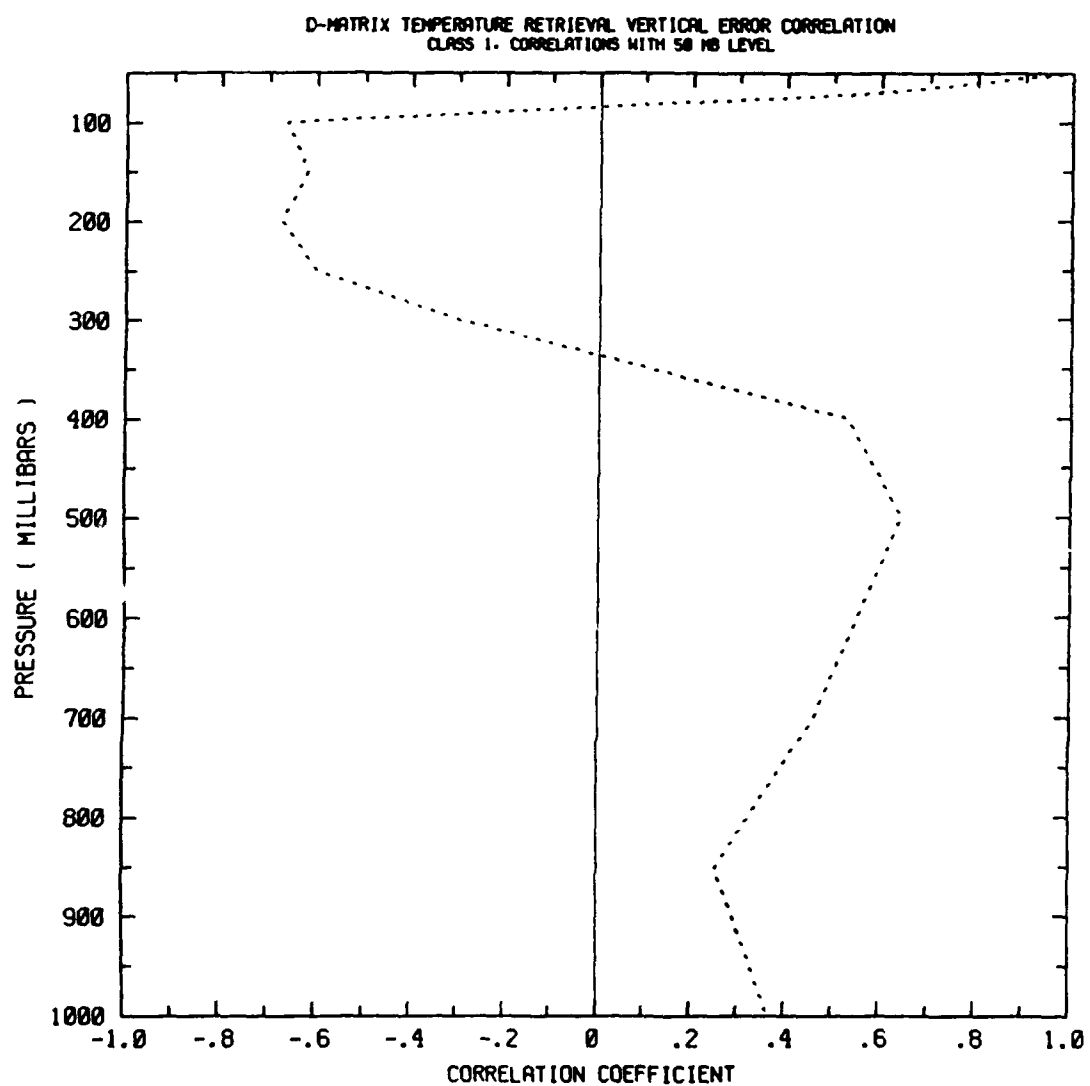


Figure 5.35 Temperature retrieval vertical correlations with 50 mb error, Class 1.

6. OSSE Design

We now describe the OSSE we have conducted which makes use of the simulated data described above. In our experiments the data assimilation system used is the AFGL system which was used by Norquist (1988) and Louis et al. (1988). This system is briefly described in Section 6.1, with special attention to changes made for the present experiments. Our verification strategy is summarized in Section 6.2.

To minimize transient behavior, i.e. spinup, we preceded our experiments with a spinup procedure which included a four day forecast and three day data assimilation as described in Section 6.3. The experiments themselves, STATSAT, NOSAT, SSM+TOVS and SSMSAT and the companion real data experiments are described in Section 6.4. The real data OSEs are described in greater detail by Louis et al. (1988).

6.1 AFGL forecast and analysis system

Each simulated data assimilation experiment described here consists of one assimilation run for seven days and three forecasts, each four days in length. The real data assimilation experiments each consist of two of these assimilation runs. Each assimilation run consists of a series of assimilation cycles, and each cycle in turn is made up of a 6-hour forecast that serves as a first guess for the analysis, an optimum interpolation analysis which combines the first guess fields with the observations, and a nonlinear normal mode initialization of the analysis. The initialized analysis is the starting point for the next 6-hour forecast, which is then used as the first guess of the subsequent assimilation cycle. The forecast model used for the 6-hour forecast is a complete global spectral model (GSM). This model is also used to produce forecasts out to 4 days starting from days 3, 5, and 7 of the assimilation runs.

6.1.1 Analysis

The AFGL Statistical Analysis Program (ASAP) (Norquist, 1986, 1988) was developed from the NMC multivariate optimal interpolation (OI) procedure as described by Bergman (1979) and by McPherson et al. (1979). The ASAP OI is a multivariate analysis of height and wind components and a univariate analysis of relative humidity, both in model sigma layers. The corrections for an

analysis grid point are weighted sums of surrounding observation-minus-first guess residuals. The equations for these weights as well as the computation of the horizontal and vertical correlation functions follow Bergman (1979). The analysis error evolves according to simple rules (Norquist, 1986). The great circle distance method for correlation functions equatorward of 70°C latitude is included as described by Dey and Morone (1985) without changing the Bergman formulation (including map factor) for latitudes poleward of 70° latitude. The analysis takes place in the sigma coordinates of the model on a Gaussian grid of 62 x 61 latitude-longitude points.

Data used by the height-wind analysis include Type 1 observations (radiosondes, pibals, etc.), Type 2 observations (aircraft), Type 4 observations (satellite retrieved temperatures or thicknesses) and Type 6 observations (cloud drift winds (CDWs)). The Type 3 surface observations are not used at all. This implies that satellite "heights" are anchored only by the 6 h forecast in regions where radiosondes are absent. In all experiments, except for the three-day preliminary assimilations, the CDW data were combined (i.e. locally averaged) into "super-obs". There are two principal reasons for doing this: First, to limit the total number of observations, so that computer memory restrictions are not exceeded, and second, the CDW errors are strongly correlated horizontally because the main error is due to height assignment. Satellite temperature profiles are not used over land in any of the experiments.

Since the statistical models used by the OI are never exact in practice, we decided for convenience and realism to leave most of the statistical models in the OI as they were for the real data OSEs described by Louis et al. (1988). The statistical models and parameters used are identical to those described by Norquist (1986), which in turn are based on NMC practice as described by Dey and Morone (1985). The OI assumes that radiosonde observational errors are correlated vertically and that satellite height observational errors are correlated vertically and horizontally. A number of studies colocating satellite and radiosonde height data were performed by Louis et al. (1988) and slightly different models and parameters for the satellite height observational errors were used in the OSEs reported here. These observational errors are described in detail in Section 2.3 of Louis et al. (1988).

In the SSM/T OSSEs we do not directly use the statistical properties described in Section 5 which were used to simulate the data. Instead we saved the actual errors used in simulating the data and used them to develop global models of the observing errors for use in the OI. Our first motivation for this is that the results of Section 5 do not allow us to estimate horizontal correlations. Secondly, the models of the observing errors used in our sensor simulation study are considerably more complex than those used by the ASAP OI and we did not wish to make major modifications to the analysis procedure. In studying the global simulated errors we grouped all errors generated for the 00 and 12 GMT intervals together. Basically we found that:

- 1) The vertical height error correlations were fairly well fit by a simple function.

$$\nu = 1/(1 + k(\Delta(\ln p))^2)$$

where we found k to be .3744 by a least squares fit. The observed correlations and the fitted function are shown in Fig. 6.1. The corresponding RH correlation were all small and deemed not significantly different from zero.

- 2) The horizontal height error correlation are close to zero. The RH horizontal error correlations are also very small except at 300 and 400 mb where they remain above .2 out to 3000 km (Fig. 6.2). In both cases we modeled the horizontal error correlations by

$$\mu = \exp(-(d/d_0)^2)$$

where we choose d_0 as 83 km for height and 198 km for RH.

- 3) No significant biases were found and the rms errors were of the expected size (see Table 6.1).

The statistical models used in the OI make use of these findings.

The ASAP OI was adjusted to assimilate the SSM/T data. The SSM retrievals of RH on mandatory pressure levels are used directly, while the

T retrievals are first converted to heights. In principle, this transformation is not necessary, the analysis scheme could make use of the fact that sigma level heights, the analyzed variables, are correlated with the observed mandatory level or layer temperatures. For SSM/T we retrieve temperature on mandatory levels directly, instead of layer temperatures. The level temperatures are interpolated linearly in $\ln p$ to the sigma levels and then integrated hydrostatically to obtain the sigma level heights. The predicted or first guess height at the first sigma level within the retrieved temperature profile is used to begin the integration. The integration also assumes temperature varies linearly in $\ln p$. The procedure used is identical to the procedure for anchoring satellite thicknesses described in Hoffman et al. (1988) from the point at which mandatory level temperatures are available. Note that the retrieved profile is not extrapolated vertically at all.

The data selection algorithm was altered to recognize the SSM/T data. The basic data selection algorithm follows Bergman (1979) as described by Norquist (1988). The first stage of data selection is done in terms of profiles: Data items in the up to 8 closest profiles are candidates to be chosen for use in the actual analysis in the second stage. Here closeness is measured by the magnitude of height height forecast error correlation times the number of non missing data items in the profile times a measure of data quality. (A Z observation is considered one data item and a (u,v) pair is considered one data item.) The data quality is taken to be unity for all data except it is 0.42 for TOVS and 0.92 for SSM/T height data. These data quality values are rough estimates of the ratio of RAOB to TOVS and RAOB to SSM/T height OESDs. Thus RAOB and other type 1 data are preferred over all others. A SSM/T profile will be preferred to a TOVS profile. The second stage of data selection, which was not altered, selects for each analysis point up to 10 data items from the selected profiles which individually would give the largest reduction in estimated analysis error. In this second stage the actual estimated OESDs are used.

6.1.2 Forecast and initialization

The AFGL normal mode initialization (NMI) is based on the NMC NMI (Ballish, 1980). The AFGL global spectral model is based on the NMC GSM designed by Sela (1980). For the version used here, the physics routines are

taken almost intact from NMC (circa 1983). The hydrodynamics, i.e., the adiabatic, inviscid dynamics including vertical and horizontal advection, time stepping, and transformations between spectral and physical space, were completely redesigned, as documented by Brenner et al. (1982, 1984).

There are a number of parameters in the forecast and initialization codes that can be adjusted. Briefly, the spectral resolution of the forecast model is defined by a rhomboidal truncation at wave number 30. The Gaussian grid of the forecast model contains 76 x 96 latitude longitude points. There are 12 layers, the first (top) 5 of which have no moisture. The sigma interfaces are at 0.00, 0.05, 0.10, 0.15, 0.20, 0.25, 0.30, 0.375, 0.50, 0.65, 0.80, 0.925, and 1.00. The time scheme used is centered semi-implicit with a time step of 17.25 minutes. Horizontal fourth order diffusion ($-\kappa \nabla^4$) is applied to all modes of divergence and to modes in the upper half of the rhomboid for vorticity, temperature and specific humidity. The diffusion coefficient used is $\kappa = 6.10^{15} \text{ m}^4 \text{ s}^{-1}$. In the NMI, two Machenauer iterations are applied to modes for the four largest equivalent depths which have periods less than or equal to 48 h.

6.2 Verification Procedures

Our verification procedures include subjective comparisons of analyses and forecasts, quantitative comparisons of rms errors of analyzed and forecast fields and a calibration of the quantitative measures making use of the OSE results. These procedures will be described in more detail in the next section. Here we describe the diagnostic fields which we compare.

One of the performance measures we use in measuring impact is the rms and bias error of a diagnosed total cloud fraction. Although the "real" simulated clouds generated during the nature forecasts were not saved, the large scale (i.e., nonconvective) cloud fraction is readily diagnosed from the RH field. This sort of measure puts a premium on proper forecasting at the higher range of RH, since errors at lower values have no effect on large scale cloud amounts.

To convert RH to level cloud coverage fraction, f_{κ} , we invert the Tibaldi scheme described by Norquist (1988, Appendix A). Level clouds are obtained at the first six mandatory layers, i.e. 1000, 850, 700, 500, 400, and 300 mb. There are combined pairwise assuming maximal overlap into low, middle and high

layer cloud fractions, f_L , f_M and f_H . The three layer cloud fractions are then combined into a total cloud fraction f_T assuming random overlap,

$$(1 - f_T) = (1 - f_L)(1 - f_M)(1 - f_H)$$

6.3 Spinup experiment

To begin our experiments we first performed two 96 h forecasts starting from "perfect" initial conditions on 00 GMT 11 and 21 November 1979. These initial conditions are taken directly from the nature run, interpolated to the model sigma structure, analyzed into spherical harmonic coefficients and initialized with the adiabatic NMI. We found the growth of forecast error (i.e., forecast - nature) to be rather slow in these forecasts. In fact the forecast ending on the 00 GMT 15 November was not much worse than a typical analysis. Accordingly, this state was used as the initial "analysis" for a three day SPINUP assimilation experiment, ending 00 GMT 18 November. SPINUP makes use of the standard STATSAT configuration.

6.4 Schedule of impact experiments

The end of the SPINUP assimilation is used as the starting analysis for all our OSSEs which therefore run from 00 GMT 18 November through 00 GMT 25 November. (The first analysis of each OSSE is at 06 GMT 18 November.) For each OSSE 96 h forecasts are made from 00 GMT 21, 23 and 25 November.

The OSSEs described here are STATSAT, NCSAT, STATSAT + SSM/T and NOSAT + SSM/T. STATSAT includes all the Level II data which were simulated by NMC as described in Section 3.2 except that surface observations are not used and satellite temperature soundings over land are not used. In NOSAT the satellite temperature soundings and CDW observations are excluded. In the other experiments the SSM/T-1 and T-2 data are added.

The OSEs STATSAT and NOSAT are analogous to the OSSEs, at least as far as data usage is concerned. The OSEs however were run for one week each during February and June 1979. These experiments are described in detail by Louis et al. (1988) and are used here primarily to calibrate the OSSE results. One notable difference between the OSSE and OSE experiments is that the OESD for satellite heights for STATSAT and NOSAT in the February OSE were substantially larger than in the other experiments. (These values are given by Louis et al., 1988.)

Table 6.1 SSM/T OESDs used in data assimilation experiments

p(mb)	1000	850	700	500	400	300	250	200	150	100	70	50
Z(m)	7.98	7.98	14.01	21.71	25.08	26.57	27.01	28.38	32.15	38.37	39.40	41.85
RH(%)	7.91	18.35	14.45	15.12	15.17	19.35	-	-	-	-	-	-

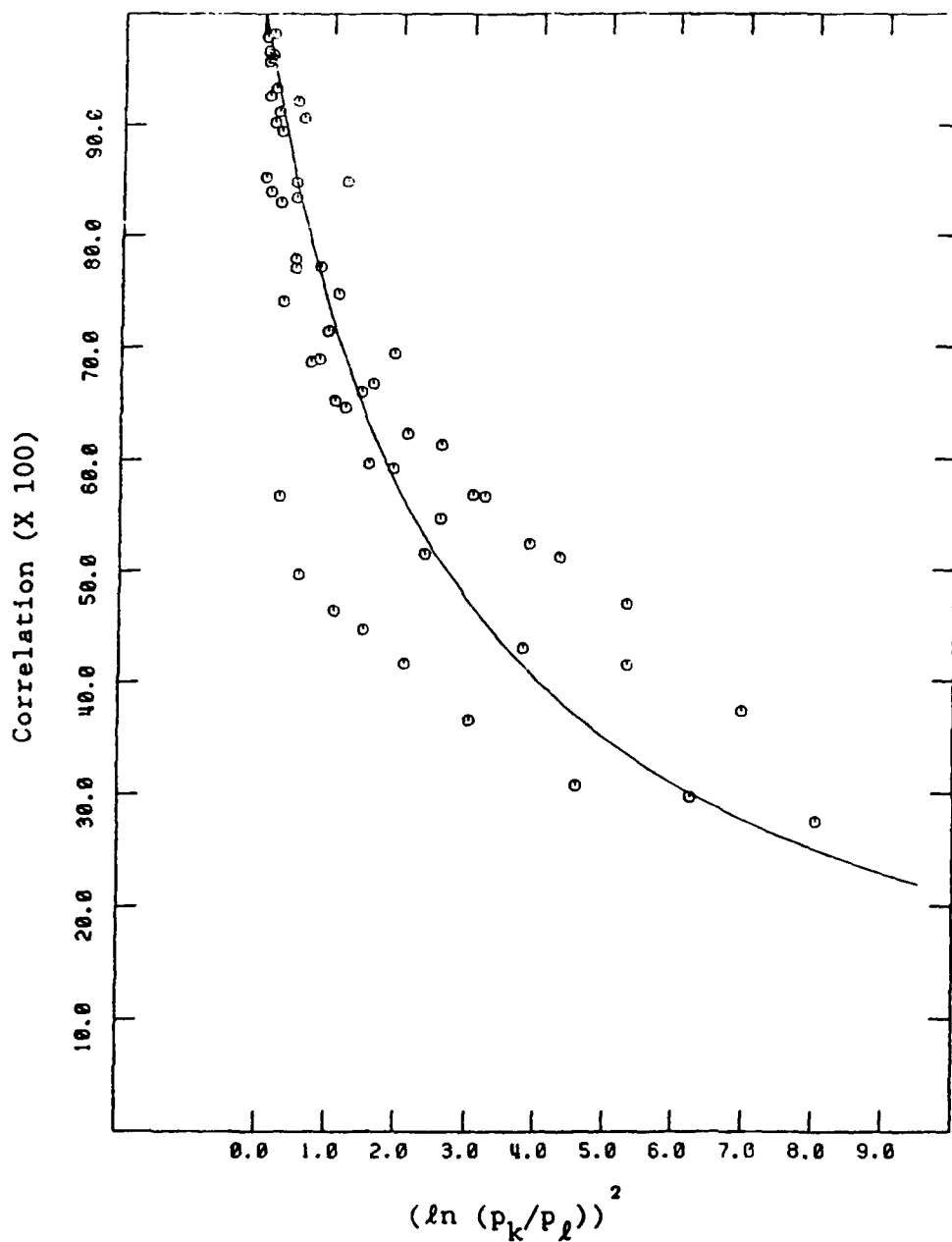


Figure 6.1 Vertical height error correlations of simulated SSM retrievals based on collocation with radiosondes. Solid curve is least squares fit to data used in OI.

+ obs @ 300

○= obs @ 500

△= fitted correlation function

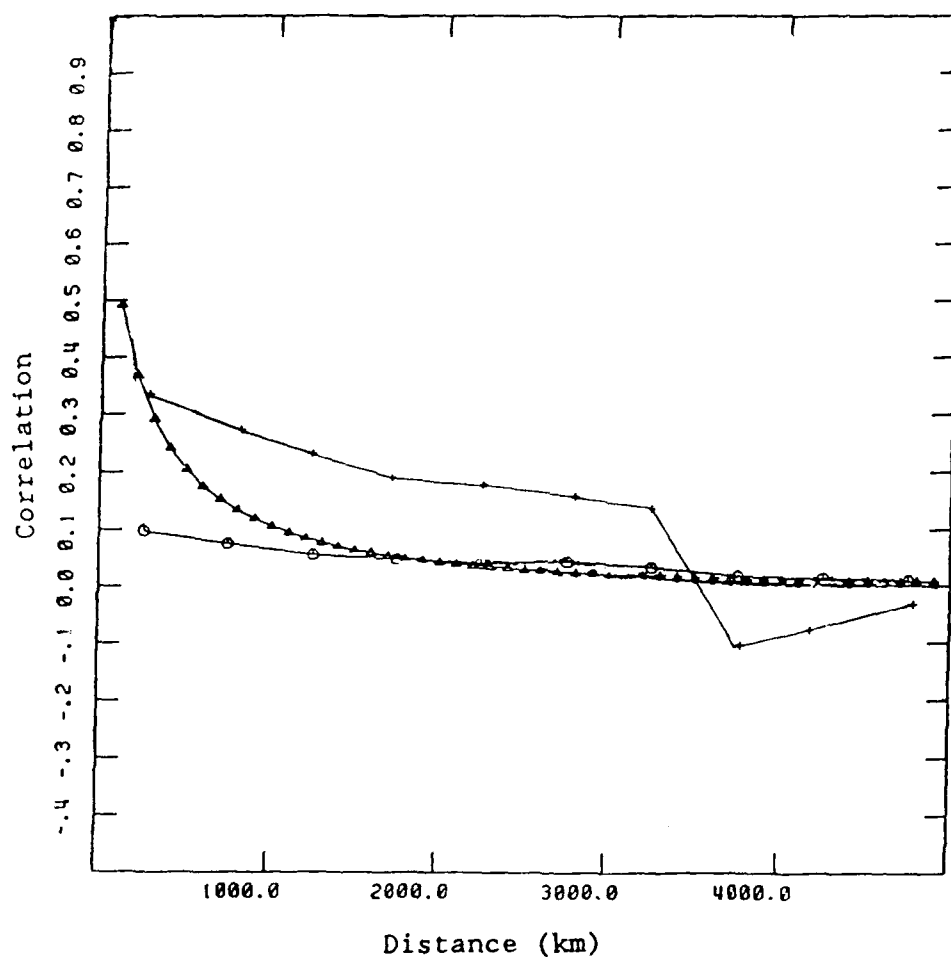


Figure 6.2 Horizontal height error correlations of simulated SSM retrievals based on collocation with radiosondes. Shown are observed errors at 300 mb, 500 mb and function used in OI.

7. OSSE Results

7.1 Subjective synoptic evaluation

The spinup forecast, starting from perfect initial conditions at 00 GMT 11 November, and the spinup assimilation, which was performed from the end of the spinup forecast at 00 GMT 15 November to 00 GMT 18 November were compared with the corresponding nature data. The spinup forecast had very similar 500 mb height patterns, but our forecast is consistently warmer than the ECMWF forecast. The possible reason for this warm bias is the lack of a radiation parameterization in our model: a typical radiative cooling of the atmosphere of 1 K/day would correspond to a 500 mb height difference of roughly 20 m/day, which is consistent with the approximate height difference of 80 m at the end of the 4-day forecast. The analyses during the spinup assimilation, which correspond to a STATSAT configuration, are also quite similar to the nature data, except that they are considerably noisier, possibly due to the warm bias of the first guess, which is only corrected at data locations.

Results for the Northern Hemisphere from the OSSE assimilation period (00 GMT 18 November to 00 GMT 25 November) are shown in Fig. 7.1 - 7.4 for 00 GMT 23 November. The 500 mb height pattern of the nature data (Fig. 7.1a) shows a distinct wavenumber four pattern, which is present throughout the entire November time period. Several smaller scale, mobile troughs are superimposed on the long-wave structure. The analyses from all three OSSEs shown in Fig. 7.2 - 7.4 are visibly noisier than nature, both at 1000 and 500 mb. The error patterns of all three OSSEs look similar: the long-wave low over Eastern Canada is too low in the OSSEs, and there is large area of negative height errors at 70°-80°N, centered at 90°E. These two features are present throughout the entire assimilation period. The error over Canada is worst in STATSAT, whereas the other feature is worse in the SSM OSSEs. There are two regions where the SSM+TOVS analysis is noticeably worse than either SSMSAT or STATSAT: one is the long-wave trough at 150°W, which is much too deep in SSM+TOVS, less so in SSMSAT, and approximately correct in STATSAT, the other a small short wave over Newfoundland, which is not captured well in any of the OSSEs, with the largest errors in SSM+TOVS, smaller errors in STATSAT, and the smallest errors in SSMSAT. At day 7 of the assimilation (00 GMT 25 November, Fig. 7.5 - 7.8) the 500 mb height errors over the Pacific have

grown, and they now appear in all three OSSEs. Over the Eastern Atlantic is an area of large height errors in SSM+TOVS (Fig. 7.8), which is virtually absent in either SSMSAT (Fig. 7.7) or STATSAT (Fig. 7.6). The fact that adding TOVS data to the SSMSAT data lead to such a drastic degradation of the analysis in those regions is troubling, since the OI is designed to optimally combine all available data, given the correct statistics of the true fields and errors.

Some possible reasons for this analysis degradation are related to the fact that the satellite thicknesses are anchored to the first guess surface pressure. Satellite data are thus not able to correct barotropic first guess height errors, i.e. errors present at both the 1000 and 500 mb levels. The error statistics used in the OI, however, do not take this anchoring error into account, thus resulting in inappropriately large weights being given to satellite "height" observations, at the expense of other, non-satellite data. Even in the absence of nonsatellite data, the addition of satellite data may worsen the 500 mb height analysis, if the first guess errors in surface pressure and 500-1000 mb thickness are compensating each other. All these potential problems would be exacerbated by adding TOVS to the SSM data. Another possibility is that in the presence of significant biases in the satellite data, which we have ignored in our OSSEs, mixing TOVS and SSM data in overlapping data swaths may introduce noise in the analysis. Finally, because of central memory limitations, some aircraft and cloud track winds used in the SSMSAT analyses could not be used in SSM+TOVS. Any of these reasons may result in initially small analysis differences, which could be amplified during the 6-hour forecast between analysis time periods, and through differences in data selection due to quality control procedures that depend on the first guess. In an effort to identify these scenarios, analyses and first guess fields for the OSSEs were studied along with the corresponding nature data and the simulated observation residuals.

The analysis error over the Atlantic and the short wave associated with it, which at 00 GMT 25 November is located over Ireland in the nature data, but is displaced about 10° West in the SSM+TOVS analysis, can be traced back to Newfoundland at 00 GMT 23 November, at which point the analysis errors for the SSM+TOVS analyses are already substantially larger than for the SSMSAT analyses. The two analyses diverge over that area in the preceding 24

hours: the 500 mb height errors at 00 GMT 22 November (Fig. 7.9) are much more similar in SSMSAT and SSM+TOVS over Newfoundland. In the time period between 00 GMT 22 November to 00 GMT 23 November, SSM and TOVS data are both present over the area only at 06 GMT and 18 GMT, i.e. at times when there are no RAOBs over the area; the impact of the TOVS data at those times should be small, given the higher data density and smaller OESDs of the SSM data. At the other times, only TOVS satellite data are present over the oceans, but there were no obvious instances where the additional thickness information might have lead to larger 500 mb height errors. It is thus not entirely clear what caused the two analyses to diverge over that area.

Whatever the reasons for initial, small analysis differences are, the persistence and amplification of these errors requires some additional explanation. As is shown in Fig. 7.8b,d and 7.10a,b, the analysis errors and the first guess errors at 00 GMT 23 November have a large barotropic component, and, as a consequence, the analysis is ineffective over the ocean areas, where there are no radiosonde observations of geopotential. In agreement with this scenario, the satellite observation residuals are small compared to the actual analysis errors. Where radiosondes are present, the analysis errors are smaller than the first guess errors right over those locations, except one radiosonde at 12 GMT 22 November (at Sept Isles, Quebec, at 50.22°N, 66.25°W) and another at 00 GMT 23 November (St. Johns, Newfoundland, at 47.62°N, 52.75°W), which were rejected by the gross error check in SSM+TOVS, but not in SSMSAT. At those locations, the first guess field in SSM+TOVS had diverged too far from the truth for the RAOBs to be used. The rapid error growth during this short period is taking place in a strongly baroclinic zone, in which a strong sensitivity to initial conditions of even a 6-hr forecast can be expected. After 00 GMT 23 November, the short wave is entirely over the ocean, thus making it impossible for the analysis to correct the by now well established height errors.

The other area of large analysis errors apparent in Fig. 7.8b is over the Pacific, near the international dateline. This error, which is associated with a longwave trough in the nature data, can also be traced back several days (it is already visible at 00 GMT 21 November), but it is an essentially stationary feature. The longwave trough is consistently analyzed too deeply

(in both SSMSAT and SSM+TOVS analyses), and at several times (including 00 GMT 25 November) a smaller scale ridge downstream of the trough is too strong. The trough is always analyzed more deeply in SSM+TOVS than SSMSAT. As was the case over the Atlantic, the analysis errors have a strong barotropic component. Since the longwave trough is entirely over the ocean, only satellite height data are available, and again the height residuals were found to be much smaller than the actual first guess height errors because of the anchoring of the satellite thicknesses. A comparison of the first guess and analysis errors at 00 GMT 23 November show the negligible impact of the analysis, allowing the persistence of the first guess errors. The reason for the initial divergence of the SSMSAT and SSM+TOVS analyses is again not entirely clear.

An example of the Southern Hemisphere height fields is given in Fig. 7.11 - 7.14 for 00 GMT 25 November. Again, the OSSE analyses are all much noisier than nature. In addition, the 500 mb heights are consistently too high over Antarctica. The nature data show a number of small scale, mobile troughs at 500 and 1000 mb, a situation typical for the entire assimilation period. Analysis errors are due to both amplitude and phase errors of these features, and are present at both 500 and 1000 mb. Overall, both the SSM+TOVS and SSMSAT analyses seem the best, and the STATSAT analyses worst over the Southern Hemisphere.

As discussed in previous sections the OSSE included simulated retrievals of relative humidity from SSM/T-2 brightness temperatures. Therefore, it is also of interest to assess the impact of such data upon the analyses and forecasts of moisture during the assimilation period. Comparisons between the analyses of different experiments is not very informative since instantaneous fields of relative humidity are rather noisy. Instead, we display only difference plots, averaged fields, and differences of averaged fields for illustrative purposes.

In Figs. 7.15 and 7.16 we show difference plots of the analyzed moisture field at 850 mb with the nature run field for 2 different times during the assimilation period (23 November and 25 November, both at 00 GMT). In each figure fields for the STATSAT, SSMSAT, and SSM+TOVS experiments are shown.

In this set of figures differences in relative humidity are plotted with a contour interval of 25% with negative differences shown as dashed lines and

positive differences shown as solid. The times shown represent analysis differences at days 5 and 7 of the assimilation period. It is quite clear that the moisture analyses created with the SSM retrievals are much improved over the STATSAT analyses. In addition, the results for SSMSAT and SSM+TOVS are very similar with only minor differences seen between the two experiments. It seems that the presence or absence of TOVS retrievals has only a small impact upon the humidity analysis and that nearly all the improvement stems from inclusion of the additional SSM data. Improvement is most dramatic over southern hemisphere ocean areas where conventional moisture data is practically nonexistent. Smaller, but equally clear improvements are seen in the northern hemisphere as well. For example, note the improved analysis over the central North Atlantic Ocean on 25 November. Also noteworthy is the fact that the analyses are improved over land areas even though SSM retrievals were confined to the oceans. This is quite evident over equatorial Africa on 25 November, and over South America on 23 November. Thus the use of the additional data source over one region has the potential to improve subsequent analyses in more distant areas downstream from the data location.

Another useful means of viewing the moisture fields associated with the OSSEs is by converting relative humidity fields to cloud cover fields. The resulting cloud cover fields offer some insight into the accuracy of the analysis/forecast relative humidity fields and the algorithm which is used for the humidity to cloud conversion.

We have used moisture fields from both the STATSAT and SSMSAT experiments to infer large scale cloudiness. For this work the inverse Tibaldi scheme was applied (see Section 6.2). We found the complete relative humidity fields (i.e. with all spectral coefficients retained) to be highly noisy making interpretation difficult. Instead, we filtered the fields by using a T15 spectral truncation which allows us to focus only on the large scale features.

Cloud cover results for STATSAT and SSMSAT at 00 GMT 25 November are shown in Figures 7.17 and 7.18, respectively. We show only the inferred low cloud cover with a contour interval of 25 percent. For a surface pressure of 1000 mb this would include clouds in the layer from 950 mb to 733 mb. In Fig. 7.17 is the cloud cover inferred from the nature run. Remaining panels show the inferred cloudiness of the analyses valid at the same time and the corresponding analysis - nature difference fields.

Main features in the nature run cloudiness include the low amounts of cloudiness over the northern hemisphere subtropics associated with the descending branch of the Hadley circulation. Note in particular regions with less than 25% cloud cover over the southwest U.S., northern Africa, and southern Asia. High cloud amounts are seen in the equatorial regions of Africa as well as South America which, it might be noted, are close to the general location of the ITCZ as it advances southward during November.

As seen in the relative humidity fields, the SSMSAT results are more realistic (relative to the nature run) than those of STATSAT. In SSMSAT the analysis of cloudiness over central Africa and South America is in reasonable agreement with the nature run while the STATSAT field completely misses the high cloud amounts in these same areas.

The difference plots also show the SSMSAT analysis to be better than STATSAT. Again note South America and equatorial Africa where the cloud amount errors in STATSAT exceed -75% over large areas. It is also interesting to note that nearly all errors in STATSAT and SSMSAT over the continents are negative. This is most likely a reflection of the fact that the physics package in the GSM contains no evaporation over land surfaces; consequently the lowest levels in the model tend to be too dry.

Finally, although we found that the inferred cloud coverage agrees with the large scale relative humidity fields in a qualitative sense, we also found that cloud amounts were generally much too high. Global statistics for the nature run, assimilations, and forecasts showed an average total cloud cover of roughly 80 percent while climatological values are known to be closer to 50 percent. To the extent that the resulting cloud fields mirror relative humidity patterns this implies that humidity in both the GSM and nature run is too high. However it is also possible that the humidity to cloud conversion method is biased. Any quantitative use of the cloudiness inferred by this means, for example simulation of satellite imager data, will require some tuning of the scheme to reduce the observed bias.

7.2 Objective statistical evaluation

As an objective measure of the quality of the analyses and forecasts, root mean square (rms) and mean (bias) statistics of the differences from nature were calculated. Fig. 7.19 shows the global 500 mb rms height error of the NOSAT, STATSAT, SSM, and SSM+TOVS analyses and forecasts. The NOSAT analysis errors increase from the 35 m typical for the STATSAT analysis to 50 m by day 4 of the assimilation, whereas the STATSAT analysis errors decrease by only 1-2 m over the assimilation period. The forecast error growth is more rapid in STATSAT, but errors remain smaller than those of the NOSAT forecast for the entire 4-day forecasts. The SSM analysis errors are consistently smaller than those of STATSAT, by up to 2 to 3 m. The day 3 forecast errors are smaller than those of STATSAT, but the day 7 forecast is worse. The SSM+TOVS analysis have larger errors than those of SSM, and the forecasts are either the same (day 7) or worse (day 3). Compared to STATSAT, SSM+TOVS analyses and the day 3 forecast is only slightly worse (by less than 1 m), whereas the day 7 forecast is noticeably worse. The objective results thus confirm our impression from the subjective evaluation that the SSMSAT analyses (and forecasts) are closest to nature. The reasons for the degradation of the analyses in SSM+TOVS discussed in the previous section in a regional context thus apply globally, as well.

Results at other levels largely mirror those at 500 mb. The 1000 mb height statistics (not shown) show a much smaller impact of the satellite data (NOSAT analysis errors differ by no more than 3 m from STATSAT), but qualitatively the same results apply. In particular, the SSMSAT analyses are closer to nature than either STATSAT or SSM+TOVS, the day 3 forecast is most skillful in SSMSAT, whereas the day 7 forecast is roughly the same.

The global error statistics of humidity analyses and forecasts for STATSAT, SSMSAT, and SSM+TOVS are shown in Fig. 7.20. The rms error curves for all three experiments were obtained by differencing the 850 mb analyses and forecasts with the corresponding nature run forecasts. In each plot the solid curves denote the assimilation errors and the broken curves the errors of the forecasts which were run off the day 3, 5, and 7 analyses.

The error statistics for the STATSAT and NOSAT experiments may be considered baselines against which to judge the other OSSEs. In STATSAT simulated TOVS temperature retrievals were included with the rest of the

conventional radiosonde network data used in the NOSAT experiment. Since the STATSAT experiment used the same moisture data we would expect the relative humidity error statistics to be quite similar. In fact, comparisons of STATSAT with NOSAT (not shown) show the analysis errors to be virtually identical, with differences in the rms errors of less than 1%. The actual values of the rms errors throughout the 7 day assimilation period are approximately 27%. Errors in the forecasts approach 30% by 4 days.

In the SSMSAT experiment the simulated SSM temperature and moisture retrievals were inserted at the same time that the TOVS data was excluded. The results shown clearly indicate an improvement in the accuracy of the moisture analyses and forecasts when such data is used. Analysis errors are roughly 5% smaller throughout the 7 day period with rms errors values of about 22%. Forecast errors are also initially less than those of STATSAT by 5% but increase more quickly so that after 4 days they differ by only 2%.

In SSM+TOVS both types of satellite data were included. As expected based on the subjective evaluations the impact of adding the TOVS data to the SSM retrievals is at best minimal. Both analyses and forecasts for the SSM+TOVS experiment have slightly larger rms errors, but in all instances the differences are less than or equal to 2%. Note the tendency for the forecast error curves to flatten out late in the forecast period at about 30%. This most likely represents the upper limit on possible analysis/forecast errors based on the natural variability of the relative humidity fields.

In sum, both the subjective and objective evaluations of the moisture data indicate a distinct positive impact upon relative humidity analyses when simulated SSM-derived moisture retrievals are added to conventional observations during the global assimilation cycle. Only minor impact (relative to SSMSAT) is seen when the SSM data is combined with TOVS temperature retrievals.

7.3 Evaluation of zonal cross sections

We examined zonal cross sections of u and v wind components, temperature and relative humidity at individual synoptic times and averaged over the last five 0000 GMT analyses of the experiments. Zonal averaging is denoted here by square brackets ([]) and time averaging by an overbar ($\bar{}$). Our purpose here is to determine how well the assimilation system is capturing the mean meri-

dional circulation, pole to equator temperature and humidity structure and zonal jets and to describe the impact of the different observing systems on these features. These features are important climate diagnostics. Errors in zonally averaged quantities are also important to NWP because errors in the climate make a persistent contribution to errors in the analyses and these errors may be useful in diagnosing faults in the physical parameterizations used in the model. In the following, the impact of the SSM OSSEs will be compared with that of the WINDSAT OSSE. The WINDSAT OSSE is identical to STATSAT, except that simulated wind observations from a proposed satellite-based lidar wind profiler were made available to the assimilation. The WINDSAT OSSE is described in more detail in a separate technical report (Hoffman et al., 1989). We concentrate here on the time averaged fields for the nature run and STATSAT and on the impact of SSM on the wind, temperature and humidity fields. These fields and differences from the nature run are displayed in Figs. 7.21 through 7.24. For comparison the some results for the WINDSAT experiment are also displayed.

Considering first the zonal time averaged zonal wind component (Fig. 7.21), we see in all cases the midlatitude jets peak near 200 mb. The N.H. jet is somewhat narrower and stronger. The jet maximum is near 30 m/s in all cases. Easterly winds extend through the depth of the atmosphere in the tropics. The trade winds (surface easterlies) are a bit stronger in the N.H. The nature $[\bar{u}]$ is quite similar to observed fields. Compared to the GFDL monthly mean $[\bar{u}]$ for November 1979 (Lau, 1984), the jets in the nature run are positioned somewhat poleward and have slightly different magnitudes. STATSAT, SSMSAT and WINDSAT $[\bar{u}]$ agree well with the nature run. In all three cases the errors are order 1 m/s with WINDSAT having somewhat smaller errors.

In Fig. 7.22, which depicts $[\bar{v}]$ both Hadley and Ferrel cells are readily apparent. On the other hand the surface southerlies in the S.H. Ferrel cell are stronger than in the N.H. The maximum convergence at the surface where the two returning branches of the Hadley cell meet is at 10°N. The corresponding upper level divergence is at 250 mb. The N.H. Hadley cell appears to be somewhat stronger than the S.H. Hadley cell. Compared to the GFDL monthly means, the surface winds agree fairly well, but the poleward branches of the Hadley cell are twice as strong in the GFDL analyses. Comparing STATSAT, SSMSAT and WINDSAT to the nature run, we see that all three analyses

are qualitatively in agreement with the nature run. Magnitudes of the $[\bar{v}]$ are all similar. However STATSAT has more small scale features in the tropopause region and SSMSAT misses the strong northerly surface flow over the Southern Ocean at 70°S. At the surface WINDSAT and STATSAT appear to be roughly equivalent.

Considering the amount of high quality wind data available to WINDSAT, the small improvements to the zonally averaged wind fields are disappointing. The lack of improvement in the tropical mean meridional circulation may be caused by deficiencies in the assimilation system. First, the analysis wind increments must be non-divergent: although the height and wind analysis decouple in the tropics, the wind analysis still uses structure functions derived from the height structure function and the assumption of geostrophy. Secondly, in the NLNMI, there is no account of the effects of cumulus convection.

The $[\bar{T}]$ has a broad maximum between 20°S and 20°N at all levels through the tropopause. Poleward of 20°, temperature decreases. The magnitude of the poleward temperature gradient decreases with elevation up to the 200 mb level where the gradient reverses. Tropopause height varies from 200 mb in the polar regions to 50 mb at the equator. The the nature run $[\bar{T}]$ agrees well with the GFDL values except that the GFDL tropical tropopause is roughly at the 100 mb level. Compared to the nature run, we see that STATSAT is too cold (by 2 K) in the tropical PBL (below about 900 mb) and too warm at the equator at 850 mb (by 1.4 K). This implies the equatorial region is too stable. In the S.H. between 60°S and 80°S STATSAT is too cold below 850 mb (up to -5 K) and there are large positive errors over Antarctica. Note that the surface is about 700 mb south of 80°S. In the Arctic below 850 mb STATSAT is also too warm. There are large errors above the tropopause; the poles are warm and the equatorial region is cold. WINDSAT has errors similar to STATSAT, however the upper level errors are substantially reduced in magnitude, the equatorial PBL is even colder (by 3 K) and the errors over Antarctica are reduced. For SSM the analyses are too cold below 850 mb at all latitudes. In the tropics the errors are larger (-5 K) and therefore the atmosphere is even more stable. The SSM analyses are very cold at 80°N (250 K). Like WINDSAT the errors above the tropopause are smaller than in STATSAT.

The $[\overline{RH}]$ in the nature run (Fig 7.24) is very moist at the surface where it has a maximum of 85% at 10°N and a minimum of 75% at 30°N. $[\overline{RH}]$ tends to decrease from the surface to 500 mb and then increase again up to 300 mb. In addition, moisture is carried upwards by the ascending Hadley circulation near the equator and dry air is brought downward by the descending branches of the Hadley cell near 30°N and S. As a result, a primary feature is the two subtropical minima which occur in the middle troposphere. The northern hemisphere minimum (about 34%) occurs at 500 mb while the southern minimum (31.2%) lies near 650 to 700 mb. This pattern is repeated, but with smaller amplitude by the Ferrel cells.

$[\overline{RH}]$ errors are relatively large in all assimilations. We may contrast nature with the cross sections for STATSAT and SSMSAT. In STATSAT the low level averaged relative humidity analysis below 850 mb is consistently too dry by 10 to 15%. At higher levels equatorial relative humidity is too high by 5 to 15%. And at higher latitudes, the upper level analysis is again too dry, exceeding 15% poleward of 70°. A major result of these analysis differences is that the northern and southern hemisphere mid-level minima are greatly increased in magnitude to 39.5 and 38.2%, respectively. Additionally, the asymmetry seen in nature with respect to height is gone and both features now occur at 650 mb. In SSMSAT the averaged low level analysis is still too dry, but the difference is smaller, often less than 5%. At higher levels the averaged analysis is also improved with differences less than or equal to 5%. One exception is the SSMSAT analysis at 850 mb near 30°S where the difference with nature is 13.8% compared with 9.5% in STATSAT. As in STATSAT, the averaged SSMSAT analysis does not retain the asymmetry in the moisture field which is seen in averaged nature data, although the magnitudes of the minima are better analyzed. In short, as determined from differences in averaged analyses, SSMSAT relative humidity analyses are closer to nature at most latitudes and at all vertical levels. However, in general, the polar regions and boundary layer are too dry and the mid latitude and tropical atmosphere above the PBL is too moist. Since moist air is more buoyant and low level moisture represents an energy source for moist convection, these errors tend to stabilize the analyses. Both the temperature and humidity errors in the tropics suggest that too much stabilizing convection may be taking place in the AFGL model. The temperature errors might also be due to the lack of a radiation parameterization.

Relative humidity is dependent not only upon the actual water vapor amount but also on the ambient air temperature which determines the saturation value. If we make the assumption that the analysis of water vapor in its conserved form (e.g. mixing ratio, specific humidity) is constant from nature to the analysis, then analysis - nature differences in the averaged relative humidity would tend to be inversely correlated with analysis - nature differences in the averaged temperatures.

For STATSAT, with the exception of a broad area of negative temperature differences over the equator at 500 mb, we do not find a strong relationship between the two variables. In fact, in some areas the temperature and humidity differences seem to be positively correlated. In the SSMSAT results the relationship is perhaps stronger with a larger area of negative temperature differences which arcs from the surface in the southern midlatitudes to the equatorial midtroposphere coinciding with positive relative humidity differences of order 5 to 10%. Nevertheless, the temperature differences tend to be less than 1.5 K in most areas of large relative humidity analysis error. We cannot then conclude, at least from the zonal-time averaged statistics, that most of the errors in the analyzed humidity are due to discrepancies in the temperature analyses.

7.4 Calibration with OSSE results

A luxury of OSSEs is the ability to exactly compute error measures. We took advantage of this in our discussion of the analyses. Analysis errors in the real world are not well known. In fact, recently Daley and Mayer (1986) presented analysis error of the OSSE experiments of Atlas et al. (1985) (which were discussed in the introduction) as surrogates for real analysis errors. We now turn to an examination of the forecast errors. In order to have a closer correspondence with the real world and to simplify our calibration procedure we have calculated rms difference between the forecasts and the simulated radiosondes. We then describe a procedure to calibrate these differences using the NOSAT - STATSAT impact observed in our previous OSEs as a yardstick, and present some results of the calibration procedure. Some discussion of the results of the companion OSSE experiments. WINDSAT is included here for comparison.

7.4.1 Rms difference between OSSE forecasts and radiosondes

Rms differences between OSSE forecasts and the simulated radiosondes used in the data assimilation experiments were calculated for different regions and for several variables at each layer in the atmosphere. The variables examined include geopotential height, temperature, vector wind, relative humidity, and cloud cover. Mean differences were also calculated and examined but were small relative to the rms difference for nearly all variables. Some regularities observed in the mean differences are described in Section 7.4.4. One aspect of the procedure we used is that the forecast heights are anchored by the verifying radiosonde report. Consequently, height errors described here are actually thickness errors. As described below we curve fit the data to determine impacts in terms of predictability time, i.e. the length of the useful forecast.

Due to the variable density of radiosonde coverage, global averages are very similar to N.H. extratropical averages and S.H. extratropical averages are based on fairly small samples. Of course, these statistics are biased towards land areas. Consequently, differences between NOSAT and STATSAT are less pronounced than they might otherwise be. As a result of these factors as well as the radiosonde errors themselves, we expect only qualitative agreement between impacts described here and impacts measured in Section 4.2 by comparing forecasts grid point by grid point to the nature run.

Examples of the growth of forecast errors as evidenced by the rms difference are displayed in Figs. 7.25 through 7.27. In each figure there are three panels, showing results averaged over 3 forecasts for the N.H. extratropics, tropics and S.H. extratropics. Here the tropics are taken to run from 30°S to 30°N. Rms difference curves for smaller regions which were studied, generally behaved as described here for the larger parent regions.

In the S.H., the rms difference curves sometimes exhibit a sawtooth pattern due to sampling problems; there are usually about 60 RAOBs at 00 GMT and only about 40 at 12 GMT in the S.H. Most of the non-reporting RAOBs are in the Australian sector.

Considering, first the rms difference for 500 mb geopotential (Fig. 7.25) we see that impacts in the N.H. are relatively small. WINDSAT lags STATSAT by approximately 7 h. Midway between these two lie SSMSAT and NOSAT. SSM+TOVS

is equivalent to STATSAT. In the tropics, the differences are all near 20 m and the growth rate is very small. Apparently, the tropical analysis errors are so large that the error growth is near saturation. At least during the initial part of the forecast WINDSAT has a slight edge, which because of the slow growth of differences corresponds to 3 or 10 hours of predictability time. Impacts in the S.H. are very large. WINDSAT is 36 h better than STATSAT, which is in turn more than 36 h better than the NOSAT forecasts. The three sounder based systems are roughly equivalent with SSMSAT and SSM+TOVS better than STATSAT by 12 and 8 hours respectively.

Next, we consider the rms vector wind differences at 200 mb (Fig. 7.26). Clearly, WINDSAT always yields a big improvement. Compared to STATSAT, WINDSAT provides 1, 2 and 2.75 day improvements in forecast skill in the N.H., tropics and S.H. respectively. NOSAT is particularly poor over the S.H. and the tropics. It is quite good over Europe, where it outperforms both SSM+TOVS and STATSAT. Of the three sounder systems, SSMSAT is generally better, improving predictability by at least a day in the S.H. and tropics.

The rms difference for relative humidity at 850 mb are shown in Fig. 7.27. Impacts in terms of forecast time are all relatively small in the N.H., generally in the range 3 to 12 h. In the extratropics, WINDSAT is the best. This might have been anticipated since the WINDSAT analyses of mass and wind are superior in the extratropics and since relative humidity is so strongly influenced by the large scale synoptic systems which are better forecast by WINDSAT. In the tropics, the SSMSAT moisture forecasts are the best. Overall the ranking is WINDSAT, SSMSAT, NOSAT, SSM+TOVS and STATSAT. It appears that using TOVS degrades the moisture analysis. Since TOVS relative humidity retrievals were not used, this poses a conundrum. TOVS data affect the model specific humidity indirectly because the analyzed variables are temperature and relative humidity. That is, in an area with only TOVS data the updated temperature field is combined with the unaltered relative humidity field to update the model specific humidity.

We also calculated rms difference in cloud cover layer by layer. Cloud cover was diagnosed from relative humidity using the inverse Tibaldi scheme (as described in Section 6.2). Invariably, the corresponding relative humidity and cloud cover plots look very similar. Fig. 7.28 shows the global rms difference for 850 mb relative humidity and cloud cover. Except for the

fact that the cloud cover errors are larger in magnitude, the curves in the two panels of Fig. 7.28 are nearly the same. For this reason we have not included any other cloud cover rms difference statistics in this report.

We examined the growth of rms difference for levels others than those described here. The results shown here are generally representative. In the next section tables summarizing all the levels are given. One notable exception to the general trend discussed so far, is the positive impact of SSM+TOVS on the upper level heights. For example, Fig. 7.29 shows the N.H. 50 mb height rms difference evolution. Here the ordering is SSM+TOVS, STATSAT, WINDSAT and NOSAT with an increment of about 6 hours between each pair; SSMSAT and STATSAT are roughly equivalent.

7.4.2 Calibration procedure

It has been observed that OSSE forecasts are too good because any two models, such as the model used in the experiments and the model used to generate nature, are more alike than any model and the real atmosphere. Consequently, it is unwise to naively carry over the forecast impacts observed in OSSEs to the real world. For example, at short forecast times, OSSE forecasts tend to be so good that there is little room for improvement; adding a new observing system might then have a smaller impact than in the real world. On the other hand, at longer forecast times, real data forecasts will be so bad that a new observing system will have no impact while the corresponding OSSE impact may be significant.

For these reasons it is desirable to calibrate the OSSE results. However, for the present experiments we find that the OSSE impacts are fairly similar to the OSE impacts and the calibration procedure does not greatly alter the conclusions one might draw from the OSSE results directly. To minimize practical and interpretive difficulties we use only very simple calibration approaches. Our principal assumption is that the OSE impact of adding or removing an observing system is proportional to the corresponding OSSE impact. In our calibrations we always take STATSAT to be our standard. We use the NOSAT - STATSAT differences to determine the constant of proportionality.

Impact may be measured in many ways. Useful impact measures should account for differences in variability from season to season and from region

to region. For example an impact of 10 geopotential meters is meaningless without the context of place, season and vertical level. Usually, for the purpose of comparison, it is reasonable to scale the squared errors by their respective climate variance.

It is also often helpful to define impact in terms of the change in predictability time. For example, one might define the predictability time as the time at which the mean squared forecast error reaches the climate variance level. Forecasts with errors this large are normally worthless. A positive impact in predictability time would then indicate the additional time that the forecast remains useful.

Measuring impact in terms of predictability time is especially useful when combined with a common idealization of the growth of forecast error. A number of simple parameterizations of the growth of error have been advanced (e.g. Dalcher and Kalnay, 1987 and references therein). Remarkably good fits to ensemble averaged forecast error growth curves have been obtained, by fitting relatively simple autonomous constant coefficient ordinary differential equations. These coefficients describe the growth of small errors, the saturation of large errors at the climate variance level and the source of errors due to modeling deficiencies. Since these constants should be the same for a set of experiments, e.g. for all our February OSEs, all fitted error growth curves for the experiments should be the same except for a translation with respect to the time axis. This shift is the impact in terms of predictability time.

A direct reading of the predictability times from the rms difference curves proved difficult because our sample is rather small. We could fit the parameterization of Dalcher and Kalnay (1987). Instead, we took advantage of the observation that our rms difference curves grow nearly linearly, at least during the forecast period from 12 to 48 hours, to fit these data with a series of straight lines having a common slope. In the N.H. these fits were very good. They are less reliable in the S.H. and tropics, presumably because the number of radiosondes in these regions is small. Our results for height, wind and relative humidity are shown in Tables 7.1 through 7.3. In the tables, each item in the columns labeled R^2 is the fraction of variance explained by the fitting procedure or equivalently the square of the correlation coefficient. The other columns in the tables display the predictability

time impacts of the various experiments, all relative to STATSAT. Some of these values have been quoted earlier. These impacts are the difference in the x (or time) intercepts of the fitted lines. (These intercepts are proportional to the y (or rms difference) intercepts with proportionality factor equal to the common slope.)

The NOSAT impact, i.e. the difference between NOSAT and STATSAT, in the OSE experiments were then used to calibrate the OSSE results according to

$$\frac{(\text{Expected OSE impact}) - (\text{NOSAT OSE impact}) * (\text{OSSE impact})}{(\text{NOSAT OSSE impact})}$$

This provided us with calibrated intercepts which we combined with the observed OSE error growth rate (the common slope) to create calibrated rms difference curves for WINDSAT, SSM and SSM+TOVS experiments. These are displayed along with the observed OSE results in the figures. The horizontal distances between the various curves are the predictability time impacts.

7.4.3 Calibration results

The calibration procedure described above allows us to translate our OSSE results into anticipated real world impacts in a quantitative manner. Several examples are provided in Figs. 7.30 through 7.32. Complete details are provided by Tables 7.1 through 7.3 and the above equation for the expected impact.

In Fig. 7.30, the S.H. 500 mb height rms difference for the STATSAT and NOSAT OSE experiments are plotted. The calibrated OSSE results for SSM, SSM+TOVS and WINDSAT are also plotted. These are the three straight lines between 12 and 48 h on the plots. They are plotted only for this period since it is only this period which was used in the curve fitting. Note that the February (a) and June (b) OSEs provide two independent calibrations. In both cases the dramatic improvement seen in the OSSEs for WINDSAT is expected to carry over in actuality. A 36 h improvement in forecast skill relative to STATSAT is anticipated and the expected impact of the SSM data is 12 h. In the N.H. (not shown) STATSAT and NOSAT OSSE results are nearly equivalent, so impacts expected from advanced observing systems cannot be calibrated.

The tropical 200 mb vector wind rms differences are shown for February (a) and June (b) OSSEs (Fig. 7.31). Because the growth rates for the differences are so small, it is difficult to judge the impacts by eye. In this case, in terms of predictability time there are significant impacts. WINDSAT has a 24 h advantage over SSMSAT, a 48 h advantage over SSM+TOVS and a 60 h advantage over STATSAT. Further SSM+TOVS has approximately a 12 h advantage over STATSAT which in turn has a 12 h advantage over NOSAT. However, not much weight should be given these results since in the tropics and S.H., the calibration procedure is not very reliable.

For the N.H. 850 mb relative humidity or cloud cover (Fig. 7.32), the actual impacts are all expected to be rather small. Note again the close relationship between relative humidity and cloud cover statistics.

The calibration procedure does have some uncertainties and drawbacks. The main drawback is the assumption of a linear relationship between impact in the OSSEs and in the OSEs. Of course the data assimilation system and nature are highly nonlinear. In the current experiments, the uncertainties are mostly due to the small sample size, especially in the S.H. where the number of radiosondes used in the verification is small. For example, in some cases the sense of impact between NOSAT and STATSAT is reversed in OSSEs and OSEs. In these cases the calibration produces nonsensical results. This occurred when calibrating the S.H. 850 mb relative humidity rms difference. In other cases the OSE impact between NOSAT and STATSAT is quite small. This implies negligible calibrated impact for any change to the data assimilation system. This occurred when calibrating the N.H. 500 mb height rms difference.

7.4.4 Forecast biases

In general the biases during the forecast are small compared to the rms difference. However in many cases the biases grow very steadily with time indicating that the AFGL model is warming and drying relative to the ECMWF nature.

We examined the biases by fitting straight lines with a common slope as described in Section 7.4.2. However in this case all data from 12 to 96 hours was used. The common slope obtained from the fit is then the rate at which the biases grow. Some of these are displayed in Table 7.4 for the N.H. OSSEs. Generally speaking the forecasts are warming relative to nature by one

third to one degree per day. The height biases reflect these temperature biases. These results are consistent with the warming seen during the spinup forecast (Section 4.1) Also the forecasts are drying in the lower atmosphere by 1 to 1.5 percentage points of relative humidity per day. For temperature and height there are many cases when the fraction of variance explained by the fit is greater than .99, indicating that the bias grows very linearly. For example Fig. 7.33 shows the evolution of bias for the N.H. 500 mb height in the OSSEs. Differences between the experiments are not significant. Results for the tropics and S.H. are not as regular and clear cut presumably because of sampling variability. This also applies to the OSEs, although there is some evidence of the forecasts warming during the February OSEs in the mid troposphere. In the N.H. the dry relative humidity biases are substantial at 1000 mb. In this case the bias at the start of the forecast is already -17 to -18 percent. At other levels the initial dry bias is only of order 5%. Typically, the analyses are dry by 5% and the forecasts continue to dry out by 1% to 2% per day for the first two days of the forecast. For example, the evolution of the biases of the 850 mb relative humidity forecasts are shown in Fig. 7.34. Again, differences in the experiments are not significant. The trends are not so clear cut in the tropics and extratropics and the OSEs. In the tropics, in the OSSEs, the atmosphere tends to moisten during the forecast. In this case the boundary layer is analyzed dry but the mid troposphere is slightly moist.

Table 7.1 Predictability impacts (days) for height (a), wind (b) and relative humidity (c) for the N.H. extratropics. Impacts for cases with R**2 less than 0.25 (i.e. for correlations less than 0.5) are not shown.

A. Height

l	P(l)	November OSSE					February OSE		June OSE	
		R**2	NOSAT	SSM/T	SSM+TOVS	WINDSAT	R**2	NOSAT	R**2	NOSAT
1	1000	.000	-	-	-	-	.603	.266	.219	-
2	850	.822	.183	-.143	.022	.601	.975	-.287	.920	-.319
3	700	.991	.168	.118	.011	.488	.996	-.048	.989	-.032
4	500	.999	.141	.144	-.008	.307	.999	.023	.985	-.003
5	400	.999	.098	.113	-.017	.255	.998	.022	.960	-.020
6	300	.998	.038	.064	-.010	.186	.998	.000	.978	-.070
7	250	.996	.019	.050	-.013	.167	.998	-.019	.958	-.115
8	200	.996	-.011	.045	.012	.103	.998	-.051	.874	-.145
9	150	.994	-.013	.060	.029	.120	.997	-.104	.778	-.175
10	100	.996	-.100	.049	.065	-.112	.993	-.121	.449	-.444
11	70	.999	-.412	.060	.214	-.294	.990	-.127	.111	-
12	50	.998	-.699	.064	.307	-.368	.972	-.220	.434	-.585

B. Vector wind

l	P(l)	November OSSE					February OSE		June OSE	
		R**2	NOSAT	SSM/T	SSM+TOVS	WINDSAT	R**2	NOSAT	R**2	NOSAT
1	1000	.969	.414	.191	-.094	.928	.909	.161	.910	.451
2	850	.963	.474	.207	-.210	.915	.987	.122	.977	-.144
3	700	.981	.458	.149	-.314	.973	.990	.040	.932	-.184
4	500	.976	.410	.179	-.176	.866	.996	.015	.948	-.160
5	400	.985	.373	.182	-.145	.846	.995	.009	.984	-.152
6	300	.980	.233	.134	-.154	.806	.977	-.058	.990	-.103
7	250	.970	.214	.147	-.163	.941	.989	-.060	.987	-.135
8	200	.948	.126	.214	-.142	1.079	.979	-.171	.990	-.235
9	150	.860	.001	.318	-.095	1.301	.965	-.292	.988	-.250
10	100	.892	.232	.489	.127	1.244	.929	-.175	.984	-.108
11	70	.884	.265	.572	.331	1.222	.893	-.035	.964	.010
12	50	.929	.245	.506	.399	1.001	.938	-.076	.970	.157

C. Relative humidity

l	P(l)	November OSSE					February OSE		June OSE	
		R**2	NOSAT	SSM/T	SSM+TOVS	WINDSAT	R**2	NOSAT	R**2	NOSAT
1	1000	.781	.213	.197	-.013	.490	.822	-.154	.107	-
2	850	.959	.320	.388	.168	.543	.935	.100	.964	.233
3	700	.954	.365	.330	-.029	.719	.856	.136	.945	.120
4	500	.906	.475	.392	.242	1.121	.973	.400	.934	.262
5	400	.921	.161	.116	.014	.763	.990	.114	.886	-.019
6	300	.853	.188	.146	.066	.908	.861	.355	.846	-.086

Table 7.2 Predictability impacts (days) for height (a), wind (b) and relative humidity (c) for the tropics. Impacts for cases with R**2 less than 0.25 (i.e. for correlations less than 0.5) are not shown.

A. Height

		November OSSE					February OSE		June OSE	
l	P(l)	-----					-----		-----	
		R**2	NOSAT	SSM/T	SSM+TOVS	WINDSAT	R**2	NOSAT	R**2	NOSAT
1	1000	.000	-	-	-	-	.158	-	.312	.181
2	850	.131	-	-	-	-	.126	-	.643	-.466
3	700	.652	-.490	-.033	.176	.445	.484	.395	.779	-.641
4	500	.551	-.224	-.145	-.623	.610	.028	-	.241	-
5	400	.569	-.348	-.302	-1.007	.398	.695	.066	.672	-.804
6	300	.381	-.687	-.364	-.917	.414	.633	.658	.545	-.800
7	250	.447	-.499	.116	-.050	.465	.000	-	.880	-.921
8	200	.411	-.147	.731	.665	.940	.001	-	.881	-.517
9	150	.191	-	-	-	-	.041	-	.962	-.348
10	100	.171	-	-	-	-	.130	-	.556	-.354
11	70	.009	-	-	-	-	.094	-	.005	-
12	50	.005	-	-	-	-	.002	-	.000	-

B. Vector wind

		November OSSE					February OSE		June OSE	
l	P(l)	-----					-----		-----	
		R**2	NOSAT	SSM/T	SSM+TOVS	WINDSAT	R**2	NOSAT	R**2	NOSAT
1	1000	.450	.802	.815	.458	1.389	.047	-	.641	.323
2	850	.846	.416	.082	.029	.846	.813	-.246	.791	-.304
3	700	.881	.771	.765	.479	1.307	.368	.968	.883	.165
4	500	.550	.882	.956	.267	1.682	.402	.023	.770	-.321
5	400	.565	.861	1.150	.664	2.000	.334	.472	.775	-.794
6	300	.494	.261	1.762	-.128	3.908	.806	-.433	.537	-.575
7	250	.398	.418	1.454	.693	3.479	.788	-.212	.638	-.089
8	200	.664	-.462	1.317	.482	2.057	.666	-.649	.345	-.449
9	150	.739	.168	.932	.350	2.624	.328	1.527	.653	-.433
10	100	.033	-	-	-	-	.577	-.536	.902	-.158
11	70	.873	.355	.854	.636	1.719	.015	-	.736	-.267
12	50	.698	1.160	2.006	1.534	3.665	.049	-	.018	-

C. Relative humidity

		November OSSE					February OSE		June OSE	
l	P(l)	-----					-----		-----	
		R**2	NOSAT	SSM/T	SSM+TOVS	WINDSAT	R**2	NOSAT	R**2	NOSAT
1	1000	.114	-	-	-	-	.256	-1.478	.522	.319
2	850	.424	1.520	2.104	1.775	1.671	.521	-.121	.944	.071
3	700	.433	.601	.349	.460	1.018	.830	.210	.816	-.285
4	500	.795	-.237	.064	.086	.149	.000	-	.899	-.098
5	400	.624	-.135	-.192	-.243	-.059	.545	1.828	.393	.016
6	300	.157	-	-	-	-	.467	-.682	.480	-.275

Table 7.3 Predictability impacts (days) for height (a), wind (b) and relative humidity (c) for the S.H. extratropics. Impacts for cases with R^{**2} less than 2.5 (i.e. for correlation less than 0.5) are not shown.

A. Height

l	P(l)	November OSSE					February OSE		June OSE	
		R**2	NOSAT	SSM/T	SSM+TOVS	WINDSAT	R**2	NOSAT	R**2	NOSAT
1	1000	.000	-	-	-	-	.062	-	.024	-
2	850	.486	-.082	2.098	2.082	1.954	.000	-	.308	-.363
3	700	.795	-1.076	.469	.471	1.357	.582	-1.396	.318	-1.958
4	500	.671	-1.597	.498	.285	1.686	.678	-1.231	.688	-1.372
5	400	.668	-1.634	.524	.323	1.491	.469	-1.625	.777	-1.783
6	300	.734	-1.709	.472	.350	1.106	.399	-1.592	.751	-2.208
7	250	.742	-1.659	.528	.448	.949	.570	-1.423	.711	-3.210
8	200	.747	-1.605	.619	.502	.784	.403	-1.765	.598	-4.398
9	150	.717	-1.768	.626	.518	.798	.369	-1.745	.689	-4.280
10	100	.647	-2.243	.318	.267	.193	.483	-1.111	.560	-5.290
11	70	.577	-3.387	-.004	.841	-1.169	.802	-.787	.013	-
12	50	.610	-4.762	-.845	1.256	-2.376	.764	-.337	.184	-

B. Vector wind

l	P(l)	November OSSE					February OSE		June OSE	
		R**2	NOSAT	SSM/T	SSM+TOVS	WINDSAT	R**2	NOSAT	R**2	NOSAT
1	1000	.145	-	-	-	-	.057	-	.304	-1.757
2	850	.716	-.518	1.674	1.119	3.372	.795	-1.274	.688	-2.197
3	700	.696	-1.133	1.117	.406	2.559	.265	-2.042	.700	-2.487
4	500	.651	-1.435	.644	.172	2.306	.672	-.651	.320	-2.112
5	400	.601	-1.615	.536	.445	2.571	.573	-.714	.454	-1.461
6	300	.852	-1.547	.333	.081	2.055	.242	-	.154	-
7	250	.819	-1.359	.135	.043	1.516	.244	-	.024	-
8	200	.808	-1.562	1.011	.539	2.749	.777	-1.113	.004	-
9	150	.520	-1.716	1.448	.390	3.460	.117	-	.016	-
10	100	.051	-	-	-	-	.016	-	.124	-
11	70	.265	-1.454	1.621	.503	4.040	.059	-	.575	-3.541
12	50	.169	-	-	-	-	.290	-.335	.418	-1.083

C. Relative humidity

l	P(l)	November OSSE					February OSE		June OSE	
		R**2	NOSAT	SSM/T	SSM+TOVS	WINDSAT	R**2	NOSAT	R**2	NOSAT
1	1000	.133	-	-	-	-	.005	-	.705	-.075
2	850	.432	.062	1.102	.510	2.193	.364	-.969	.140	-
3	700	.741	.398	.832	.314	1.263	.188	-	.067	-
4	500	.322	-.026	2.434	.407	2.980	.045	-	.662	.225
5	400	.427	.014	1.667	.293	2.778	.493	-.037	.005	-
6	300	.168	-	-	-	-	.158	-	.705	.664

Table 7.4 Growth rate of forecast bias for height (m/day), temperature (K/day) and relative humidity (%/day) for the N.H. extratropics. Impacts for cases with R**2 less than 0.64 (i.e. for correlations less than 0.8) are not shown.

1	P(1)	R**2	Z	R**2	T	R**2	RH
1	1000	.000	-	.175	-	.673	-1.467
2	850	.561	-	.879	.443	.753	-.948
3	700	.963	4.232	.983	.718	.848	-1.074
4	500	.989	12.625	.991	.937	.284	-
5	400	.992	18.747	.986	.903	.014	-
6	300	.992	25.569	.986	.689	.057	-
7	250	.993	28.995	.985	.544	-	-
8	200	.994	31.843	.979	.426	-	-
9	150	.995	35.529	.955	.371	-	-
10	100	.996	39.334	.970	.375	-	-
11	70	.998	43.682	.964	.406	-	-
12	50	.997	47.277	.973	.415	-	-

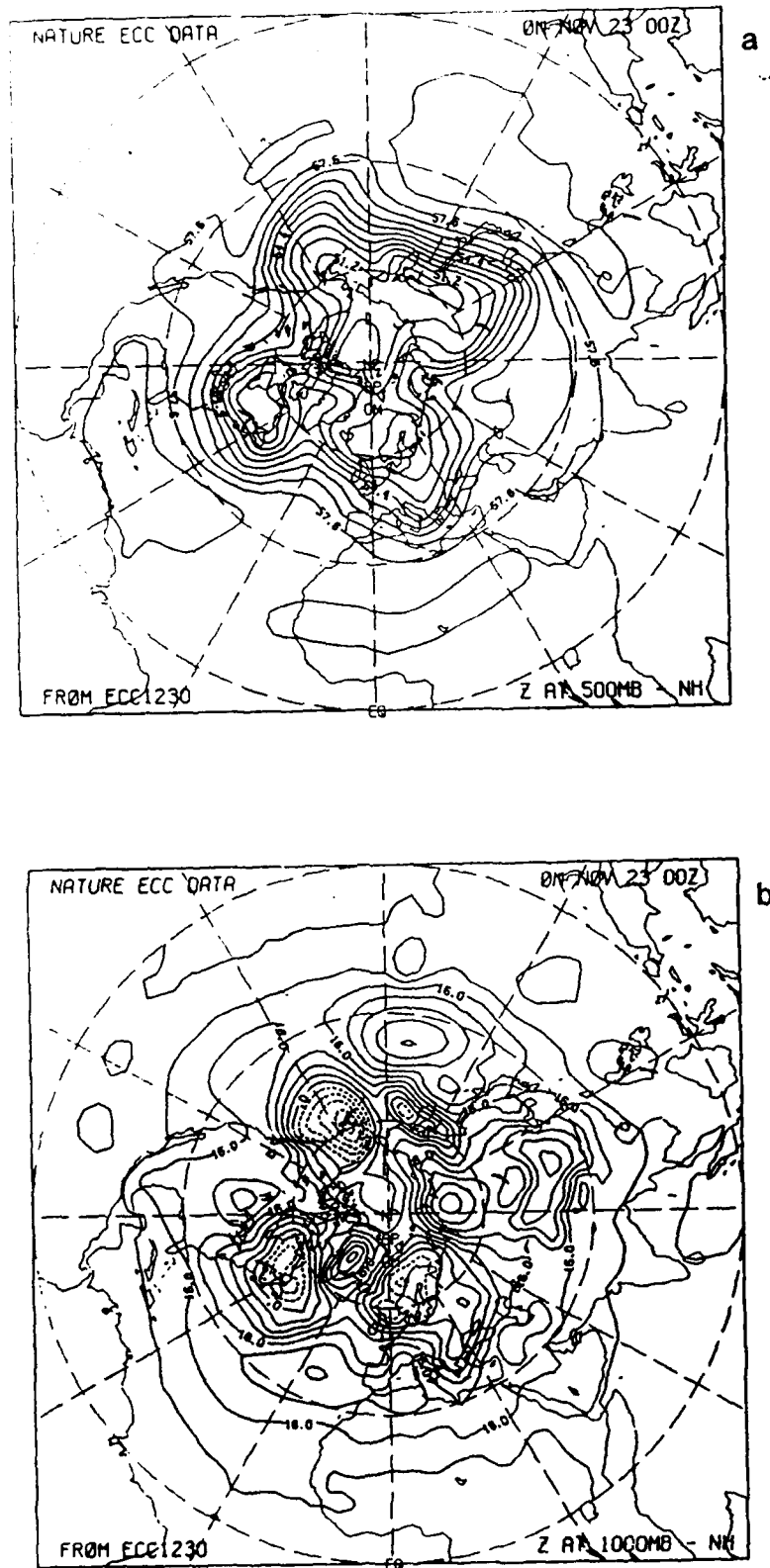


Figure 7.1 Northern hemisphere height analyses and analysis errors at 00 GMT 23 November. The contour interval in the 500 mb analyses is 80 m, at 1000 mb it is 40 m. The contour interval of the error maps is 40 m at both 1000 and 500 mb. Shown are 500 mb nature data (a), 1000 mb nature data (b).

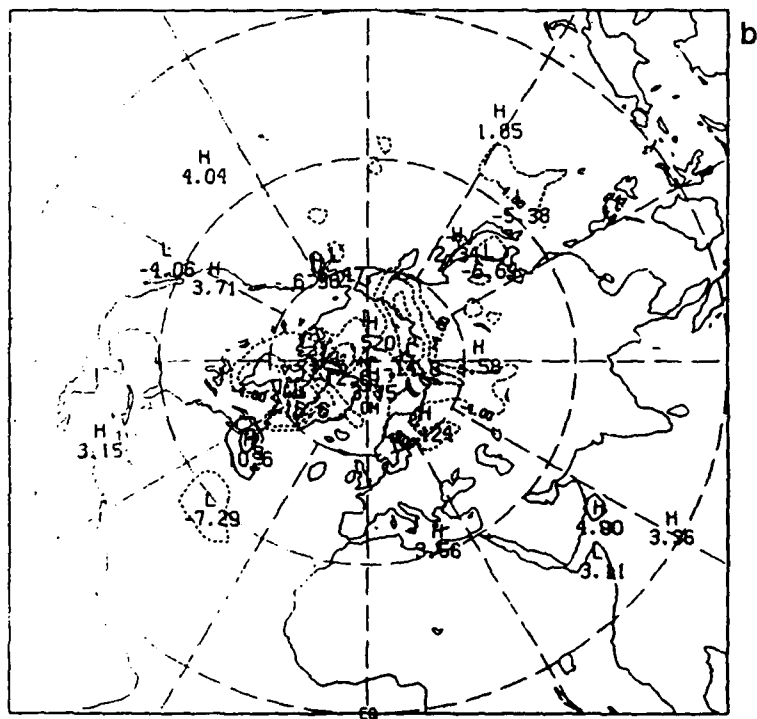
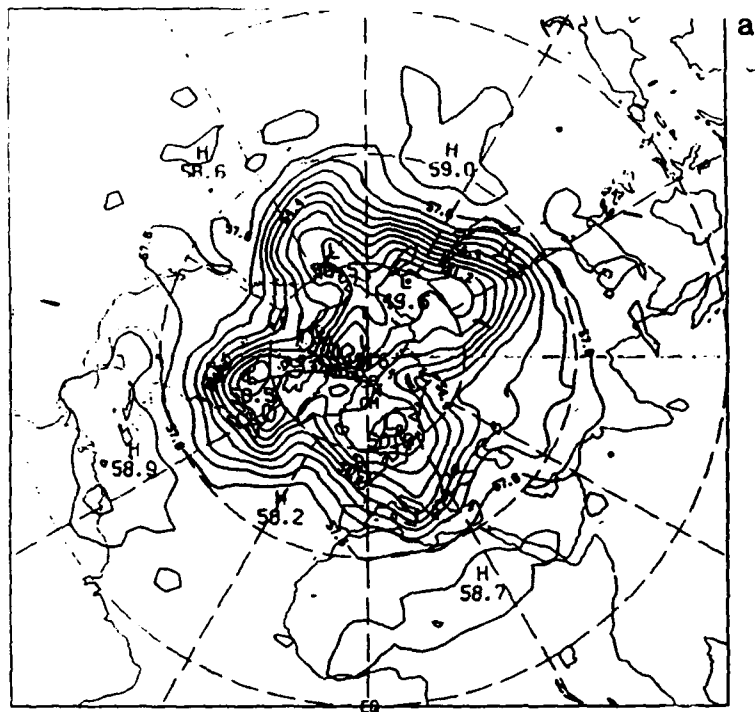


Figure 7.2 Format as in Fig. 7.1. STATSAT analysis (a) and analysis error (b) at 500 mb, and at 1000 mb (c,d).

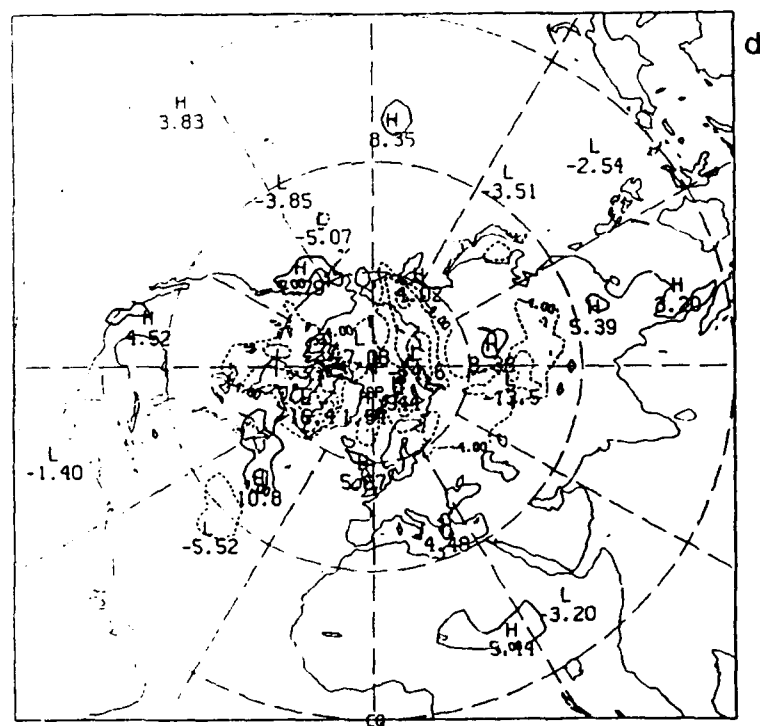
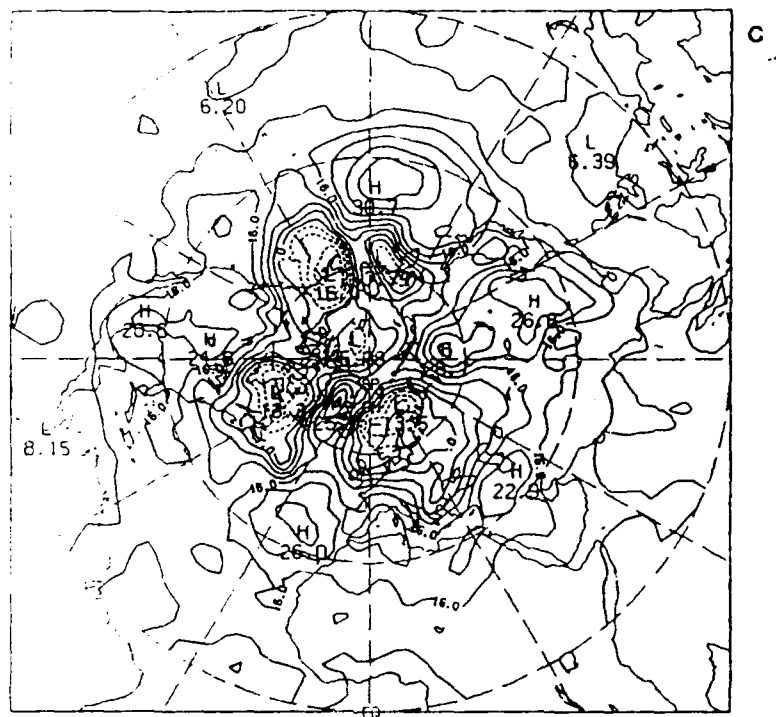
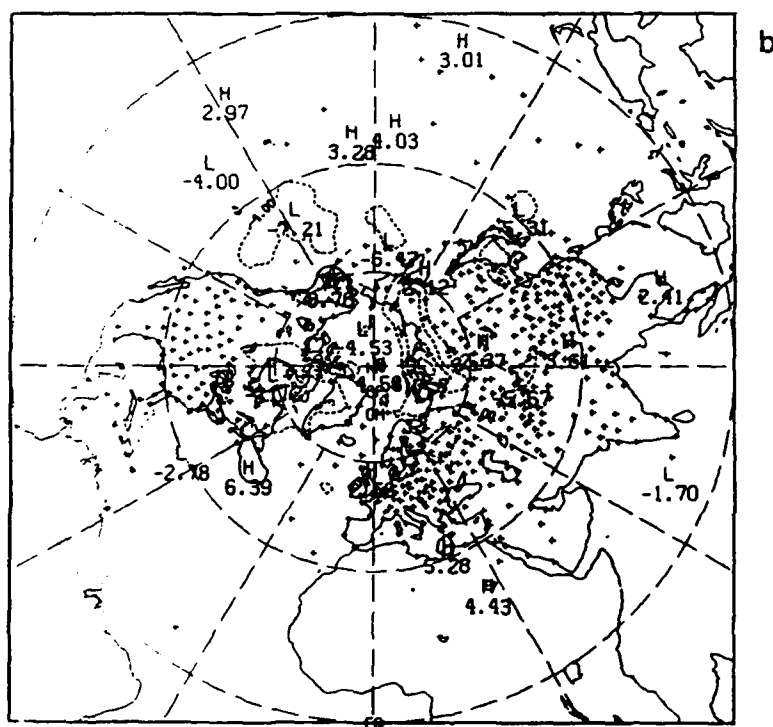
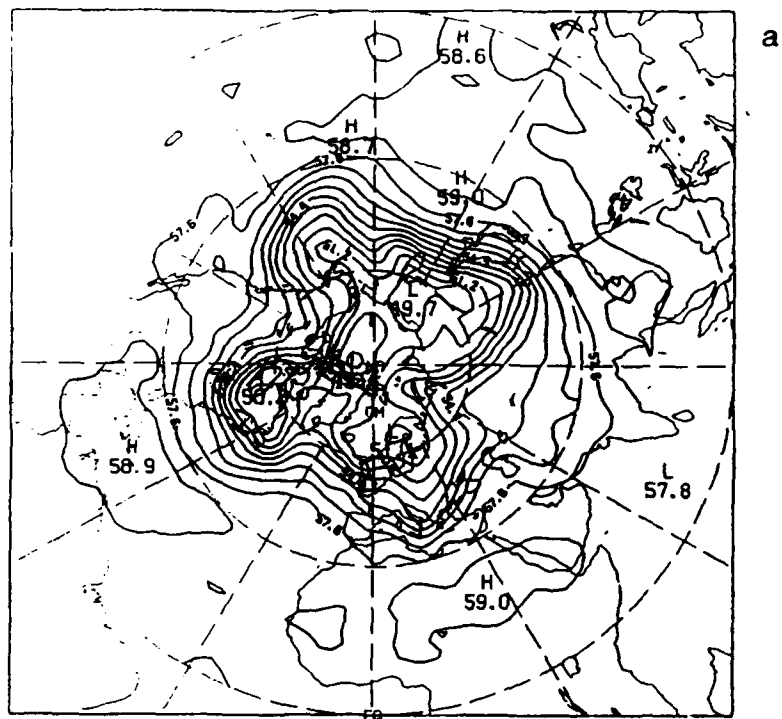


Figure 7.2 (continued).



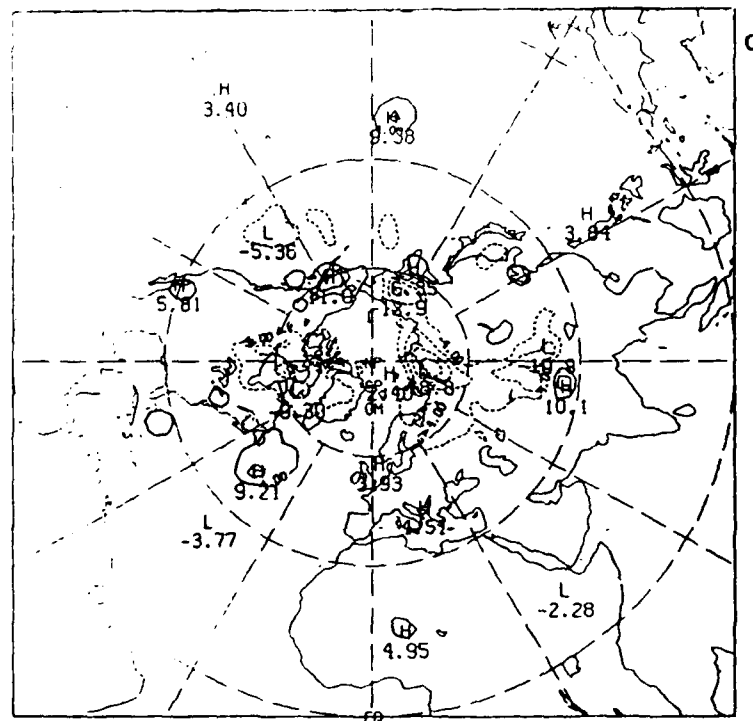
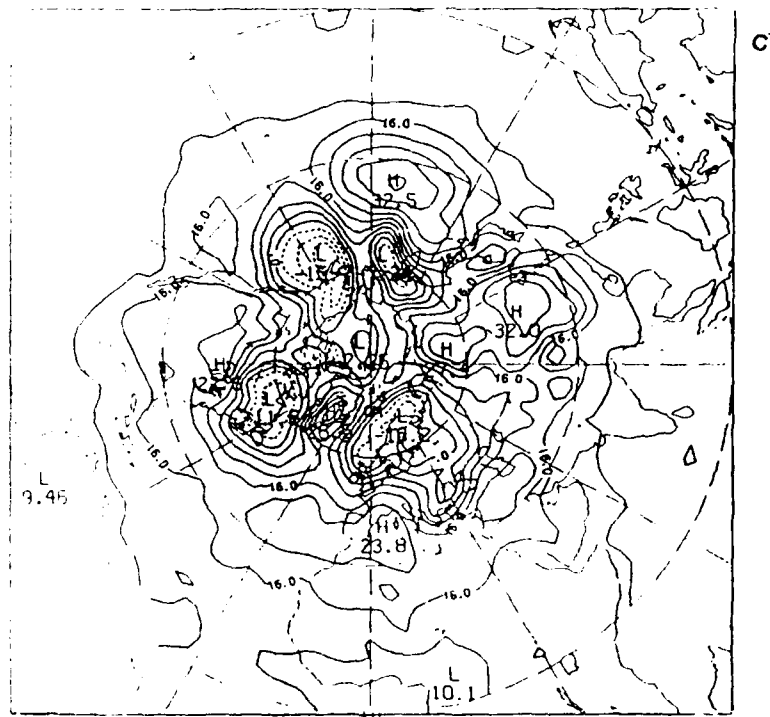


Figure 7.3 (continued).

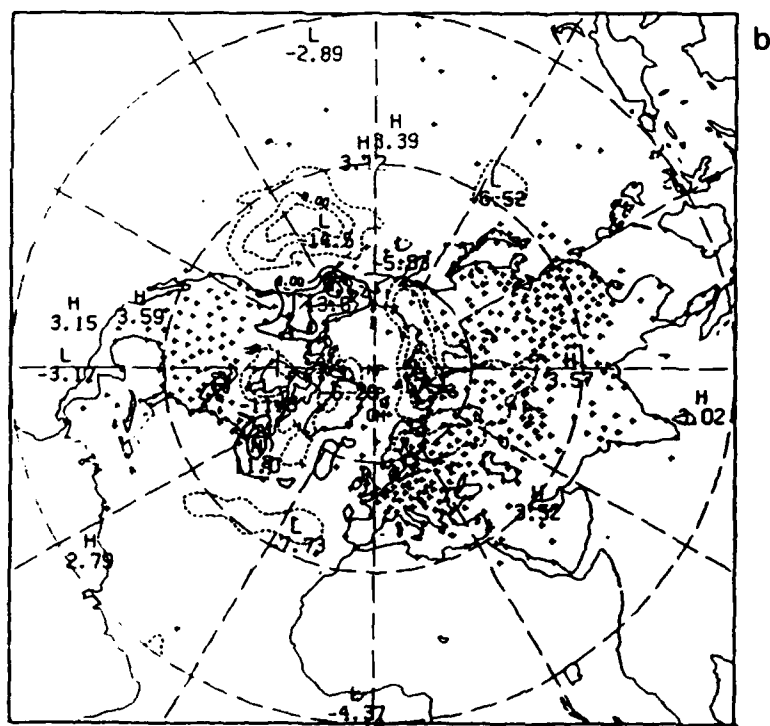
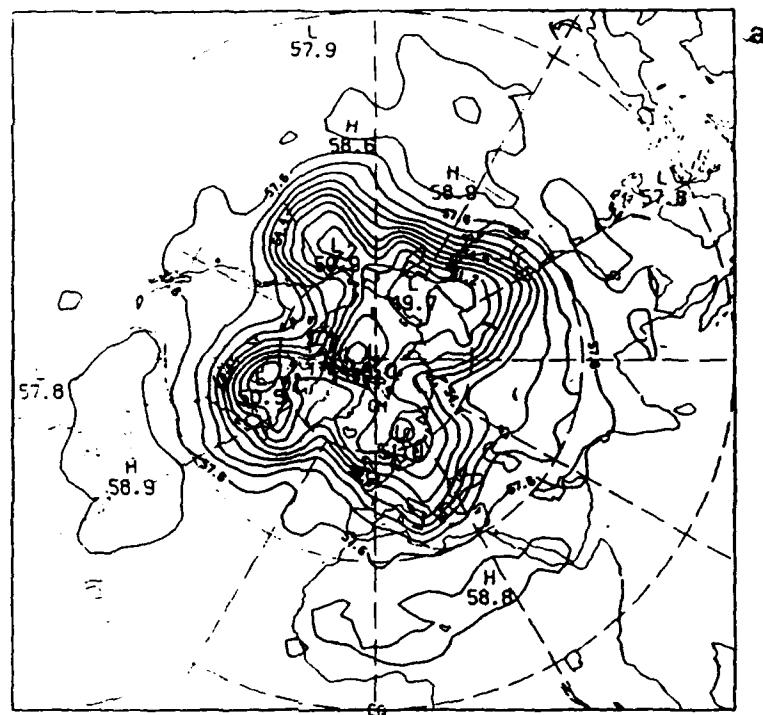


Figure 7.4 Format as in Fig. 7.1. SSM+TOVS analysis (a) and analysis error (b) at 500 mb, and at 1000 mb (c,d). Raob height residuals at $\sigma=0.5$ used in the analyses are marked by crosses in panel b.

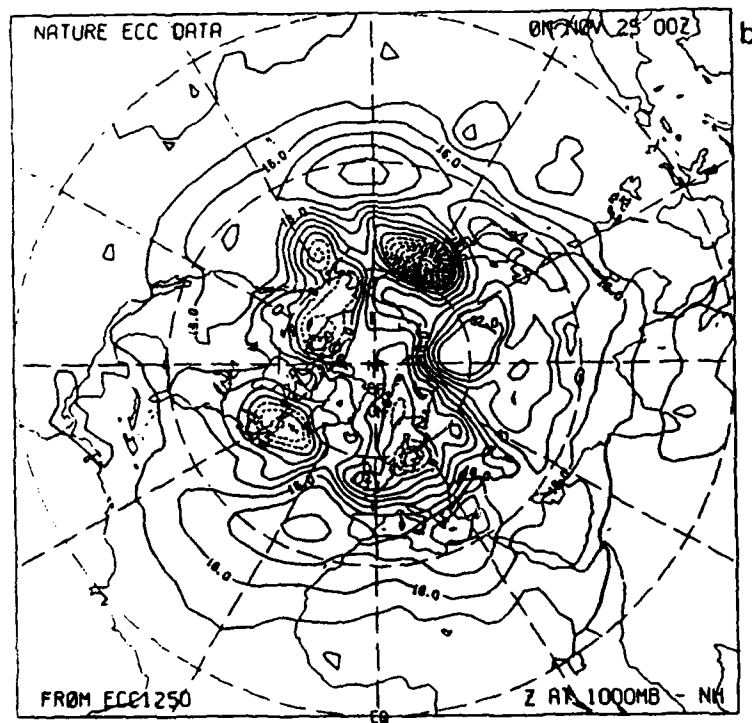
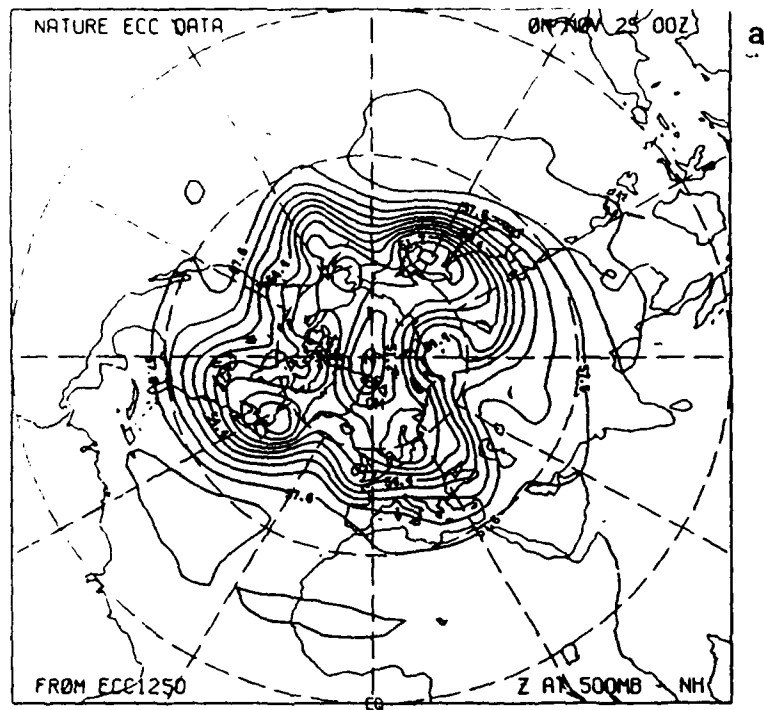


Figure 7.5 Northern hemisphere height analyses and analysis errors at 00 GMT 25 November. The contour interval in the 500 mb analyses is 80 m, at 1000 mb it is 40 m. The contour interval of the error maps is 40 m at both 1000 and 500 mb. Shown are 500 mb nature data (a), 1000 mb nature data (b).

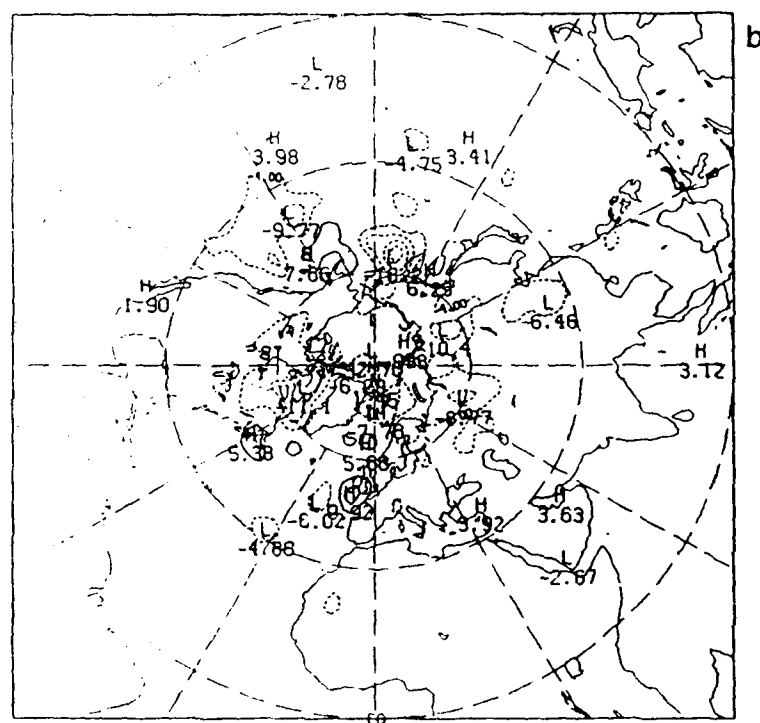
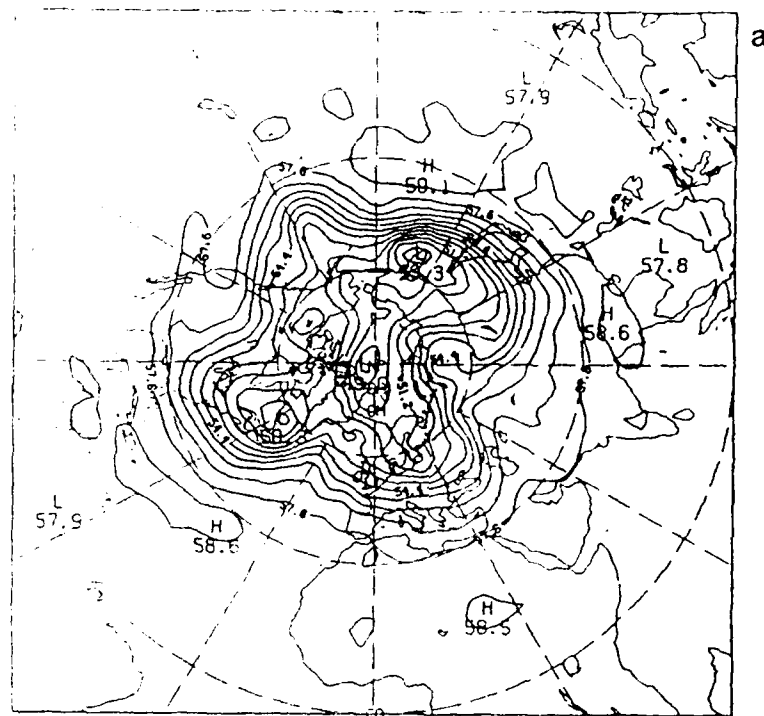


Figure 7.6 Format as in Fig. 7.5. STASAT analysis (a) and analysis error (b) at 500 mb, and at 1000 mb (c,d).

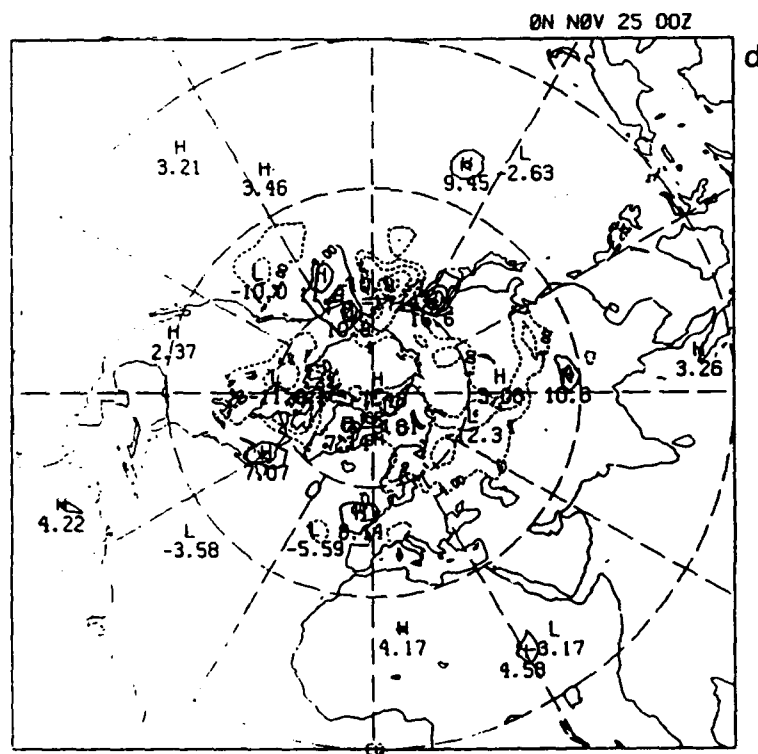
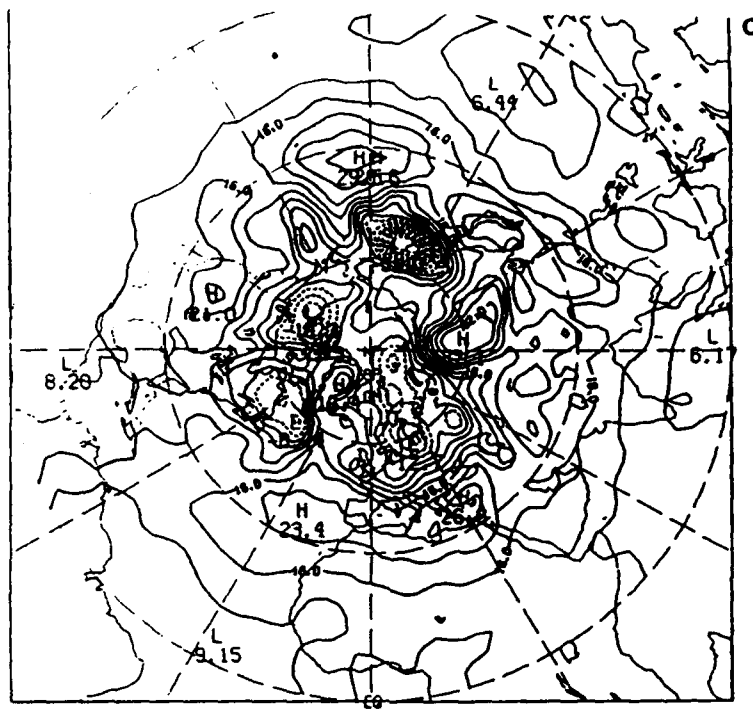


Figure 7.6 (continued).

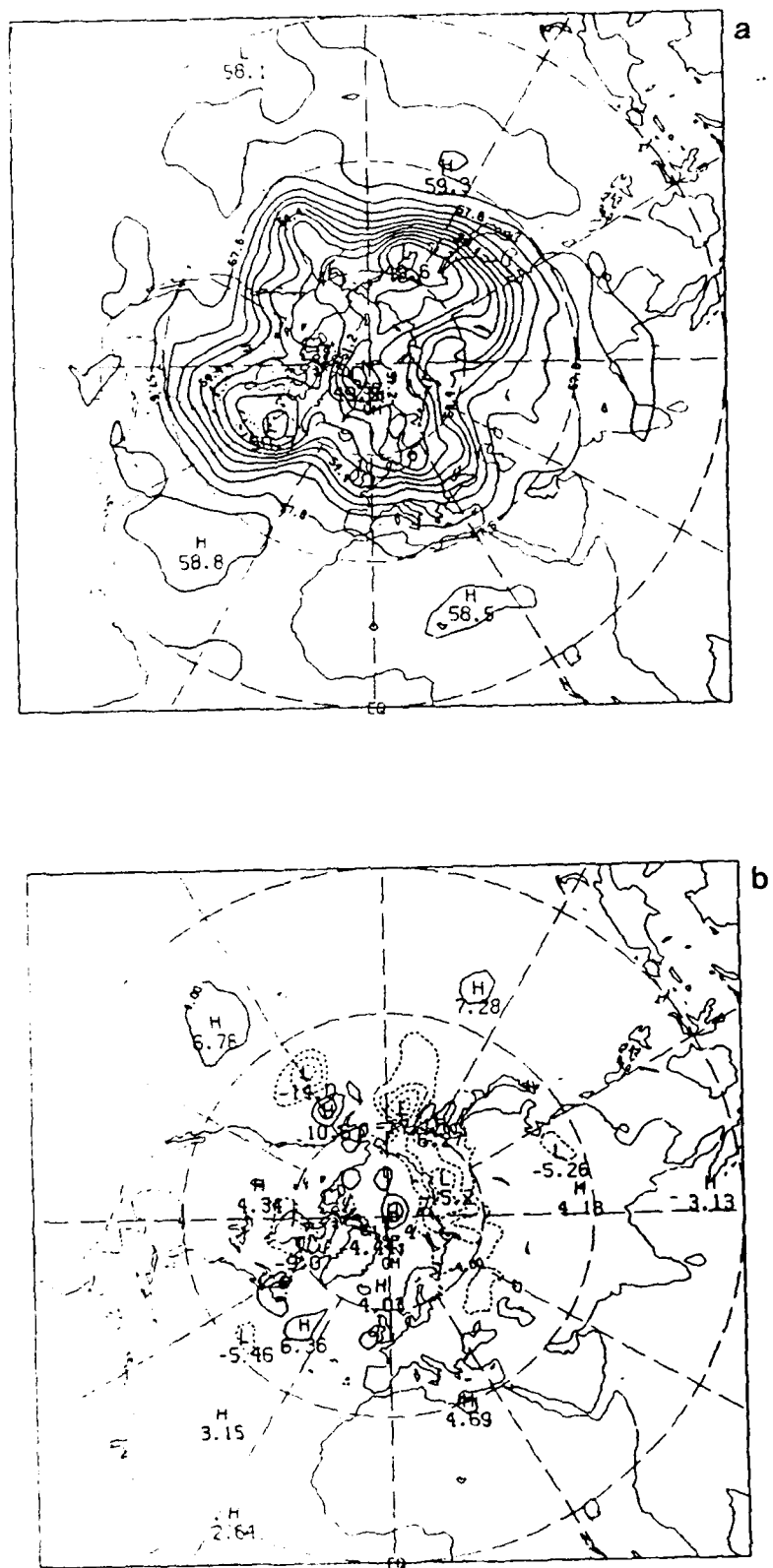


Figure 7.7 Format as in Fig. 7.5. SSMSAT analysis (a) and analysis error (b) at 500 mb, and at 1000 mb (c,d).

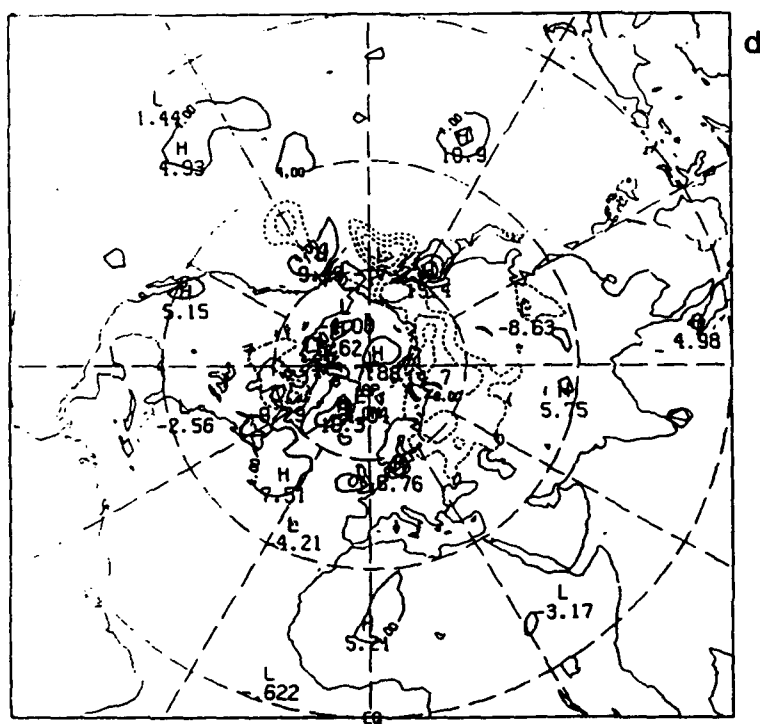
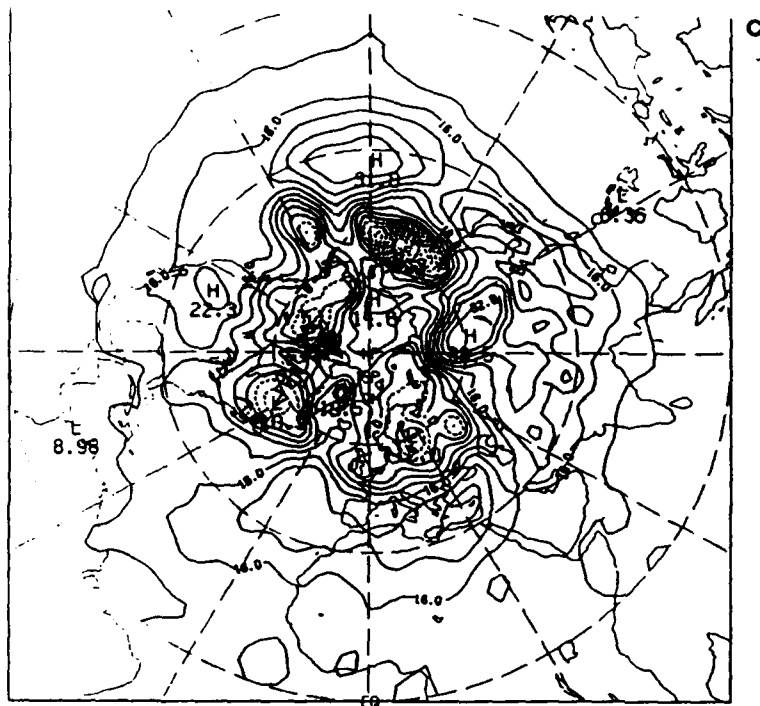


Figure 7.7 (continued).

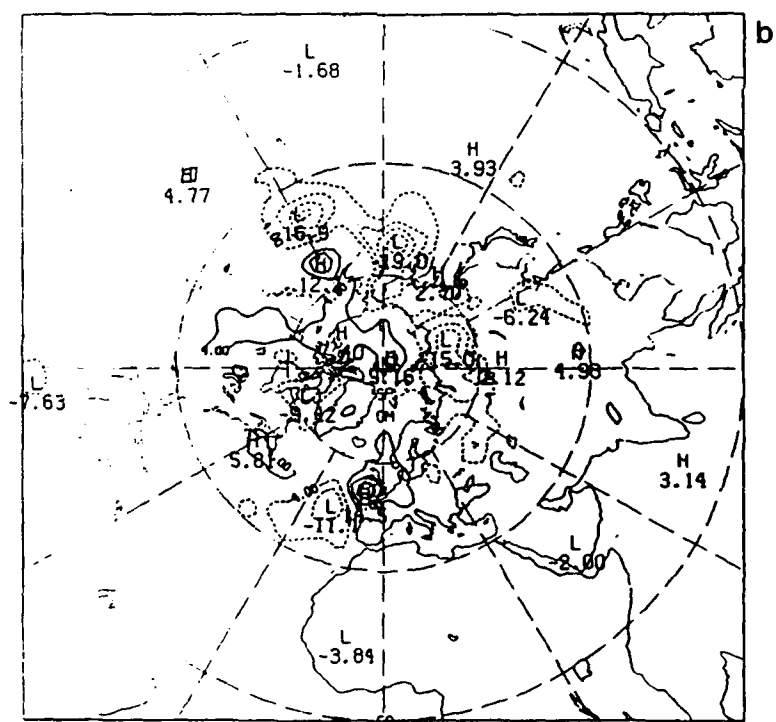
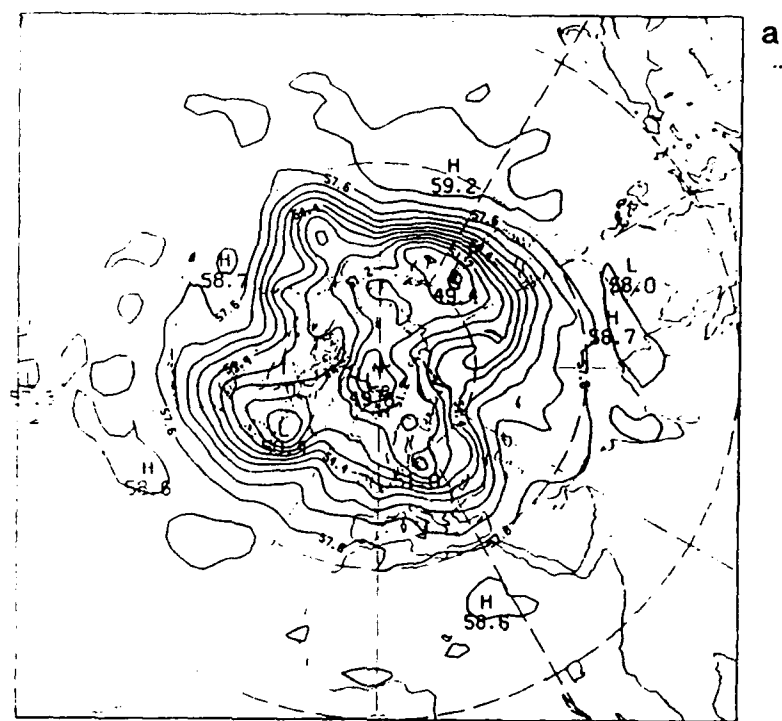


Figure 7.8 Format as in Fig. 7.5. SSM+TOVS analysis (a) and analysis error (b) at 500 mb, and at 1000 mb (c,d).

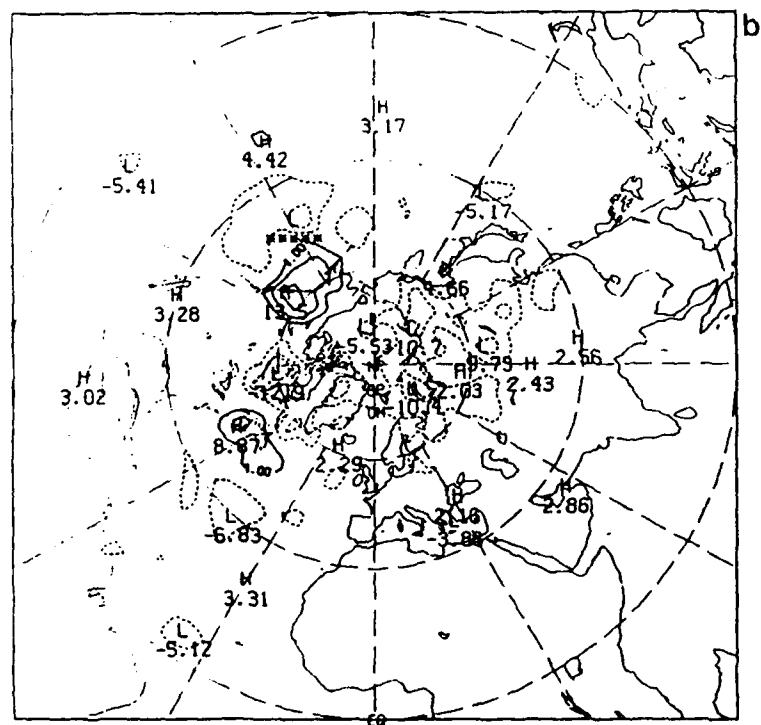
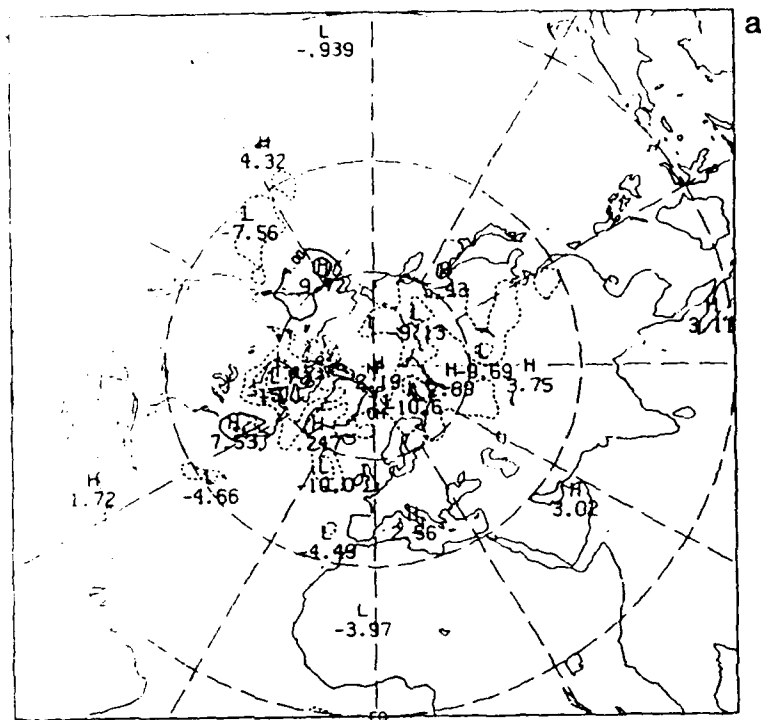


Figure 7.9 Northern hemisphere SSM/SAT (a) and SSM+TOVS (b) analysis errors at 500 mb for 00 GMT 22 November.

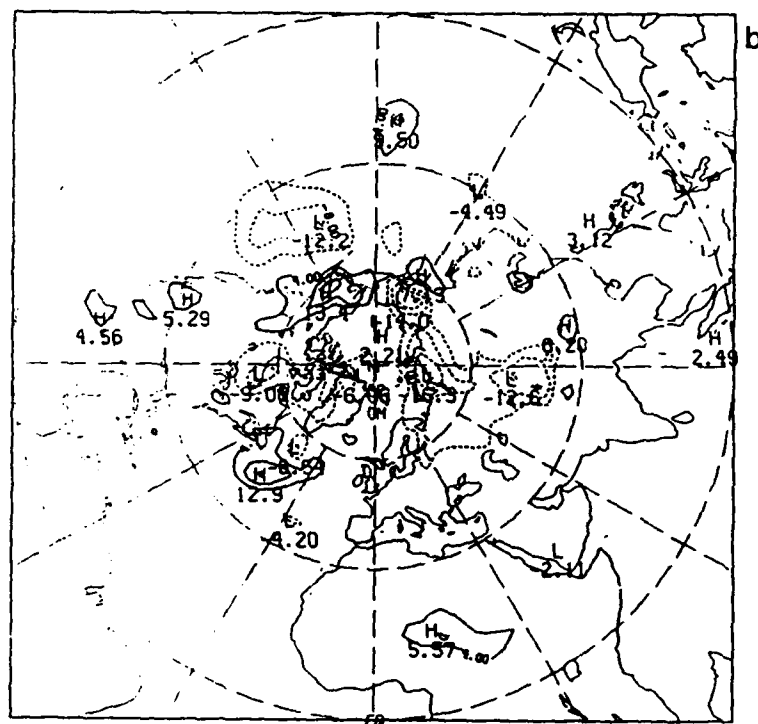
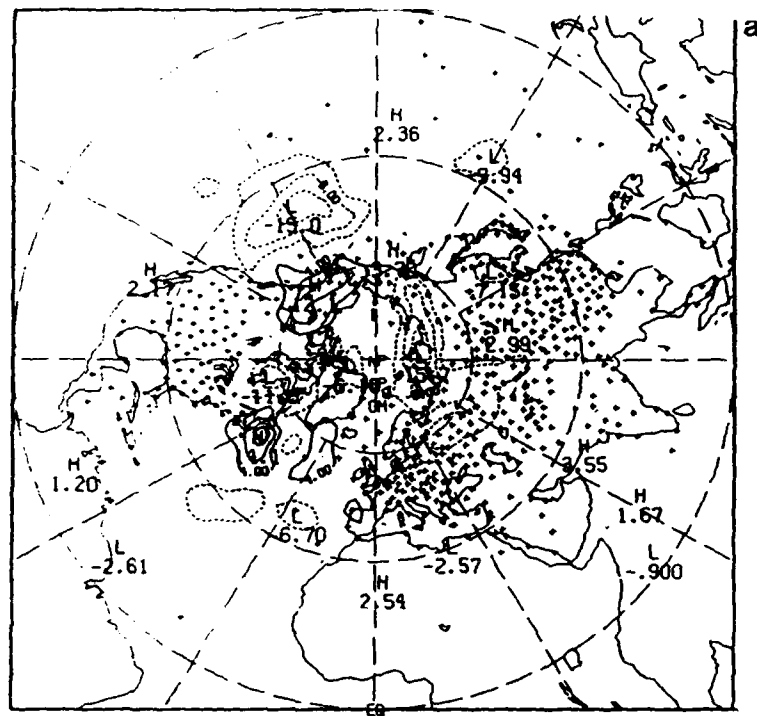


Figure 7.10 Northern hemisphere SSM+TOVS first guess errors at 500 mb (a) and 1000 mb (b) for 00 GMT 23 November. Raob height residuals at $\sigma=0.5$ used in the analysis are marked by crosses in panel a.

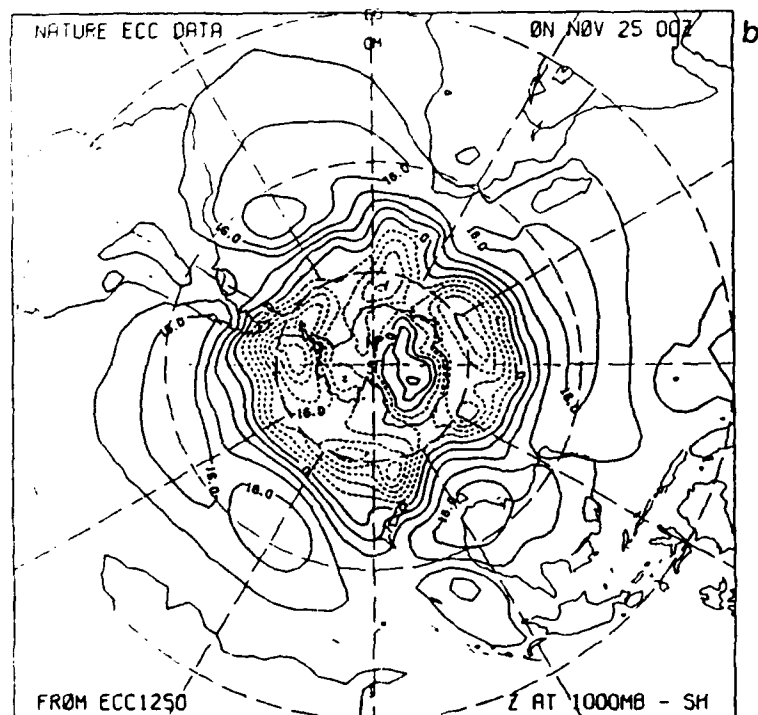
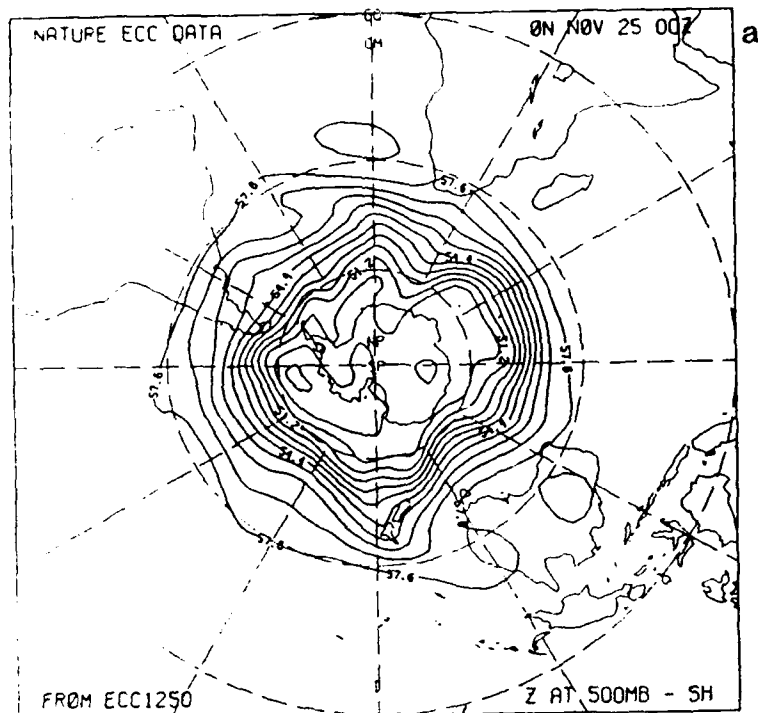


Figure 7.11 Southern hemisphere height analyses and analysis errors at 00 GMT 25 November. The contour interval in the 500 mb analyses is 80 m, at 1000 mb it is 40 m. The contour interval of the error maps is 40 m at both 1000 and 500 mb. Shown are 500 mb nature data (a), 1000 mb nature data (b).

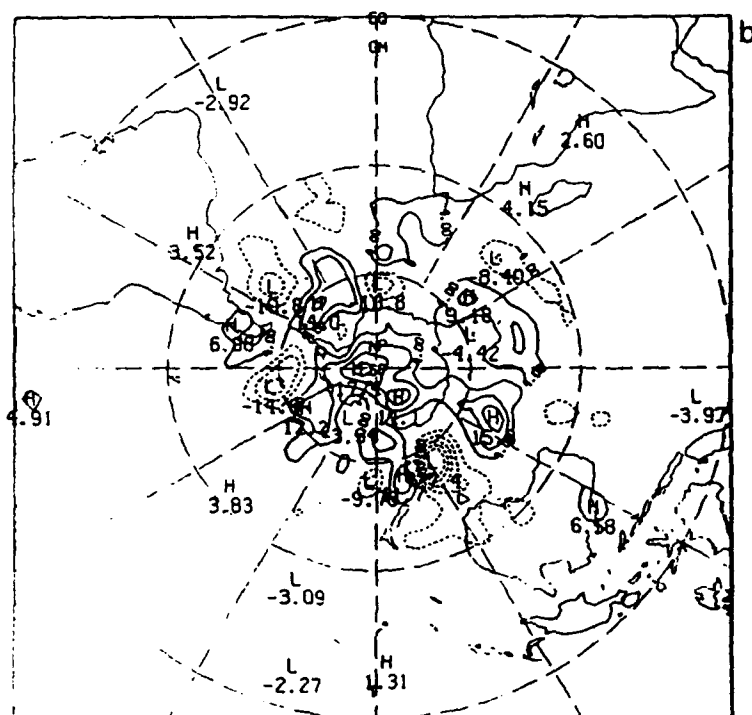
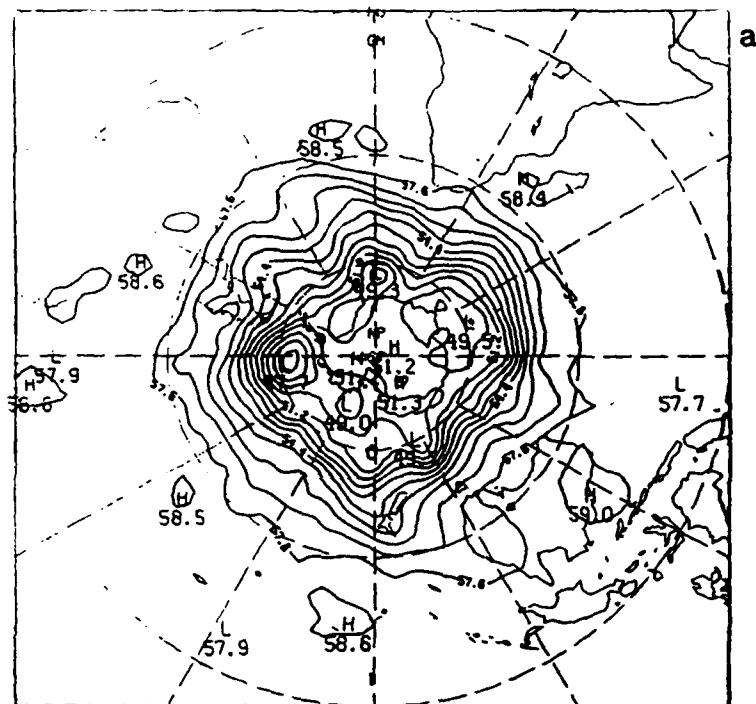


Figure 7.12 Format as in Fig. 7.11. STATSAT analysis (a) and analysis error (b) at 500 mb, and at 1000 mb (c,d).

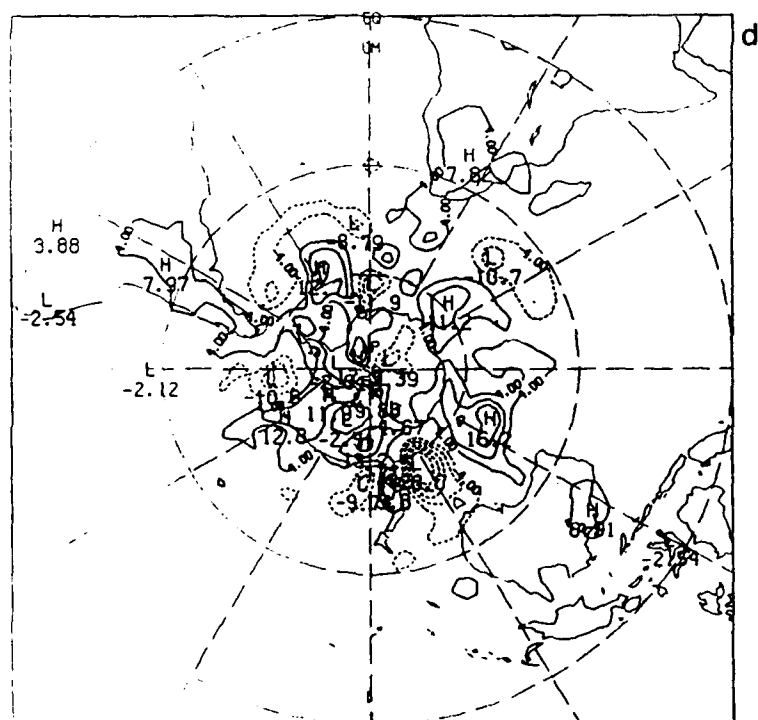
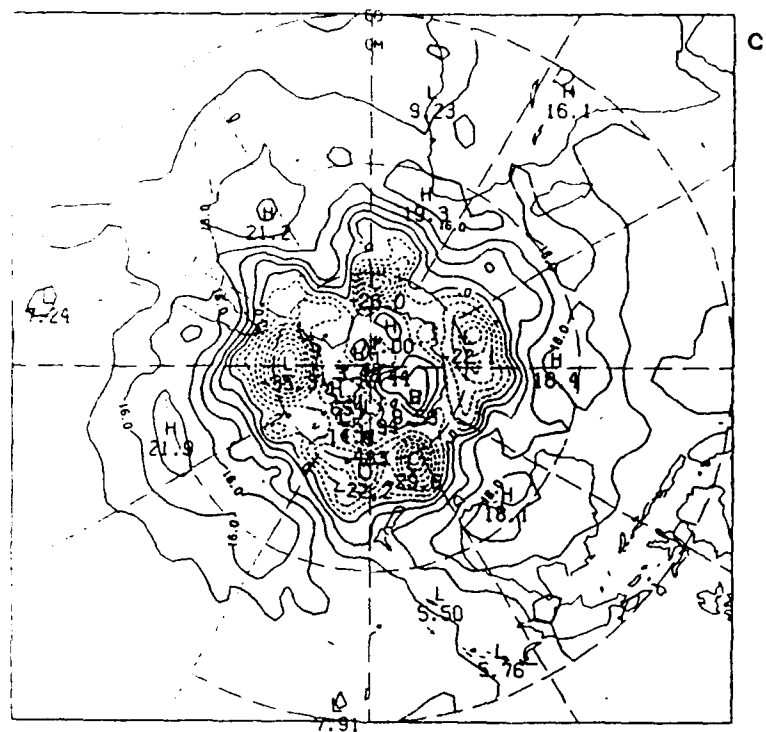


Figure 7.12 (continued).

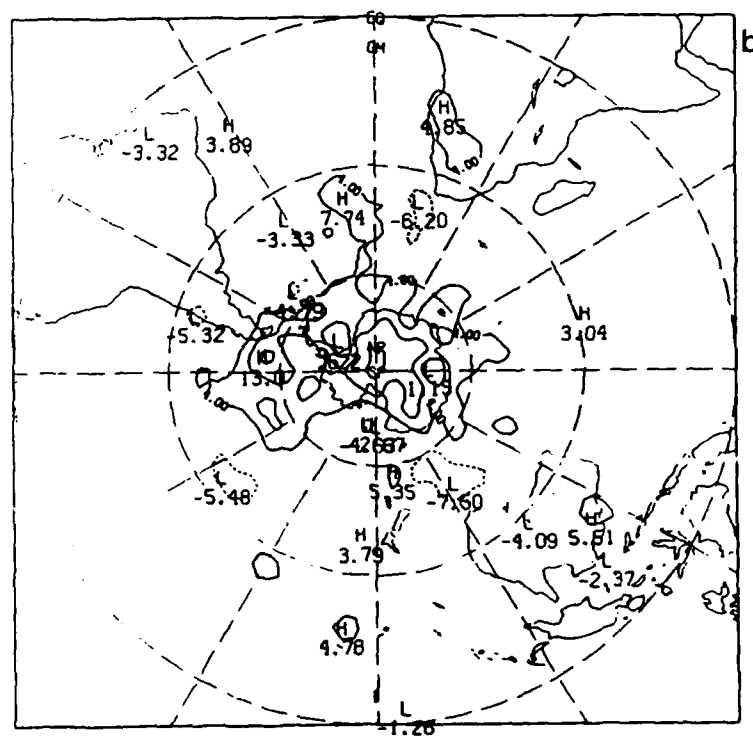
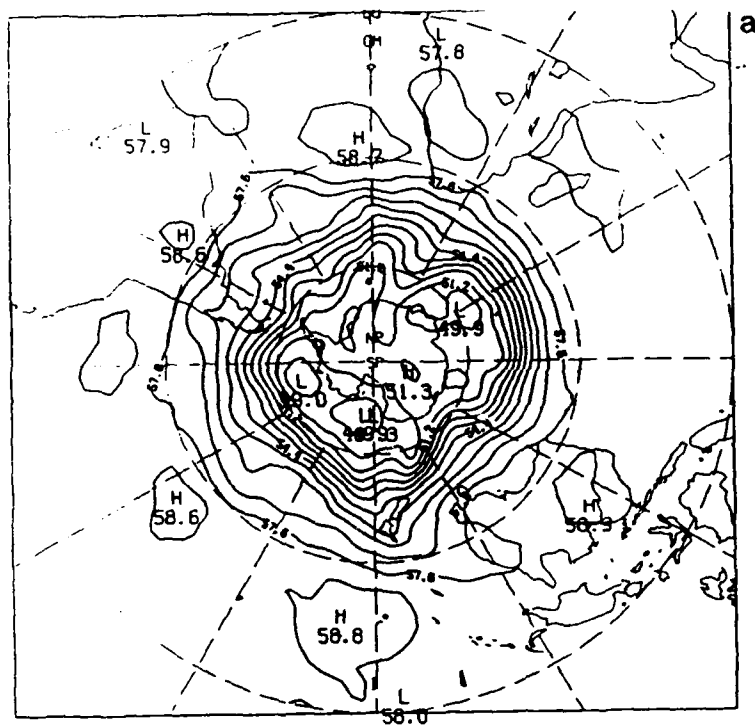


Figure 7.13 Format as in Fig. 7.11. SSMSAT analysis (a) and analysis error (b) at 500 mb, and at 1000 mb (c,d).

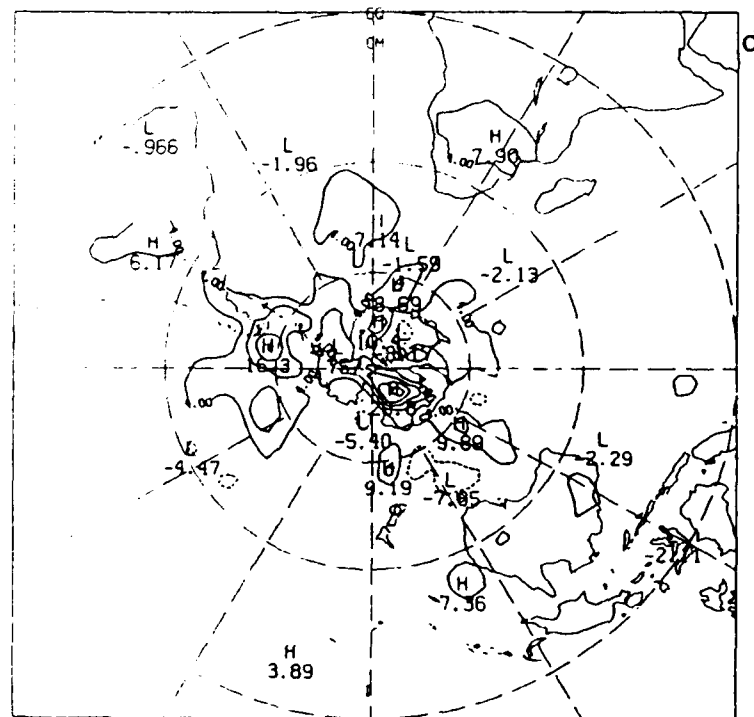
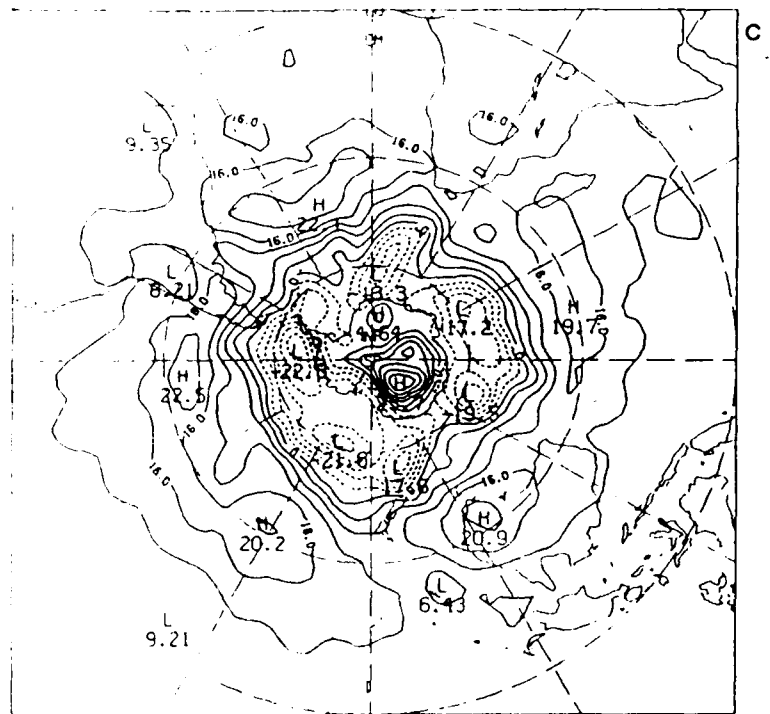


Figure 7.13 (continued).

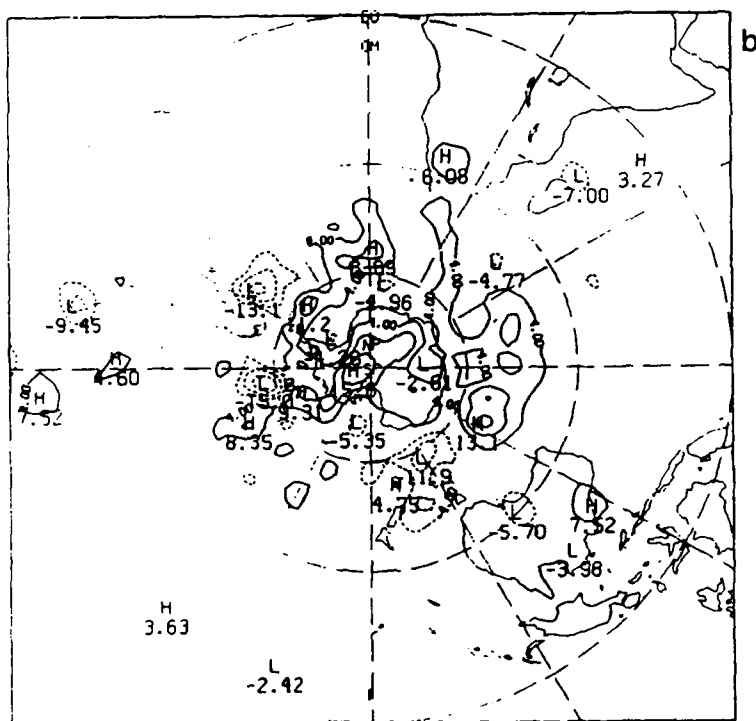
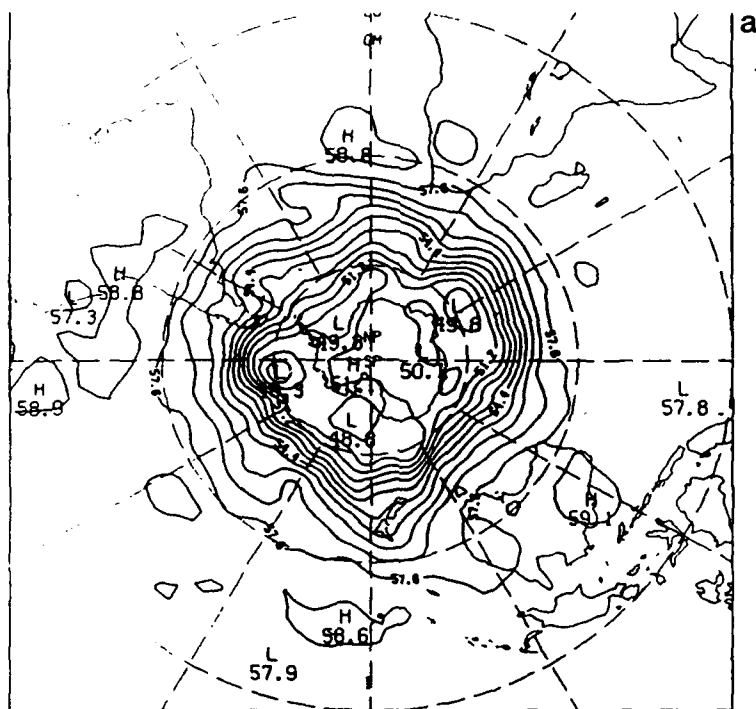


Figure 7.14 Format as in Fig. 7.11. SSM+TOVS analysis (a) and analysis error (b) at 500 mb, and at 1000 mb (c,d).

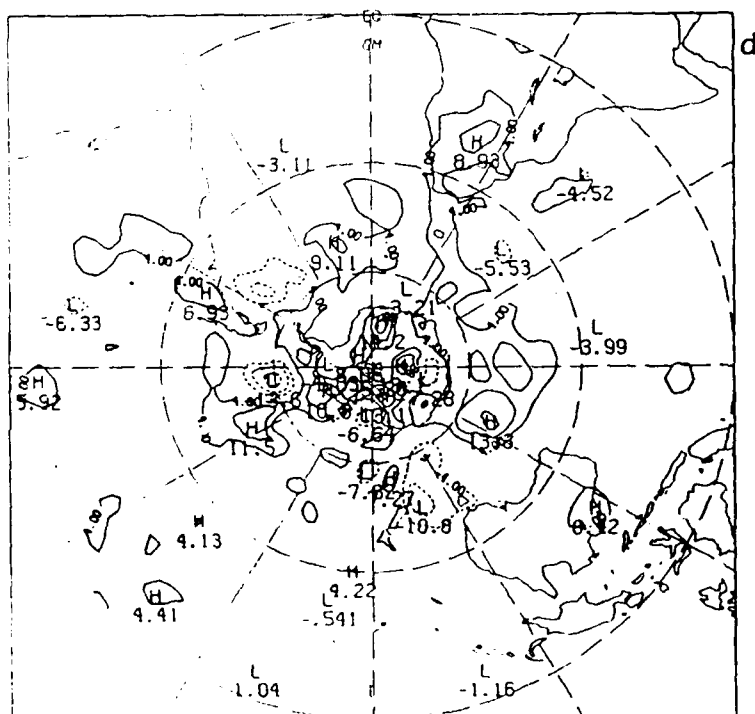
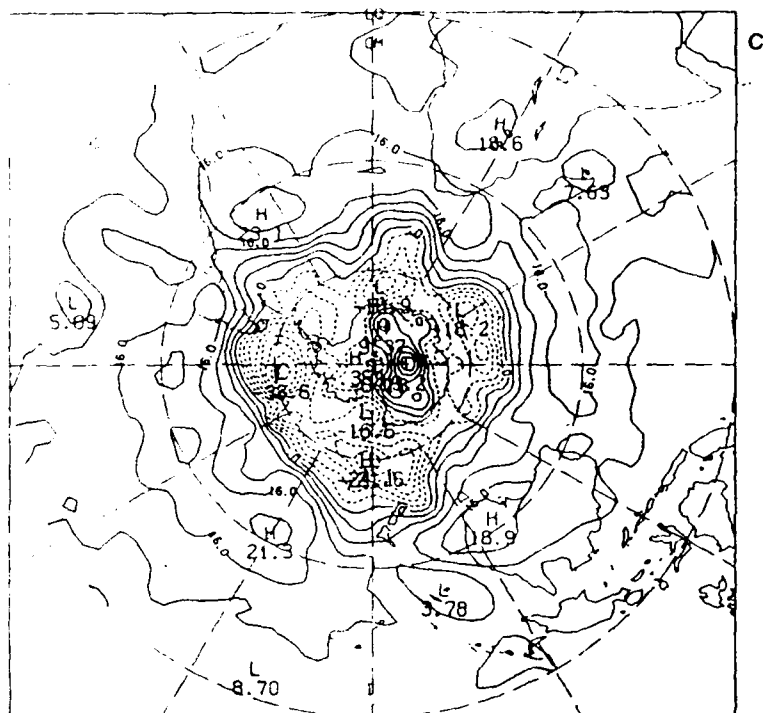


Figure 7.14 (continued).

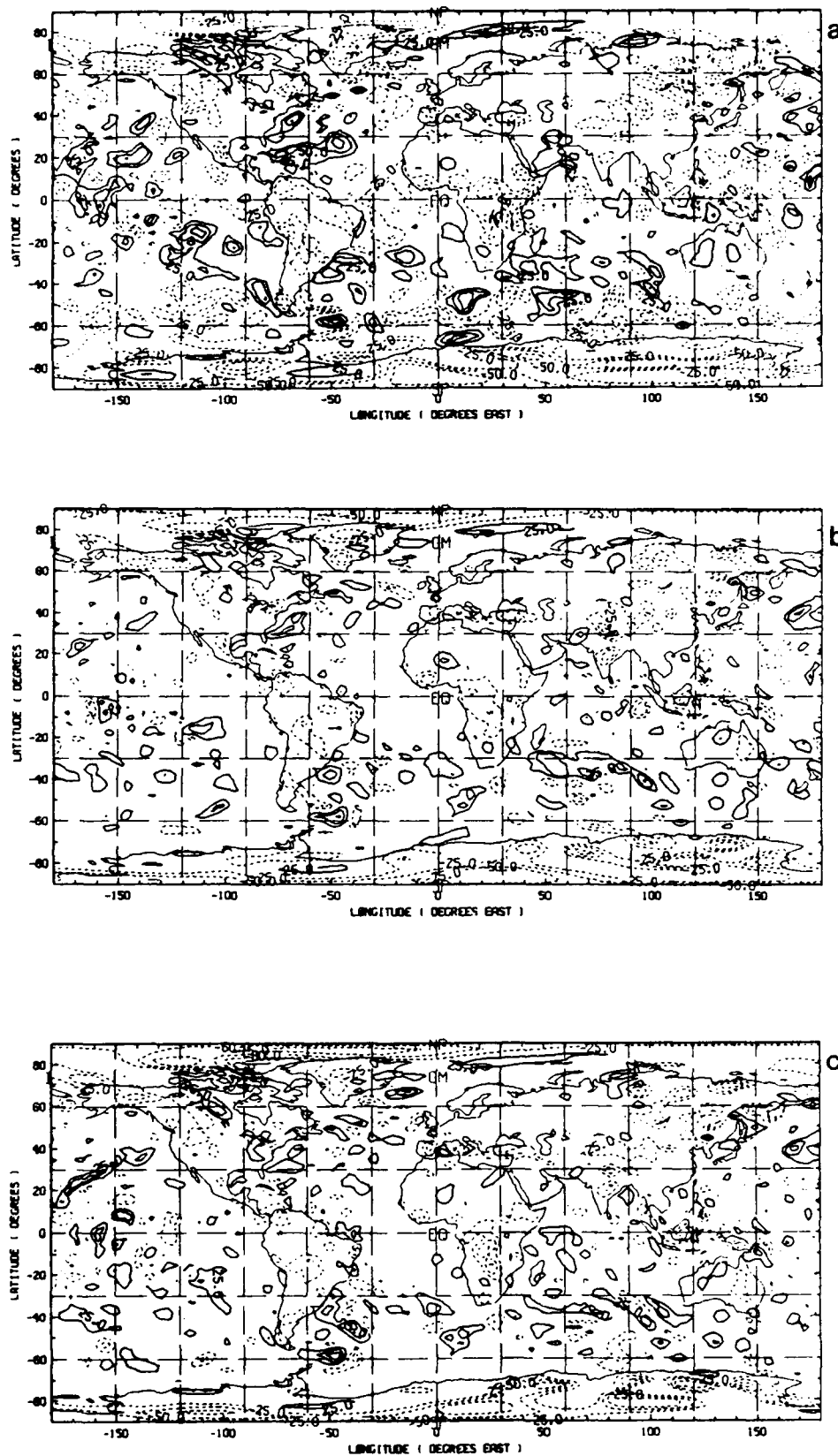


Figure 7.15 Analysis error for 850 mb relative humidity valid 00 GMT 23 November. (a) STATSAT, (b) SSMSAT, (c) SSM+TOVS. Contour interval is 25% with zero line omitted. Negative values are dashed.

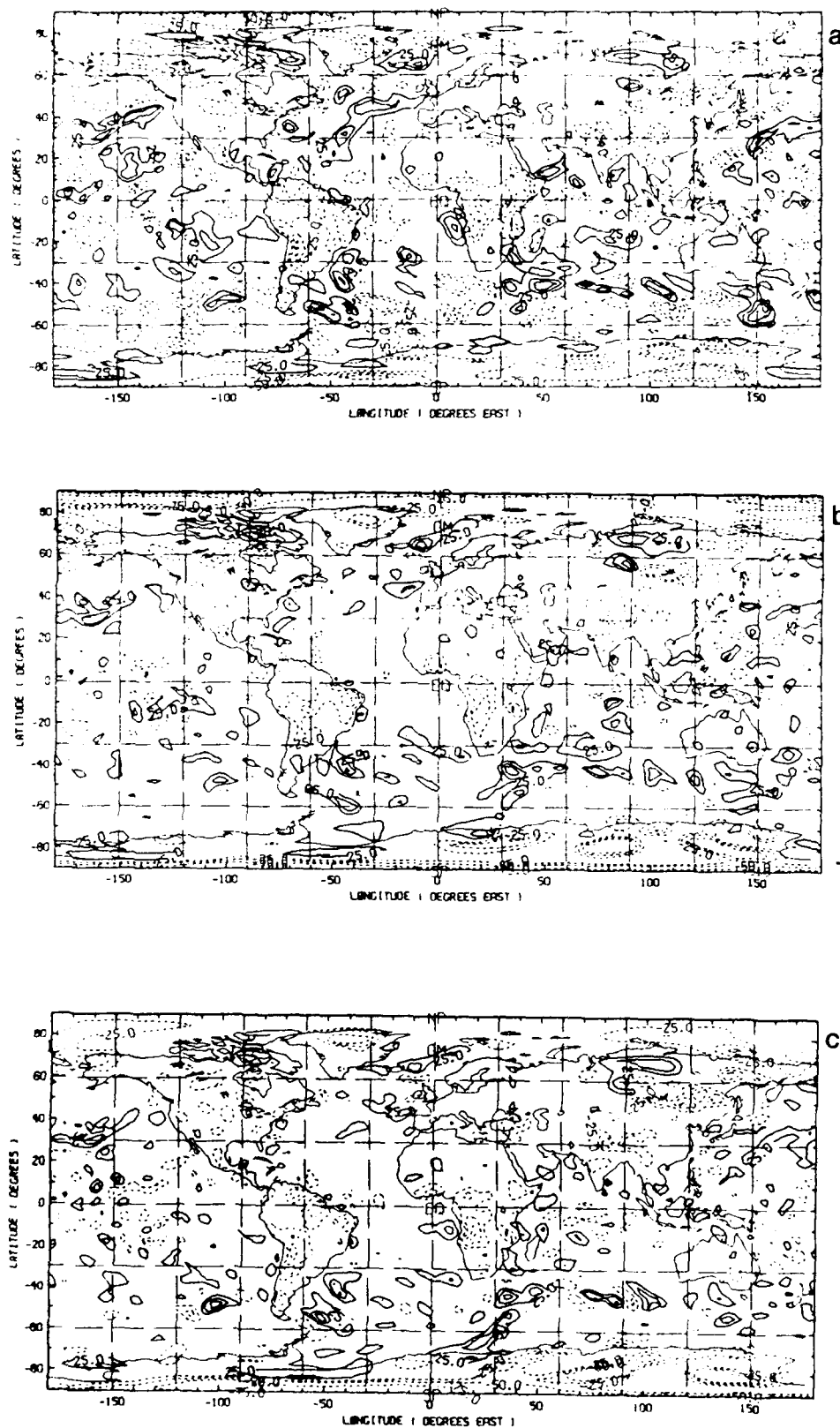


Figure 7.16 Analysis error for 850 mb relative humidity valid 00 GMT 25 November. Format is as in Fig. 7.15.

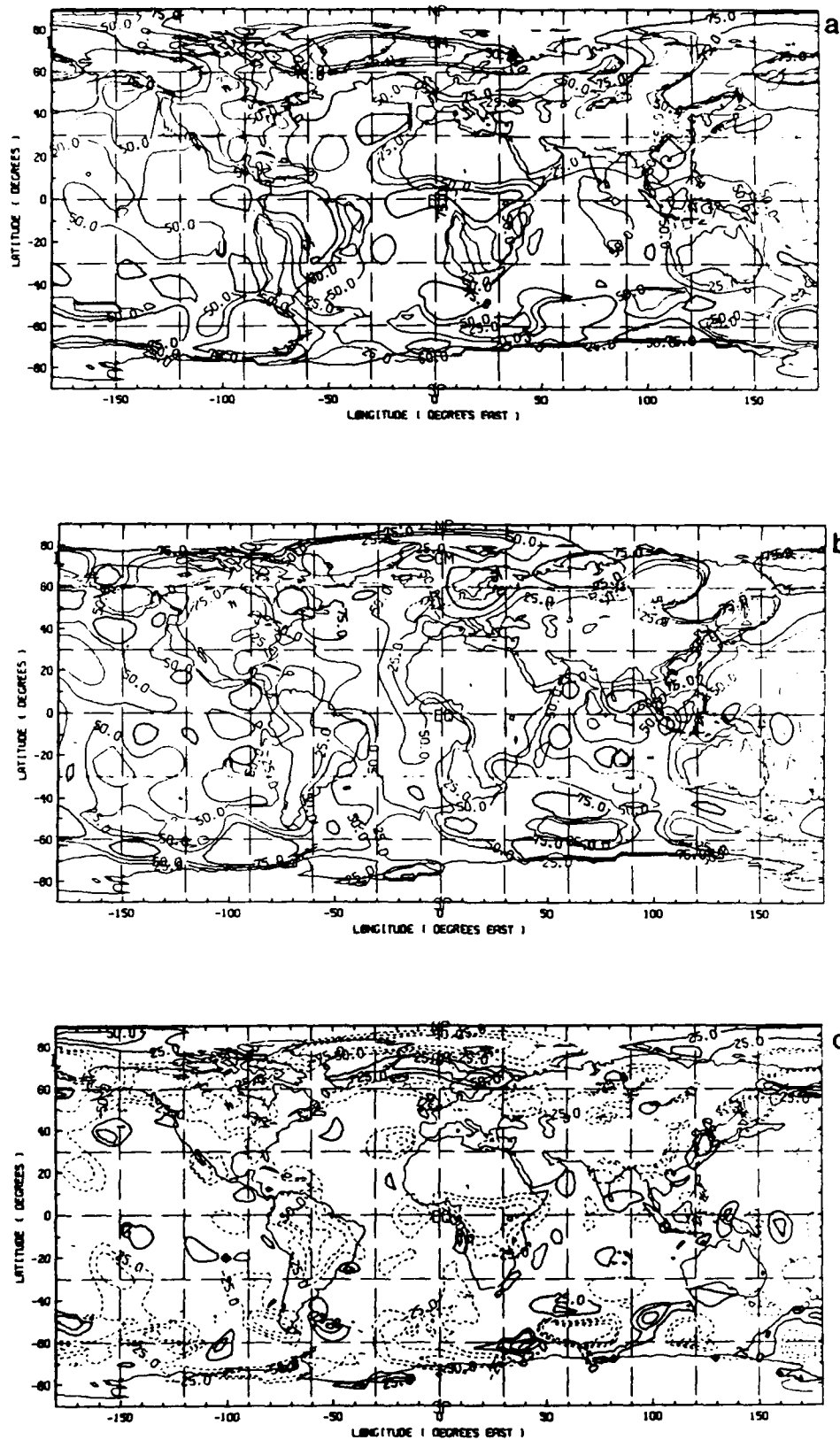


Figure 7.17 Inferred low cloud cover from relative humidity valid 00 GMT 25 November. (a) Nature, (b) STATSAT analysis, (c) STATSAT - Nature. Contour interval is 25% with zero line omitted. In difference field, negative values are dashed.

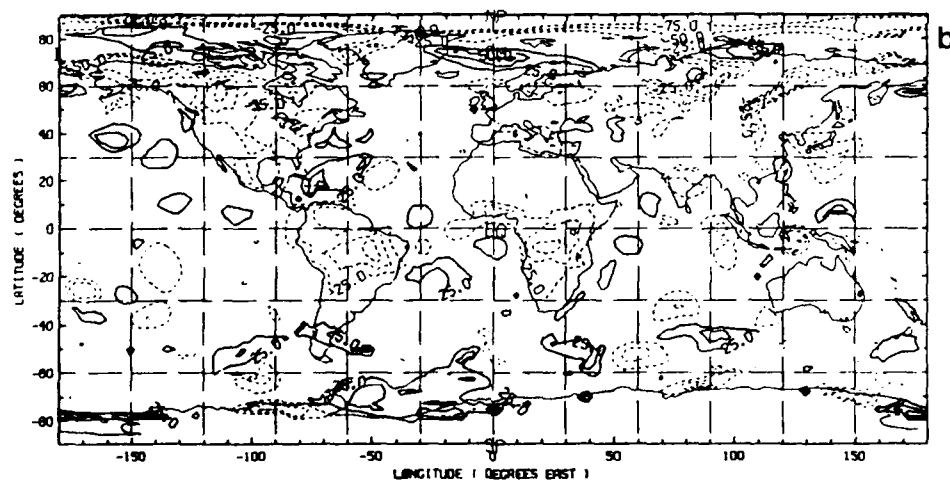
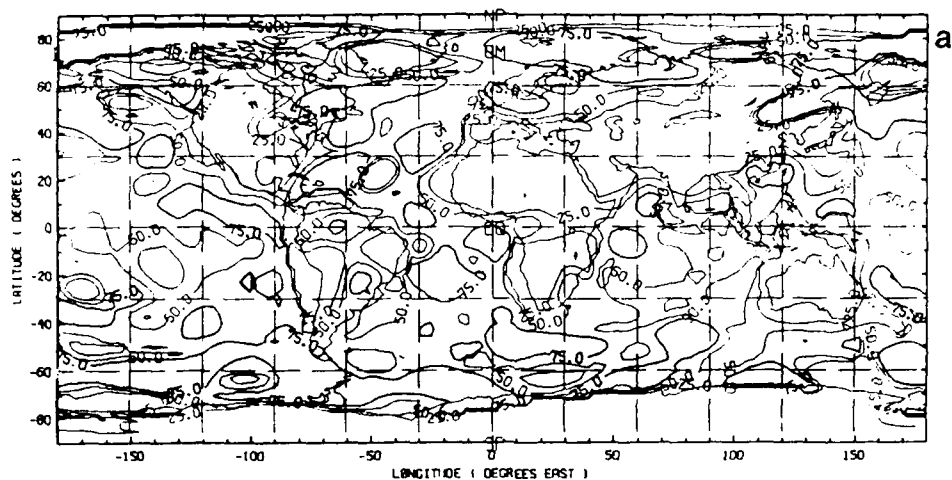


Figure 7.18 Inferred low cloud cover from relative humidity valid 00 GMT 25 November. (a) SSMSAT analysis, (b) SSMSAT - Nature. Contour interval is 25% with zero line omitted. In difference field, negative values are dashed.

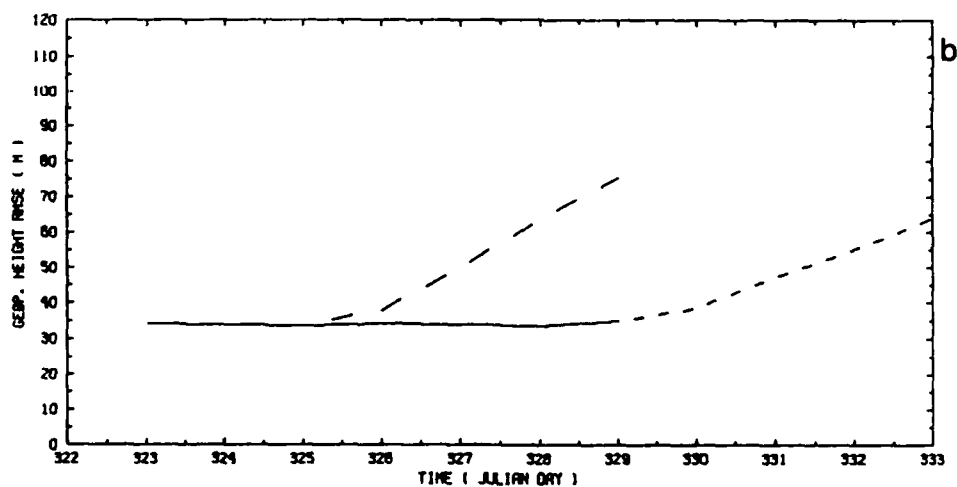
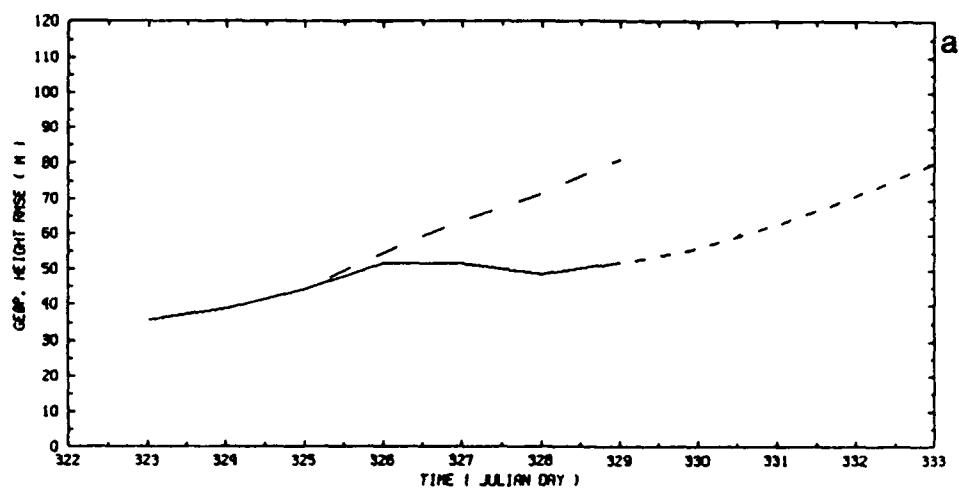


Figure 7.19 Rms height errors at 500 mb. (a) NOSAT, (b) STATSAT, (c) SSMSAT, (d) SSM+TOVS. Analysis errors are shown in solid curves, forecast errors in dashed curves. Julian day 322 corresponds to 00 GMT 18 November.

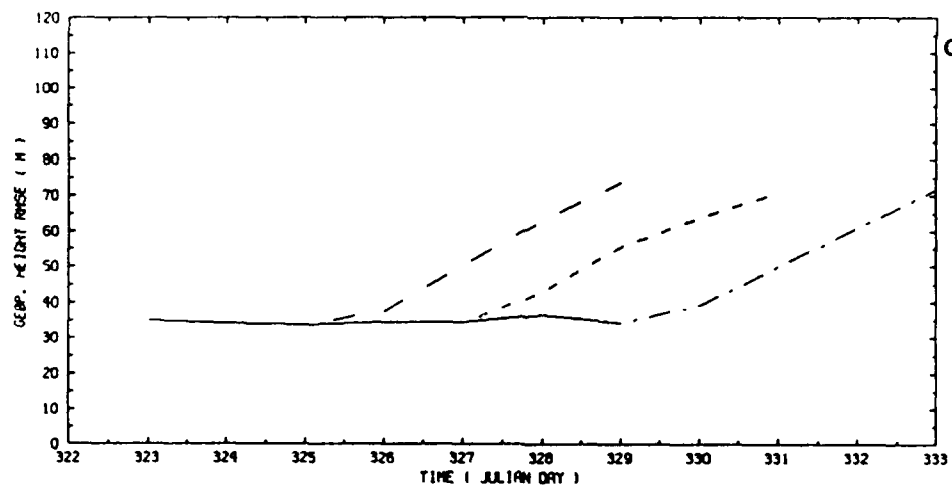
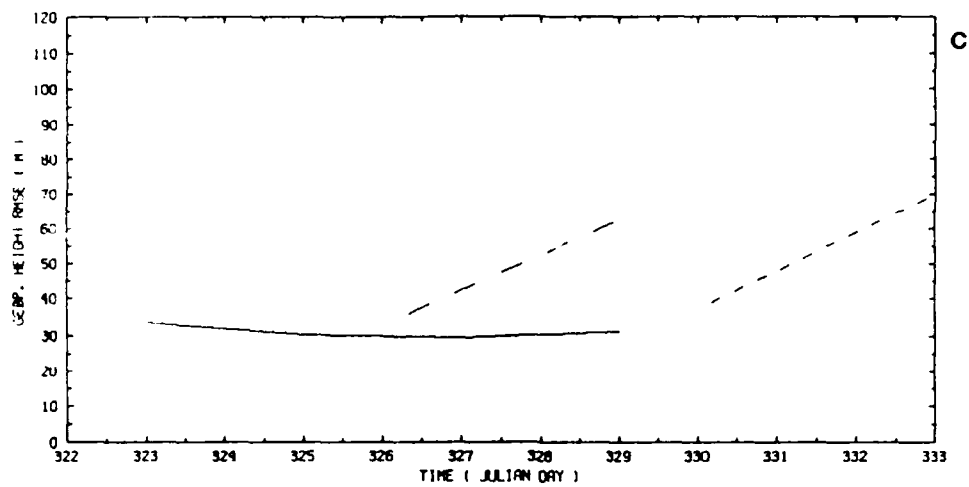


Figure 7.19 (continued).

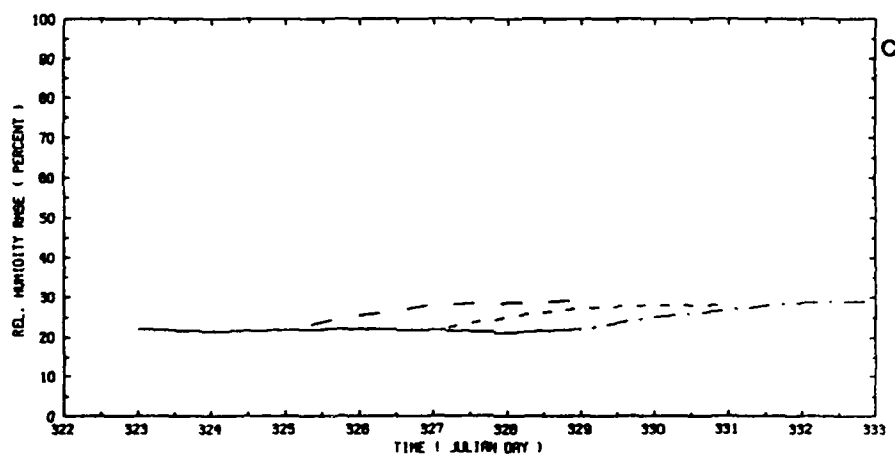
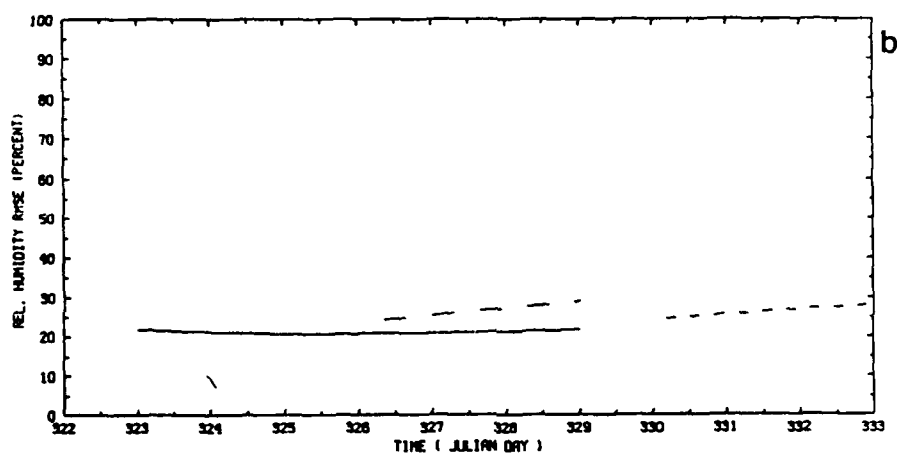
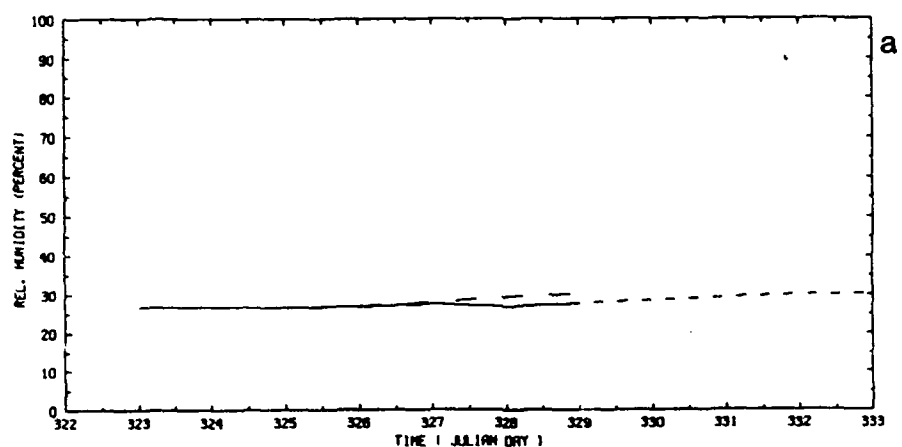


Figure 7.20 Global rms analysis/forecast errors for 850 mb relative humidity. (a) STATSAT, (b) SSMSAT, (c) SSM+TOVS. Solid curves denote analysis, broken curves are forecasts.

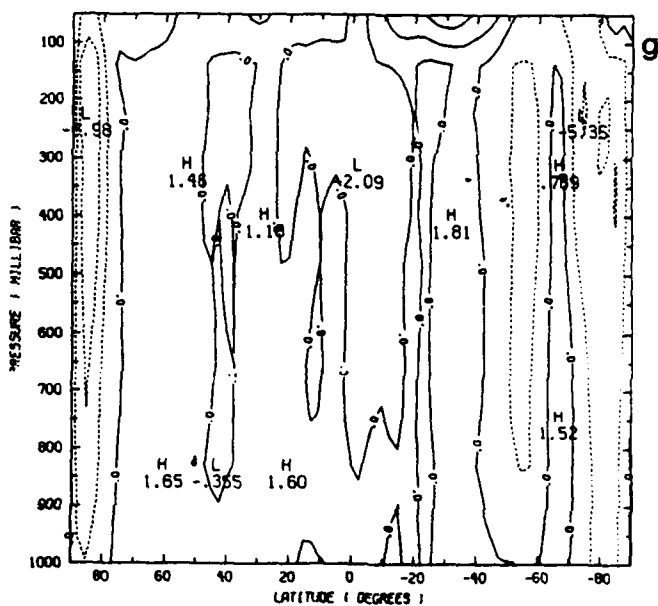
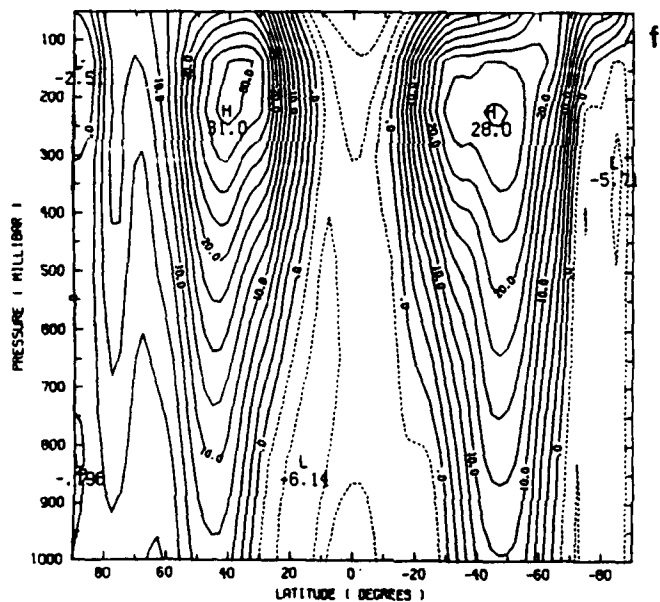
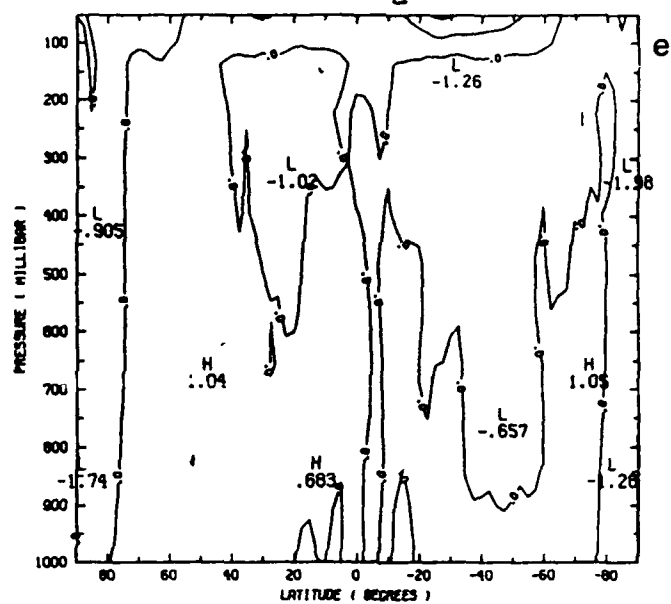
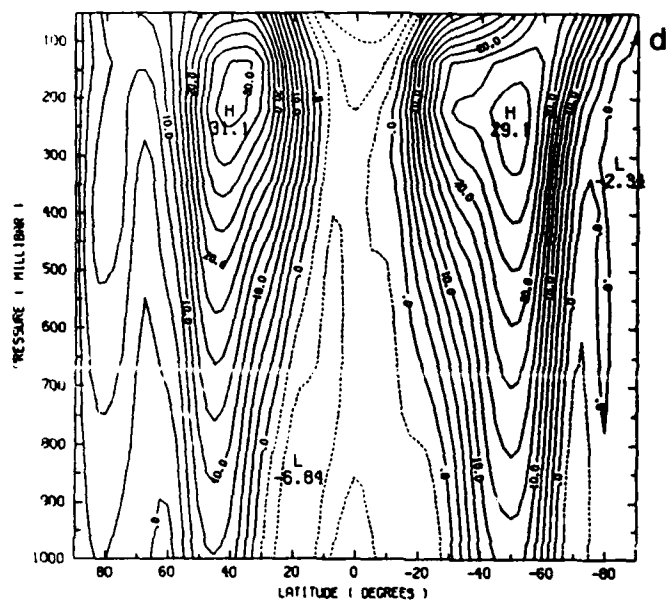


Figure 7.21 (continued).

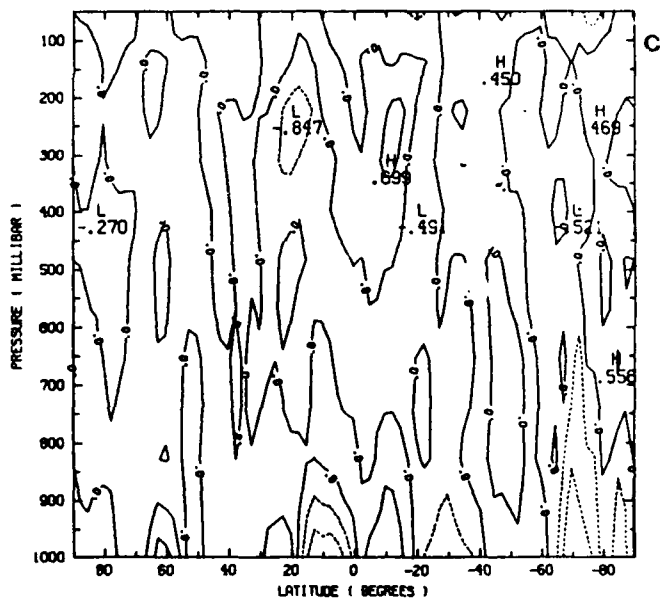
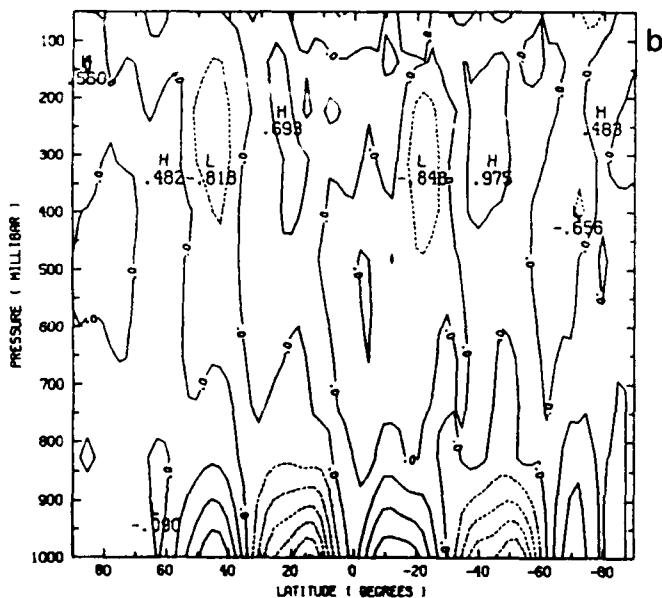
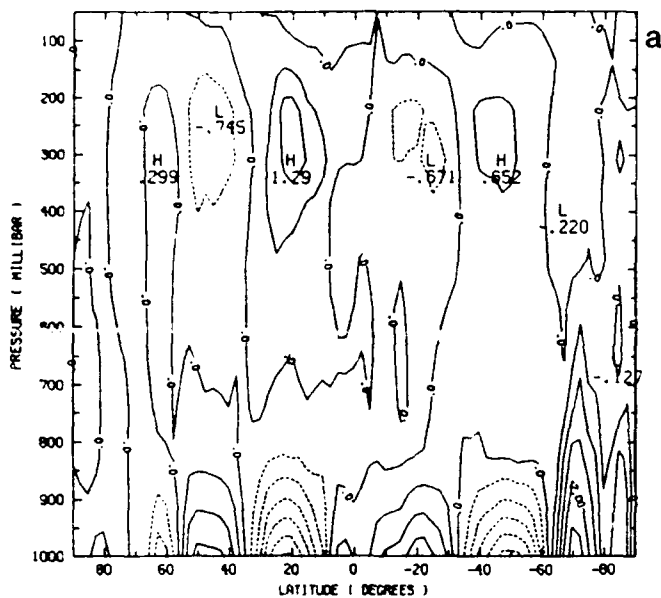


Figure 7.22 Zonal time averaged v component of wind. (a) Nature, (b) STATSAT, (c) STATSAT - Nature, (d) WINDSAT, (e) WINDSAT - Nature, (f) SSMSAT, (g) SSMSAT - Nature. Contour interval is 0.5 ms^{-1} , negative values are dashed.

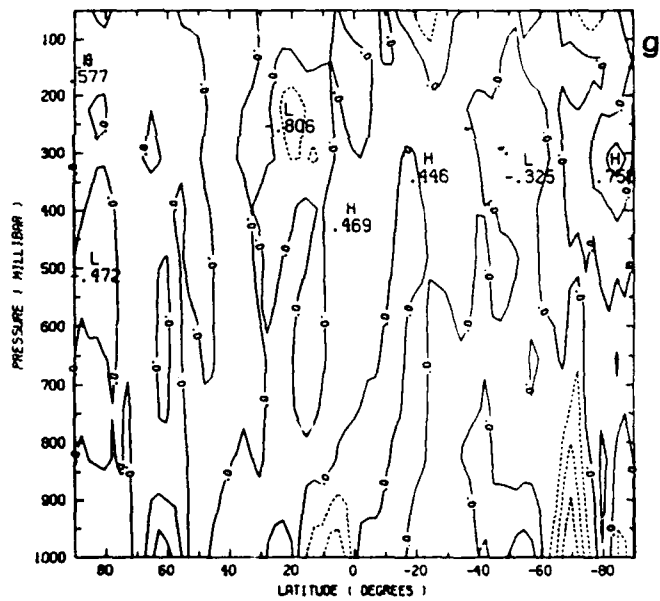
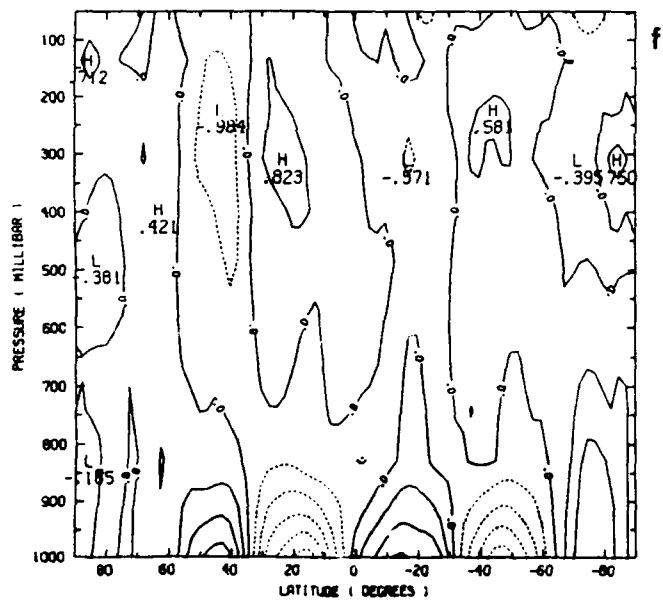
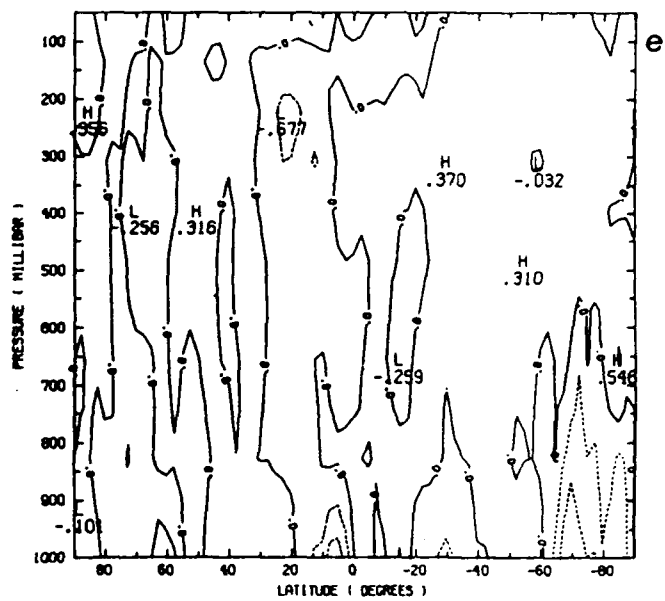
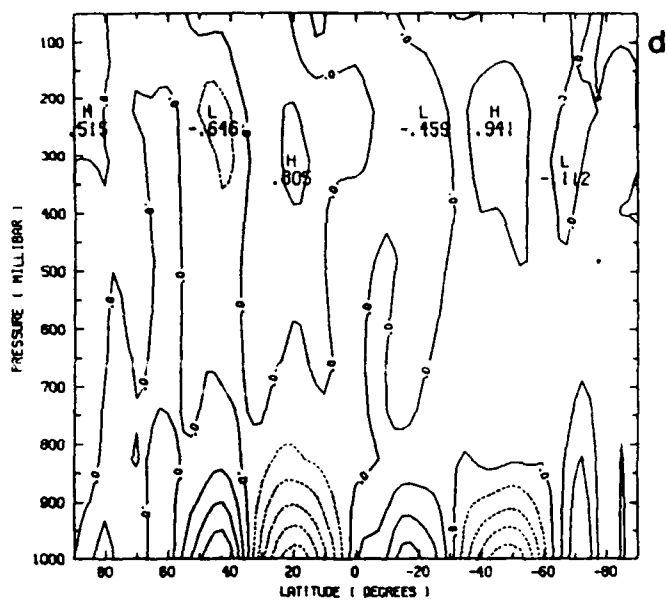


Figure 7.22 (continued).

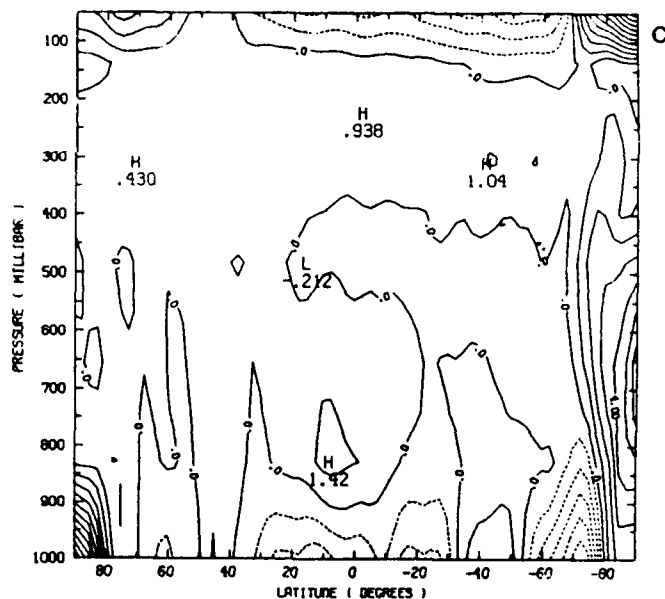
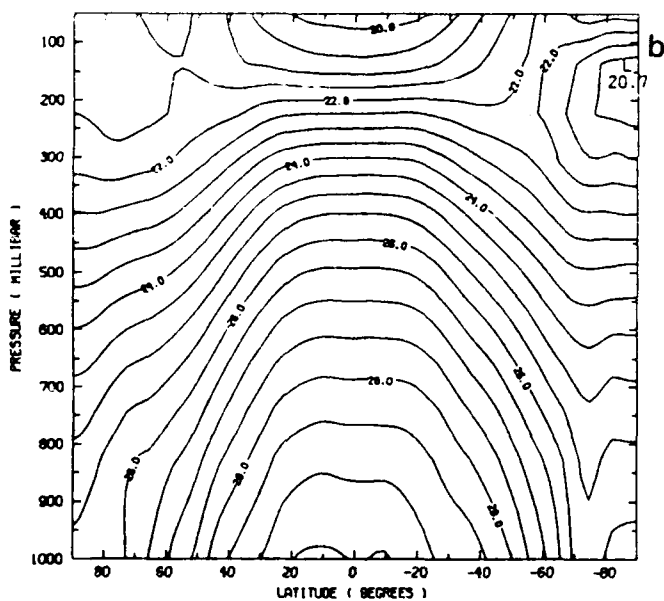
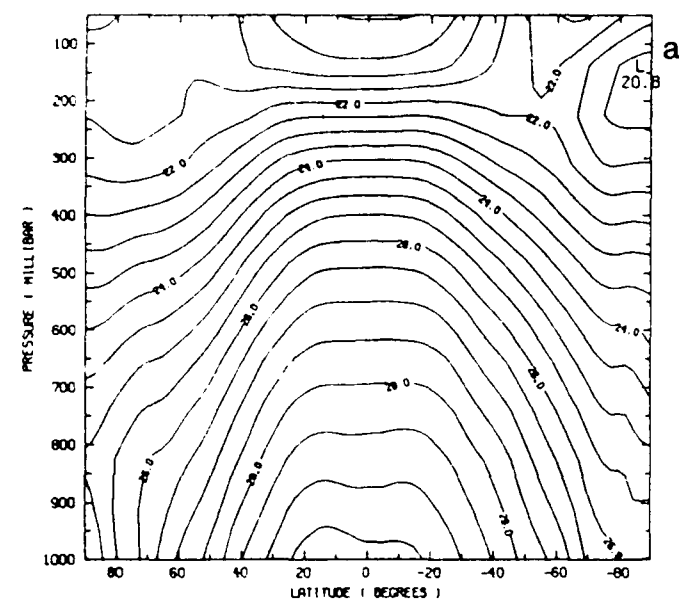


Figure 7.23 Zonal time averaged temperature. (a) Nature, (b) STATSAT, (c) STATSAT - Nature, (d) WINDSAT, (e) WINDSAT - Nature, (f) SSMSAT, (g) SSMSAT - Nature. In analyses, values (in K) have been multiplied by 0.1, contour interval 0.5 (K/10). In differences values are unscaled, contour interval is 1K.

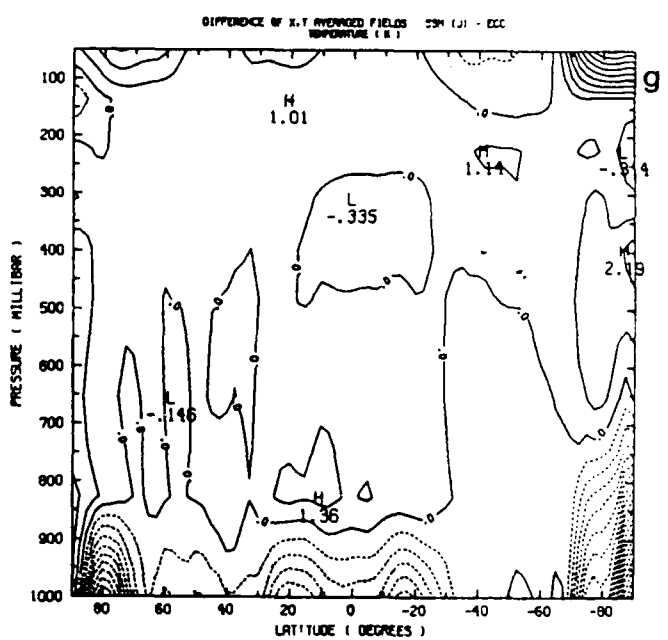
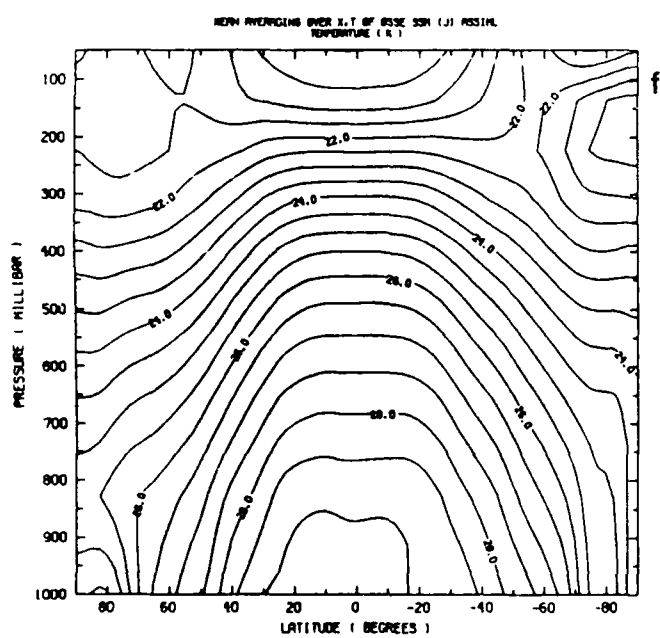
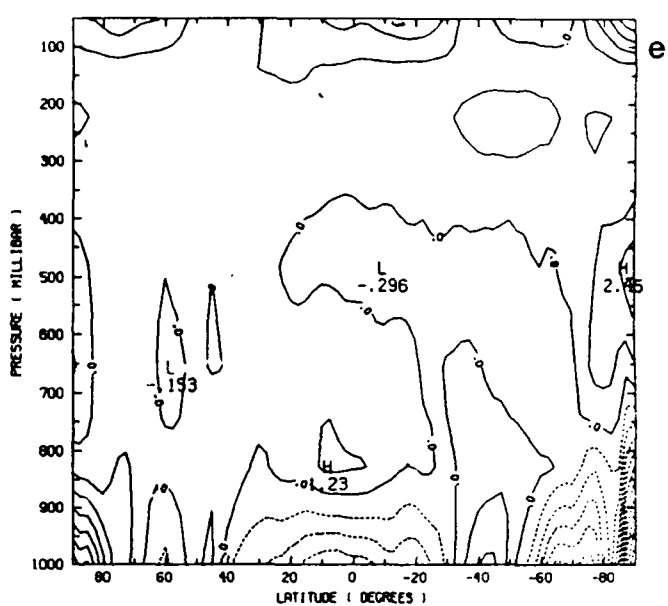
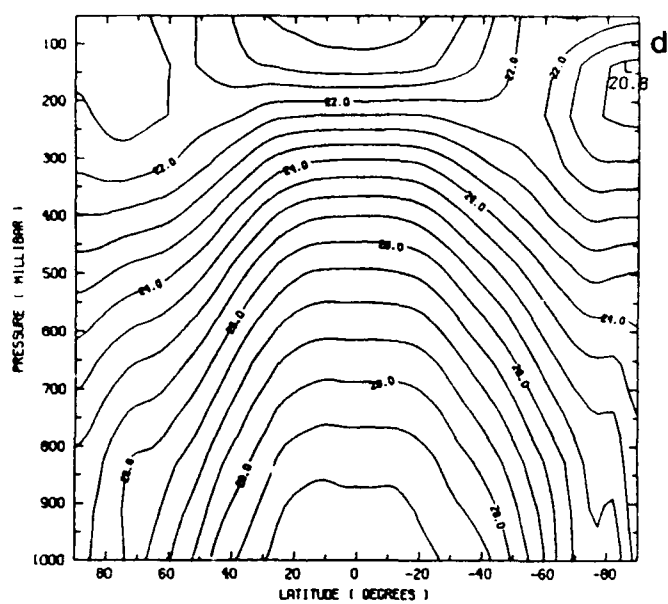


Figure 7.23 (continued).

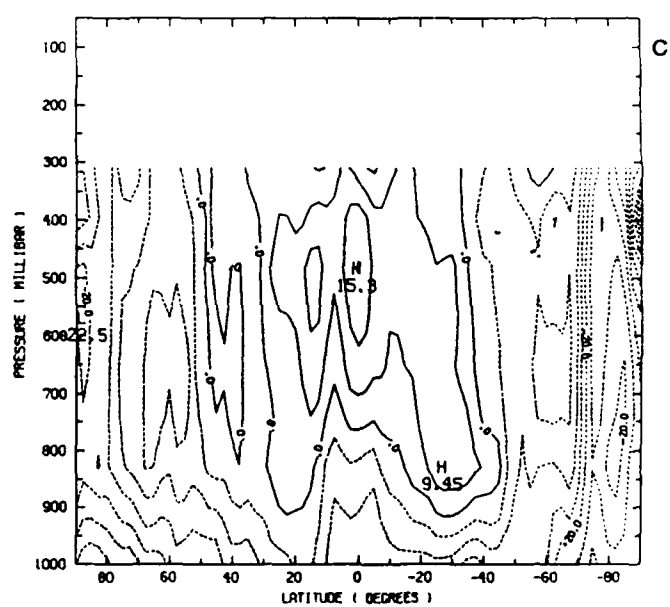
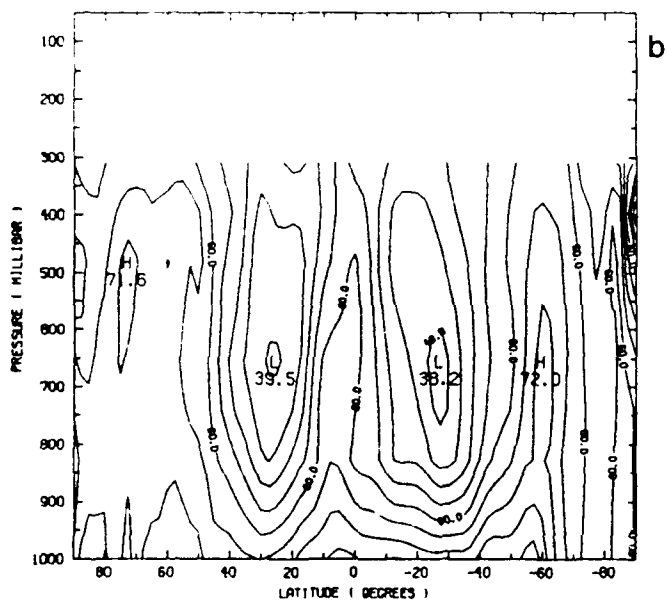
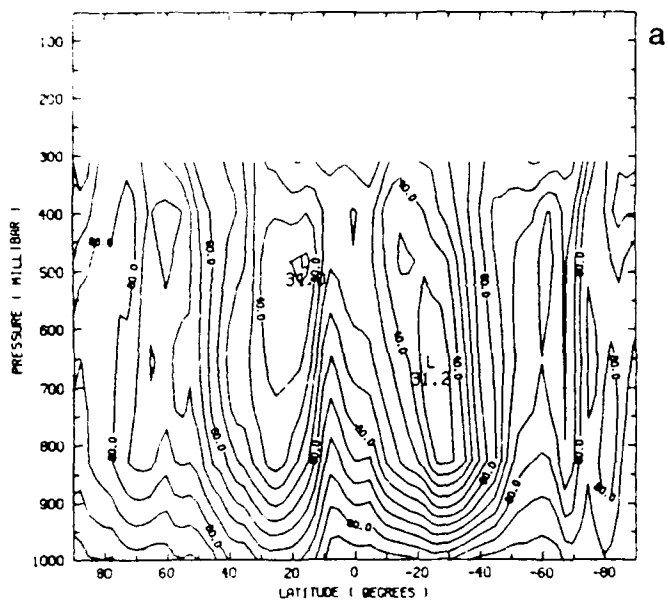


Figure 7.24 Zonal time averaged relative humidity. (a) Nature, (b) STATSAT, (c) STATSAT - Nature, (d) WINDSAT, (e) WINDSAT - Nature, (f) SSMSAT, (g) SSMSAT - Nature. Contour interval is 5 percent. negative values are dashed.

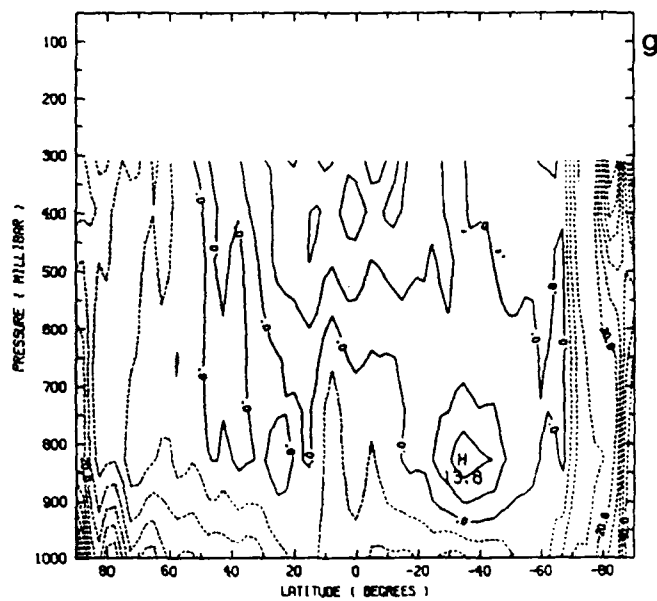
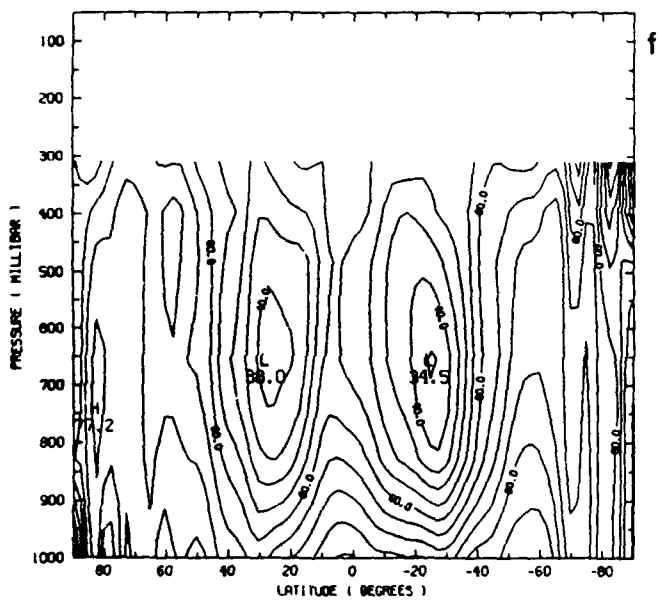
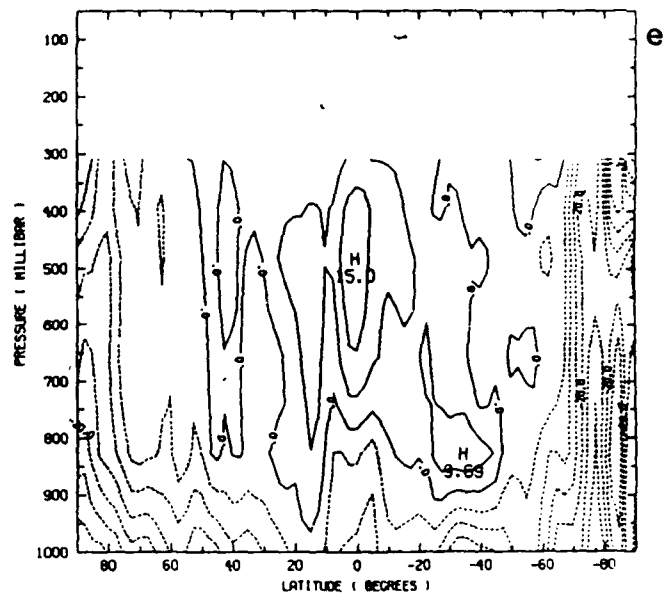
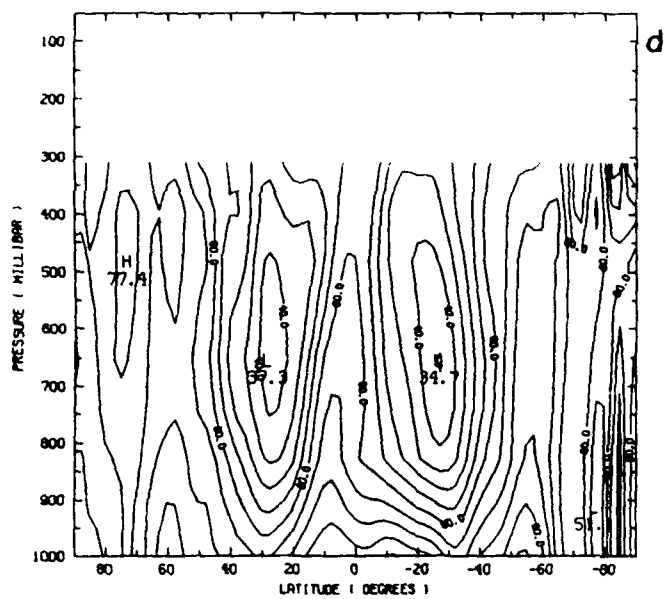


Figure 7.24 (continued).

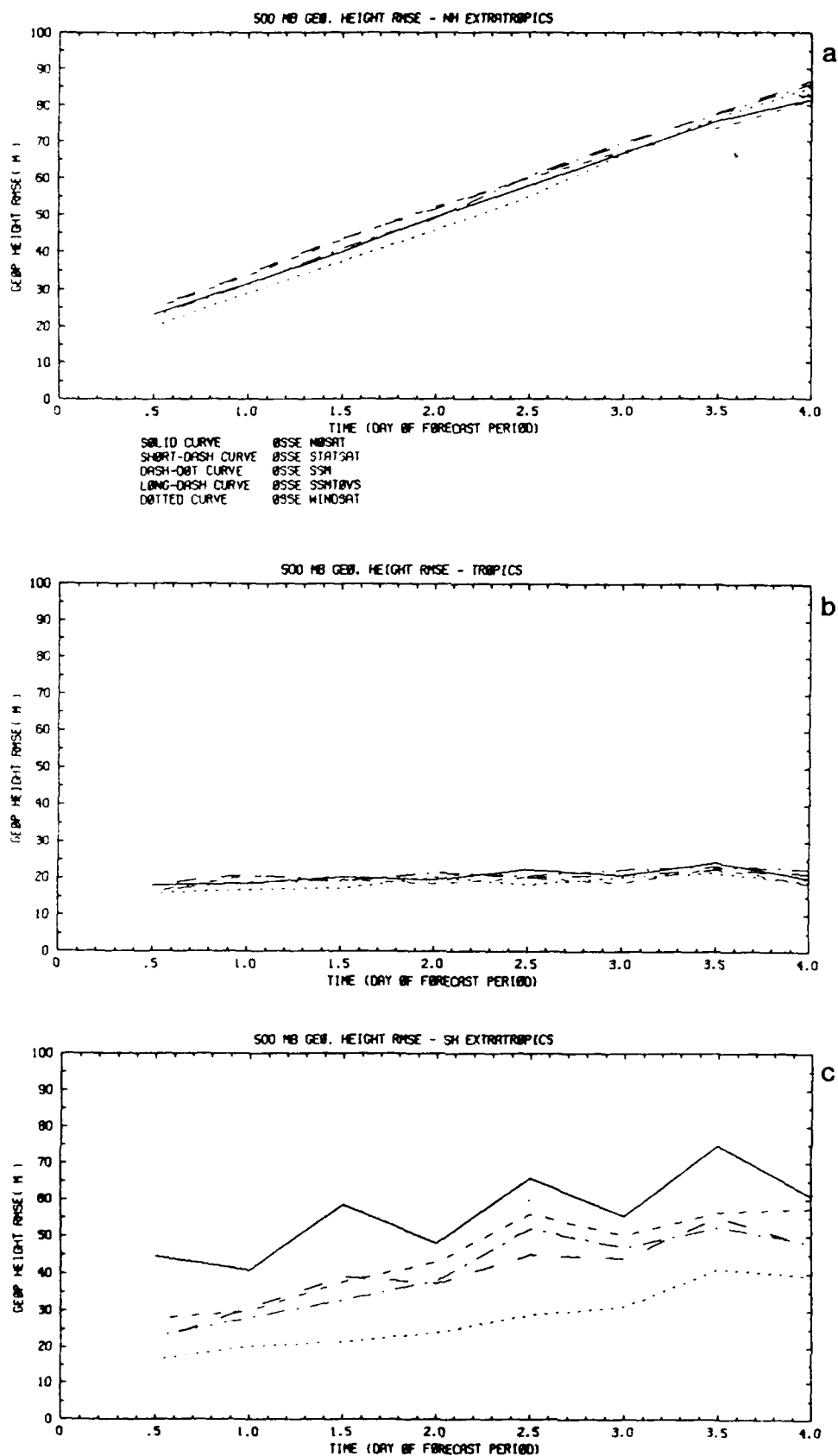


Figure 7.25 Forecast rms error growth, 500 mb height. (a) Northern hemisphere extratropics, (b) Tropics, (c) Southern hemisphere extratropics.

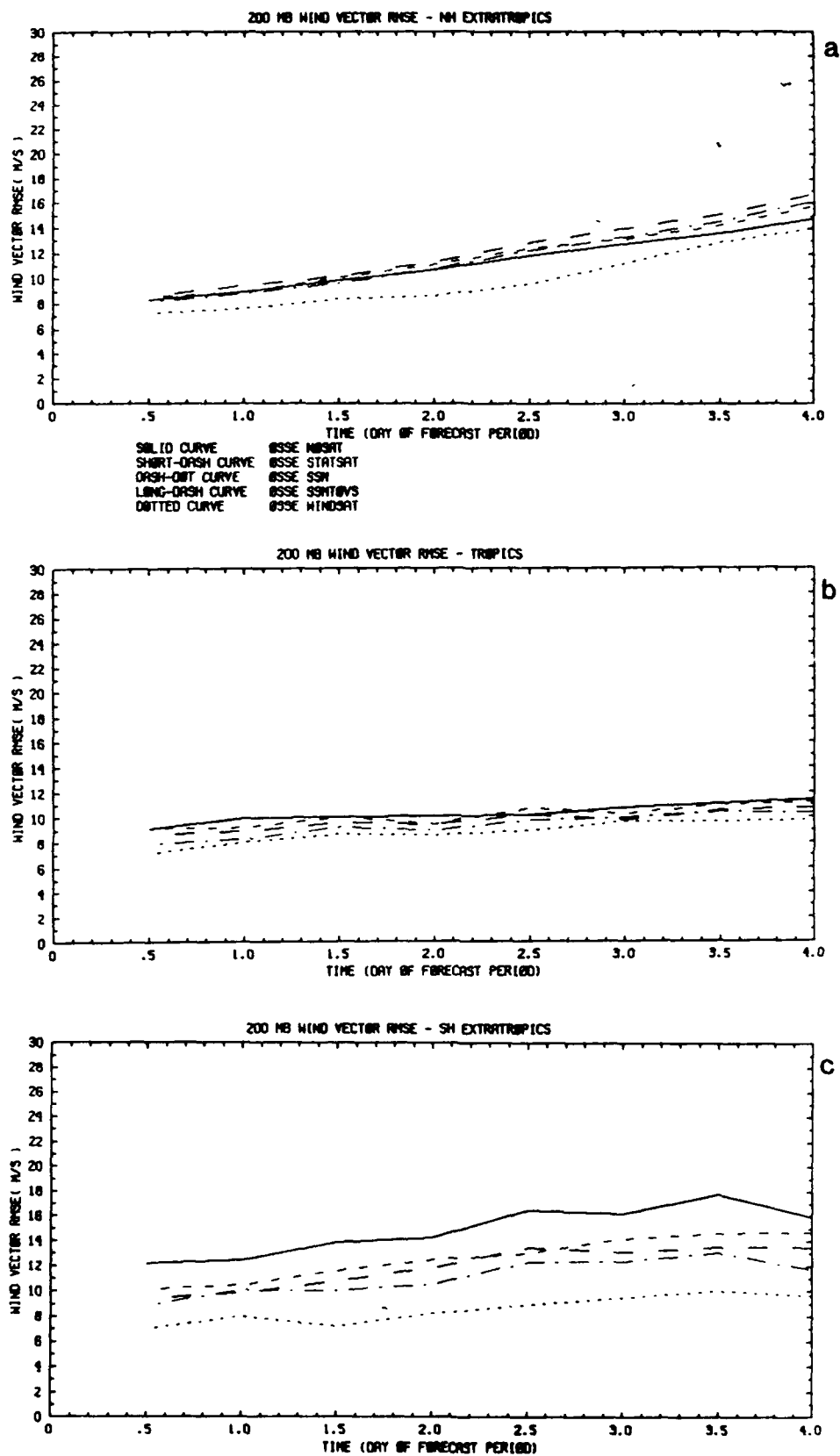


Figure 7.26 Forecast rms error growth, 200 mb wind vector. (a) Northern hemisphere extratropics, (c) Southern hemisphere extratropics.

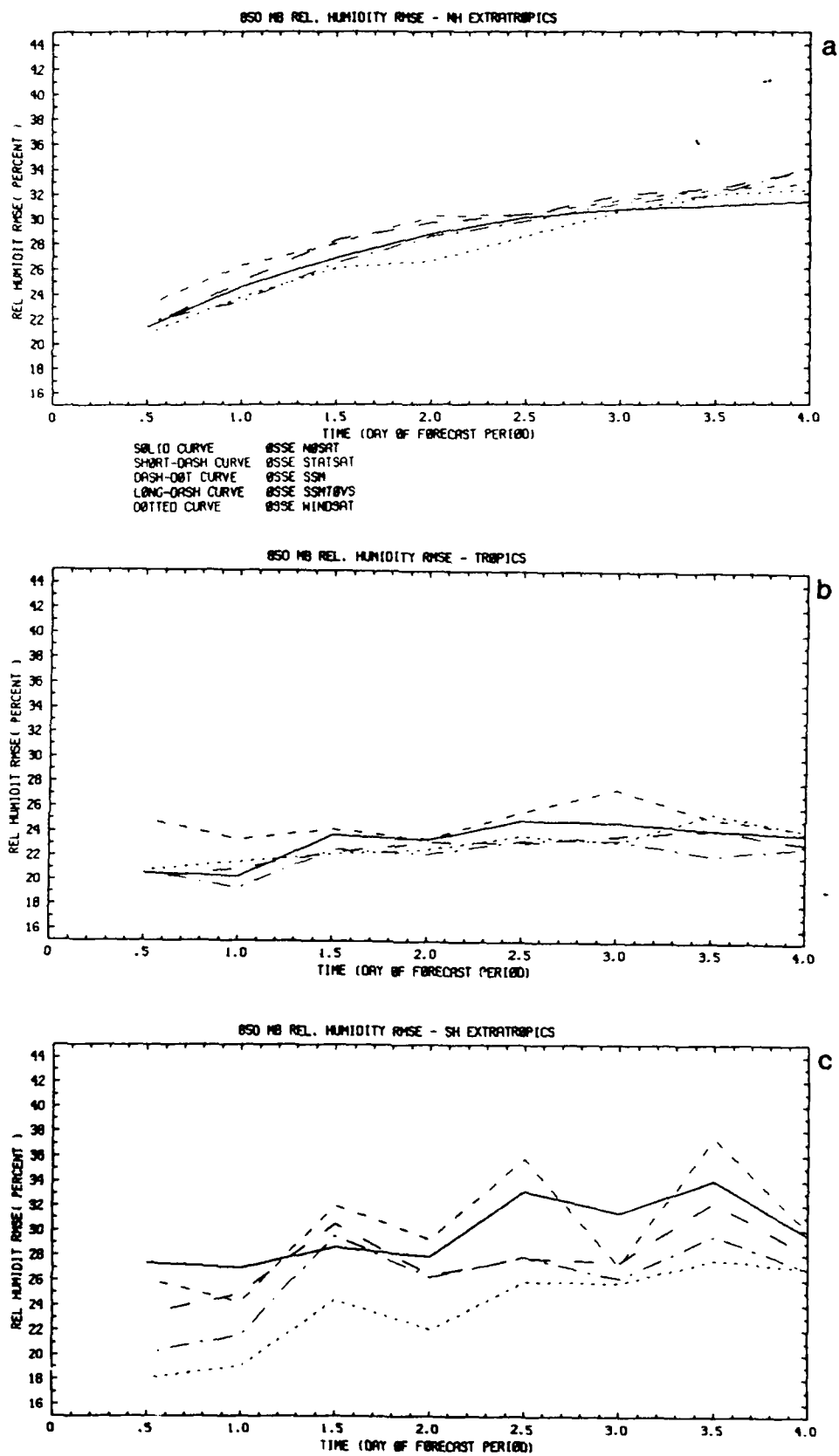


Figure 7.27 Forecast rms error growth, 850 mb relative humidity.
 (a) Northern hemisphere extratropics, (b) Tropics, (c) Southern hemisphere extratropics.

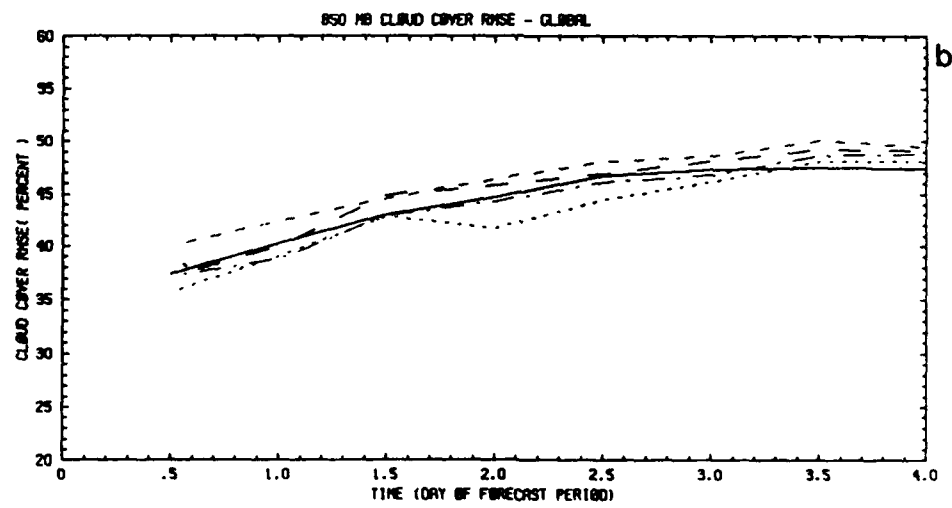
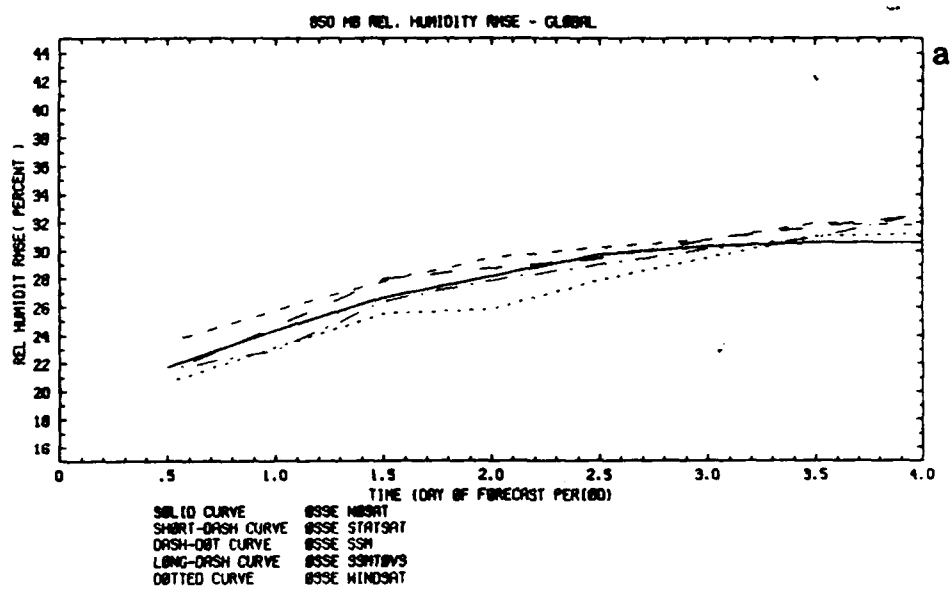


Figure 7.28 Forecast rms error growth. (a) 850 mb relative humidity, global statistics, (b) 850 mb cloud cover, global statistics.

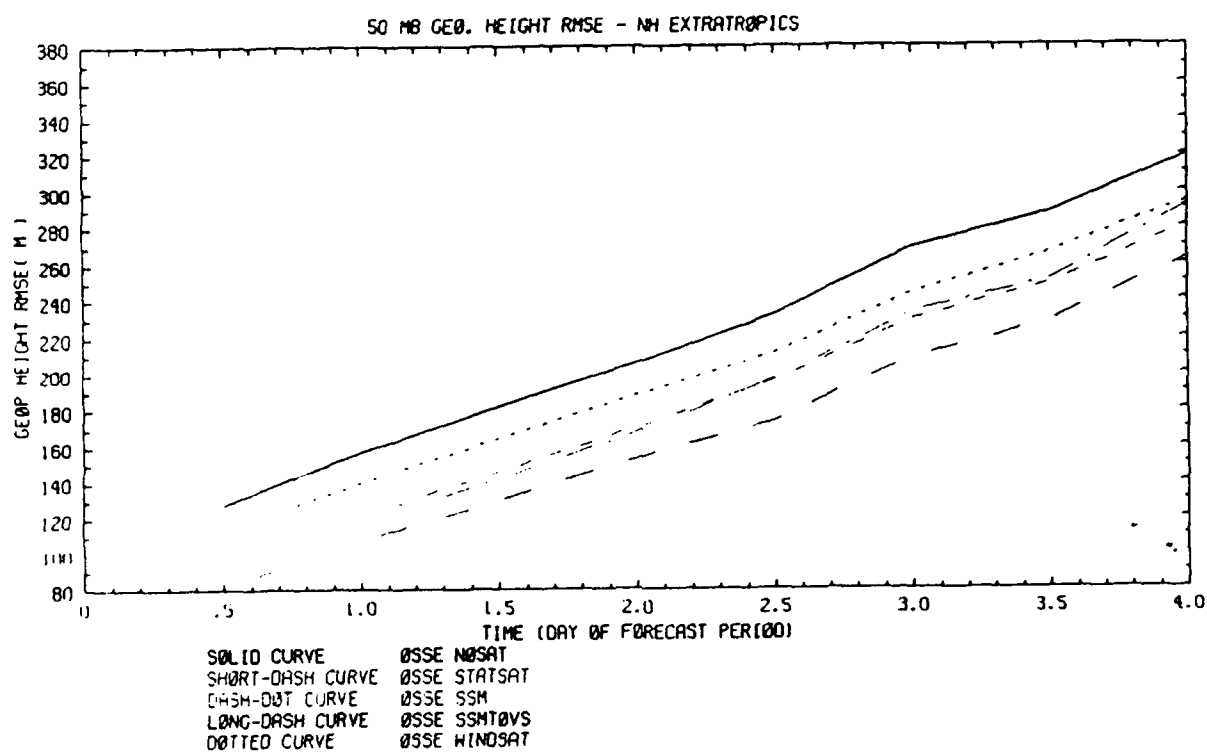


Figure 7.29 Forecast rms error growth, 50 mb height, northern hemisphere extratropics.

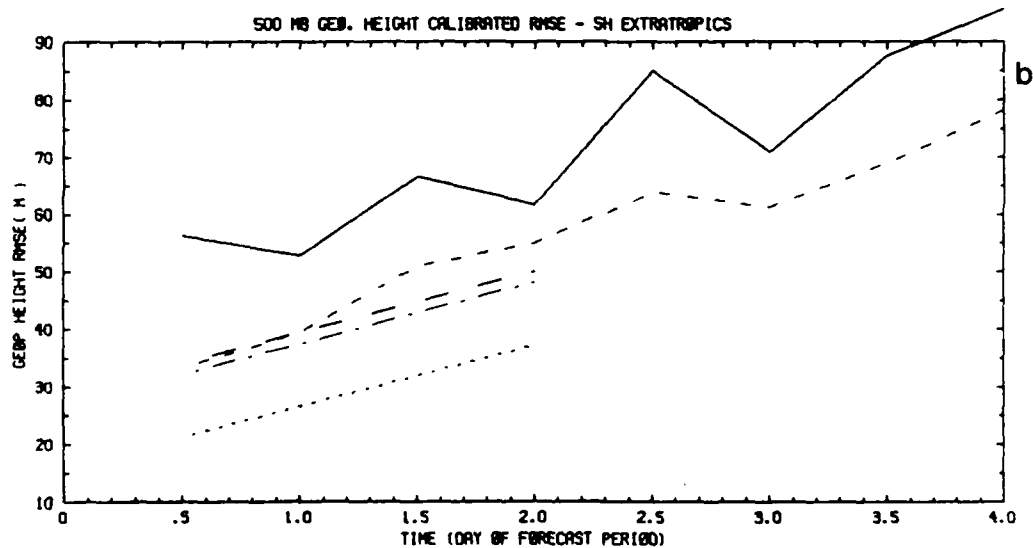
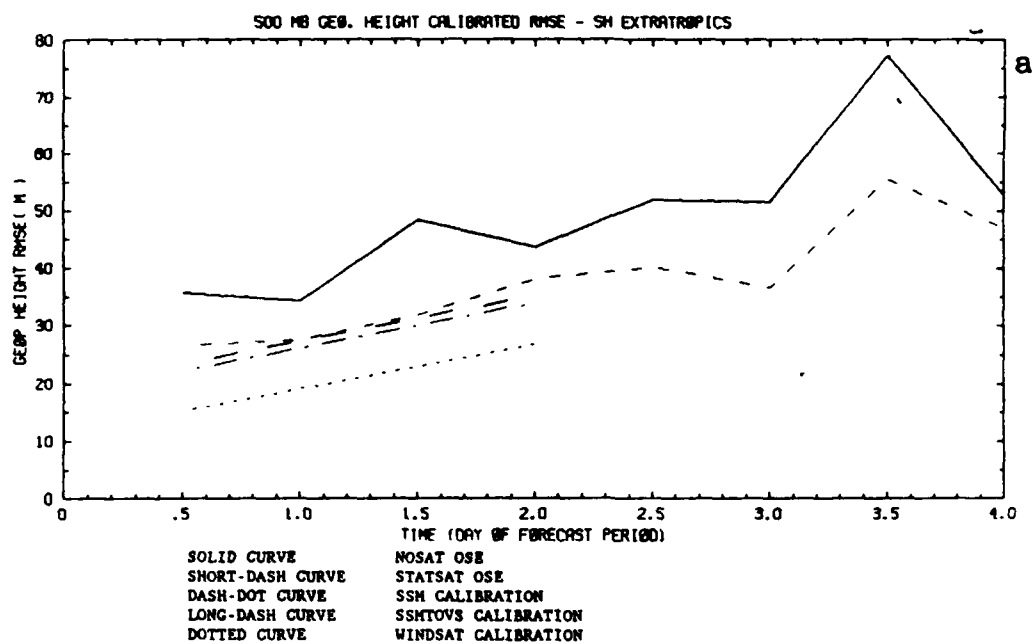


Figure 7.30 Calibrated 500 mb height rms errors for southern hemisphere extratropics. (a) Winter OSEs, (b) Summer OSE's.

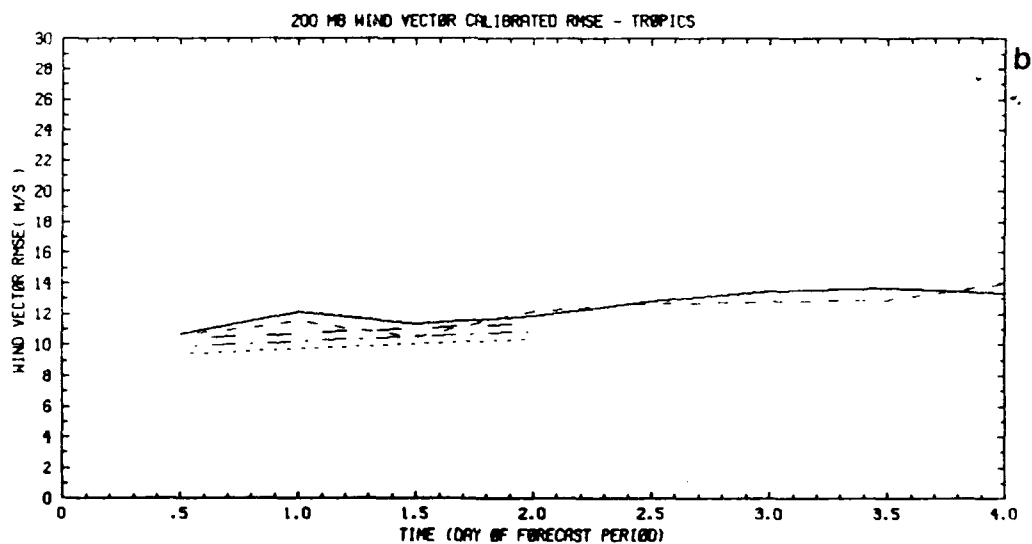
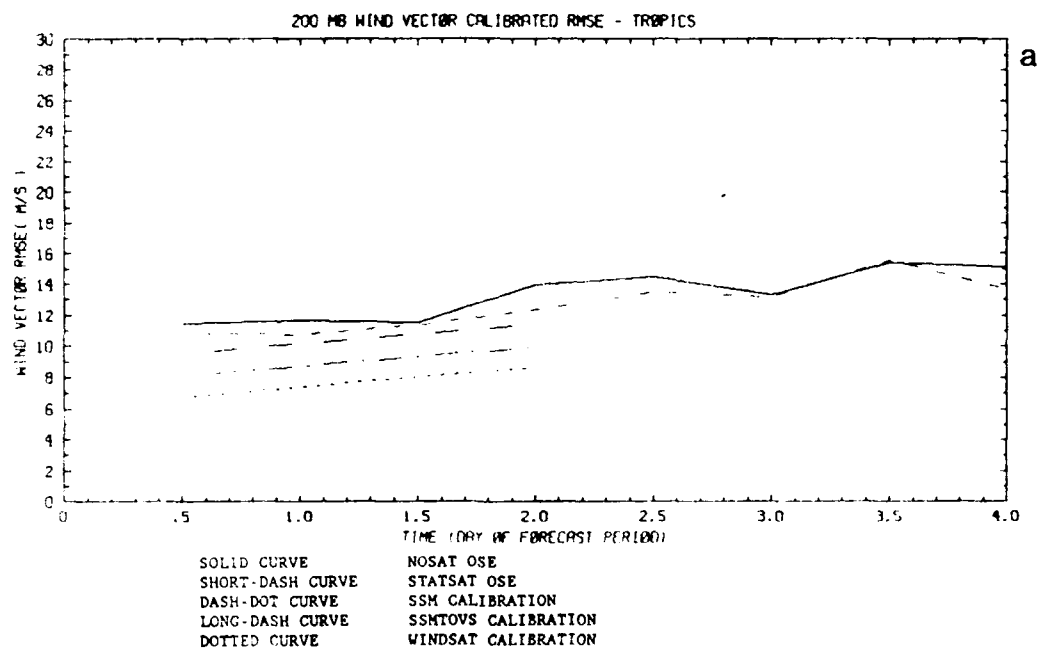


Figure 7.31 Calibrated 200 mb wind vector rms errors for tropics. (a) Winter OSEs, (b) Summer OSEs.

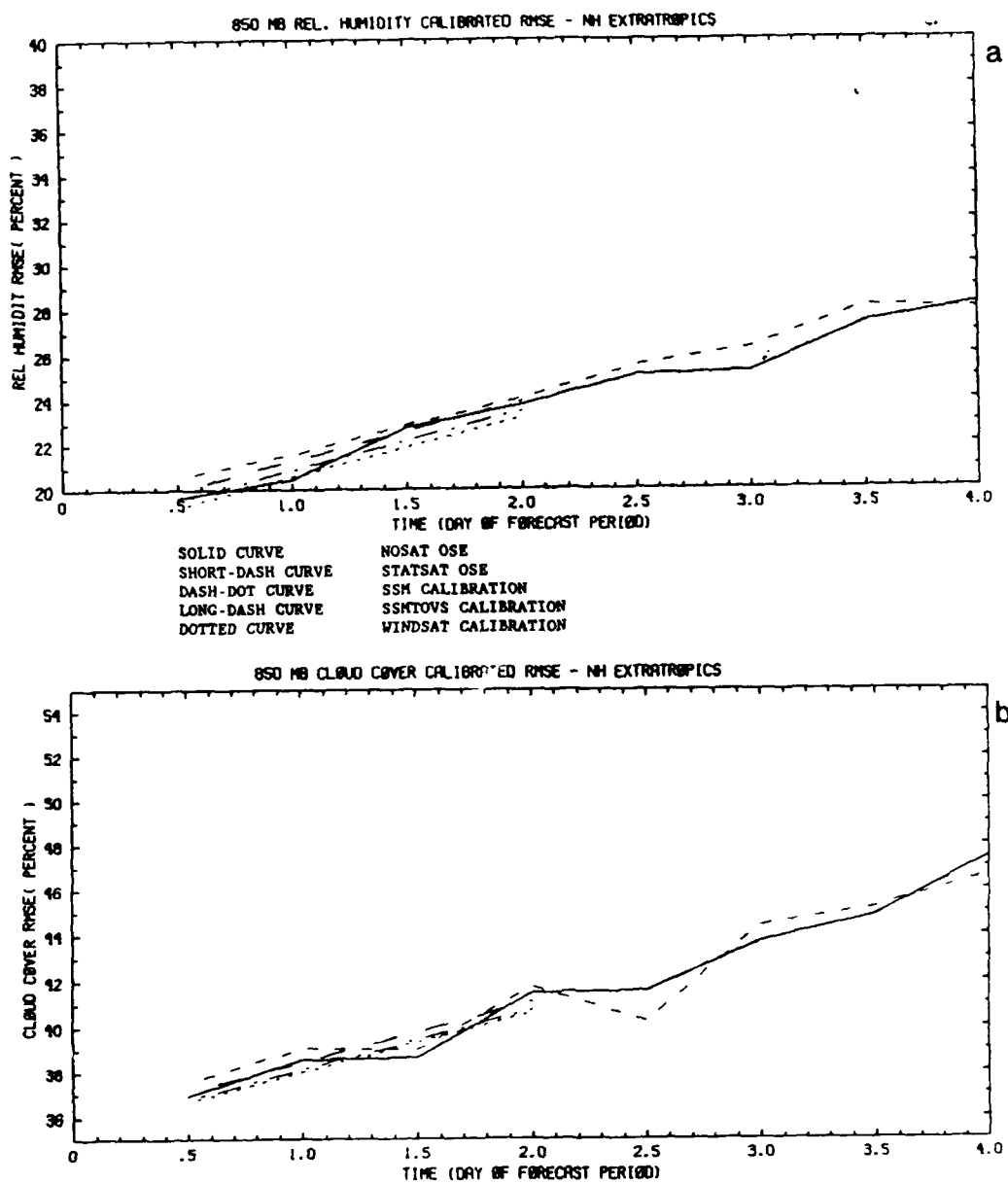


Figure 7.32 Calibrated 850 mb relative humidity summer OSSE rms errors for northern hemisphere extratropics. (a) Relative humidity. (b) Cloud cover.

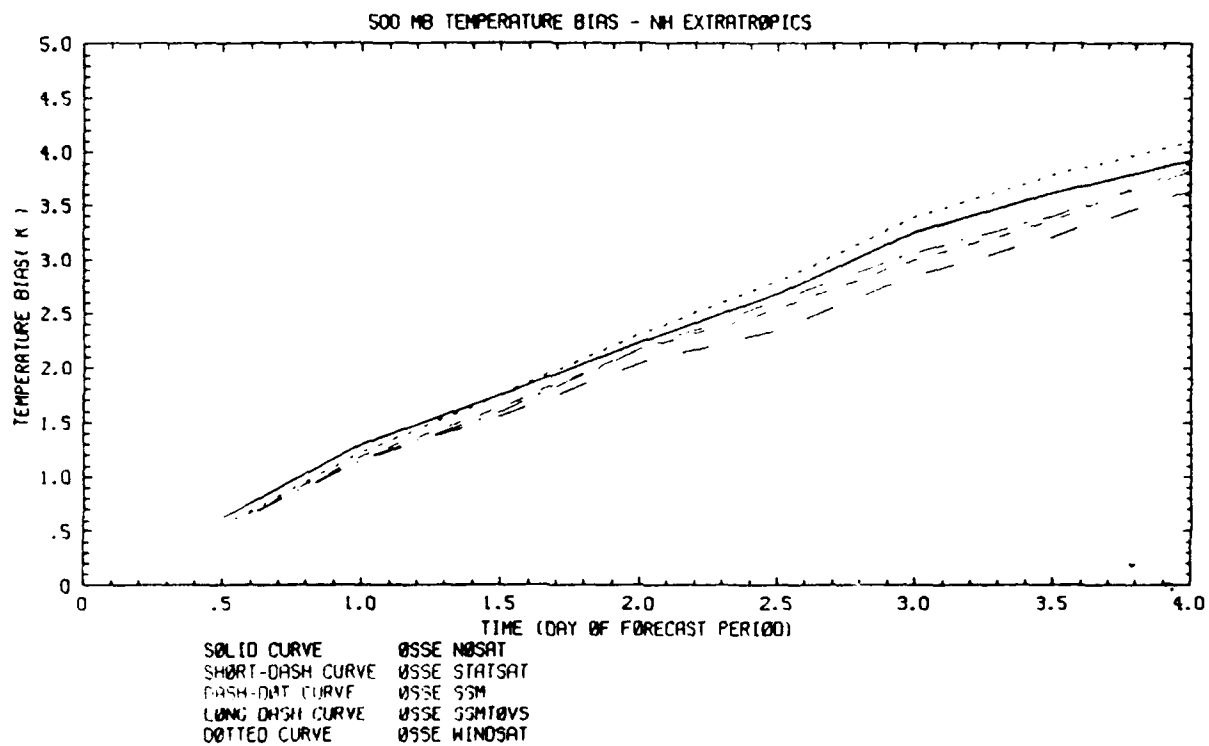


Figure 7.33 Forecast 500 mb temperature bias for northern hemisphere extratropics.

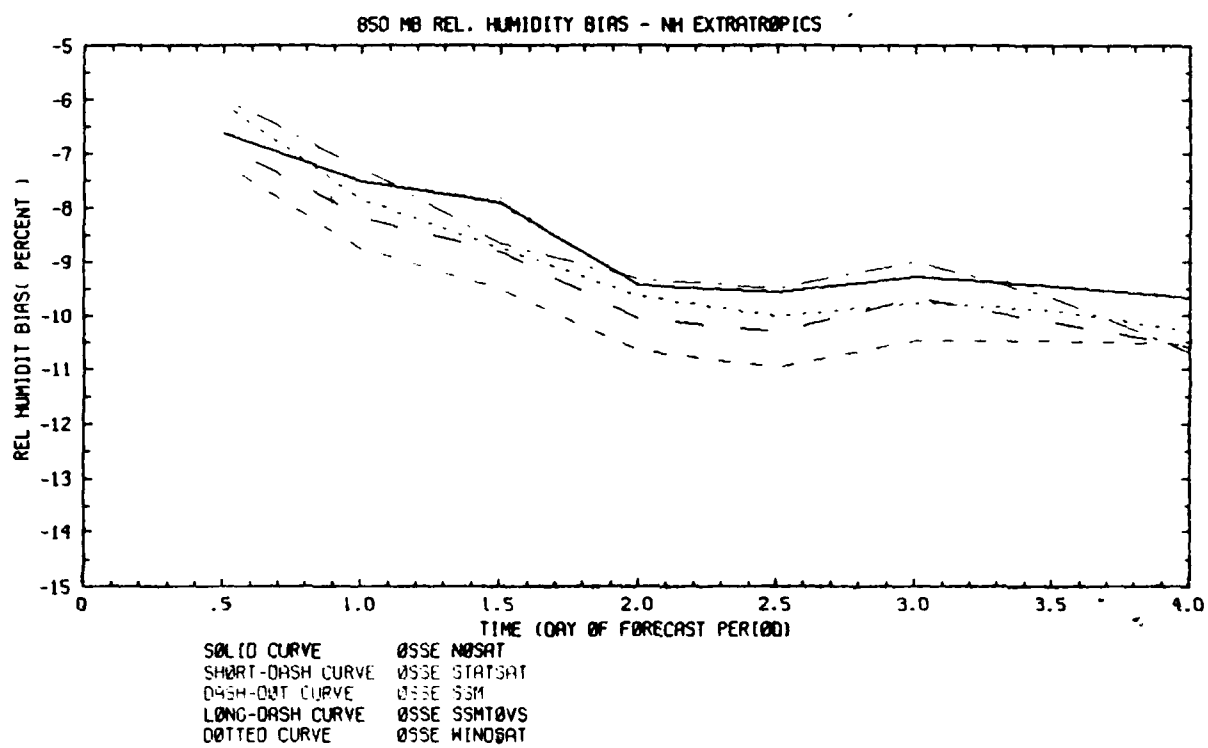


Figure 7.34 Forecast 850 mb relative humidity bias for northern hemisphere extratropics.

8. Summary and Conclusions

The impact of the 183 GHz temperature and RH retrievals on the AFGL GDAS was evaluated by comparing the results of OSSEs using the SSM data instead of (SSMSAT) or in addition to TOVS data (SSM+TOVS) with baseline OSSEs using the full FGE data set (STATSAT) and, for calibration purposes, no satellite data at all (NOSAT). Our principal findings are that the RH forecast errors were slightly affected in the Northern Hemisphere extratropics, but a marked improvement could be seen in the tropics and the Southern Hemisphere extratropics. Interestingly, though, WINDSAT moisture forecasts were superior to SSMSAT in the extratropics, even though only RAOB moisture data were used in WINDSAT, reflecting the dominant role of the mass and wind fields in forcing the moisture field in the extratropics.

Gridpoint to gridpoint comparisons of the OSSE analyses with the corresponding nature data showed the SSMSAT height analyses to be superior to SSTATSAT and SSM+TOVS, when measured in terms of global rms errors. Moisture analyses were clearly improved by the addition of SSM data: rms errors of SSMSAT and SSM+TOVS, which were almost identical, were approximately 5% less than those of SSTATSAT and NOSAT (22% vs. 27%). SSM+TOVS and SSTATSAT had comparable height errors. Weather features were identified by subjective synoptic evaluations which were analyzed better in SSMSAT than SSM+TOVS. The somewhat surprising result that adding TOVS data led to a degradation of the height analyses was caused by a combination of factors, some of which were related to the anchoring of satellite thicknesses, others to data selection and quality control procedures.

Cloud cover estimates derived from the relative humidity fields were too high. Either the model is too moist or the relative humidity to cloud cover algorithm needs to be tuned. In any case, cloud cover differences or comparisons are still useful since all relative humidity fields converted to cloud cover will be too cloudy in the same way. The comparisons of rms differences of cloudiness yield the same results as comparisons of rms differences of relative humidity. This might have been expected in view of the facts that the statistics calculated the averages over large samples and that the relative humidity to cloud cover relationship is simple. This relationship is nonlinear but it is 1-to-1 and monotonic and it does not depend on any other model parameters known to impact cloudiness such as

temperature lapse rates, vertical wind shears, vertical velocity or divergence.

The OSSE analyses were all found to be noisier than the corresponding nature data. We also found that the the AFGL model has a tendency to warm and dry out relative to the ECMWF nature model. This warming was seen in all the forecasts. We note that the version of the AFGL model which we used has no radiation parameterization and hence no cooling mechanism although there is a constant source of warming due to the fixed sea surface temperature.

To calibrate these OSSE results with previously conducted OSEs, error statistics were also computed between the OSSE forecasts and the simulated radiosonde observations. Impacts in the N.H. forecasts were larger when calculated as grid point rms errors than when calculated as radiosonde rms difference. As seen in the synoptic charts the greatest impacts tend to be polar, however the verifying radiosondes tend to be midlatitude. The impact of the SSM data was found to be generally small in the Northern Hemisphere, but quite substantial in the Southern Hemisphere. This result is in agreement with numerous previously conducted OSSEs and OSEs which measured the impact of satellite data. When measured in terms of 500 mb height, Southern Hemisphere forecast errors of SSMSAT (SSM+TOVS) lagged those of STATSAT by about 12 (8) hours. By comparison, addition of lidar wind profiler data to STATSAT led to a gain of 36 hours of forecast time. These forecast time gains were essentially unchanged when the OSSE results were calibrated by the ratio of OSSE vs OSE STATSAT-NOSAT impact. The RH impact could not be calibrated with OSE results because there is essentially no difference between STATSAT and NOSAT OSE moisture errors.

There are some important caveats that apply to the results reported here. As is the case with all OSSEs and OSEs, the measured impacts apply to the particular data assimilation system used here. While the assimilation system is reasonably "state of the art", some aspects, in particular the anchoring of the satellite thicknesses and the limitations of data selection, may limit the extent to which our conclusions are generally valid. Since we used simulated data in our experiments, the realism of our OSSE results depends on how realistic the simulated observation errors were. We took particular care that they were of sufficient size and had the appropriate error correlation structure. Finally, the calibration of our OSSE results

with CSE RAOB statistics suffers from the usual problems of the uneven distribution of radiosondes, particularly the bias toward land areas (where no satellite data were used), and the small sample sizes over the Southern Hemisphere.

There is considerable opportunity to improve and refine the experiments reported here and elsewhere. Such efforts would allow the quantification of the relative impact of proposed advanced temperature sounders and doppler wind lidars. In addition cost benefit analyses of observational accuracies could be supported by such studies. It is also important that the assimilation system be modified to best take advantage of the novel observations. And in future studies it will be important to carefully simulate the geographical coverage and error characteristics of proposed instruments. In particular, natural phenomena which give rise to correlated observational errors should be included to the extent possible.

The error characteristics and distribution of simulated temperature and RH retrievals for example should depend on the global distribution of clouds. These geophysical parameters are in turn associated (correlated) in the real world with the geophysical parameters which are to be measured. This is one cause of spatial and temporal error correlations and as such it should be included in our simulation of observational errors. Hence, it is important that the model used to generate nature also can provide a realistic description of the cloud field. In future work we anticipate using a newer nature run generated by the ECMWF using a T106 spectral truncation and more complete physical parameterizations. This nature run includes many diagnostic fields generated by the physical parameterizations.

No existing global model has fine enough resolution to represent all scales of motion which exist in nature. In fact, the smallest scales represented by models are usually severely damped for computational reasons. In real data assimilation these small scales are considered part of the observational error. In fact, for radiosondes, this is the greatest source of error. Although the length scale is small, these errors are correlated. Therefore simulated observations should include spatially correlated errors. This could be accomplished by unfiltering the nature run, thereby restoring the smallest resolvable scales as suggested by Hoffman (1988).

REFERENCES

- Arnold, C.P., C.H. Dey and W.J. Bostelman, 1985: Results of an observing system simulation experiment based on the proposed WINDSAT instrument. In Global Wind Measurements, edited by W.E. Baker and R.J. Curran, A. Deepak Publishing, Hampton, VA, pp. 81-83.
- Atlas, R., E. Kalnay, W.E. Baker, J. Susskind, D. Reuter, and M. Halem, 1985: Simulation studies of the impact of future observing systems on weather prediction. In Preprint volume. Seventh Conference on Numerical Weather Prediction. American Meteorological Society, Boston, MA, pp. 144-151.
- Ballish, B., 1980: Initialization, theory and application to the NMC spectral model. Ph.D. Thesis, Dept. of Meteorology, University of Maryland, College Park, MD, 151 pp.
- Bengtsson, L., M. Kanamitsu, P. Källberg, and S. Uppala, 1982: FGGE 4-dimensional data assimilation at ECMWF. Bull. Am. Meteorol. Soc., 63, 29-43.
- Bergman, K.H., 1979: Multivariate analysis of temperature and winds using optimum interpolation. Mon. Weather Rev., 107, 1423-1444.
- Brenner, S., C.-H. Yang, and S.Y.K. Yee, 1982: The AFGL spectral model of the moist global atmosphere: Documentation of the baseline version. AFGL-TR-82-0393, AFGL, Hanscom AFB, MA, 65 pp [NTIS AD A129283].
- Brenner, S., C.-H. Yang, and K. Mitchell, 1984: The AFGL global spectral model: Expanded resolution baseline version. AFGL-TR-84-0308 [NTIS ADA160370].
- Dalcher, A., and E. Kalnay, 1987: Error growth and predictability in operational ECMWF forecasts. Tellus, 39A, 474-491.
- Daley, R., and T. Mayer, 1986: Estimates of global analysis error from the global weather experiment observational network. Mon. Weather Rev., 114, 1642-1653.

- Deirmendjian, D., 1975: Far-infrared and submillimeter wave attenuation by cloud and rain. J. Appl. Meteorol., 14, 1584-1593.
- Dey, C.H., and L.L. Morone, 1985: Evolution of the National Meteorological Center Global Data Assimilation System: January 1982-December 1985. Mon. Weather Rev., 113, 304-318.
- Dey, C., C.P. Arnold, and W. Bostelman, 1985: Design of a windsat observing system simulation experiment. In Global Wind Measurements, W. E. Baker and R. J. Curran (Eds.), A. Deepak Publishing, Hampton, VA, pp 73-79.
- Falcone, V.J. and R.G. Isaacs, 1987: The DMSP Microwave Suite. Passive Microwave Observing from Environmental Satellites. NOAA Technical Report NESDIS 35, 174-185.
- Falcone, V.J., L.W. Abreu, and E.P. Shettle, 1979: Atmospheric attenuation of millimeter and submillimeter waves: Models and computer code. AFGL-TR-79-0253, 79 pp [NTIS ADA084485].
- Falcone, V.J., L.W. Abreu, and E.P. Shettle, 1982: Atmospheric attenuation in the 30-300 GHz region using RADTRAN and MWTRAN. Proc. Soc. Photo Opt. Instrum. Eng., 337, 62-66.
- Fye, F.K., 1978: AFGWC automated cloud analysis model. Report AFGWC-TM-78-007, 97 pp.
- Gaut, N.E., M.G. Fowler, R.G. Isaacs, D.T. Chang and E.C. Reifenshtein, 1975: Studies of microwave remote sensing of atmospheric parameters. Air Force Cambridge Research Laboratories. AFCRL TR-75-C007, 75 pp. [NTIS ADA008042].
- Hoffman, R.N., 1987: Documentation of the AFGL statistical analysis program (ASAP) for the global multivariate analysis of heights and winds. AFGL-TR-87-0155, Air Force Geophysics Laboratory, Hanscom AFB, MA, 92 pp [NTIS ADA182600].

- Hoffman, R., 1988: Sampling data for OSSEs. Preprints, Eighth Conference on Numerical Weather Prediction, February 22-26, Baltimore, MD, Amer. Meteor. Soc.
- Hoffman, R.H., M. Mickelson and T. Nahrkorn, 1988: Enhancements to the AFGL statistical analysis program (ASAP) for the global multivariate analysis of heights and winds. AFGL-TR-88-0279, AFGL, Hanscom AFB, MA, 110 pp [NTIS ADA202912].
- Hoffman, R.N., J.-F. Louis, T. Nahrkorn, M. Mickelson, and R. Isaacs, 1989: A study of the impact of simulated satellite lidar wind observations. GL-TR-89-0094, AFGL, Hanscom AFB, MA, 77 p.
- Hollingsworth, A., K. Arpe, M. Tiedtke, M. Capaldo and H. Savijärvi, 1980: The performance of a medium range forecast model in winter - impact of physical parameterization. Mon. Wea. Rev., 108, 1736-1773.
- Isaacs, R.G., 1987: Review of 183 GHz moisture profile retrieval studies. AFGL-TR-87-0127, Air Force Geophysics Laboratory, Hanscom AFB, MA, 45 pp [NTIS ADA182417].
- Isaacs, R.G. and G. Deblonde, 1985: Water vapor profile retrievals at 183 GHz: land vs. ocean, clear vs. cloudy. AFGL-TR-85-0095 [NTIS ADA170033].
- Isaacs, R.G. and G. Deblonde, 1987: Millimeter wave moisture sounding: The effect of clouds. Radio Science, 22, 367-377.
- Isaacs, R.G., G. Deblonde, R.D. Worsham, and M. Livshits, 1985: "Millimeter wave moisture sounder feasibility study: the effect of cloud and precipitation on moisture retrievals. Air Force Geophysics Laboratory, AFGL TR-85-0040, 44 pp [NTIS ADA162231].
- Isaacs, R.G., R.N. Hoffman, and L.D. Kaplan, 1986: Remote sensing of geophysical parameters for numerical weather prediction. Rev. of Geophys., 24, 701-743.

- Isaacs, R.G., G. Deblonde, Y.-Q. Jin, R.D. Worsham, C. Grassotti, A.M. Vogelmann, and B.L. Lindner, 1988: Microwave moisture sounder feasibility study, Phase II: Retrieval optimization. AFGL-TR-88-0058, Air Force Geophysics Laboratory, Hanscom AFB, MA, 117 pp [NTIS ADA196495].
- Isaacs, R.G., Y.Q. Jin, G. Deblonde, and V.J. Falcone, 1989: The RADTRAN microwave surface emissivity models. IEEE Transactions on Geoscience and Remote Sensing, 27, (in press).
- Kakar, R.K., 1983: Retrieval of clear sky moisture profiles using the 1983 GHz water vapor line. J. Clim. and Appl. Meteorol., 22, 7, 1282-1289.
- Kakar, R.K. and B.H. Lambrigtsen, 1984: A statistical correlation method for the retrieval of atmospheric water vapor by microwave radiometry. J. Climate and Appl. Meteor., 23, 7, 1110-1114.
- Louis, J.-F., R.H. Hoffman, T. Nehrkorn, T. Baldwin and M. Mickelson, 1987: Baseline observing system experiments using the AFGL global data assimilation system. AFGL-TR-87-0327, AFGL, Hanscom AFB, MA, 92 pp [NTIS ADA 188861].
- Louis, J.-F., R.N. Hoffman, T. Nehrkorn, T. Baldwin, and M. Mickelson, 1988: Four-dimensional data assimilation experiments using the AFGL GDAS. Preprints, Eighth Conference on Numerical Weather Prediction, February 22-26, 1988, Baltimore, MD., AMS, Boston, MA.
- McPherson, R.D., K.H. Bergman, R.E. Kistler, G.E. Rasch, and D.S. Gordon, 1979: The NMC operational global data assimilation system. Mon. Weather Rev., 107, 1445-1461.
- Moore, D.A. and R.E. Peterson, 1984: Air Force Air Weather Services Requirements for Global Meteorological Data. Appl. Opt., 18, 3457-3473.
- Nehrkorn, T., and R.N. Hoffman, 1988: Inferring relative humidity profiles from 3DNEPH cloud data: Technique development and data impact study. AFGL-TR-88-0327, AFGL, Hanscom AFB, MA, 47 pp.

- Newell, R.E., J.W. Kidson, D.G. Vincent, and G.J. Boer, 1974: The General Circulation of the Tropical Atmosphere and Interactions with Extratropical Latitudes. Vol. 2, MIT Press, Cambridge, 371 pp.
- Norquist, D.C., 1983: Development and testing of a multivariate global statistical analysis system. In Objective Analysis and Prediction Techniques, A.M. Gerlach (ed.), AFGL-TR-83-0333, AFGL, Hanscom AFB, MA, pp. 10-48 [NTIS ADA142441].
- Norquist, D.C., 1986: Alternative forms of moisture information in 4-D data assimilation. AFGL-TR-86-0194 [NTIS ADA179792].
- Norquist, D.C., 1988: Alternate forms of humidity information in global data assimilation. Mon. Wea. Rev., 116, 452-471.
- Phillips, N., J. Susskind, and L. McMillin, 1988: Results of a joint NOAA/NASA sounder simulation study. J. Atmos. Ocean. Tech., 5, 44-56.
- Ray, P.S., 1972: Broadband complex refractive indices of ice and water. Appl. Opt., 11, 1836-1844.
- Rodgers, C.D., 1976: Retrieval of atmospheric temperature and composition from remote measurements of thermal radiation. Rev. Geophys. Space Phys., 14, 609-624.
- Rosenkranz, P.W., M.J. Komichak, and D.H. Staelin, 1982: A method for estimation of atmospheric water vapor profiles by microwave radiometry. J. Attp. Meteorol., 21, 1364-1370.
- Schaerer, G. and T.T. Wilheit, 1979: A passive microwave technique for profiling of atmospheric water vapor. Radio Sci., 14, 371-375.
- Schlatter, T., 1981: An assessment of operational TIROS-N temperature retrievals over the United States. Mon. Weather Rev., 109, 110-119.

- Sela, J.G., 1980: Spectral modeling at the National Meteorological Center. Mon. Weather Rev., 108, 1279-1292.
- Selby, S., 1969: Standard Mathematical Tables. The Chemical Rubber Co., Cleveland, OH.
- Smith, W.L., and H.M. Woolf, 1976: The use of eigenvectors of statistical covariance matrices for interpreting satellite sounding radiometer observations. J. Atmos. Sci., 33, 1127-1140.
- Tiedtke, M., J.-F. Geleyn, A. Hollingsworth and J.-F. Louis, 1979: ECMWF model parameterization of subgrid scale processes. ECMWF Tech. Rep. No. 10. Available from ECMWF, Reading, Berkshire, U.K.
- U. S. Standard Atmosphere Supplements: 1966, Washington D.C., 289 pp.
- Van de Hulst, H.C., 1957: Light Scattering by Small Particles. Wiley, New York.
- WMO, 1986: Formats for International Exchange of FGGE Level II Data Sets, International Council of Scientific Unions/World Meteorological Organization, The World Climate Research Programme, WMO/TD-No. 100, WMO, Geneva, 86 pp.
- Wang, J.R., J.L. King, T.T. Wilheit, C. Szejwack, L.H. Gesell, R.A. Nieman, D.S. Niver, B.M. Krupp, and J.A. Gagliano, 1983: Profiling atmospheric water vapor by microwave radiometry. J. Clim. Appl. Meteorol., 22, 781-788.

Appendix A. MICROWAVE SOUNDER FIELDS-OF-VIEW FOR THE 183 GHz OSSE

A.1 Approach

A basic element of the 183 GHz observing system simulation experiment (OSSE) is the inclusion of simulated retrievals of water vapor and temperature from the SSM/T-2 and SSM/T-1 millimeter moisture and microwave temperature sounders, respectively. These sensors along with the SSM/I microwave imager will define the special sensor complement relevant to meteorology to be carried aboard the polar orbiting DMSP satellites in the 1990's time frame. In order to locate the additional initialization data potentially available from this observing system in space and time for the purpose of the OSSE, it is necessary to develop a simple sensor scan line generation program (SLGP) for these sensors. The approach consists of a simple model assuming nominal characteristics both for the DMSP orbital platform and the SSM/T-1 and SSM/T-2 cross-track scanning sensors. Using basic information regarding both platform and sensor and latitude and longitude of each possible instrument specific field-of-view (FOV) is calculated along with the time associated with the observation. The resulting output, therefore, provides a simulated data ephemeris for each sensor which can be used to locate the available satellite data for assimilation into the numerical weather prediction (NWP) model. Once the potentially available data is located in this manner, the appropriate errors in vertical temperature and moisture profiles may be assigned based on their dependence on such factors as latitude and surface type (i.e. ocean vs. land).

The problem is simplified considerably by assuming that the DMSP orbit is circular, the earth is a sphere, and the satellite subtrack can be assumed to be a great circle. In this case concepts from spherical trigonometry can be applied to both subtrack and sensor scan line location calculations. The calculation should thus provide a useful simulation of an operational sensor ephemeris. The calculation may be divided into two parts: (a) location of the satellite subtrack position when the sensor (i.e. SSM/T-1 or SSM/T-2) is observing a specified FOV, and (b) location of the center of the FOV itself.

A.2 Platform and Sensor Characteristics

It is assumed that the DMSP platform is in a circular orbit at an altitude of 833 km with a nominal period of 101.35 minutes. The inclination of the orbital plane with the equatorial plane of the earth is 98.7 degrees insuring sun synchronicity. Other key satellite parameters are summarized in Table A-1. These include the time and longitude of the ascending node chosen to start the calculation. The ascending node positions the satellite at the equator crossing from southern to northern hemisphere. The longitude and time of the ascending node determine the local solar time at which the satellite transmits the meridian. This determines whether data is being collected from a morning or noon satellite.

Both the SSM/T-1 and SSM/T-2 sounders are cross-track scanning sensors. Data coverage is provided by scanning perpendicular to the satellite subtrack in a specifiable scanning pattern. The desired scanning pattern consists of a fixed number of scan positions incremented along the scan and an interscan calibration period. Each scan position determines a field-of-view. It should be noted that modeled FOV's are approximate. One source of error are those associated with pointing angle accuracy. For example, the beam position repeatability, scan plane alignment, and distribution of the actual beam position about the desired beam position have tolerances of about 0.4 degrees. Additionally, the beamwidth for the SSM/T-2 used in our calculation corresponds to the 183 GHz channels only. The two lower frequency channels at 91.6 and 150 GHz have beamwidths of 3.7 and 6.7 degrees, respectively. Finally, since beamwidths for both sensors are determined by the 3 dB power points, there is some overlap.

The SSM/T-1 views 7 positions, one at nadir and three to either side. The scan angle increment is 12 degrees and the FOV is twelve degrees for a total scan from -36 to 36 degrees of nadir. The total swath width is thus 42 degrees to either side of nadir. The SSM/T-2 has a total of 28 viewing positions which scan from -40.5 to 40.5 degrees of nadir in steps of 3 degrees. Each FOV is approximately 3 degrees so that the total swath width is identical to that of the SSM/T-1. The SSM/T-2 never actually views the nadir position along the satellite subtrack. Two scan positions, those denoted 14 and 15 view -1.5 and 1.5 degrees, respectively, from nadir. The scan patterns for the SSM/T-1 and SSM/T-2 sensors are illustrated in Figure A-1.

The total scan cycle period, T' , for the SSM/T-1 sensor, i.e. the time it takes to sweep out a full 360 degrees including FOV sampling and calibration is 32 seconds. The scan cycle period for the SSM/T-2 is 8 seconds. During the scan cycle period each sensor views FOV's for 42 degrees and calibrates etc. for the rest of the cycle. Assuming a constant rotation rate for the optics, a FOV sampling time and an interscan period can be calculated. These and other sensor related characteristics are given in Table A-2. In order to keep account of the sensor position at any time, we define a scan line index, m^j , and a scan position index, n^j , for each sensor j , where $j = 1, 2$ denote the SSM/T-1 and SSM/T-2, respectively. Associated with each index pair (m^j, n^j) will be a longitude, latitude, and time (λ, ϕ, τ) . The calculation is initialized by specifying the time and longitude of the ascending node and the initial sensor positions. (By definition, the latitude at the ascending node time is zero.) The initial sensor positions are:

$$\begin{aligned} (m^1, n^1)t_0 &= (m_0^1, n_0^1) \\ (m^2, n^2)t_0 &= (m_0^2, n_0^2) \end{aligned} \tag{A.1}$$

and provide a starting point for simulating the scan cycle. The scan position index is incremented by one until the total number of scan positions, N^j , for each sensor is reached. At this point, the scan line index is incremented. Based on these indices the sensor scan angle and time past the ascending node can be evaluated. The scan angle at scan position n^j is given by:

$$\psi_n^j = \psi_o^j + \left\{ n^j - \text{INT}\left(\frac{N^j}{2}\right) + 1 \right\} \Delta\psi^j \tag{A.2}$$

where ψ_o^j is the initial scan angle, n^j is the scan position index, N^j is the total number of scan positions, and $\Delta\psi^j$ is the scan angle increment for sensor j . Scan angles can take on values which are both positive and negative depending whether they are to the starboard or port side, respectively, of the spacecraft velocity vector. The time along the satellite subtrack can be evaluated by noting the elapsed time since the ascending node indexed by the number of scan lines acquired and the current scan position. Thus the current time will be:

$$t(m^j, n^j) = t_0 + [(N^j - n_0^j) + n^j](t^j/N^j) + m^j - m_0^j) \Delta t^j \quad (A.3)$$

$$+ (m^j - m_0^j - 1)N^j$$

where t^j is the FOV sampling time and Δt^j is the interscan period.

Table A-1. DMSP Satellite Platform Characteristics

Parameter	Description	Assumed Value
P	Satellite period (m)	101.35 min
ϵ	Satellite inclination to equatorial plane (deg)	98.7 deg
Z_0	Satellite altitude (km)	833 km
R_0	Radius of the Earth (km)	6371 km.
t_0	Time of ascending node (h,m,s)	0:0:0 (GMT)
ϕ_0	Longitude of the ascending node (deg)	0.0 deg

Table A-2. Sensor Characteristics for the SSM/T-1 and SSM/T-2 Sensors

Parameter	Description	Assumed Value	
		SSM/T-1	SSM/T-2
ψ_0^j	Initial scan angle sensor j (deg)	0.0	1.5
$\Delta\psi^j$	Cross-track scan angle increment for sensor j (deg)	12.0	3.0
n^j	Total number of scan positions for sensor j	7	28
T	Scan period for sensor j (s)	32.0	8.0
t^j	FOV sampling time for sensor j (s)	7.47	1.87
Δt^j	Interscan period for sensor j (s)	24.53	6.13
m^j	Scan line index for sensor j		
n^j	Scan position index for sensor j		
$\psi^j(n^j)$	scan angle at scan position index n^j for sensor j (deg)		
$e^j(n^j)$	Azimuth angle at scan position index n^j for sensor j (deg)		

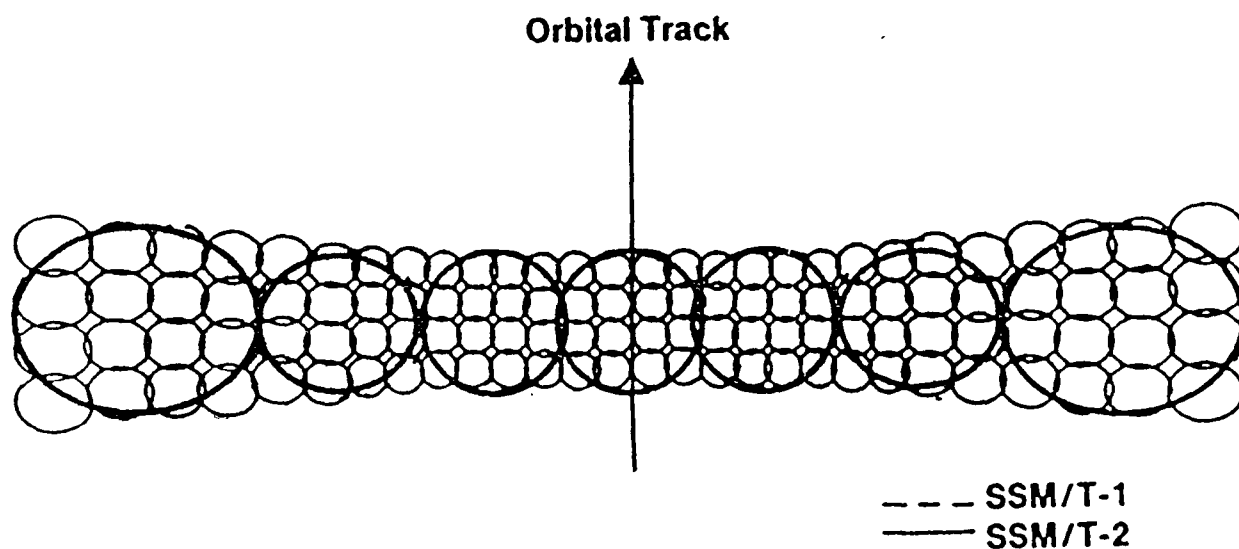


Figure A-1. SSM/T-1 and SSM/T-2 FOV scan line pattern.

A.3 Field-of-View Location

The geometry required to calculate locations for each field-of-view is illustrated in Figure A-2. Here the ascending node is denoted by the letter A, a general point along the satellite subtrack as letter B, and the starboard extent of a general scan line denoted by the letter E. The pole is letter C. Assuming the satellite subtrack (arc AB) to be a great circle, we can calculate the latitude and longitude of point B by applying Napier's analogies (Selby, 1969, p. 223) for the spherical triangle ABC. The latitude at point B will be given by the arc length (in degrees) of side a:

$$\lambda(t) = 90.0 - a \quad (\text{A.4})$$

while the longitude will be given by the angle C:

$$\phi(t) = \phi_0 + C + (t - t_0) \omega \quad (\text{A.5})$$

where ω is the angular velocity of the earth. The longitude increment is added to that of the ascending node and a correction is made for the rotation of the earth since the ascending node time.

The unknowns a and C are obtained from our knowledge of sides c and b and angle A. Angle A is a constant and is equal to the difference in angle between the orbital plane of the satellite and a typical meridian or:

$$A = e - 90.0 = 8.7 \text{ deg} \quad (\text{A.6})$$

Side b is simply the arc length from point A (on the equator) to the pole point C, or:

$$b = 90.0 \text{ deg} \quad (\text{A.7})$$

The length of side c is obtained from the elapsed time since the ascending node realizing that one orbital period corresponds to 360 degrees. Thus:

$$c = 360 (t - t_0) / p \quad (\text{A.8})$$

$$a = 2 \tan^{-1} [h(b, c, B, C)] \quad (\text{A.9})$$

$$C = \tan^{-1} [f(b,c,A)] - \tan^{-1} [g(b,c,A)] \quad (A.10)$$

where

$$B = \tan^{-1} [f(b,c,A)] - \tan^{-1} [g(b,c,A)] \quad (A.11)$$

and the functions f , g and h are given by:

$$f(b,c,A) = \tan \frac{1}{2} (B+C) = \cos \frac{1}{2} (b-c) \sec \frac{1}{2} (b+c) \cot \frac{1}{2} A \quad (A.12)$$

$$g(b,c,A) = \tan \frac{1}{2} (B-C) = \sin \frac{1}{2} (b-c) \csc \frac{1}{2} (b+c) \cot \frac{1}{2} A \quad (A.13)$$

$$h(b,c,B,C) = \tan \frac{1}{2} a = \tan \frac{1}{2} (b-c) \sin \frac{1}{2} (B+C) \csc \frac{1}{2} (B-C) \quad (A.14)$$

Upon substitution of the quantities A (A.6), b (A.7), and c (A.8) into equations (A.11) through (A.14), the unknowns a (A.9) and C (A.10) can be evaluated. Equations (A.4) and (A.5) then yield the desired subtrack point latitude and longitude, respectively.

Similar considerations apply to the location of specified fields-of-view along the scan line. In this case the spherical triangle BEC (Figure A-2) is considered. The length of side a (equation A.4) is simply:

$$a = 90.0 - \lambda(t) \quad (A.15)$$

The angle at B is determined from the orbital inclination and is:

$$B = 81.3 \text{ deg} \quad (A.16)$$

The length of the scan line segment f_n^j at position n^j in degrees can be obtained from the scan angle (A.2) and the local zenith angle given by:

$$\theta_n^j = \sin^{-1} \left[\frac{R_0 + Z_0}{R_0} \sin \psi_n^j \right] \quad (A.17)$$

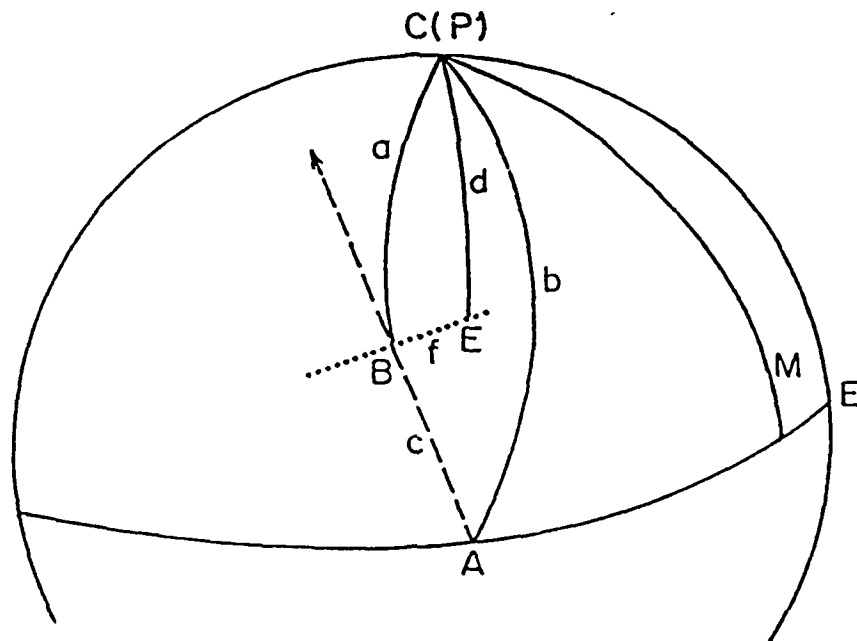
From Figure A-3, it can be seen that this angle is:

$$f_n^j = \theta_n^j - \psi_n^j \quad (A.18)$$

The Napier analogies (equations (A.9) through (A.14)) can now be applied to solve for the latitude and longitude for the FOV specified by each sensor's scan indices. The unknowns are the length (in degrees) of the side d and the new angle C included by ECD in Figure A-2. Given these, the latitude and longitude of the field-of-view are:

$$\lambda(n^j, m^j) = 90.0 - d \quad (A.19)$$

$$\phi(n^j, m^j) = \phi_s - c \quad (A.20)$$



--- Satellite Subpoint Track
 Sensor Scan Line

Figure A-2. Geometry for location calculation.

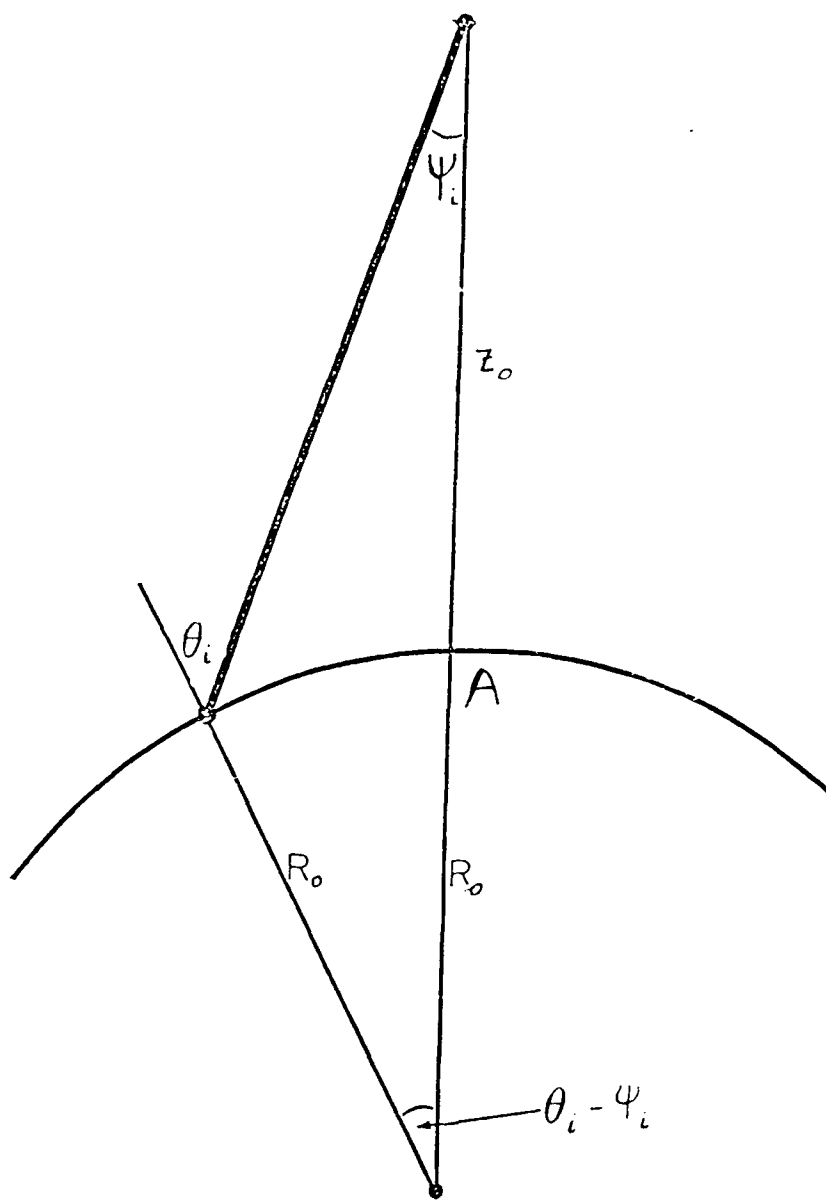


Figure A-3. Scan angle geometry.

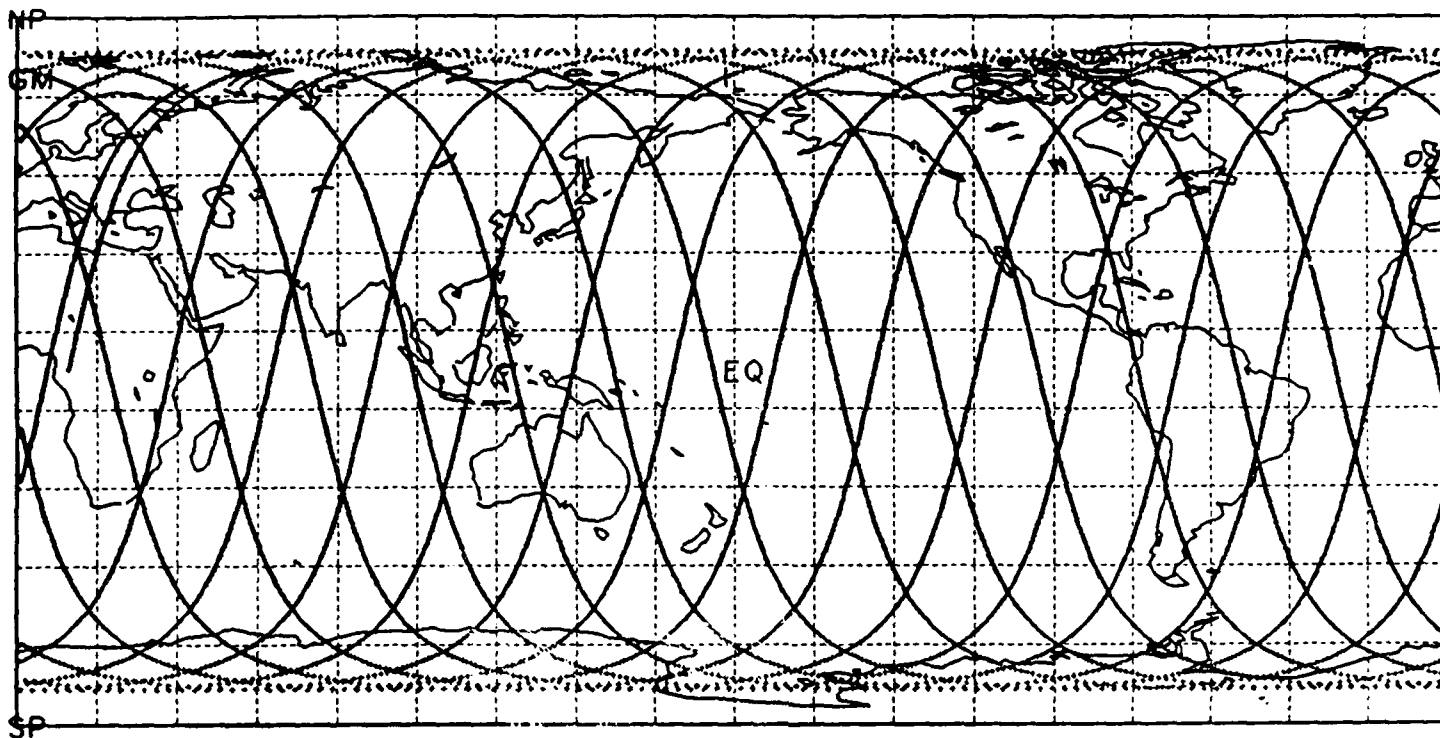


Figure A-4. Subsatellite track for polar orbiting platform (24 hours of orbits).

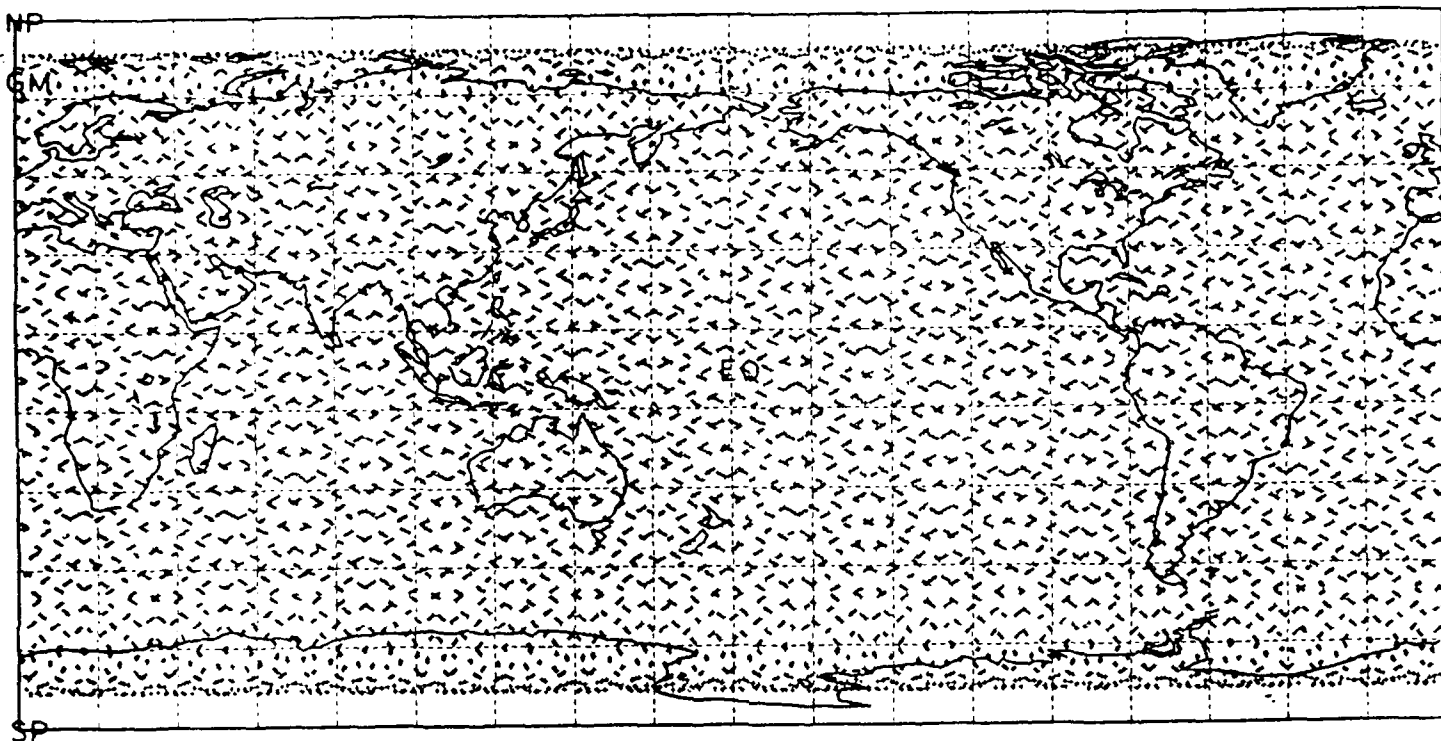


Figure A-5. Subsatellite points indicating coverage density for two weeks of orbits.

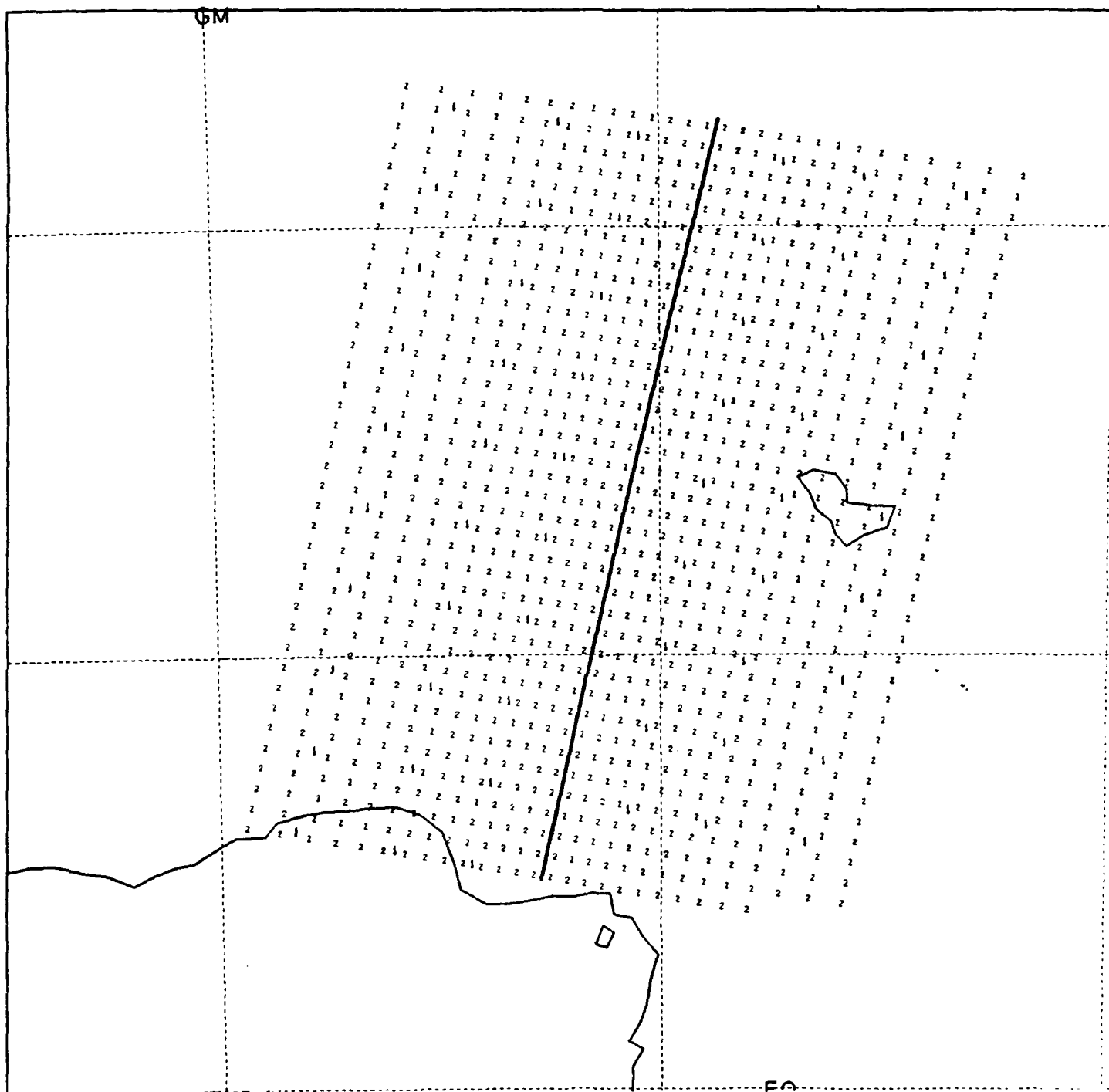


Figure A-6. Location of SSM/T-1 temperature soundings (1) and SSM/T-2 water vapor soundings (2) assuming FOV's of 180 and 50 km, respectively.